The Use of Biopolymers In the Synthesis and Electrode Preparation Of P3-$Na_{2/3}Ni_{1/3}Mn_{2/3}O_2$ Na-ion Cathode Material

Silvija Zilinskaite

For the degree of Doctor of Philosophy

Supervisors:
Primary - Dr Rebecca Boston
Secondary - Dr Nik Reeves-McLaren

The University of Sheffield
Faculty of Engineering
Department of Materials Science and Engineering

October 2022

Abstract

The increased demand for lithium-ion batteries (LIBs), and the stain this will place on supply, has sparked significant interest in sodium-ion batteries (NIBs). Sodium is cheaper and more abundant than Li, making NIBs a more sustainable option for certain applications. While numerous NIB electrode materials which seek to maximise electrochemical properties have been developed, it is also important to consider other aspects of sustainability when developing NIBs, such as synthesis methods and the components used to cell fabrication. The aims of this thesis is to use a low energy intensity synthesis method for Na-ion cathode materials and investigate the use of environmentally friendly binders in cathode preparation using polymers derived from nature.

$Na_{2/3}Ni_{1/3}Mn_{2/3}O_2$ (NNM) is a strong candidate for use in Na-ion battery cathodes, due to its relatively high theoretical capacity of 173 mAh g^{-1} and working voltage around 3.7 V Na^+/Na, giving it one of the highest theoretical energy densities compared to other Na-ion transition metal layered oxides. NNM can form two polymorphs depending on final calcination temperature: a high temperature phase which occurs above 800 °C, and a low temperature phase which should have lower energy requirements during synthesis. This low temperature phase is often overlooked, due to the challenges associated with forming phase pure materials at low temperatures using solid state synthesis, since high temperatures are required to fully react the NiO precursor. In previous work, however, this low temperature NNM phase was successfully synthesised at 550 °C using an emergent method known as biotemplating. The work presented herein takes the next steps in the understanding and application of this synthesis method.

Biotemplating is a synthesis method that utilises water-soluble naturally-occurring polymers to spatially distribute a homogenous mixture of different metal cation precursors. During initial stages of calcination, the polymer prevents recrystallisation of the reagent phases, preserving the atomic level mixing found in solution. As the template combusts during calcination, numerous nucleation sites form, allowing for reactions to occur quickly and at lower temperatures vs solid state. Thus, less energy-intensive reaction conditions are required for synthesis of product phases. Biotemplating is therefore a promising synthesis method for complex oxides, because some polymers are able to interact with a number of different cations in solution due the deprotonated functional groups.

To gain a better understanding of the factors which affect biotemplating, the crystallisation process with different dextran concentrations was investigated and was compared to solid state synthesis. It was found that with sufficient dextran, the low temperature NNM phase began to crystallise at a much lower temperature of 300 °C, whereas in solid state synthesis it appears at 500 °C. In addition, the final phase fractions after calcination were significantly impacted depending on the concentration of dextran; the higher the concentration, the lower the amount of secondary phases, such as NiO.

The low temperature phase synthesised with a low concentration of dextran had a large phase fraction of NiO, and was likely to be Ni-deficient in the transition metal layers. It exhibited a lower initial discharge capacity compared to stoichiometric NNM phase, because the main capacity contribution is from the $Ni^{2+/3+/4+}$ redox, although the cycling stability was found to be better. This improvement was attributed to vacancies in the transition metal layers, which are able to better accommodate structural distortions during electrochemical cycling, as found in the literature. This brings opportunity to investigate alternative methods for improving cycling stability of these types of materials.

Regardless of synthesis conditions, the low temperature phase NNM exhibited poor cycling stability when charged to 4.5 V. This was found to be due to a phase transition which occurs during cycling, and is associated with volume change and structural instability. To further stabilise the structure to higher voltages, a substitutional doping scheme was investigated, introducing some Cu in place of Ni in$Na_{2/3}Ni_{1/3-x}Cu_xMn_{2/3}O_2$ (x = 1/12, 1/6 and 1/3). Again dextran biotemplating synthesis was used, to preserve the lower reaction temperatures and atomic level mixing. Specimens with Cu content of x= 1/12 and 1/6 formed a minimal amount of secondary phases (<2 wt.%), further demonstrating the ability to synthesise complex oxides using biotemplating. Specimen x = 1/6 exhibited improved cycling stability at extended voltage range of 2 – 4.5 V, with a capacity retention of 77.6 % after 50 cycles, whereas NNM (x = 0) was 53 %.

Finally, in order to consider the materials used in the wider battery architecture, water-based binders were investigated. Binders play a key role in maintaining the structural integrity of the electrode but often use toxic and expensive solvents, and polymers with low flexibility. Here I investigate the water stability of NNM cathodes, and thereafter the use of xanthan gum as a water-based binder. The electrochemical performance was comparable to electrodes prepared with more traditional materials. This shows that biopolymers are a viable option for binders in such electrode materials.

It has been demonstrated that dextran biotemplating is a facile synthesis method for complex Na-ion layered oxide cathodes. It enables early onset crystallisation at low temperatures of the desired phase, thus reducing the overall required energy intensity for synthesis. The investigated materials have shown to be stable against water intercalation, thus allowing the use of sustainable water-soluble binders in cathodes. Here, biopolymers have shown great versatility in the cathode preparation process, improving the sustainability across different aspects of Na-ion batteries.

Acknowledgements

I would first like to thank my supervisor Dr. Rebecca Boston for all the opportunities that she opened up for me and her support and encouragement throughout my whole PhD journey, especially with the difficulties caused by the Covid-19 pandemic. I am grateful to have had such an understanding and kind supervisor, who also pushed me to do better.

I would also like to thank my second supervisor, Dr. Nik Reeves-McLaren who I started my research journey with during my MEng research project. Thank you for teaching me so much about XRD and refinement techniques, I have learned so much during this project.

I would like to extend my gratitude to the individuals that have trained and supported me at the University of Sheffield; the staff at the Sorby Centre, Dr Rob Moorehead for his support with XRD, the members from the Kroto battery lab, Functional Materials L-floor labs and I06 Battery Fabrication lab. I would also like to thank Dr. Laura Wheatcroft who was always there when I needed help and willing to answer all my questions. I also have big thanks for my thesis mentor Dr. Jenny Prisutova, who made me realise thesis writing wasn't so bad.

I have the greatest gratitude to the Energy Storage CDT for giving me this opportunity. I enjoyed being part of such a diverse community and learned so much from everyone. I also want to thank the International Consortium of Nanotechnologies, who also funded this project and gave me the opportunity to go to Singapore to meet fellow students around the world, which was a highlight during my PhD.

I would also like to thank everyone in the Sustainable Oxide Processing group. I have really enjoyed working with all of you and I am very grateful for all you support and all the long lunch breaks we have had. I also want to thank Yu-han Huang for being the best office neighbour.

The friends I have made during my Masters course that also went on to do PhD, I want to thank you for all the venting sessions. I also want to thank my mum, stepdad, grandparents and my partner's family for all the support, encouragement and love. Finally I want to thank my partner, Adam, who has been there through all the good and the bad. This would not have been possible without you.

Contents

1 Introduction

1.1 Motivation & Aims

There is a great drive to develop sustainable electrochemical storage, not just from the perspective of battery materials, but also the processing and manufacturing methods. Demand for Li-ion batteries (LIBs) is increasing, especially with the rise of electric vehicles (EVs) and stationary grid storage,[1,2] which will likely put a strain on lithium supply in the future. The high energy densities in LIBs make them ideal for portable electronics and small EVs, however, such performance indicators are not always as important in other applications. One such example is stationary grid storage, where mass and space is not an issue. This opens up the opportunity to develop alternative battery chemistries that may help to lessen the demand on lithium supply, as well as using more sustainable materials, such as Na-ion batteries (NIBs).

The advantages of NIBs over LIBs is that Na is cheaper and significantly more abundant than Li, and they operate similarly to LIBs, so the technology can be easily transferred.[3] There are, however, many challenges associated with Na-ion electrode materials due to the large Na^+ ionic radius, causing multiple phase transitions during electrochemical cycling, and therefore affecting Na^+ diffusion kinetics and structural stability.[4] Different methods have been employed to overcome this, such as substituting in other metal cations to stabilise the structure at higher voltages,[5] and reducing the particle size or forming porous microstructures, to improve diffusion kinetics.[6,7]

One promising cathode material, $Na_{2/3}Ni_{1/3}Mn_{2/3}O_2$ (NNM), can form the form two polymorphs depending on the synthesis calcination temperature.[8] Previous research has mostly focussed on the high temperature phase, where charge compensation, degradation mechanisms and different ways to overcome them were investigated.[5,9,10] The low temperature phase has not been studied to the same extent, potentially due to the difficulties with synthesis using traditional methods such as solid state synthesis. Recent studies have shown that it is possible to synthesise the low temperature phase at calcination temperatures around 550 °C using an emergent biotemplating technique using dextran.[6] This is a much lower temperature, compared to what is required for the high temperature phase (800 °C).[8,11] This makes the low temperature polymorph more sustainable in terms of energy use during synthesis.

Secondary phases tend to be present after synthesis using dextran biotemplating and can persist to some extent at temperatures as high as 850 °C.[6] The aim of results chapter 3 was to investigate why this occurred and the role dextran has in the synthesis of the low temperature NNM polymorph, especially at temperatures where dextran combusts. This gave insight into the interactions between the different precursors and the biotemplate, and allowed for optimisation in terms of the ratio of precursors to template. Increasing the concentration of dextran during synthesis led to a lower fraction of secondary phases after calcination, and the impact of the different concentrations on electrochemical performance was also investigated. Phase progression was compared to conventional solid state synthesis, which highlighted how in dextran biotemplating the reaction temperature and time was significantly reduced, enabling early onset crystallisation NNM.

NNM exhibited poor cycle life at extended voltage cycling range due to phase transitions. To stabilise the structure at higher voltage, electrochemically inactive or less redox active metals can be substituted into the structure, [12,13] which has not been done for the low temperature NNM polymorph in the literature. As biotemplating is intrinsically ideal for synthesis of complex materials such as ternary and quaternary oxides,[14] the addition of another metal cation should be simple in the synthesis process. The aim of chapter 4 was to substitute some Ni^{2+} for Cu^{2+} in $Na_{2/3}Ni_{1/3-x}Cu_xMn_{2/3}O_2$, using the same dextran biotemplating synthesis method, where x = 0, 1/12, 1/6, 1/4 and 1/3. The solid solution limit of Cu was found to be slightly below x = 1/6, however specimens with Cu content x = 1/12 and 1/6 exhibited improved cycling stability compared to NNM. The water stability of Cu substituted P3 materials was also investigated, as substitution normally deteriorates the ability to prevent water intercalation.

Polyvinylidene fluoride (PVDF) is a commonly used binder in both NIBs and LIBs which requires N-Methyl-2-pyrrolidone (NMP), a toxic, expensive and flammable solvent, to dissolve it.[15] A variety of sustainable water soluble biopolymers have the necessary electrochemical stability and adhesion properties for application as binders in electrode materials.[16] Many Na-ion electrode materials are not suitable for such binders, as exposure to water can cause deleterious impact on electrochemical performance.[17,18] However, the low temperature NNM polymorph is stable after exposure to water.[19] Results chapter 5 contains a literature review on water soluble binders, in particular xanthan gum as it was chosen to prepare cathodes in this work, where performance was compared with cathodes prepared with PVDF and NMP. The work presented in this chapter has been published in Frontiers in Energy Storage (Front. Energy Res., 10, 909486 (2022). doi: 10.3389/fenrg.2022.909486)

The use of biopolymers can improve the sustainability of various aspects in NIB fabrication, from reducing the energy requirements of synthesis of electrode materials, to replacing the use of toxic and expensive electrode components such as binders, which is the main aim in this thesis. Here, this has been demonstrated with the low temperature NNM polymorph.

1.2 Literature Review

1.2.1 Overview of Electrochemical Energy Storage

With the rise of climate change, global efforts are needed to ensure contributing factors such as greenhouse gas emissions are significantly limited. As of November 2021, there are 193 parties, including the European Union that have signed on to the Paris Agreement which began in December 2015.[20] The goal of the agreement is to limit global warming to below 2 °C. To achieve this goal, many countries are striving to achieve net zero emissions by 2050.[21] The UK intends to cut emissions by 78 % by 2035 compared to 1990 levels to be set on track for net zero emissions.[22] Globally, the sectors with the greatest greenhouse emissions are from electricity production, heat and transport,[23] therefore the greatest impact can be achieved by targeting such sectors. Hence, there has been significant global uptake in electric vehicles,[2] as well as increased electricity generation from renewable and/or low carbon sources.[24] In the UK, for the past 10 years there has been significant shift from electricity generation from coal to wind, solar and biofuels.[25]

Although this shift may address the issues associated with emissions, renewable energy presents another set of challenges. Wind and solar can be unpredictable to some extent and availability of these sources may not always match demand, making grid balancing in terms of supply and demand more of a challenge. This leads to curtailment, where renewable energy power stations are disconnected from the grid due to lack of demand,[26] causing a negative impact on revenues and reduced utilisation.[27] To overcome this issue, the unused energy can be stored either using large scale pumped hydroelectric, thermal storage or batteries, where the latter is the easiest to deploy anywhere and has relatively low maintenance.[1] Electrochemical energy storage is capable of responding within seconds, so ideal for situations such as unplanned power outages, load shifting and can also maintain accurate grid frequency.[1,28] It has already been demonstrated that Li-ion battery technology improved utilisation of renewable energy, making energy from such sources more competitive in the market.[29–31] However, as usage of Li-ion batteries increases in various applications, especially in EVs, there has been growing speculation as to whether LIB production can meet the demand of all these industries.[32,33] Another issue associated with current commercial LIBs is the use of unsustainable, unethical and expensive raw materials such as cobalt.[34,35] Hence there is opportunity to develop batteries that made from abundant and economical materials.

1.2.2 Li-ion Batteries

The first Li-ion battery was commercialized by Sony in 1991, based on the hard carbon/$LiCoO_2$ system, [36,37] later updated to replace the hard carbon with graphite as the anode.[37] Compared to what was already on the market at the time, these cells had the highest specific energy density for rechargeable batteries.[38] Since then, other Li-ion chemistries have been commercialised with cathodes such as lithium nickel manganese cobalt oxide (NMC) and lithium nickel cobalt aluminium oxide (NCA) [39], mostly for use in EVs, due to greater energy densities compared to LCO [40]. LIBs have shaped the modern world, making portable electronics possible,[41] and continue to do so in with EVs and grid-scale energy storage. However, the increased demand is likely to put a strain on lithium supply in the future,[32,33] and recycling of LIBs in Europe still requires at least another 10 years of development.[42] Alternative battery chemistries can alleviate some of these issues as not all applications require high gravimetric energy densities, such as Na-ion batteries (NIBs).

1.2.3 Na-ion Batteries

Na-ion batteries were first developed similar time as LIBs, however due to the higher energy densities of LIBs, NIBs were mostly forgotten about, up until the last decade,[43] spurred on by the potential issues with lithium supply. Na is cheap and has an abundance of 23,600 ppm in the Earth's crust, significantly higher than Li with an abundance of 20 ppm.[44] Other advantage of NIBs is that they have similar working principles as LIBs, therefore manufacturing and other processes can easily be transferred to NIBs, making adoption easier.[43] NIBs can also be discharged to 0 V, making shipping and storage cheaper and safer compared to LIBs.[45] Li-ion cells cannot be discharged to 0 V, because this causes the anode potential to increase significantly, leading to oxidation of the Cu current collector.[46] At this point Cu dissolution occurs, weakening the adhesion with the anode. In addition, Cu deposition onto the cathode can occur, where Cu dendrites can form leading to internal short circuit. In NIBs, Al current collector is used for the anode because Na does not alloy with it due to the slightly higher redox potential of Na/Na^+ compared to Li/Li^+ and is very resistant to oxidation.[46]

Energy densities in NIBs are lower compared to LIBs because of the larger mass and ionic radius (1.02 Å for Na vs 0.76 Å for Li^+ [47]) and slighter lower standard electrochemical potential (2.71 V for Na vs 3.01 V for Li) based on metallic sodium and lithium anode.[48] This would make it difficult to match the energy densities that LIBs are capable of.[49] However the alkali ion in cells takes up a relatively small volume and mass fraction in a full cell, and when considering other components in a cell, there is scope to improve energy density in NIBs, and as such there has been ongoing research.[3,50]

The main challenges of NIBs are associated with the larger ionic radius of Na^+ compared to Li^+, causing multiple complex phase transitions during electrochemical cycling,[51] which can be identified by the multiple plateaus in the voltage profile, as shown in figure 1.1 that compares $LiCoO_2$ and $NaCoO_2$. Such phenomena causes sluggish Na^+ diffusion kinetics and structural instability due to the significant volume changes.[52] There has been significant development in improving structural stability of NIB electrodes, [5,53] which will be discussed in more detail in later sections.

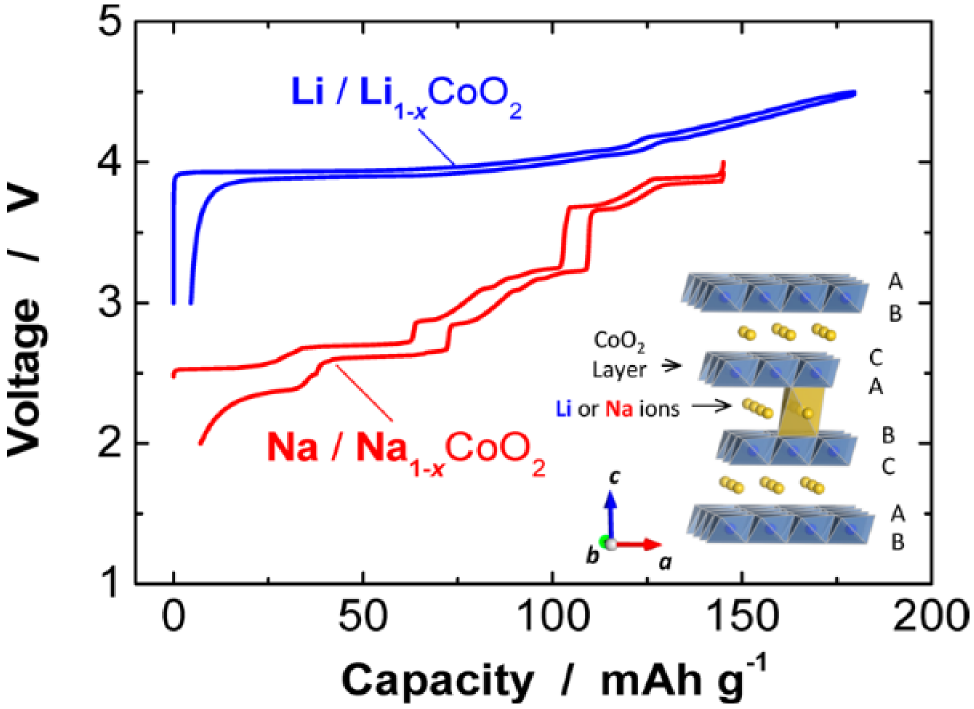

Figure 1.1: *Voltage profile comparison if $LiCoO_2$ and $NaCoO_2$. Taken from ref*[44].

1.2.4 Principles of Electrochemical Cells

A standard rechargeable intercalation battery consists of an anode (negative electrode), cathode (positive electrode), figure 1.2. They are separated by an electrically insulating barrier that allows Li^+/Na^+ to pass through, transferred by an electrolyte. There are also current collectors at both electrodes that are conductive and allow the flow of electrons to the external circuit. The electrodes are connected via an external circuit and during discharge electrons pass through the circuit from the anode to the cathode, whereas Li^+/Na^+ ions pass through the electrolyte to the cathode. The shuttling of these ions between the cathode and anode during charge and discharge is known as the “rocking chair” mechanism.[49]

During discharge when the electrodes are connected to the external circuit, because the chemical potential on the anode side is higher than cathode side, the anode is oxidised and the cathode is reduced.[54–56] These processes are favourable, allowing for the spontaneous reactions to occur.[54] During charge, the reverse reactions are less favourable, therefore external current is needed to reduce the anode and oxidise the cathode.

For a typical $LiCoO_2$/graphite cell, the half-cell reactions upon discharge are:

Cathode: $CoO_2 + Li^+ + e^- \rightarrow LiCoO_2$, $E^0 = 1$ V vs. Li/Li^+

Anode: $LiC_6 \rightarrow C_6 + Li^+ + e^-$, $E^0 = 3$ V vs. Li/Li^+

And the full-cell reaction is:

$LiC_6 + CoO_2 \leftrightarrow C_6 + LiCoO_2$ $E^0_{cell} = 3 - 1 = 2$ V

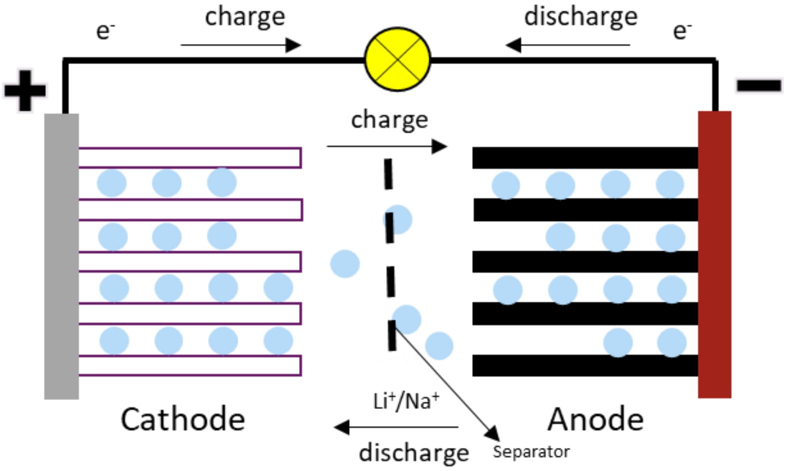

Figure 1.2: *Diagram of working principle of Li-/Ni-ion battery.*

The theoretical capacity in mAh g^{-1} of electrode materials are calculated by the equation:

$$Q_{th} = \frac{nF}{3.6M_w}$$

Equation 1.1

Where n is the number of electrons transferred per unit formula (equal to the number of Na^+/Li^+), F is the Faraday constant (96485 C mol^{-1}), M_w is the molecular weight and 3.6 is the conversion from As to mAh.[57]

The voltage of an electrochemical cell, which is equivalent to open-circuit voltage, is given by the equation:

$$V_{cell} = \frac{\mu_C - \mu_A}{F}$$

Equation 1.2

Where μ_C and μ_A are the chemical potentials of the cathode and anode respectively and F is the Faraday constant.[58]

The drive to achieve a high V_{cell} is that is leads to increased energy density:[58]

$$E_{stored} = Q_{cell} \times V_{cell}$$

Equation 1.3

In NIBs, the working potential of hard carbon anode is *ca.* 0.25 V vs. Na/Na$^+$,[59] therefore V_{cell} is governed by the working potential of the cathode. Hence there are has been work on developing high-voltage cathodes.[60]

V_{cell} is also limited by the electrochemical stability window of the electrolyte, figure 1.3, hence it is not possible to simply choose a cathode with the highest potential and an anode with a lowest potential. The stability window of the electrolyte is governed by the energy difference between the lowest unoccupied molecular orbital (LUMO) and the highest occupied molecular orbital (HOMO). Ideally the potentials of the electrodes should be within the electrochemical stability window. If μ_C is below the HOMO, the electrolyte can oxidise and if μ_A is above the LUMO, then it can reduce. In both cases, a passivating layer can form at the electrode/electrolyte interface. However, in some cases a stable passivating layer can prevent further electrolyte degradation and protect the electrode material from exfoliation and thus improve cycling life.[61,62] This passivating layer can also increase the resistance due to impeded Na$^+$ diffusion as well as consumption of Na$^+$ from the electrolyte, causing poor electrochemical performance, especially if it is unstable.[63] Electrolyte additives can improve stability of this layer, [64] which is important as the potential of carbon based anodes is often above the LUMO of the electrolyte.[65,66]

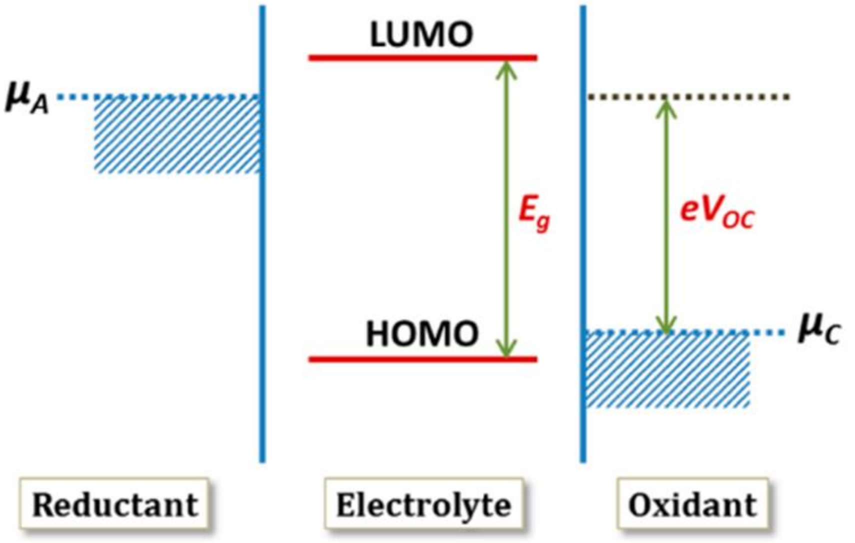

Figure 1.3: *Electrolyte stability window, E_g, in relation to the potentials μ_A and μ_C. Taken from ref*[67].

1.2.5 Cathode Materials for Na-ion Batteries

Various groups of materials have been studied for cathodes in NIBs such as polyanionic compounds,[68] metal hexacyanometalates (Prussian blue analogues),[69] metal oxides,[70] and organic compounds,[49] as summarised in figure 1.4. Polyanionic compounds display good cycling stability but exhibit low specific capacities and energy densities due to sluggish kinetics and hexacyanometalates can exhibit high specific energies and wide operating potentials, however suffer from poor cycle life.[71] Organic compounds can achieve high specific capacities, but have low operating voltages thus limiting energy densities.[71] The following sections discuss these materials in more detail.

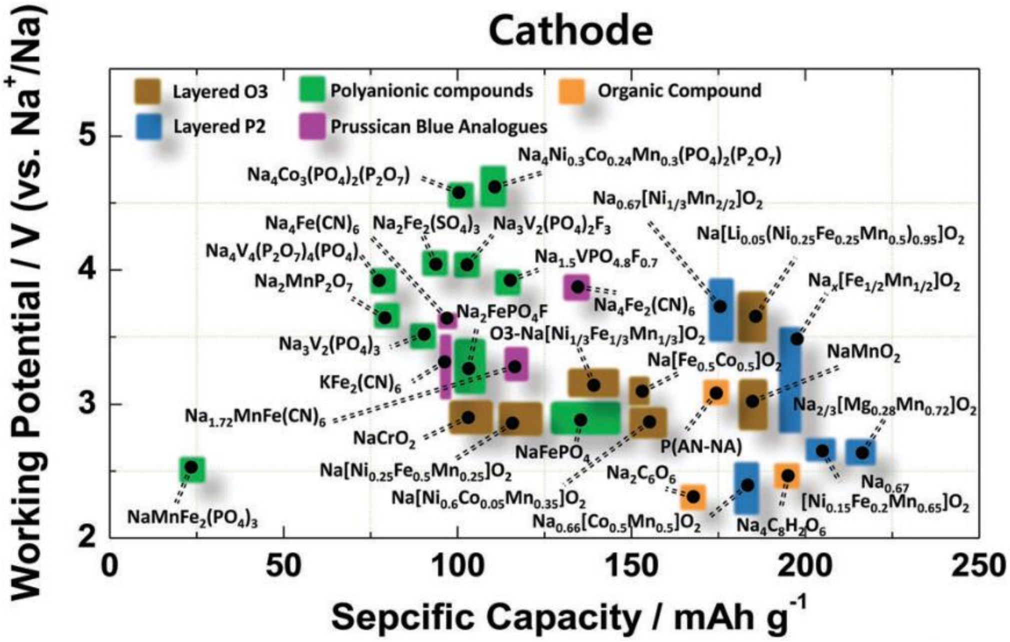

Figure 1.4: *Operating voltages vs. specific capacities for different Na-ion cathode materials. Taken from ref*[49].

1.2.5.1 Polyanionic phosphate compounds

There are various types of polyanionic compounds that have been considered for NIBs, of which olivine-type structures have been considered the best. Generally they consist of TMO_6 octahedrons that share corners or edges with XO_4, where X can be S, P, Si, As, Mo or W,[68] figure 1.5. This forms 1D tunnels for Na^+ diffusion. Such materials undergo very minimal structural change during (de-)intercalation of Na ions, enabling good cycling stability. In addition, they exhibit suitable operating voltages, figure 1.4. However, they intrinsically exhibit low conductivity, limiting capacity and rate capability.[68,72]

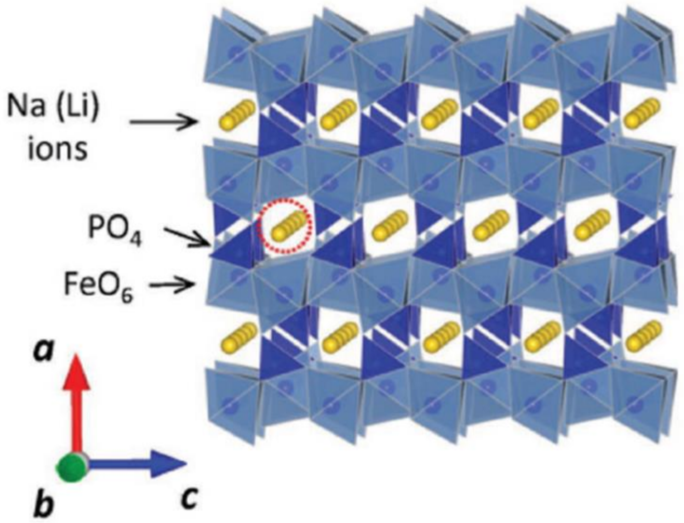

Figure 1.5: *Structure of olivine-type $NaFePO_4$ phosphate-based compound. Taken from ref*[68].

Various methods have been employed to improving electronic conductivity, such as reducing the particle size, carbon coating and elemental substitution.[72] With the aid of a virus template, $FePO_4$ was mineralised onto single walled carbon nanotubes (SWCNT) to form a composite material.[73] The material had reduced electron transport length due to the nanosized particles of the active material and the comprehensive mixing between active material and conductive component. The impact of the CNT were investigated by comparing the performance with material without them. When cycled between 1.5 and 4.0 V at C/5 both materials exhibited good cycling stability, however with CNTs the discharge capacities remained around 100 mAh g^{-1} for 200 cycles and without it was *ca.* 60 mAh g^{-1}. In another study, porous $NaFePO_4$/C microspheres exhibited discharge capacities of *ca*. 110 mAh g^{-1} for 240 cycles at 0.1 C when cycled between 2.1 and 3.6 V.[74] Discharge capacities of 46 mAh g^{-1} were observed at 2 C.

Despite this, discharge capacities are relatively low compared to other structures,[68,72] limiting the number of applications they can be used in.

1.2.5.2 Metal hexacyanometalates and Prussian blue analogues

Metal Hexacyanometalates consist of a cubic structure, where metal ions are located at the corners of the cube and are bridged along the cube edge with nitrogen or carbon from the cyanide groups,[69] figure 1.6. This forms a large open cubic framework, with large interstitial sites ideal for Na (de-)intercalation. In addition to this, interest is such materials arise from facile room temperature synthesis and low material cost. A common issue with such materials is that water coordinates to the metal ions, which intrinsically occurs due to the synthesis method. This mostly occurs in Prussian blue, $Fe_4[Fe(CN)_6]_3 \, . \, nH_2O$, where the resultant structure contains a large number of vacancies for H_2O molecules to occupy and the presence of Fe^{3+} that can strongly coordinate with water, making it difficult to remove.[75] The presence of water can cause a variety of issues such as side reactions with non-aqueous electrolytes, lower capacities and coulombic efficiencies.[69,76] Prussian blue analogues (PBA), $Na_xTM[TM'(CN)_6]_{(1-y)} \, . \, \square_y \, . \, nH_2O$ ($\square$ = vacancies) exhibit better performance as there are fewer vacancies and is able to form a more dehydrated structure. However, some water still remains as a result of the synthesis method, where the fast precipitation and grain growth of the PBA phase produces some vacancies.[77] Hence, synthesis is one of the main challenges associated with such materials.[75]

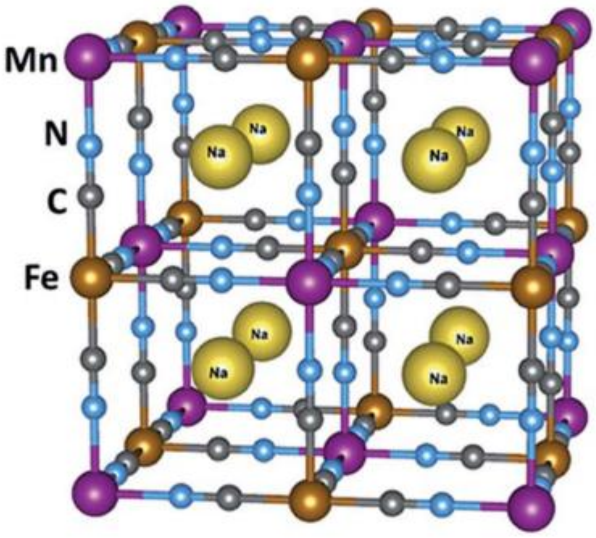

Figure 1.6: *Structure of Prussian blue analogue (PBA)* $Na_xMnFe(CN)_6$. *Taken from ref*[76].

If such issues can be addressed, PBAs are able to exhibit high capacities and energy densities with good cycle life,[77] such as ($Na_2Mn^{2+}[Mn^{3+}(CN)_6]$), which exhibited an initial discharge capacity of just over 200 mAh g^{-1} and *ca.* 160 mAh g^{-1} after 200 cycles, when cycled between 1.5 and 4.0 V at C/5.[78]

1.2.5.3 Organic metal-free compounds

Some metal-free organic compounds have shown to be promising NIB cathode materials. The main advantages of such materials is that they are environmentally friendly and are easy to recycle.[57] Research on organic compounds for NIBs is still nascent, therefore there is plenty of room for improvement, as on average they have low operating voltages.[57] For example, tetrasodium salt of 2,5-dihydroxyterephthalic acid ($Na_4C_8H_2O_6$), figure 1.7, has an average operating voltage of 2.3 V.[79] However when cycled between 1.6-2.8 V at 0.1 C exhibited an initial discharge capacity of 183 mAh g^{-1} and retention of 84 % after 100 cycles. Because of the low operating voltage, the energy density was only about 65 Wh kg^{-1}. This is significantly lower compared to layered oxides which can easily exhibit values above 500 Wh kg^{-1}.[48]

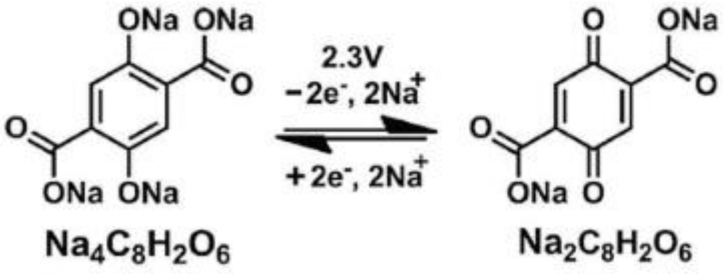

Figure 1.7: *redox mechanism of* $Na_2C_8H_2O_6/Na_4C_8H_2O_6$. *Taken from ref*[79].

1.2.5.4 Layered transition metal oxides

Of the different material classifications discussed so far, layered transition metal oxides (LTMOs) are one of the most promising structures for Na-ion cathodes. This is due to the simple structure, ease of synthesis and relatively high operating voltage.[4] Unfortunately, the multiple phase transitions that occur during cycling causes structural instability, reducing cycling life and rate capability.[71] There has been development of different approaches to improve the performance of this family of materials; from substituting in other elements to manipulating morphology.[12,80,81]

1.2.6 Layered Transition Metal Oxides

The general formula for LTMOs is Na_xTMO_2 (TM = Fe, Mn, Ni, Co, Cu or a combination of these) and are built up of Na layers, sandwiched between edge-sharing TMO_6 layers. Layered oxides can exhibit different structures or polymorphs depending on how the TMO_6 layers are stacked along the *c*-axis. The most common structures the literature refers to are the P2 and O3 structures. According to the notation by Delmas *et al.*, the number represents the number of the different TMO_2 layers in the unit cell, with respect to atomic coordinates.[82] The "P" and the "O" denotes whether the sodium resides in a prismatic or octahedral site, respectively. Figure 1.8 shows typical TMO_2 stacking sequences within the unit cell, shown with black lines. For each different TMO_2 layer, there is a shift in the *a*-*b* plane. P2 structures have the space group $P6_3/mmc$, meaning that along the *c*-axis, there is a six-fold screw axis with a translation of half a unit cell and a mirror plane, there is also a mirror plane perpendicular to the *a*-axis and a glide plane along the c-axis in the viewing direction of the [210] plane. This leads to a stacking sequence of "AABB". P3 structures have the space group $R3m$, where there is a 3-fold rotation along the *c*-axis and a mirror plane perpendicular to the *a*-axis, with a stacking of "AABBCC". The O3 structure has a space group of $R\overline{3}m$, where there is a 3-fold rotoinversion along the *c*-axis and has a stacking sequence of "ABCABC".

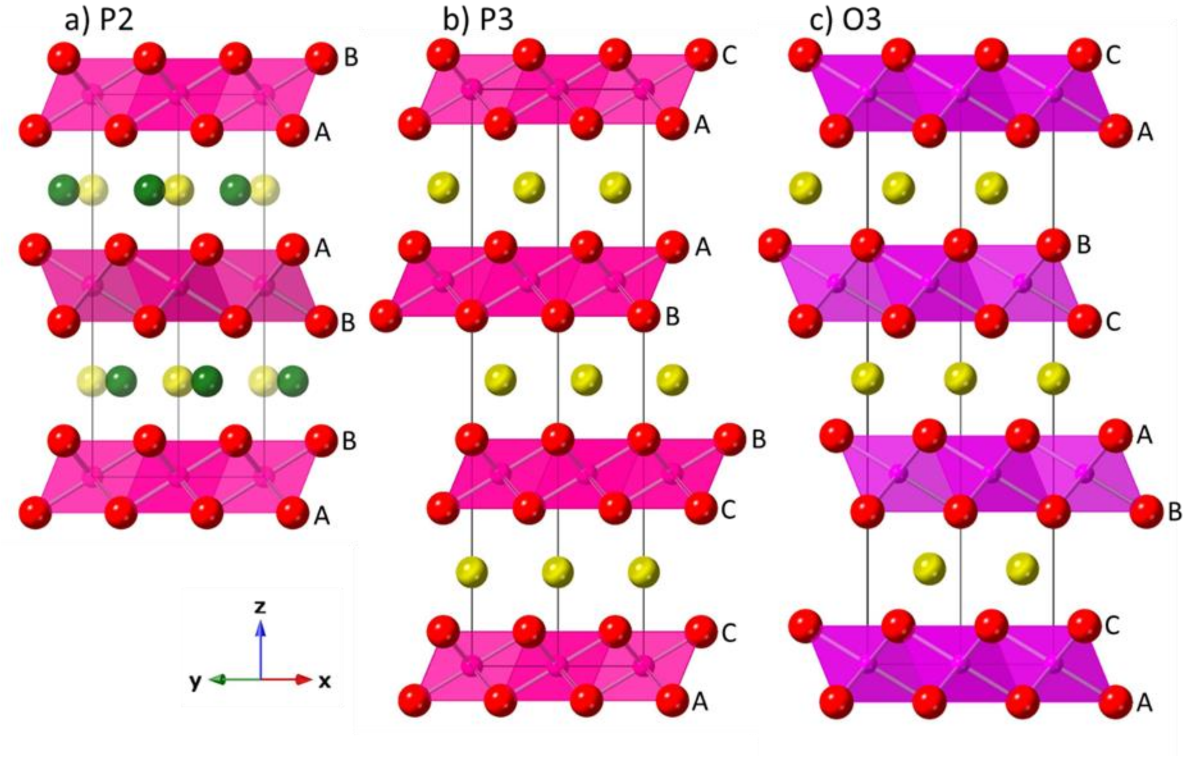

Figure 1.8: *Structural diagrams of a) P2, b) P3 and c) O3 phases. Yellow and green balls are Na, red balls are oxygen and purple/pink is TMO_6 units. The black lines indicate the trigonal unit cell.*

In the P-type structure, the oxygens form a trigonal-prism around the sodium, where the oxygens are mirrored below and above, figure 1.9a. In O-type materials, the oxygen layers above and below Na form a octahedral shape around the Na site, so the oxygens are not mirrored, and therefore not directly in line with each other along the *c*-axis, figure 1.9b. Because of this arrangement, P-type structures generally have larger Na interlayer distance due to the increased repulsion from TMO_2 slabs which facilitates faster Na^+ diffusion.[83,84]

The O- and P-type structures also exhibit different Na^+ migration pathways. In P-type, Na^+ migration proceeds through face sharing prismatic sites, figure 1.9a, which compared to O-type, is a more direct pathway and hence has a lower diffusion barrier.[44] In O-type materials, the Na^+ octahedral sites are edge sharing, creating face-sharing interstitial tetrahedral, shown in blue in figure 1.9b. Na^+ migrates through adjacent octahedral sites, via the tetrahedral site. This generally has a high energy barrier, because occupation of the tetrahedral site is unfavourable. The activation energy for such diffusion pathways in P2- and O2-$Na_xNi_{1/3}Mn_{2/3}O_2$ were 170 meV and 290 meV respectively.[85] Hence, O-type materials tend to have relatively more sluggish diffusion kinetics.

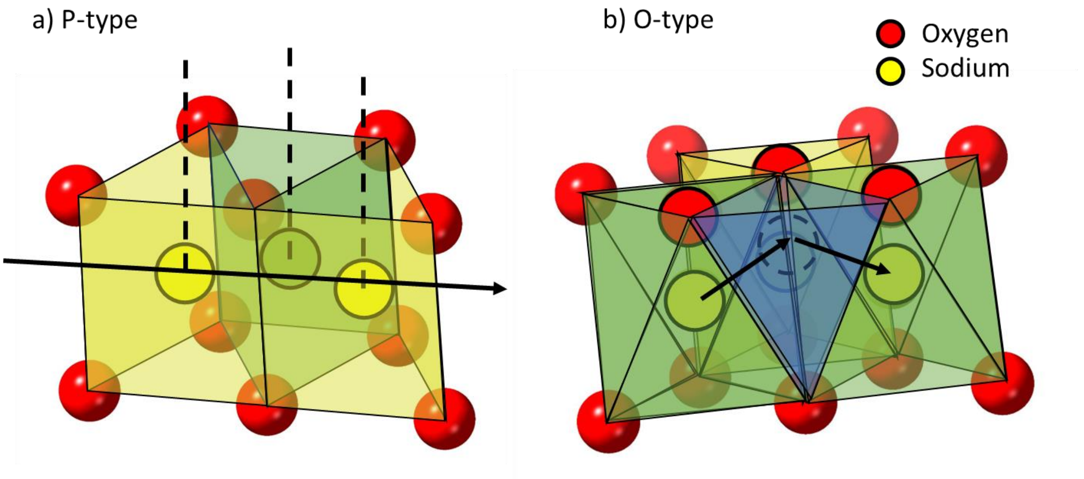

Figure 1.9: *Na^+ diffusion pathway indicated by a black arrow in a) P-type and b) O-type materials.*

Various factors can influence the stacking sequence of the as synthesised layered oxide. P2 structures form at higher calcination temperatures, *ca.* 800 °C, whereas P3 forms below this.[6,86] O3 type materials have Na content closer to 1,[87] whereas the P-type structures tend to have Na content below 0.8.[88,89] The literature generally lacks further detailed explanations on what governs the formations of certain structures, which can make designing specific layered structures challenging. However, a study by Zhao *et al.*, found that ionic potential may govern the driving force for either O3 or P2 formation.[90] P2 formation is favourable if the TM species have a high oxidation state and atomic mass, which leads to higher TM cationic potential and stronger electrostatic cohesion forces between TM and oxygen, increasing the repulsion between adjacent TMO_2 layers which causes larger Na interlayer spacing. Such affects are intensified with low Na concentration due to less shielding. The opposite favours O3 formation; low cationic potential and high Na concentration, allowing for a smaller Na interlayer spacing due to greater electrostatic cohesion forces between Na and oxygen. While such model is in agreement for many materials, it cannot correctly predict the structure of metastable, disordered or non-equilibrium materials. This may be the case for some of the structures that form upon electrochemical cycling. In addition, the formation of phases are strongly dependant on synthesis conditions. Therefore further research is needed to understand what governs the formation of such structures.

During electrochemical cycling when sodium is (de-)intercalated, transition metal layered oxides undergo structural changes. Typical phase transformations during charge, when Na is extracted, are the P2↔O2 or O3↔P3 transitions. They occur by gliding of the TMO_2 layers in the *a*-*b* plane without breaking TM-O bonds. In the P2 phase, the change to O2 is to overcome the repulsive forces between the TMO_2 layers due to lack of shielding for the Na layers.[85] For example, P2-$Na_{2/3}Ni_{1/3}Mn_{2/3}O_2$ undergoes the P2-O2 phase transition upon charge to 4.2 V, when Na content is approximately 1/3.[10] In the O3 structures, partial extraction of Na^+ leads to prismatic sites being more energetically favourable, hence transition to P3 phase.[53] Phase transitions like P2↔P3, O2↔O3 or P2↔O3 are not possible during electrochemical cycling as TM-O bonds need to be broken and reformed, which requires high temperatures.[44,91] The P3-P2 phase transition is exothermic, indicative of bond formation.[91]

Although the P2 and P3 structures appear to be very similar, the Na prismatic site environment differs between the two, hence exhibit different diffusion kinetics.[92] In P2, there are two different sodium sites; Na_f and Na_e, figure 1.10a. In the Na_f site (yellow), the Na trigonal prism shares faces with the TMO_6 units (light blue triangles) below and above. In the Na_e site (green), the trigonal prism share edges with TMO_6 units below and above. The TMO_6 units create interstitial tetragonal units (shaded blue) in the TMO_2 layers, which the Na_e prism essentially share a face with. The Na_e sites are more energetically favourable and tend to be more occupied than the Na_f site, due to the lower electrostatic repulsion between Na^+ and TM^+.[85] From the perspective of Na_e, in line with it along the *c*-axis, there is an oxygen above and below. Whereas with Na_f there is TM^+, therefore Na_f experiences greater electrostatic repulsion. Such preferential occupation has led to Na ordering in P2 materials, impacting Na^+ diffusion kinetics.[93]

In P3 materials, there is only one Na site.[92] Above the Na prism, it shares a face with a TMO_6 octahedron and below shares edges with three TMO_6 units, figure 1.10b. In line with the Na along the *c*-axis, there is a TM above and an oxygen below it. Hence, P3 materials generally do not exhibit Na ordering as all Na environments are equivalent. However, some materials have shown to exhibit Na ordering, depending on whether the TM layers are ordered.[94]

A study by Guo *et al.* compared diffusion kinetics of P2-$Na_{0.62}Ti_{0.37}Cr_{0.63}O_2$ and P3-$Na_{0.63}Ti_{0.37}Cr_{0.63}O_2$.[92] Although both have very similar compositions, the electrochemical performance differed. In the single Na vacancy model, the P3 phase had a lower diffusion barrier compared to P2, whereas in the multi Na vacancy model the P2 phase has a lower diffusion barrier. These models were not discussed in terms of the extent of Na (de-)intercalation or concentration. However it could be that the single vacancy model is dominant at high Na concentration in the material and multivacancy at low Na concentration. In P2-$Na_{2/3}Ni_{1/3}Mn_{2/3}O_2$, it was found that effects of preferred Na occupation was more prevalent at concentrations between 2/3 and 1/3, where there was in plane Na ordering.[85] Whereas below Na=1/3, Na_e and Na_f sites are filled uniformly. As Na^+/vacancy ordering can negatively impact the diffusion kinetics,[5] the high diffusion barrier for the single vacancy model in the P2 material could be linked to ordering at Na concentrations above 1/3 due to in-plane rearrangement.

It is evident that there are different Na diffusion mechanisms in P2 and P3 due to different Na site environment. However, the literature lacks a greater number of such comparative studies for different compositions.

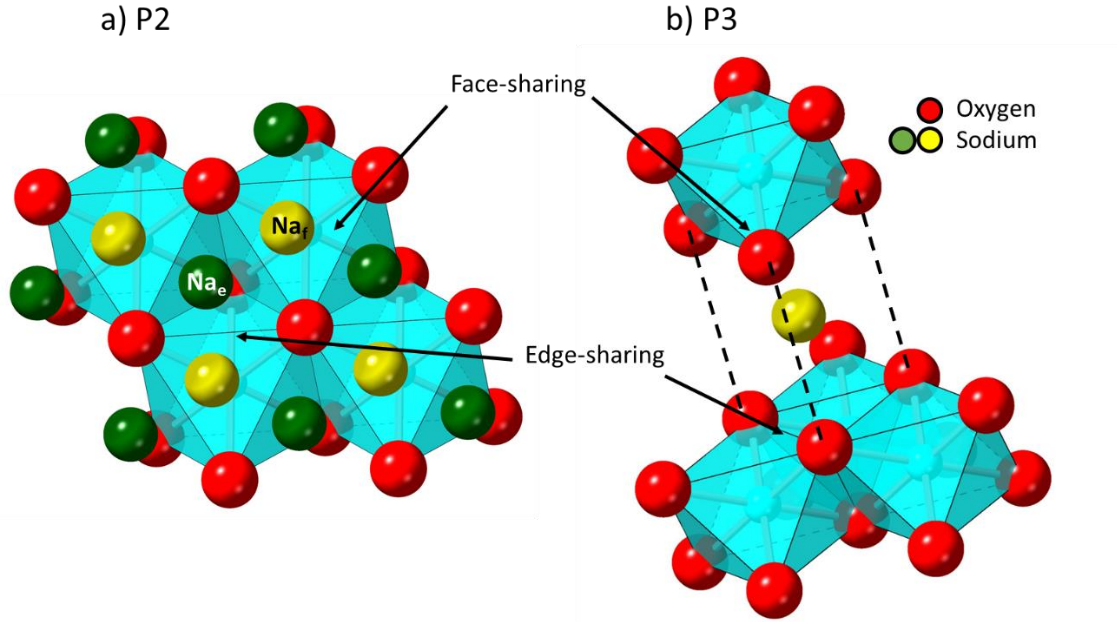

Figure 1.10: *Na sites in a) P2 and b) P3 structures.*

Each structure has their own advantages and disadvantages. For example, the O3-type structures are Na^+ reservoirs due to the high Na content which is beneficial in full cells for coulombic efficiency.[95–97] Coulombic efficiency is defined by the ratio of discharge capacity over charge capacity. It is common to have lower initial coulombic efficiencies due to side reactions with electrolyte causing consumption of Na^+ from the electrolyte, however this improves upon subsequent cycles once stable interfaces are formed. However, P-type structures can exhibit initial coulombic efficiencies that exceed 100 %, meaning more Na^+ enter the structure than leave upon charge.[44] In a full cell with an anode does not supply an infinite source of Na^+, this would reduce the capacity, therefore sacrificial Na compounds are needed to overcome this.[96] Regardless, P2-type materials are considered to be superior in terms of cycle life and rate capability, as they tend to undergo less structural changes compared to O3-type materials,[98–101] hence the large number of studies on this type of structure.[4,5,53,102]

O3-$NaNi_{0.5}Mn_{0.5}O_2$ exhibits poor cycle life due to the complex phase transitions it undergoes ($O3_{hex.}$-$O'3_{mon.}$-$P3_{hex.}$-$P'3_{mon.}$-$P3''_{hex.}$), causing structural instability.[103] The cycling stability was improved when cycled in a narrow voltage range as some of the phase transitions were avoided, however this lowered the discharge capacity. The voltage profiles for these materials show multiple plateaus due to the phase transitions, but a slight change in stoichiometry and substituting in other elements, such as Fe, can smoothen the voltage profile, improve cycling stability and diffusion kinetics.[104,105] This has only been demonstrated at a narrow voltage range, therefore the full extent of Fe substitution and stoichiometry variation is not realised as most severe phase transitions occur above 4 V.

P3 materials have not been given the same attention as their P2 analogue due to the fact they are considered to be inferior in terms of electrochemical performance. For example, P3-$Na_{0.63}Ti_{0.37}Cr_{0.63}O_2$ exhibited greater volume change and poorer cycling stability, compared to P2-$Na_{0.62}Ti_{0.37}Cr_{0.63}O_2$.[92] Other studies have, however, shown promising performance from P3-type cathodes which warrant further investigation.[19,106–108] P3-$Na_{0.9}Ni_{0.5}Mn_{0.5}O_2$, with almost 100% coulombic efficiency, exhibited an initial discharge capacity of 102 mAh g^{-1} at 1 C and after 500 cycles, it was 79 mAh g^{-1}.[106] Another study, investigated the performance of P3-$Na_{2/3}Mg_{1/3}Mn_{2/3}O_2$ which had an discharge capacity of 200 mAh g^{-1} and 153 mAh g^{-1} after 30 cycles at C/10 when cycled between 1.6 and 4.4 V.[108] A large portion of capacity was attributed to oxygen redox, however the material exhibits severe voltage hysteresis due to the P3-O3 phase transition. There is potential to improve structural stability of P3 materials, as done so with P2-type cathodes.[13,109]

Another reason for the lack of P3 studies is that most traditional solid state synthesis methods require high temperatures and long reaction times to produce LTMOs.[106–108] This is especially true for materials containing Ni, where NiO impurity phases are commonly observed.[8,106,110,111] Higher temperatures decrease intensity of NiO peaks through continued solid state reaction, necessitating the energy-intense and lengthy synthesis protocols.[111] This in turn means that it is often challenging to create phase-pure P3 materials, especially for the Ni containing compounds.[112–115] Therefore careful selection of synthesis method is required to ensure careful control of intermediates such as NiO, to prevent large quantities forming that would otherwise persist unless higher temperatures are used. If higher temperatures are used, P2 phase would likely to start forming.[6] The ability to synthesise P3 would lower the required energy for synthesis, hence the interest in developing alternative synthesis methods.

1.2.7 $Na_{2/3}Ni_{1/3}Mn_{2/3}O_2$

1.2.7.1 Overview

$Na_{2/3}Ni_{1/3}Mn_{2/3}O_2$ can form two different structures; P2 and P3. Of the two, the P2 structures is widely studied. Although the results chapters in this thesis focus on P3-$Na_{2/3}Ni_{1/3}Mn_{2/3}O_2$ (P3-NNM), there are only a small handful of studies in the literature on such material. Therefore, this section of the introduction will summarise the findings on P2-$Na_{2/3}Ni_{1/3}Mn_{2/3}O_2$ (P2-NNM), as similar redox and degradation mechanisms may also occur in P3-NNM.

The great interest in P2-$Na_{2/3}Ni_{1/3}Mn_{2/3}O_2$ (P2-NNM) is mainly due to its relatively high theoretical capacity of 173 mAh g^{-1} and high average working voltage of around 3.7 V vs. Na^+/Na.[5] It is also stable under ambient atmosphere,[18,53,116] unlike other Na-ion LTMOs such as P2-$Na_{2/3}Fe_{1/2}Mn_{1/2}O_2$, P2-$Na_{0.67}Mn_{0.8}Mg_{0.2}O_2$, P2-$Na_{0.67}Co_{0.5}Mn_{0.5}O_2$, O3-$NaNi_{0.5}Mn_{0.5}O_2$ and many others,[17,53] where water is able to intercalate into the Na layers.[117] This means that storage of NNM is likely to be cheaper and easier, and is also a good candidate for water soluble binders. Figure 1.11 compares different Na- and Li-ion cathode materials and P2-NNM has almost comparable volumetric energy density to $LiCoO_2$ and $LiNi_{0.5}Mn_{0.5}O_2$.[118] Practically, this has not been demonstrated, as it suffer from structural instability during cycling, causing rapid capacity fade.[5] Different avenues have been pursued in improving cycling stability,[5] such as substituting in other transition metal cations such as Cu^{2+}, Fe^{3+} and Mg^{2+} to stabilise the structure during cycling,[13,119,120] protective coating around active particles,[110] and inhibiting Na^+/vacancy ordering.[93] Similar approaches can be used with P3-NNM.

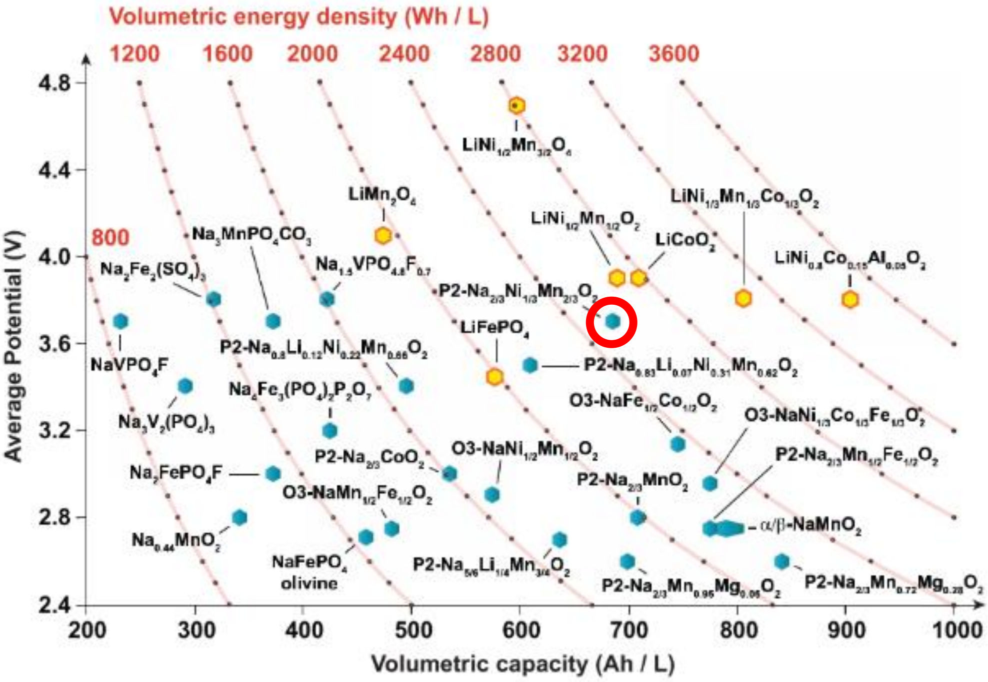

Figure 1.11*: Average discharge potentials (of Na-ion cathodes vs Na^+/Na and Li-ion cathodes vs Li^+/Li) vs volumetric capacity. The volumetric energy densities are compared for the different cathodes. Figure taken from ref[118]. P2-$Na_{2/3}Ni_{1/3}Mn_{2/3}O_2$ is highlighted with a red circle.*

1.2.7.2 Water Stability

Many Na-ion layered oxides are not stable in ambient conditions, as water is able to intercalate into the Na layers due to the large interlayer spacings.[17,53,121] After water intercalation, a significant increase in the *c*-axis can be observed, associated with the shift in the 00*l* peaks to lower angles, figure 1.12.[53] Such reactivity with water can cause leaching of Na from the layered structure, [18,122] Na^+ diffusion pathways can be blocked, side reactions with electrolyte can occur, as well as structural damage such as delamination and intergranular cracks [18]. This causes poor cycle life as shown in figure 1.12 for P2-$Na_{2/3}Fe_{1/9}Ni_{5/8}Mn_{2/3}O_2$, where the water exposed material exhibited significant capacity fade compared to the pristine material.[17] Therefore careful handling and storage is required for such materials which would increase costs.[117]

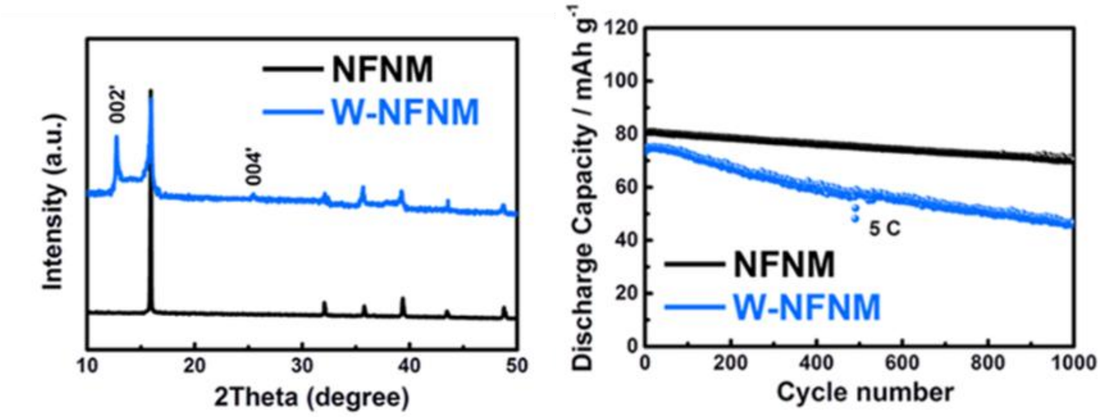

Figure 1.12: *XRD pattern of P2-$Na_{2/3}Fe_{1/9}Ni_{5/8}Mn_{2/3}O_2$ before (black) and after exposure to air for 24 h, then soaked in water for 24 h and then finally dried at 60 °C overnight (blue). Resulting cycle stability of the two specimens when cycled between 2.4 and 4.1 V at 5 C. Taken from ref*[17].

There are a few LTMOs that have shown to be relatively stable under ambient conditions, one being P2-NNM.[17,121] This has mostly been attributed to strong interlayer interactions due to ordering of TM and the high adsorption energy, making water intercalation unfavourable.[17,85,117]

In recent work, the water stability of P2-NNM was tested more rigorously under different conditions.[18] After 3 days of exposure in 93% relative humidity and CO_2, there were no differences in the x-ray diffraction (XRD) pattern, although $NaHCO_3$ was found on the surface of the particles which was identified using energy-dispersive spectroscopy (EDS) mapping and Fourier-transform infrared spectroscopy (FTIR). This indicated that some Na was leached from the structure. The effects of exposure were more prevalent in $Na_{2/3}MnO_2$, with significant formation of the hydrated phase and cracks on particle surface. After 15 days of exposure to 93 % relative humidity and CO_2, P2-NNM still showed no sign of any hydrated phases, and just a small amount of $NaCHO_3$. However, after such exposure, there was an impact on the cycling stability, figure 1.13. Pristine NNM exhibited an initial discharge capacity of around 85 mAh g^{-1} when cycled between 2.0 and 4.0 V at 120 mA g^{-1} and was maintained for 100 cycles. Whereas specimens that were exposed to water and high humidity with CO_2 exhibited initial discharge capacities around 80 mAh g^{-1} and dropped to about 50 mAh g^{-1} after 100 cycles.

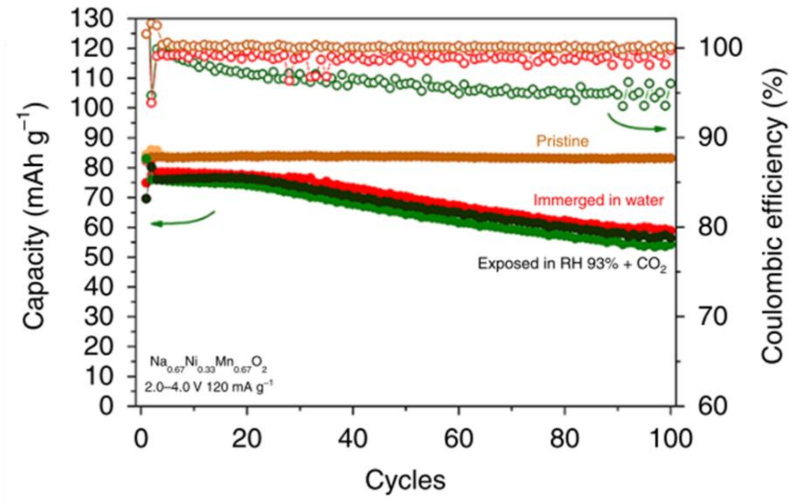

Figure 1.13: *Cycling performance between 2.0 and 4.0 V of pristine P2-NNM (orange) compared with specimen immersed in water for 20 days (red) and exposed to relative humidity of 93 % + CO_2 for 3 days (green). Filled circles are capacity and hollow circles are coulombic efficiency. Taken from ref*[18].

Fortunately the phases formed after exposure, such as $NaCHO_3$, can be removed upon heating to at least 130 °C, although in this study the electrochemical performance was not assessed after heat treatment, so it is not clear whether impact of moisture exposure is fully reversible.[18] Other studies found that P2-NNM is stable after immersion in water for up to a year [123] and exposure to humidity for 10 days [121]. In another study, P2-NNM that was immersed in water for 24 h then dried at 60 °C overnight prior to electrode preparation, exhibited no difference in electrochemical performance compared to the pristine material.[17] Unless stored under very humid conditions or immersed in water for a long period of time, which is unlikely in a lab setting, P2-NNM shows very good stability in ambient conditions. This makes handling of the material easier and cheaper. Such materials are good candidates for water soluble binders, removing the need for N-Methyl-2-pyrrolidone (NMP), a toxic and expensive solvent which is required to dissolve the commonly used polyvinylidene fluoride (PVDF) binder.

1.2.7.3 Electrochemical Performance

Electrochemical properties of P2-NNM greatly vary depending on the cycle potential range. Higher capacities were achieved when cycled at 2.0 – 4.5 V, with an initial discharge capacity of 140 mAh g^{-1} at 0.1 C, but exhibited poor cycling stability as after 100 cycles the capacity was *ca.* 40 mAh g^{-1}.[124] When cycled between 2.0 and 4.0 V at 0.1 C, initial discharge capacity was about 88 mAh g^{-1} and after 100 cycles did not drop below 80 mAh g^{-1}. P2-NNM exhibits a step-like voltage profile, indication that various phase transitions occur during cycling, figure 1.14. Upon charge the plateaus located at 3.31 V and 3.70 V are attributed to Na^+/vacancy ordering and the plateau at 4.25 V is due to the P2-O2 phase transition.[125] Such numerous phase transitions have a negative impact on rate capability and cycle life due to higher migration energy barrier for Na^+.[17,85] The P2-O2 phase transition causes structural instability due to large volume changes of up to ~23%.[126,127] One study found that cracks initiated at the P2/O2 phase boundary and propagated on subsequent cycles.[9]

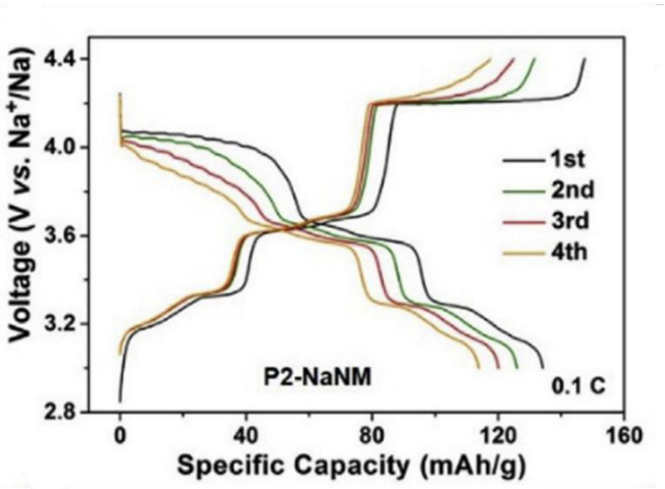

Figure 1.14: *voltage profile of P2-NNM between 3.0 and 4.4 V at 0.1 C for cycles 1 to 4. Taken from ref*[99].

1.2.7.4 Improving electrochemical performance of P2-NNM through metal cation substitution

There are a few approaches in improving cycle life of P2-NNM. One method is cycling within a narrower voltage range that avoids the P2-O2 phase transition, however, this is at the expense of discharge capacity.[124] This is because above 4.0 V there is additional anionic redox of lattice oxygen that contributes to capacity [128] and therefore charging to lower voltages misses activation of this redox couple. Another method to improve cycling stability is to substitute in other metal species that are electrochemically inactive. This stabilises the P2 structure over a winder voltage range as more Na remains in the structure.[12]

In P2-$Na_{2/3}Ni_{1/3-x}Mg_xMn_{2/3}O_2$, cycling stability was improved when some Ni^{2+} was substituted for Mg^{2+}.[109] Specimens with x = 0 and 0.10 exhibited an initial discharge capacities of around 145 and 110 mAh g^{-1} respectively when cycled between 2.5 and 4.35 V at 0.1 C and after 50 cycles capacities of 70 and 90 mAh g^{-1} were observed. The voltage profiles were smoother with increased Mg content, indication that Na^+/vacancy ordering and the P2-O2 phase transition was supressed. Another study found that in P2-$Na_{2/3}Ni_{1/3-x}Mg_xMn_{2/3}O_2$, where x = 0.1, above 4.3 V, the P2 to OP4 transition was observed, which is less severe in terms of volume change than the P2-O2 phase transition in P2-NNM, as the OP4 phase is an intergrowth structure.[119]

Doping Zn^{2+} in P2-$Na_{0.67}Ni_{0.23}Zn_{0.1}Mn_{0.67}O_2$ also improved cycling stability compared to P2-NNM, by the same mechanism as Mg^{2+} as it is also electrochemically inactive.[129] Normally in P2-NNM, cycling to below 2 V activates the Mn^{4+}/Mn^{3+} redox couple which can increase the capacity, cycle life is significantly reduced as surface Mn^{3+} can disproportionate to Mn^{2+} and Mn^{4+}, where dissolution of Mn^{2+} occurs.[130] This does not seem to be the case in Zn containing material, as cycling stability was improved at an extended voltage range of 1.5 – 4.3 V due to the suppression of the P2-O2 phase transition. This lead to less volume change, preventing new surface areas from being exposed to the electrolyte, therefore further Mn^{2+} dissolution is prevented. It is likely this would be the case for other element substitutions that prevent the high voltage phase transition.

The disadvantage of using electrochemically inactive species is the reduced concentration of redox active species, which lowers observed discharge capacities. There are other redox active species that are capable of supressing the P2-O2 phase transition by transferring fewer electrons compared to

Ni^{2+}/Ni^{4+} redox, allowing for more Na remains in the structure at higher voltages. The addition of Fe $Na_{2/3}Ni_{1/3}Mn_{7/12}Fe_{1/12}O_2$ lead to an initial discharge capacity of 141 mAh g^{-1}, whereas P2-NNM exhibited 145.5 mAh g^{-1} when cycled between 2.2 and 4.4 V at 0.1 C.[131] After 50 cycles the observed discharge capacities were *ca.* 130 and 80 mAh g^{-1} respectively. Such small level of Fe substitution retained the P2 structure at 4.4 V, however a greater degree of substitution like in P2-$Na_{2/3}Ni_{1/3}Mn_{1/2}Fe_{1/6}O_2$ lead to lower discharge capacities and worse cycling stability. This was due Fe^{3+} migrating into to the Na layers and Jahn-Teller active Fe^{4+} causing distortions in the material.

Cu^{2+} substitution for Ni^{2+} in P2-NNM also suppresses the P2-O2 phase transition while being electrochemically active (Cu^{2+}/Cu^{3+}).[13,132,133] When cycled at 0.1 C between 2.0 and 4.3 V, P2-$Na_{0.67}Ni_{0.18}Cu_{0.15}Mn_{0.67}O_2$ exhibited an initial discharge capacity of 120 mAh g^{-1} and after 200 cycles it was 100 mAh g^{-1}, whereas P2-NNM had initial discharge capacity of 145 mAh g^{-1} and dropped to 35 mAh g^{-1}.[132] In another study P2-$Na_{0.6}Ni_{0.2}Cu_{0.1}Mn_{0.7}O_2$ was cycled between 2.0 and 4.5 V at 0.1 C and exhibited an initial discharge capacity of *ca.* 130 mAh g^{-1} and P2-$Na_{0.6}Ni_{0.3}Mn_{0.7}O_2$ displayed 150 mAh g^{-1}.[122] After 100 cycles, capacities were 100 and 75 mAh g^{-1} respectively, figure 1.15.

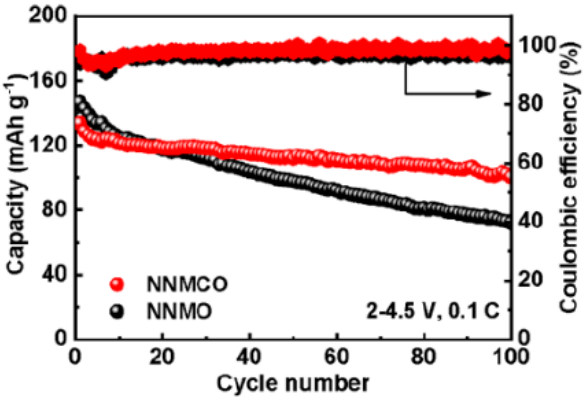

Figure 1.15: *cycling performance of P2-$Na_{0.6}Ni_{0.2}Cu_{0.1}Mn_{0.7}O_2$ and P2-$Na_{0.6}Ni_{0.3}Mn_{0.7}O_2$. Taken from ref*[122]*.*

With substitution, there is a balance between discharge capacity and cycling stability, and most of the time a small change is enough to supress the high voltage phase transition without sacrificing too much capacity.

Cu content of x = 1/12 in P2-$Na_{2/3}Ni_{1/4}Cu_{1/12}Mn_{2/3}O_2$ was found to be enough to supress the P2-O2 phase transition upon charge to 4.4 V.[116] Although, it does undergo the minor P2-OP4 phase transition,[134] as found in other studies with different TM.[119] This is a more gradual phase transition leading to less strain on the material, than the P2-O2 transition in P2-NNM which quickly occurs when charge voltage surpasses 4.2 V.[10,85] Another study investigated the impact of x = 0, 0.1, 0.2 and 0.3 in P2-$Na_{0.6}Ni_{0.3-x}Cu_xMn_{0.7}O_2$ and found the x = 0.2 was the optimal Cu concentration when cycled at 2.0 – 4.5 V at 0.1 C and at faster c-rates of up to 5 C, despite having lower initial discharge capacities compared to x = 0 and x = 0.1.[13]

It is difficult to compare between the different studies to determine which dopant is the best for P2-NNM as various other factors can affect performance such as electrode thickness, electrolyte and cell assembly. What is evident from within each study is the effective suppression of the P2-O2 phase which leads to better cycling stability.

1.2.7.5 Na$^+$/vacancy and transition metal ordering in P2-NNM

P2 materials tend to exhibit Na$^+$/vacancy ordering due to the preferred occupation of the Na$_e$ site, which impacts Na$^+$ diffusion kinetics during electrochemical cycling.[53,135] In P2-$Na_{2/3}Ni_{1/3}Mn_{2/3}O_2$ (P2-NNM), when Na concentration is between 2/3 an 1/3, preferential occupation of the Na$_e$ site is at its greatest.[85] During charge, Na$_e$ are extracted faster than Na$_f$ potentially due to in-plane Na$^+$-Na$^+$ repulsion as there is a greater concentration of filled next nearest neighbour Na$_e$ sites. During discharge, the lower electrostatic repulsion between Na$^+$ and TM$^+$ make occupation of the Na$_e$ more favourable, hence such sites are more filled than Na$_f$,[85] as mentioned in section 1.2.6. Distinct patterns in the Na layers form, which can be identified in high resolution XRD as superstructure peaks at angles between 25 and 30 °2θ.[17,116,136]

The Na in the Na$_f$ sites form a zig-zag pattern at Na = 1/3 with the next nearest Na$_f$ at a distance of $2|a_{hex}|$, figure 1.16a, because simultaneous occupation of the immediate next nearest site is energetically unfavourable due to in-plane electrostatic repulsion.[85] At Na=1/2, a different ordering pattern occurs, where there is one row of Na$_f$ then two rows of Ne$_e$ sites, figure 1.16b. When Na occupancy is below 1/3, both sites are uniformly extracted.

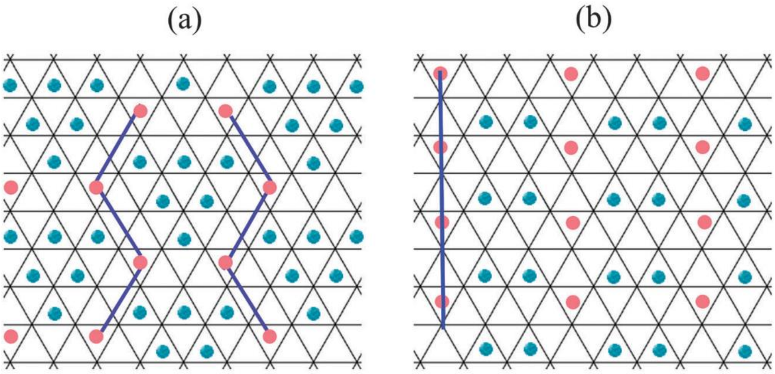

Figure 1.16: In plane Na ordering in P2-NNM at Na concentration of a) 2/3 and b) 1/2. Blue balls are Na$_e$ sites and pink balls are Na$_f$ sites. Taken from ref[85].

In P2-NNM, TM ordering also occurs to also minimise the electrostatic repulsion between adjacent Mn^{4+} where by the atoms are in an arrangement to minimize the number of Mn^{4+}-Mn^{4+} in the TM layer.[137] Such effects are exacerbated by the Mn/Ni ratio of 2:1.[125] The ordering of TM species affects the Na$^+$/vacancy ordering and therefore the electrochemical performance. [125] Altering this ratio can supress ordering, for example a Mn/Ni ratio of 3:1 can add another metal centre, Mn^{3+}, that can introduce defects in the charge order within the TM layers.[125]

Many of the elements that were used to prevent the P2-O2 phase transition, had also inhibited Na$^+$/vacancy ordering. This is dependent on the species in the host structure to have similar ionic radii but greatly different Fermi levels (redox potential).[5,138,139] Mg^{2+} in $Na_{0.67}Mn_{0.67}Ni_{0.33-x}Mg_xO_2$ has a similar ionic radius of 0.72 Å to Ni^{2+} of 0.69 Å.[109] The voltage profiles were smoother with greater level of Mg substitution, an indication that the ordering supressed. Other elements that have shown to suppress ordering include Co^{3+}, Ti^{4+} and Zn^{2+}, [93,129,137] however Cu^{2+} did not appear to have prevented Na$^+$/vacancy ordering but the P2 material still exhibited improved cycling performance.[116] This was attributed to improved diffusion kinetics due to the slightly increased lattice parameters. One disadvantage of destroying Na$^+$/vacancy ordering, is that the structure becomes more susceptible to water intercalation into the Na layers.[17,121] As Cu^{2+} does not prevent ordering, such materials have shown to be stable in ambient conditions.[116]

1.2.7.6 Anionic redox

In P2-NNM, upon charge to 4.2 V, anionic oxidation is activated and as the voltage increases the redox reaction $O^{2-}/O_2^{n-}/O_2$ proceeds, leading to oxygen gas evolution.[120,128] This leads to severe capacity fade as the surface of the particles form a densified layer that impedes on Na^+ diffusion. Addition of Fe in P2-$Na_{2/3}Fe_{2/9}Ni_{2/9}Mn_{5/9}O_2$ can prevent over oxidation due to the high covalent Fe-(O-O) bonding and hence supress O_2 gas evolution, while maintaining reversible O^{2-}/O_2^{n-} redox couple.[120] Figure 1.17 shows the cycling performance between 2.6 and 4.3 V at 0.5 C of P2-NNM which exhibited a capacity retention of 44 % compared to P2-$Na_{2/3}Fe_{2/9}Ni_{2/9}Mn_{5/9}O_2$ with a retention of 78 % after 100 cycles.

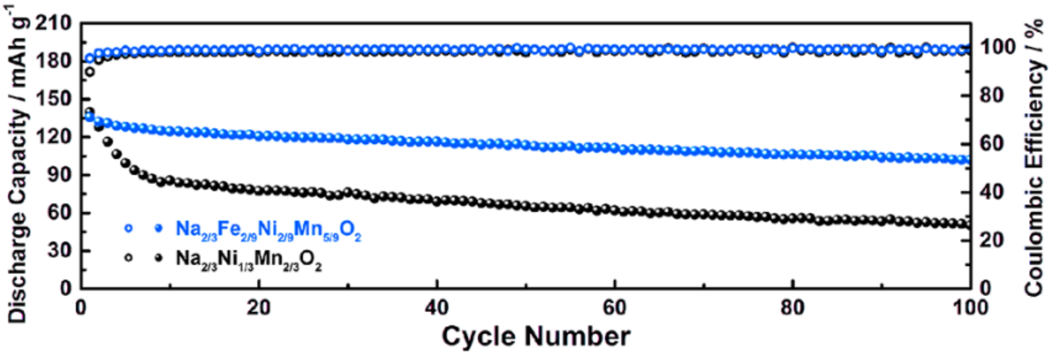

Figure 1.17: *Cycling performance of P2-$Na_{2/3}Fe_{2/9}Ni_{2/9}Mn_{5/9}O_2$ and P2-$Na_{2/3}Ni_{1/3}Mn_{2/3}O_2$ when cycled between 2.6 and 4.3 V at 0.5 C. Taken from ref*[120]*.*

As both the P2-O2 phase transition and anionic oxidation occur at similar voltages,[119,120] deconvoluting the impacts of the different degradation mechanisms is difficult and to date, there have not been any studies that have determined which one has the biggest impact on cycling stability. Although it appears that metal cation substitution in P2-NNM not only supresses the P2-O2 phase transition, but also the over oxidation of lattice oxygen.

1.2.8 P3-$Na_{2/3}Ni_{1/3}Mn_{2/3}O_2$

Recent studies have shown that P3 materials are promising candidates in Na-ion batteries due the relatively high capacities and operating voltages.[106,108,140] The additional benefit of such structures is that they can be synthesised at lower calcination temperatures, therefore less energy is required during the synthesis process which important for sustainability. As research on this structure is lacking, there is plenty of scope to investigate performance and attempt various methods to improve them that have been successfully been implemented in P2-type structures. Methods include metal cation substitution to inhibit phase transitions to improve cycle life and rate capability, [5,119,122] as discussed earlier.

Compared to P2-NNM, there are only a handful of studies on P3-NNM, of which the former appears to have better performance. When cycled between 2.0 and 4.0 V at 0.1 C, the initial discharge capacities of P2-NNM and P3-NNM were 86 and 62 mAh g^{-1} and after 200 cycles the capacities were *ca.* 80 and 50 mAh g^{-1}.[8] Despite this, in another study, when the two materials were cycled between 1.5 and 4.5 V at 0.1 C, both exhibit a rapid decline in capacity.[141] Therefore, degradation needs to be addressed in both the P2 and P3.

P3-NNM has shown to exhibit TM ordering due to the Mn/Ni ratio of 2:1,[137] which affects Na^+/vacancy ordering as Na prefers to occupy sites around Ni.[94] Similarly to P2-NNM, performance of P3-NNM can be improved by inducing TM disorder.[142] When cycled between 2.0 and 4.1 V at 1 C (100 mA g^{-1}), ordered and disordered materials exhibited similar initial discharge capacities, but after 350 cycles the disordered material had better capacity retention, figure 1.18a.

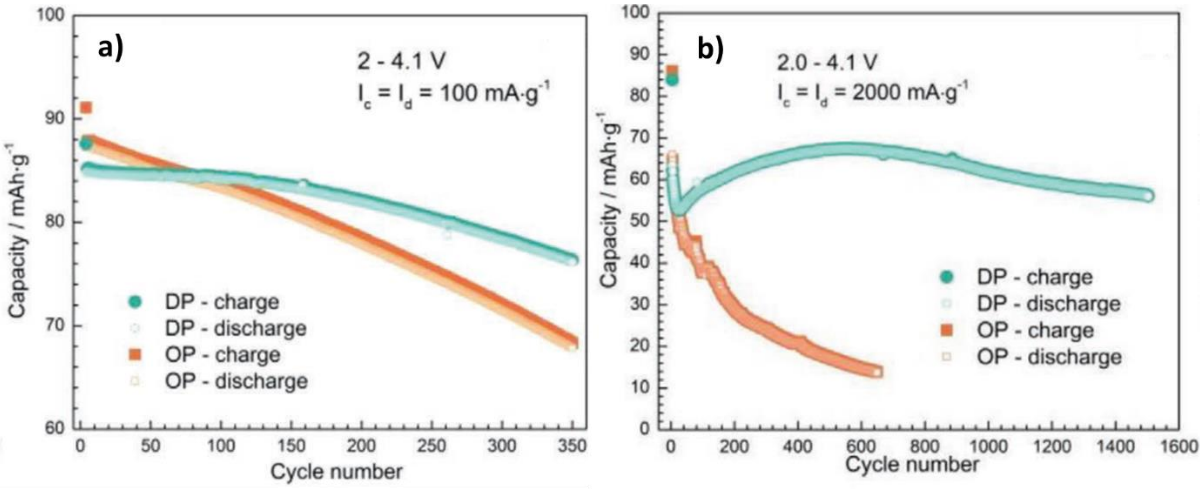

***Figure 1.18**: Cycling performance of ordered (OP) and disordered (DP) P3-NNM cycled between 2.0 and 4.1 V at a) 1 C and b) 20 C. Taken from ref[142].*

At 20 C initial discharge capacities for both materials were around 65 mAh g^{-1} but after 1500 cycles discharge capacity of 55 mAh g^{-1} was observed for disordered P3-NNM, whereas the ordered structure only exhibited 14 mAh g^{-1} after 650 cycles, figure 1.18b.[142] Such improvement in performance was attributed to less severe distortions in the disordered material. Ni is the redox active species in P3-NNM between 2.0 and 4.1 V, the NiO_6 units experience greater distortions and as Na prefers to occupy sites around Ni, the NaO_6 units are also affected.[143] This can lead to local areas that experience significant strain due to the distortions compared to the disordered TM arrangement, where Na is able to occupy sites around both Ni and Mn. Although not discussed in this study, it is likely that reducing Na^+/vacancy ordering has improved the Na^+ diffusion kinetics,[5] hence the better performance at 20 C. Here, there needs to be further investigation into how the Na site environment impacts the diffusion kinetics to further explain the performance at high c-rates. The impressive cycling stability can also be linked to the use of 1 wt.% of fluoroethylene carbonate (FEC) electrolyte additive, which is known to aid the formation of stable passivating layers on the electrode, preventing further side reactions with the electrolyte.[49]

Similarly to P2-NNM, the P3 structure exhibits a P3-O3 phase transition at 4.2 V,[141] TM ordering and thus Na^+/vacancy ordering.[94,137] Similar approaches used in P2-NNM could improve the performance of the P3 phase, such as substituting in other transition metals like Mg^{2+}, Fe^{3+}, Cu^{2+} etc. This has been demonstrated with Mg^{2+} substitution in P3-NNM (P3-NNMM) where the cycling stability due to lack of P3-O3 phase transition was improved.[19] When cycled between 2.0 and 4.4 V at 0.1 C, the observed initial discharge capacities for P3-NNM and P3-NNMM were 150 and 125 mAh g^{-1} respectively and after 50 cycles it was 60 and 105 mAh g^{-1}.

1.2.9 Water-Soluble Binders for Na-ion Cathodes

Binders play an important role in electrodes by ensuring good adhesion with the current collector and effective dispersion of active material and conductive additive, which facilitates ionic and electronic transfer.[15,144] Hence the choice of binder can have a significant impact on performance. Polyvinylidene fluoride (PVDF) binder is commonly used in both LIBs and NIBs due to its electrochemical and thermal stability and good adhesion properties.[145] During slurry preparation, to dissolve PVDF, N-methyl pyrrolidone (NMP) solvent is required which is toxic, combustible and expensive. Therefore careful handling and specialised equipment is required, driving up manufacturing costs.[15] For materials that are susceptible to water intercalation, the use of non-aqueous solvent like NMP is important.

Materials like P2- and P3-NNM that are stable after exposure to ambient conditions and immersion in water are ideal candidates for water-soluble binders. Many biopolymers contain numerous -OH and -COO^- groups that contribute to good adhesion between the different components in the electrode and have shown to be electrochemically stable.[16] Such biopolymers are cheaper and safer compared to PVDF and NMP.

The use of such binders has been demonstrated with P2-NNM, as electrodes were prepared with conventional PVDF, xanthan gum (XG), sodium alginate (SA) and guar gum (GG).[16] When cycled between 1.5 and 4.3 V at 0.2 C, all electrodes containing biopolymer binders exhibited better cycling stability than specimen containing PVDF, figure 1.19. Although PVDF exhibited the highest initial discharge capacity, after 80 cycles it was the lowest compared to the other specimens which had better cycling stability. This was attributed lower charge transfer resistance in the cathodes containing the biopolymers. This is likely linked to the higher viscosity of the cathode slurries, which prevent segregation of the active material and conductive additive, hence the conductive network is better maintained compared to the slurry with PVDF. [146,147] This study also found that there was less Mn dissolution and structural damage in the XG containing cathodes post cycling.

XG has also been used a binder for $LiFePO_4$ electrodes, where there was great improvements in rate capability due to better dispersion of LFP and conductive additive.[147]

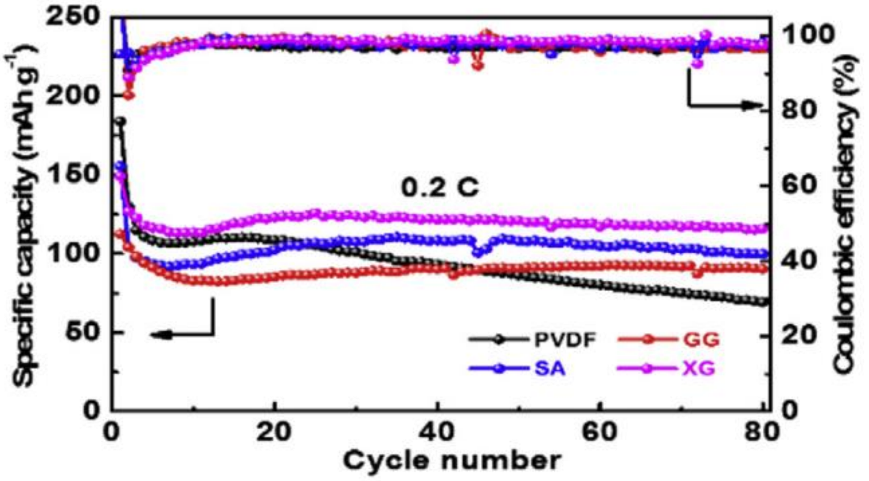

Figure 1.19: *cycling performance of P2-NNM with different binders; PVDF, guar gum (GG), sodium alginate (SA) and xanthan gum (XG). Taken from ref*[16].

PVDF is also not a suitable binder for materials that exhibit very large volume change, such as Si anodes which can exhibit changes of up to 300%.[148] This is because of the weak Van der Waals interaction, that can lead to cracking of the electrode and areas that are electrochemically isolated.[144,149]

PVDF is able to accommodate volume changes of potentially up to 15 %,[150,151] however P2-NNM exhibits volume change of up to 20 % during the P2-O2 phase transition.[44,52] Current studies currently lack in-depth investigations as to whether PVDF can accommodate slightly larger volume changes that are common in Na-ion layered oxides.[4] Biopolymers, that form hydrogen bonds due to the -OH and -COO$^-$ groups, may be more appropriate as they are self-healing and have better adhesion strength with the different electrode components.[63,123]

1.2.10 Synthesis Methods for Electrode Battery Materials

New electrode battery materials are constantly being developed, with improved performance indicators such as safety, sustainability, cost, higher capacities and working potentials.[48,152,153] Such developments are increasingly important due to the anticipated significant growth in demand electrochemical energy storage. Whilst novel chemistries are a focal point of research, there are scenarios in which a material with promising capacity could be dismissed if it did not perform well in initial electrochemical tests. The reasons for this poor performance, however, may not be purely based on composition: volume expansion, or poor diffusion and conduction, can negatively impact the overall electrochemical performance. In some cases, this could be overcome through particle engineering or structural manipulation which can be aided by novel synthesis and manufacturing methods. Nanoscaling of particles or introduction of pores can, for example, help improve diffusion of Li^+ in LIBs and thus improve rate capability.[154,155] This is especially important in Na-ion batteries, where diffusion can be more sluggish due to the larger Na^+ ionic radius.[49]

Solid state synthesis is one of the most mature methods for oxide materials,[156] however the main drawback are the high calcination temperatures and long dwell times that are required to overcome limitations associated with mass transport and diffusion of reactants to the reaction interface.[14,157] This is due to the relatively large particle size of the precursors that lead to an inhomogeneous mixture of reactants. Hence, some layered oxide cathode materials require synthesis temperatures exceeding 800 °C and long dwell time over 12 h. [6,158–160] In some cases, additional grinding and heat treatment steps are sometimes necessary, making the process more lengthy. Such conditions make it difficult to control the particle size, therefore additional ball milling steps may be required or alternative synthesis to be developed to achieve reduce the particle size and therefore improve the performance of battery materials.

Nanoscaling of materials, using either top-down or bottom-up approaches, has been widely researched, with numerous methods now available. A common example of a top-down approach is mechanical milling which is simple and can scaled-up.[161,162] It can be easily employed post synthesis, especially after traditional solid state methods where particle size can be on the microscale.[158,163,164] Ball milling has been used for various Li-ion battery materials; to synthesise materials during the process at low temperatures, control morphology or form coatings as summarised by Tarascon *et al.*.[165] However, high energy ball milling for long periods of time can cause formation of unwanted secondary phases in some materials, as well as increased SEI reactions due to a very small particles size.[166,167] Therefore determining the ideal milling conditions is important. Bottom-up approaches include some chemical and biological methods such as chemical vapour deposition,[168] spray pyrolysis,[169] sol-gel,[170] hydrothermal,[171] and polymer templating [172] which have been used to synthesise battery materials. Of the solution-based chemistry methods, bio-inspired (or "biotemplated") methods take many of the benefits associated with e.g. sol gel (e.g. reduced processing temperatures/times [6,173]), and add some additional potential benefits such as higher order/macro structuring.[172,174,175]

1.2.10.1 Overview of sol-gel synthesis

Sol-gel synthesis is a common method for nanomaterials, as mixing of reagents occurs at the atomic level which helps to overcome such issues associated with solid state synthesis. The most common form of sol-gel uses metal alkoxides as the precursors.[14,176,177] In the solution, hydrolysis and partial condensation of the metal alkoxides occurs, then a gel is then formed through further condensation, essentially forming a polymer network containing metal-oxygen-metal linkages. This is then calcined to form powder of nanoparticles. The main drawbacks of this type of synthesis is that different metal alkoxides have different rates of hydrolysis,[14] making it difficult to form more complex oxides as phase separation can occur. As well as the limited availability of different types of metal alkoxides and the high reactivities in water which can make handling difficult.

Other forms of sol-gel synthesis involve dissolving metal salts, such as acetates or nitrates, and a small molecule chelating agents, such as citric acid, glycolic acid or EDTA, to form a viscous gel upon heating. This gel is formed as the metal/organic complexes are weakly bound to each other by intermolecular bonding, figure 1.20a. The chelating agents make hydrolysis of the cations less favourable, which allows for evaporation of the solvent, to leave behind a glassy-like composite. The citric acid/organic matrix controls when nucleation occurs and ensures that precursor cations are homogenously distributed. This method is good for complex oxides with multiple metal species, as different rates of hydrolysis is not an issue. The use of different chelating agents changes the combustion temperature of the complex, which can have an effect on particle size and crystallinity.

Pechini method is a modified form of sol-gel synthesis, which involves converting the metal/citrate solution into a polymer network with the addition of ethylene glycol. The solution is then heated to initiate polyesterification, forming a polymer network, figure 1.20b. The advantages of this method is that the polymer network ensures greater spatial separation of the precursor ions and ability to synthesise oxides with greater complexity. In addition the higher thermal decomposition temperatures compared to small chelating agents allow for greater control of nucleation and growth of intermediate phases.[176]

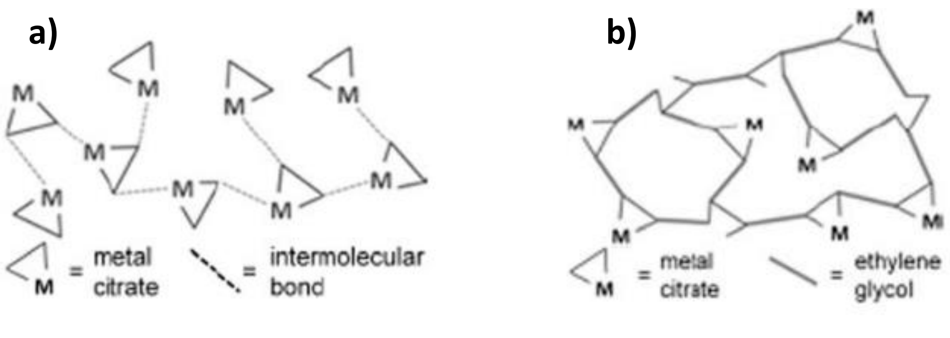

Figure 1.20: *a) mechanism of small molecule metal complex that weakly connected by intermolecular bonding and b) mechanism of Pechini method where polyesterification of metal citrate and ethylene glycol form a polymer network. Taken from ref*[14].

Alternatively, precursor ions can be mixed with a polymer, thus negating the extra step of polymerisation. This is known as polymer assisted sol-gel, or biotemplating (where the polymer has been derived from natural sources).[14] As well as delaying the combustion of the organic matrix, polymer assisted sol-gel has an added advantage where some polymers can form superstructures that can influence morphology at different length scales. Synthetic polymers can be used such as polyvinyl alcohol (PVA), polyethylene glycol (PEG), polyvinylpyrrolidone (PVP) or biopolymers that are derived from nature and are cheap and abundant and so offer some advantages over these synthetic polymers. In addition, some biopolymers form ordered structures which can be used as hard template,[175] as well as manipulating particle morphology.[176]

1.2.10.2 Synthesis methods for P3-type Layered Transition Metal Oxides

At least for P3-type materials, not many are synthesised using traditional solid state methods with metal oxide precursors. Those of which do use solid state methods, use modified protocols, using mixed transition metal compounds or alternative precursors such as nitrates. For example, in the synthesis of P3-$Na_{2/3}Mg_{1/3}Mn_{2/3}O_2$ precursor nitrates and carbonates were hand mixed and ground before a pre heat treatment at 500 °C for 12 h.[108] The powder was then reground, pressed into pellets before final calcination at 600 °C for 24 h, producing phase pure final product.

The mixed transition metal precursors are normally prepared using precipitation methods, prior to the synthesis process of the P3 material. Formation of such compounds can help to improve the atomic mixing, which would aid the crystallisation of the P3 phase. However this adds complexity and time to an already lengthy synthesis process. This includes the synthesis of P3-$Na_{0.9}Ni_{0.5}Mn_{0.5}O_2$ that used a nickel-manganese carbonate powder that was prepared prior to mixing with sodium carbonate.[106] The powder mixture was calcined at 500 °C for 5 h and then finally 800 °C for 18 h. The final product contained particle sizes ranging from about 200 nm to just under a micron and contained about 3.1 wt.% of NiO. P3-$Na_{0.65}Mn_{0.75}Ni_{0.25}O_2$ used a preprepared manganese-nickel oxide that was ground with sodium carbonate which was then calcined at 700 °C for 10 h.[171] The morphology of the manganese-nickel precursor was micron sized spheres, made up of nanoparticles of 100 – 200 nm in size and the final product retained this with no secondary phases. The mixed metal precursor for the synthesis of P3-$Na_{0.6}Ni_{0.25}Mn_{0.5}Co_{0.25}O_2$ was prepared by a co-precipitation method, where soluble salts of nickel, cobalt and manganese were dissolved in water and added dropwise into ammonium hydroxide.[178] The resultant precipitate was ground with sodium hydroxide, and then pressed into a pellet before calcination at 600 °C for 13 h, then ground and pelletised at heated again for 30 minutes. A final heat treatment was employed at 750 °C for 8 h. There were no obvious signs of secondary phases and the morphology consisted of aggregates composed of 300 – 500 nm particles. Similar method to obtain the mixed metal precursor precipitate was used for P3-$Na_{0.67}Mn_{0.67}Ni_{0.33}O_2$.[142] The mixed metal precipitate was ground with sodium carbonate and pelletised. Final calcination proceeded at 700 °C for 24 h. A phase pure material was formed with micron sized aggregates composed of nanoparticles.

Sol-gel is another common method for such materials. For example, P3-$Na_{2/3}Ni_{1/3}Mn_{2/3}O_2$ and P3-$Na_{2/3}Ni_{1/4}Mg_{1/12}Mn_{2/3}O_2$ involved mixing the different nitrate salts with citric acid.[19] A gel was formed after mixing at 60 °C for 6 h with evaporation of water which was then dried at 120 °C overnight. The dried precursor gel was ground into a powder, anneals at 450 °C for 6 h, finally followed by calcination at 700 °C for 12 h. The resultant product produced phase pure P3 phases with plate-like morphologies (common for these types of materials) with particle size ranging between 180 and 300 nm. P3-

$Na_{0.9}Fe_{0.5}Mn_{0.5}O_2$ was also synthesised using a similar sol-gel method, where precursors were dissolved in a citric acid solution and dried for up to 10 h to form a hard gel.[140] This was then ground to form a powder. The calcination process proceeded at 900 °C for 15 h, then at 500 °C for 1 h, before quenching to 250 °C. The final product exhibited no obvious secondary phases and aggregated micron sized particles. P3-$Na_{0.67}Ni_{0.2}Mn_{0.8}O_2$ was synthesised by dissolving and mixing precursors metal acetate and carbonates and then water was removed using a rotary evaporator, forming a hard gel.[112] This was then heated to 275 °C for 12 h, cooled, then ground to form a powder before final calcination at 625 °C for 3 h followed by quench cool. The final product contained 2 wt.% of NiO and the morphology consisted of agglomerated 100 nm sized particles. P3-$Na_xCo_{1/3}Ni_{1/3}Mn_{1/3}O_2$ used oxalic acid as the chelating agent, where an initial thick paste was made with sodium hydroxide before addition of nickel and manganese acetates.[115] The mixture was heated to 400 °C, before final calcination between 700 or 800 °C for 10 h where the final product consisted of small particles ranges from 20 to 100 nm. In addition to the P3 structure, relatively large quantities of secondary phases were present, including a spinel type structure and NiO. This synthesis is simple, however the large fraction of secondary phases may be attributed to the lack of additional mixing and griding steps that other methods contained. P3-$Na_{0.5}Ni_{0.25}Mn_{0.75}O_2$ was prepared without a chelating agent, instead the precursor acetates and nitrates were simply dissolved in water, stirred on a hot plate till a gel was formed.[113] The gel was heated to 400 °C, then resultant powder was ground and heated again to 650 °C for 24 h. the final powder contained 3.6 wt.% NiO.

Although many of these synthesis methods produced fairly small particle sizes, multiple steps are involved in the synthesis of these materials, adding extra level of intricacy which may bring into question the suitability of scaling up.

1.2.10.3 Biotemplating synthesis

Nature is able to produce fine intricate structures made up of materials such as oxides and carbonates.[179] Means to create such structures have been developed over millennia, and evolved to directly benefit the organism that has created them. For example, structural nacre is used as a strong protective coating by some molluscs, and is composed of a composite of chitin (or lustrin) and aragonite platelets.[180] The platelets show a preferential growth direction, which is thought to be moderated by the surrounding organic material.[179,181] The factors which control this preferential crystal growth direction are of great interest for the oxide materials field, where properties of some materials are enhanced in particular crystallographic directions. This is true for battery materials, where diffusion of the alkaline ion is anisotropic through certain crystallographic planes.[182–184] One way to enhance the exposure of these planes is to manipulate morphology so that the diffusion pathway along these crystallographic is shortened, which can be achieved through anisotropic morphologies such as nanorods and plates and ensuring growth proceeds in preferential directions.[185,186] There are significant opportunities to use existing natural structures (and the chemistry there of) as a scaffold or structural directing agent in the synthesis of functional materials. These biotemplating techniques can be broadly split into two categories, soft templating, where the chemistry of the template influences the final structure of the product indirectly, or hard templating where the product forms a direct structural replica of the template on the nano, micro or even macro scale.

1.2.10.3.1 Hard Biotemplating

Some artificial templates such as anodic aluminium oxide (AAO), have successfully been used to create different structures such as nanowires,[187,188] although such templates can be difficult to completely remove without damaging the material of interest.[7,189] Structures with greater complexity that are present in nature can be easily accessible through biotemplating synthesis,[175] for example cellulose nanocrystals from cotton linters can help to form nanowires and nanotubes,[175,190] butterfly wings can be used to form ordered porous structures with photonic properties,[191] and bacteria to form spheres.[192] Some of these morphologies could improve performance of some Li- and Na-ion intercalation electrode materials, by improving diffusion and accommodating volume change which is especially important in NIBs where such effects are greater.

Hard biotemplating methods have been used in a number of battery materials, such as $LiCoO_2$ (LCO), where cotton hard template formed a twisted fibre microstructures, figure 1.21.[172] Compared to LCO synthesised using solid state methods, the biotemplated material exhibited significantly better cycle life and rate capability. At 6 C, both materials exhibited initial discharge capacities *ca*. 125 mAh g^{-1} and after 100 cycles, the discharge capacity of cotton-LCO was 100 mAh g^{-1} and almost zero mAh g^{-1} for solid-LCO. It is not clear whether the structure of the solid-LCO has been damaged at this point because there is no attempt to continue cycling these materials at slower C-rates, which would indicate the structural stability. However, the poor cycling stability of solid-LCO can be attributed to the large particle size of 1.5 – 3 µm, which would impact the Li^+ diffusion kinetics leading to significant polarisation. Nanoparticles can have a negative impact on electrochemical performance due to the large surface that increases the side reactions with the electrolyte.[155] The cotton-LCO appears to have a primary particle size of around a few hundred nanometres, however the secondary particles (twisted fibres) can excessive exposure of the particle surface to electrolyte.

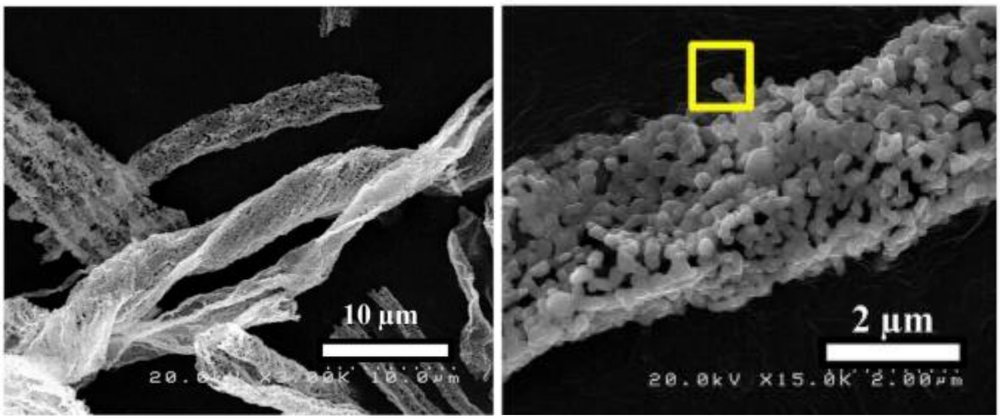

Figure 1.21: *SEM images of cotton templated $LiCoO_2$ at different magnifications. Images taken from ref*[172]*.*

Corn plant stem template used during the synthesis of $LiMn_2O_4$ (LMO) formed a porous structure with primary particle size of 100 nm, figure 1.22a. [7] LMO synthesised without the template formed a very agglomerated microstructure and appeared to have poorer crystallinity due to less visible octahedral facets, figure 1.22b. The two materials exhibited similar capacities at rates up to 5 C. At 10 C and higher, the difference in performance was evident. At 10 C, templated LMO exhibited discharge capacities of *ca.* 95 mAh g^{-1} and non-templated LMO was *ca.* 75 mAh g^{-1}. At 15 C templated and non-templated LMO exhibited discharge capacities of around 70 and 20 mAh g^{-1} respectively.

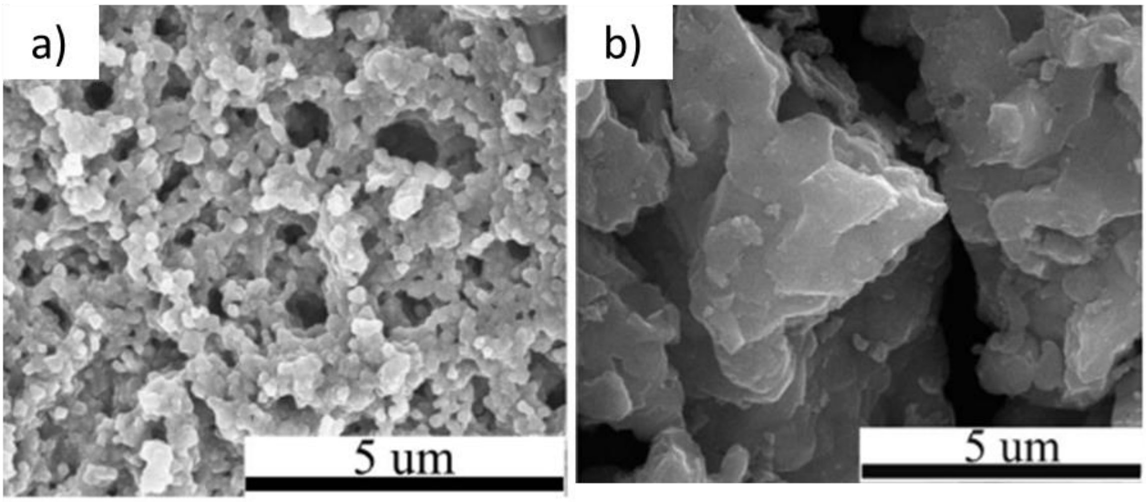

Figure 1.22: *SEM images of LMO synthesised a) with corn plant stem and b) without template. Images taken from ref*[7]*.*

A pinewood template was used to synthesise porous $LiNi_{0.5}Mn_{1.5}O_4$ (LNMO) which also exhibited improved rate capability compared to its non-templated counterpart.[193] The biotemplating method proceeded by making a precursor solution before immersion of the pine wood template for a period of time. Then the template complex was dried and calcined to remove the template and start crystallisation of LNMO. Similar method is used with the corn plant stem for LMO.[7]

Conductive additive is normally added to the electrode to improve electronic conductivity however, ensuring a uniform distribution of the additive can be difficult since it consists of nanoparticles that tend to agglomerate, making dispersion in the slurry challenging. Such problem can also be seen with nano active material. [194] The electronic transport length could be greater than the active material particle size if only a fraction of the particles are in contact with the conductive additive, thus increasing the interfacial resistance.[195] Therefore it is important that majority of active material particles are in contact with the conductive additive, [194] which can be achieved by coatings, essentially reducing electronic transport lengths to equivalent of the particle size.[195] Biotemplates can be used to form carbon coating either in post treatment or simultaneously during the crystallisation and growth of the active material.

Spirulina, a type of algae, was used as a template for $LiMn_2O_4$ (LMO) and formed porous hollow curved rods made up of primary particles 10 – 300 nm in size, figure 1.23.[196] After synthesis of LMO, the carbon coating was applied by immersing the powder in a sucrose solution then fired at 600 °C. Electrochemical performance was compared to a non-templated LMO synthesised using sol-gel synthesis, with carbon coating also obtained through the same sucrose solution method. Biotemplated LMO had better rate capability than sol-gel LMO, with discharge capacities around 90 and 20 mAh g^{-1} respectively at 20 C when cycled between 3.0 and 4.2 V. Although both specimens had a carbon coating, the porous hollow rods enable fast Li^+ diffusion, helping to reduce resistance of the material.

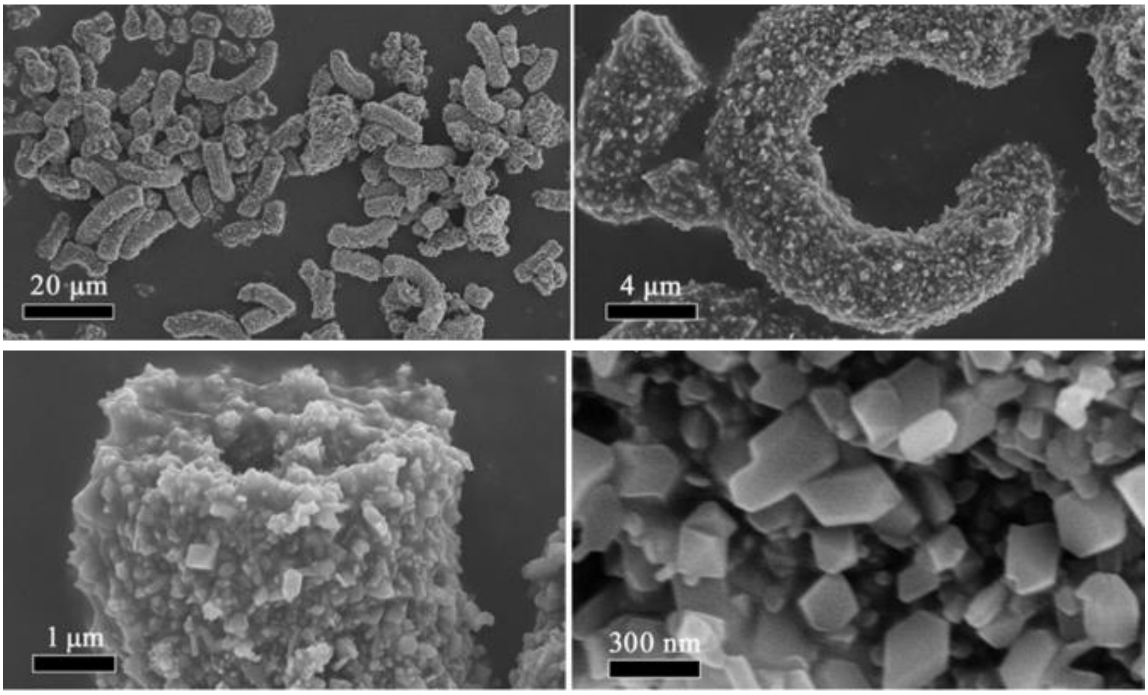

***Figure 1.23**: SEM images of spirulina templated $LiMn_2O_4$. Images taken from ref*[196].

Spirulina has also been used as template and the source for the carbon coating in $LiFePO_4$ (LFP),[197] in order to mitigate intrinsic issues of poor electronic conductivity and Li^+ diffusion.[198] To achieve this, the spirulina precursor suspension went through a hydrothermal treatment, washed then heated under a flow of high nitrogen concentration. This formed a porous hierarchal structure with primary particles between 50 - 400 nm in size with 3 - 5 nm thick carbon coating. Carbon nano-interconnectors were present between particles which helped to further reduce interfacial resistance.

Yeast biotemplated aided the formation of carbon coated microspheres of $LiFePO_4$/C composite.[199] Synthesis of this material involved multiple steps; firstly the yeast precursor solution was prepared with the addition of citric acid as a chelating and reducing agent. This was stirred at slightly elevated temperatures to form a gel before calcination under a nitrogen atmosphere. The primary particles formed spheres with diameters of 100 – 300 nm with a carbon layer of about 20 nm in thickness. This material exhibited excellent cycling stability at various c-rates. At 0.5, 2 and 5 C, initial capacities were about 135, 120 and 105 mAh g^{-1} respectively, with minimal drop in capacity after 50 cycles. Cycle stability was not compared with non-templated LFP in this study. However phosphate materials such as $LiFePO_4$ intrinsically exhibit poor electronic conductivity, limiting rate capability, where initial discharge capacities can be around 55 mAh g^{-1} at 0.2 C [200].

Various materials experience volume change during electrochemical cycling, putting stress on the structure leading to mechanical fracture and instability of the solid electrolyte interphase.[5,148,201,202] Hollow and/or spherical morphologies are able to accommodate large volume changes,[203] or embedding active particles in a carbon matrix can act as a buffer.[204]

MnO, an anode material in LIBs, has a high theoretical capacity of 756 mAh g^{-1} and is sustainable however it exhibits slow kinetics, agglomeration during cycling and large volume change resulting in poor cycle life.[205,206] *Nannochloropsis oculata* (*N. oculata*) biotemplate, a spherical microalgae has been used to form MnO/C composite where MnO nanoparticles were embedded in hollow porous carbon sphere matrix, figure 1.24.[207] With the help of such microstructure, MnO/C exhibited excellent cycle stability and rate capability.

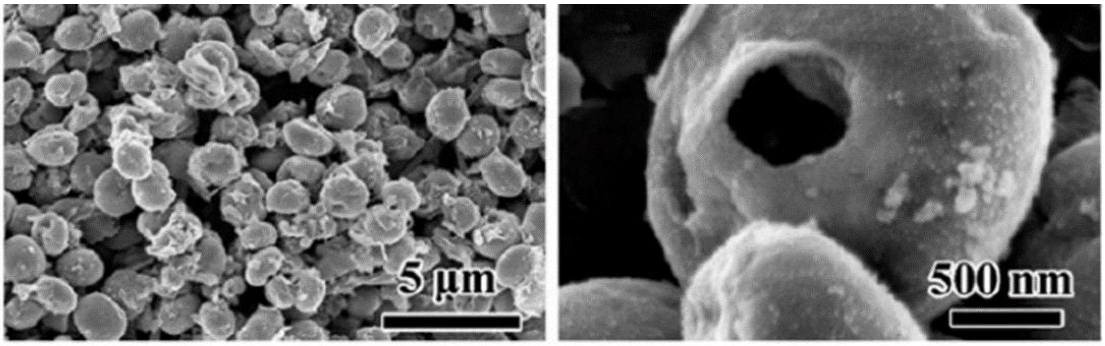

Figure 1.24: *SEM images of MnO/C microspheres using a microalgae as a biotemplate. Taken from ref*[207]*.*

Other biotemplates have also been used to form MnO/C composite, with similar results. Filamentous spirogyra, another type of algae was used to form hollow tube carbon matrix with embedded MnO nanoparticles.[208] Pollen biotemplate also forms porous hollow half sphere structures that exhibited stable cycle life and rate capability due to the voids and pores.[206]

Hard templating is a facile and versatile method to improve various aspects on battery electrode materials. Many natural templates can be used to achieve different micro and macro morphologies depending on the requirement of the material.

1.2.10.3.2 Soft Biotemplating

Soft templating works by dissolving soluble metal salt precursors and biopolymer in a solution where the functional groups in the biopolymer deprotonate or dissociate, forming negatively charged chelation sites where cations from precursors can bind to.[209,210] The solution is then dried to form a gel or a glassy solid, essentially freezing the homogenous distribution of precursors ions, and preventing recrystallisation. In the furnace, the biotemplate prevents agglomeration of intermediates and impedes particle growth up until the point the it combusts, creating numerous nucleation sites. Crystallisation is able to occur at lower temperatures, thus reducing reaction temperature and time. Figure 1.25 shows the process for soft biotemplating synthesis. Dextran, for example, begins to decompose at 300 °C,[174] which is beneficial for controlling intermediate phases, as nucleation and growth is impeded. Some soft templates can indirectly influence formation of more complex morphologies, such as nanowires using alginate, a type of seaweed.[211] However the mechanism of growth for such morphologies is still not fully understood.

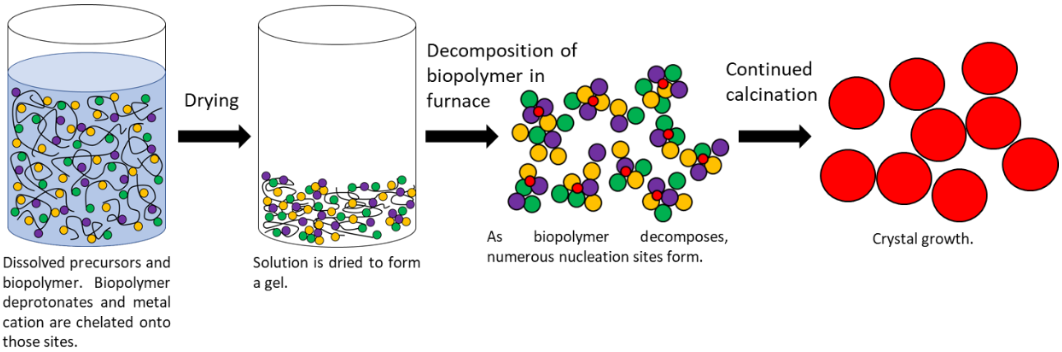

Figure 1.25: *schematic of soft biotemplating synthesis.*

P3-NNM synthesised using solid state method requires significantly long dwell times, under O_2 flow at 650 °C for 10 hours,[212] whereas biotemplated P3-NNM was successfully synthesised at 650 °C for 2 h.[6] Particle size of dextran biotemplated P3-$Na_{2/3}Ni_{1/3}Mn_{2/3}O_2$ (NNM) was easily reduced and controlled just by simply controlling the furnace conditions.[6] Dextran was dissolved in water with the precursors salts and dried to form a hard glassy composite, before calcination. Smaller particles were formed at lower furnace temperature and/or shorter dwell times, showing improved electrochemical performance in terms of capacity, attributed to shorter Na^+ diffusion lengths. Materials synthesised closer to the conditions of 650 °C for 2 h or 550 °C for 12 h exhibited higher capacities and particles size was just over 100 nm. These materials had smoother voltage plateaus and high degree of reversibility especially when calcined at 550 °C 12h. Although all biotemplated materials exhibited the same crystal structure, the impact of the particle size is apparent. Samples treated above 750 °C for up to 12 h had almost double the particle size and hence lower discharge capacities. Figure 1.26 shows the SEM images of dextran biotemplated P3-NNM calcined at different temperatures and dwelled for 12 h. At lower temperatures, the particles are smaller and greater size homogeneity. Under the same synthesis conditions, the particle size appears smaller for the biotemplated P3-NNM, compared to solid state synthesis.

In dextran-biotemplated P3-NNM, weight fractions of NiO were above 5 wt.% in the specimens calcined at low temperatures and short dwell times and persisted to high temperatures to some extent at higher calcination temperatures.[6] Dextran has shown to have preferential binding in a mixed solution of other metal cations,[213] which may impact the crystallisation process during biotemplating synthesis. Preferential binding at the expense of Ni during P3-NNM biotemplating synthesis could cause unconstrained growth of NiO which may be why it was able to persist in measurable quantities to temperatures above 750 °C.

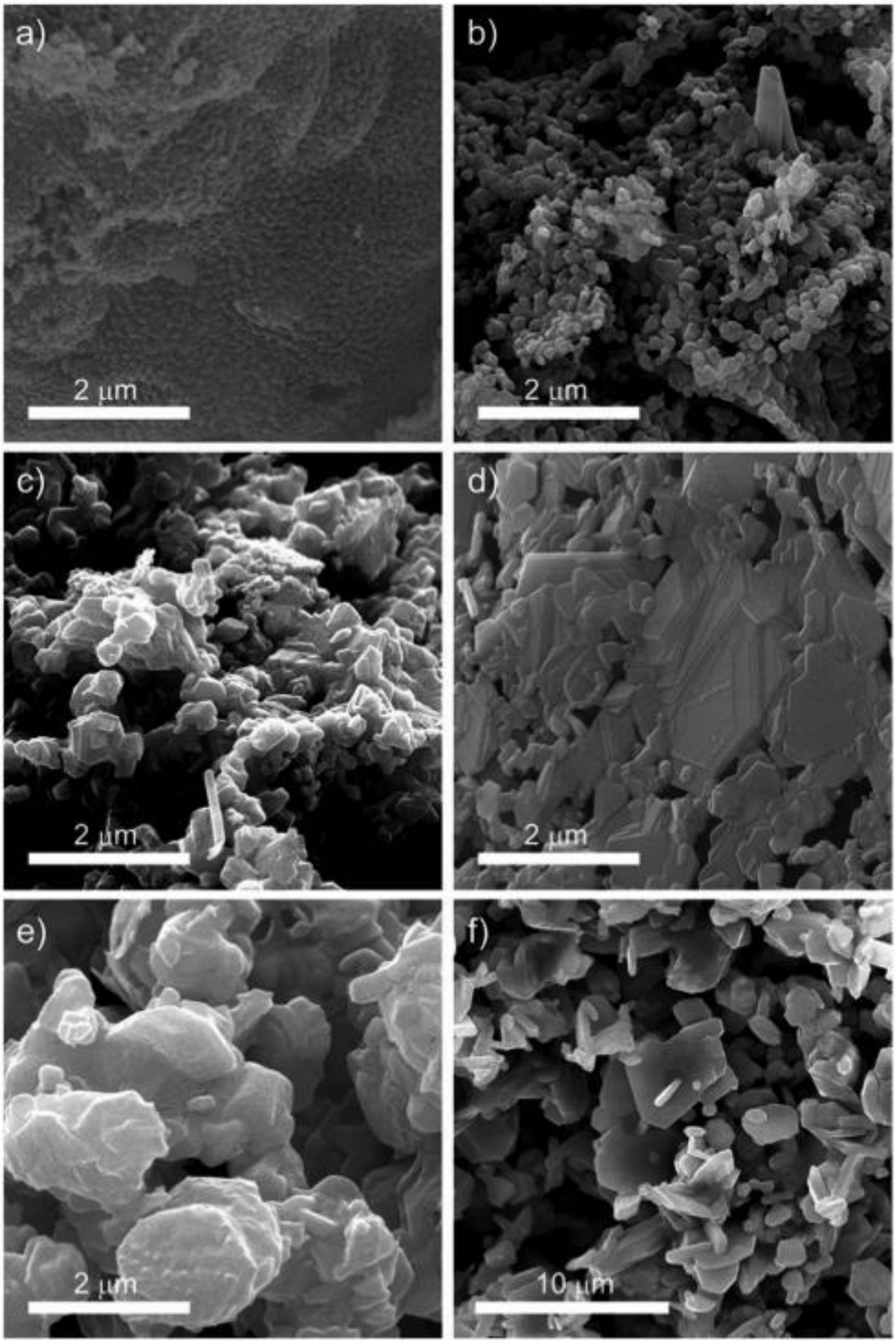

Figure 1.26: *SEM images of P3-$Na_{2/3}Ni_{1/3}Mn_{2/3}O_2$ prepared by dextran biotemplating calcined for 12 h at a) 550 °C, b) 650 °C, c) 750 °C and d) 850 °C. e,f) are prepared via solid state synthesis calcined at 850 °C for 12 h. Taken from ref*[6].

In another example, gelatin was used as a soft template in the synthesis of $LiNi_{0.5}Mn_{1.5}O_4$ (LNMO).[214] The biopolymer helped to reduce the quantity of secondary phase after calcination, as well as reduce the particle size, increase particle uniformity and crystallinity. When cycled between 3.5 and 4.9 V at 1 C, gelatin and non templated LNMO exhibited initial discharge capacities of 105 and 95 mAh g^{-1} and after 100 cycles it was 110 and 70 mAh g^{-1} respectively. The templated specimen also had significantly better rate capability and lower charge transfer resistance.

1.2.10.3.3 Interactions between biopolymers and metal cations in soft biotemplating

One of the main benefits of solution-based synthesis is its applicability to complex materials, [14] such as LTMOs that are commonly ternary or quaternary systems .[11,101,104,158,215] In biotemplating synthesis of these materials, there would be various metal cation species in the solution interacting with the polymer. A factor to consider is that different metal cations have different binding strengths for the same polymer/ligand and preferred binding could lead phase separation if a relatively large concentration of the same type of cation is not chelated with the biopolymer. Such phase separation can happen alkoxide sol-gel due to different rates of hydrolysis between the different metal alkoxides.[14] Therefore, it is important there is an excess of binding sites as well as ensuring all precursor cations are actually able to bind with the biopolymer.

Dextran has been used as a biotemplate in the synthesis of various functional materials.[216–218] It is a polysaccharide glycosidic polymer, consisting of an α1-6 backbone with α1-3 side chains, figure 1.27.[176] It is produced by bacteria by enzymatic fermentation of sucrose and is very soluble in water compared to cellulose or starch, which is important for soft templating and creating chelating sites.[179]

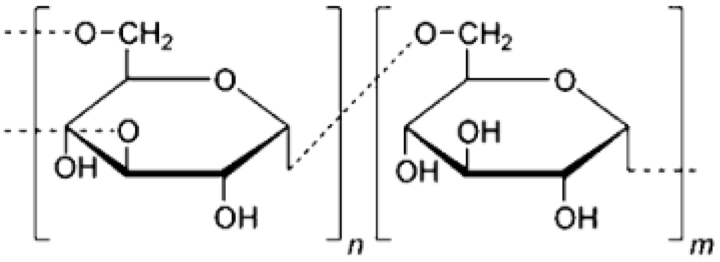

Figure 1.27*: molecular structure of dextran taken from ref*[176]*.*

There are a number of studies on the interactions between bioplymers and cations for water treatment which can potential give some insight into the interactions during biotemplating synthesis of oxides. Biopolymers like chitosan and dextran may be used polymer assisted ultrafiltration (PAUF) due to their affinity towards metal cations, where the metal-polymer complex solution is passed through a filter. The filter prevents the metal-polymer complex from passing through, thus allowing metals to be removed from water. Due to the varying binding strengths of the metal cations, some metals cations me still pass through the filter. There have been a few studies in PAUF on complex stability where there were multiple metal cation species in the solution. Such studies may shed some light on template-cation affinity,[213,219–221] and help to identify suitable biopolymers for certain materials.

For example, dextran has shown preferred complexation with Fe^{3+}, where degree of complexation decreases in the order of $Fe^{3+}>Ni^{2+}>Cu^{2+}$.[213] The affinity to Ni^{2+} and Cu^{2+} are quite similar and are both significantly lower compared to Fe^{3+} due to electrostatic attraction. The pH of the solution also has a significant impact on cation retention. The retention of Fe^{3+} increased up to pH 4, and remained somewhat constant up to pH 6, and then gradually decreased as the pH increased. For Ni^{2+} and Cu^{2+} the retention increased to a maximum at pH 6 and remained constant as pH up to around pH 8 and gradually decreased as pH increased. Functional groups on the biopolymer can too affect the affinity towards different cations.[222]

The competing reactions that occur in solution with dextran and dissolved precursors is hydrolysis of the metal cations and deprotonation of functional groups in the biopolymer. At low pH, hydrolysis of cations is less likely, however deprotonation of the biopolymers is more difficult. At high pH, this would enhance deprotonation of the biopolymer but increase the likelihood of hydrolysis of the metal cations, eventually leading to precipitation. Therefore, careful consideration of pH is needed to ensure the cations are able to bind to the biopolymer. For example, dextran and Cu^{2+} complex is destroyed at pH levels above 12.[223] The proposed binding mechanisms for Cu-dextran complex at different pH is shown in figure 1.28. At pH 7.5, figure 1.28a, Cu^{2+} is bound to deprotonated hydroxyl group and protonated hydroxyl groups and water molecules through hydrogen bonding[223] As the pH increases to 9.2 and 11.4, the water molecules are gradually replaced with OH groups, figure 1.28b and 1.28c respectively. Similar binding mechanism is likely with other transition metal cations and octahedral coordination is very common in metal/ligand complexes. As each metal cation is likely to take up at least four hydroxyl groups to bind to dextran, it is important even more important that excess biotemplate is used, especially with preferred affinity for some cations. A lack of biotemplate is likely to lead to a large concentration of one type of metal cation species unbound which would likely cause phase separation and unconstrained growth of some intermediate phases. Such phases could persist to high temperatures, therefore requiring more intense synthesis conditions which biotemplating normally reduces.

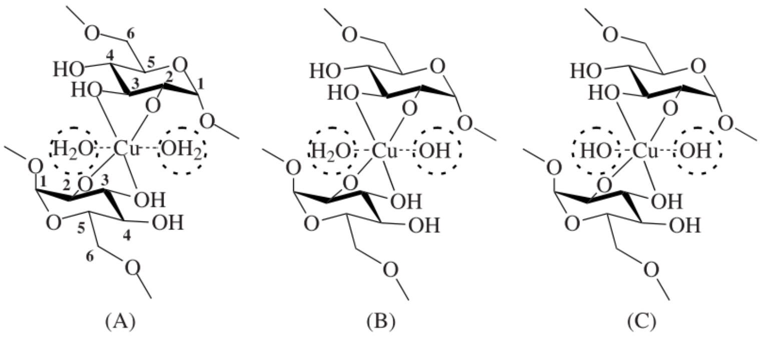

Figure 1.28: *Complexing mechanisms of Cu^{2+} and dextran at pH of a) 7.5, b) 9.2 and c) 11.4. Image taken from ref*[223].

The pKa of the biopolymer is also an important parameter to consider when determining the right pH conditions for complexing. If the pH of solution containing the biopolymer is at the pKa, then half of the functional groups are deprotonated. If the pH is below the pKa, the level of deprotonation of the functional groups (e.g. hydroxyl, carboxylate etc) significantly drops and the uptake in metal cations drop. If the pH is above the pKa, then there is likely to be a significant number of binding sites due to increased deprotonation. In the literature there are no values for the pKa of dextran. However, for most polysaccharide (such as alginate, chitosan, pectin and dextran derivatives) the pKa ranges roughly between 3 and 6.5.[224–226] These values, however are mostly based on other functional groups such as carboxylate, sulphate and amine groups. Dextran had greater retention for Cu^{2+} and Ni^{2+} at pH 6-8.[213] Therefore, the value of pKa for dextran may be below 6. Hydrolysis of Cu, Ni, and Mn ions would start to become an issue if the pH is increase beyond 8,[227,228] which coincides with the decreased retention of Cu^{2+} and Ni^{2+} ions with dextran.[213] Therefore, in this thesis, dextran biotemplating synthesis was conducted around pH 7 to ensure majority of the hydroxyl groups are deprotonated and that hydrolysis of the metal cations are less likely.

1.3 Summary

There are only a handful of studies on P3-$Na_{2/3}Ni_{1/3}Mn_{2/3}O_2$ (P3-NNM) which show that performance is lagging behind P2-NNM. However, P2-NNM does also exhibit poor cycling stability at extended voltage range (1.5 – 4.5 V), mostly caused by the P2-O2 phase transition and irreversible anionic redox of lattice oxygen. Such degradation mechanisms can be eliminated, at least to a decent extent, through addition of other metal ions such as Cu^{2+}, Fe^{3+} and Mg^{2+}. An understanding of the degradation mechanisms that occur in P2-NNM can give an insight into what may occur in P3-NNM and the potential routes that can be used to improve performance. As development is still lacking in P3-NNM, there opportunity to improve the performance of this material. In-depth characterisation of P3-NNM and attempting different routes to improve performance can show this material is a viable sustainable electrode material. In previous studies, dextran biotemplated P3-NNM was able to be synthesised at 550 °C, significantly lower compared to the temperatures required to crystallise the P2 phase. The ability to synthesise P3-NNM at lower temperatures, is one of the main benefits of such material.

Biotemplating is a versatile synthesis method that can enable the replication of the complex microstructures that are found in nature to improve specific properties of functional materials. It can also reduce calcination temperatures and dwell times due to the ability to mix precursors at the atomic level. The biopolymer ensures good spatial distribution of the precursors, prevents agglomeration and impedes growth of intermittent phases up until it decomposes, around 300 °C. This allows for a large number of nucleation sites for P3-NNM, allowing for formation of smaller particles as well as early on-set crystallisation. Biotemplating is also an ideal synthesis method for complex oxides, hence the addition of another metal species during synthesis is simple, for example substituting some Ni^{2+} for Cu^{2+} in P3-NNM with the aim of improving cycling stability.

At least in dextran biotemplated P3-NNM, secondary phases have shown to persist to high temperatures. Therefore, it is important to understand the interactions between the precursor metal cations and the biopolymer as this would affect the phases formed at lower temperatures which would greatly affect the quality of the final product. Studies from polymer assisted ultrafiltration (PAUF) have shown that dextran has different affinities for different metal cations, which causes preferred binding over other cations. In biotemplating synthesis, this could cause phase separation and unconstrained growth of some intermediate phases, negating the benefits mentioned earlier. Therefore it is important to understand the role and the impact a biopolymer has on the crystallisation process during synthesis of layered oxides.

1.4 References

1. Dunn, B., Kamath, H. & Tarascon, J.-M. Electrical Energy Storage for the Grid: A Battery of Choices. *Science (1979)* **334**, 928–935 (2011).
2. *Global EV Outlook 2022 Securing supplies for an electric future*. www.iea.org/ (2022).
3. Rudola, A. *et al.* Commercialisation of high energy density sodium-ion batteries: Faradion's journey and outlook. *J Mater Chem A Mater* **9**, 8279–8302 (2021).
4. Han, M. H., Gonzalo, E., Singh, G. & Rojo, T. A comprehensive review of sodium layered oxides: powerful cathodes for Na-ion batteries. *Energy Environ Sci* **8**, 81–102 (2015).

5. Zhang, J., Wang, W., Wang, W., Wang, S. & Li, B. Comprehensive Review of P2-Type $Na_{2/3}Ni_{1/3}Mn_{2/3}O_2$, a Potential Cathode for Practical Application of Na-Ion Batteries. *ACS Appl. Mater. Interfaces* **11**, 22051–22066 (2019).

6. Zilinskaite, S., Rennie, A. J. R., Boston, R. & Reeves-McLaren, N. Biotemplating: A sustainable synthetic methodology for Na-ion battery materials. *J. Mater. Chem. A* **6**, 5346–5355 (2018).

7. Liu, G., Kong, X., Li, Y. & Wang, B. Porous $LiMn_2O_4$ with improved rate capability synthesised by facile biotemplate method. *Mater. Technol.* **31**, 299–306 (2016).

8. Lee, S. Y., Kim, J. H. & Kang, Y. C. Electrochemical properties of P2-type $Na_{2/3}Ni_{1/3}Mn_{2/3}O_2$ plates synthesized by spray pyrolysis process for sodium-ion batteries. *Electrochim. Acta* **225**, 86–92 (2017).

9. Wang, K., Yan, P. & Sui, M. Phase transition induced cracking plaguing layered cathode for sodium-ion battery. *Nano Energy* **54**, 148–155 (2018).

10. Lu, Z. & Dahn, J. R. In Situ X-Ray Diffraction Study of P2-$Na_{2/3}[Ni_{1/3}Mn_{2/3}]O_2$. *J Electrochem Soc* **148**, A1225–A1229 (2001).

11. Liu, G., Wen, L., Li, Y. & Kou, Y. Synthesis and electrochemical properties of P2-$Na_{2/3}Ni_{1/3}Mn_{2/3}O_2$. *Ionics (Kiel)* **21**, 1011–1016 (2015).

12. Zhao, W., Kirie, H., Tanaka, A., Unno, M. & Yamamoto, S. Synthesis of metal ion substituted P2-$Na_{2/3}Ni_{1/3}Mn_{2/3}O_2$ cathode material with enhanced performance for Na ion batteries. *Mater Lett* **135**, 131–134 (2014).

13. Wang, L. *et al.* Copper-substituted $Na_{0.67}Ni_{0.3-x}Cu_xMn_{0.7}O_2$ cathode materials for sodium-ion batteries with suppressed P2-O2 phase transition. *J Mater Chem A Mater* **5**, 8752–8761 (2017).

14. Danks, Ashleigh. E., Hall, S. R. & Schnepp, Z. The evolution of 'sol-gel' chemistry as a technique for materials synthesis. *Mater. Horiz.* **3**, 91–112 (2016).

15. Patra, J. *et al.* A Water-Soluble NaCMC/NaPAA Binder for Exceptional Improvement of Sodium-Ion Batteries with an SnO_2-Ordered Mesoporous Carbon Anode. *ChemSusChem* **11**, 3923–3931 (2018).

16. Zhang, Y.-Y. *et al.* Improvement of electrochemical properties of P2-type $Na_{2/3}Mn_{2/3}Ni_{1/3}O_2$ sodium ion battery cathode material by water-soluble binders. *Electrochim. Acta* **298**, 496–504 (2019).

17. Zhang, Y. *et al.* Water-Stable Cathode for High Rate Na-Ion Batteries. *ACS Appl. Mater. Interfaces* **12**, 15220–15227 (2020).

18. Zuo, W. *et al.* The stability of P2-layered sodium transition metal oxides in ambient atmospheres. *Nat Commun* **11**, 3544 (2020).

19. Zhou, Y. N. *et al.* Air-Stable and High-Voltage Layered P3-Type Cathode for Sodium-Ion Full Battery. *ACS Appl. Mater. Interfaces* **11**, 24184–24191 (2019).

20. The Paris Agreement | United Nations. https://www.un.org/en/climatechange/paris-agreement.

21. Net Zero Coalition | United Nations. https://www.un.org/en/climatechange/net-zero-coalition.

22. UK enshrines new target in law to slash emissions by 78% by 2035 - GOV.UK. https://www.gov.uk/government/news/uk-enshrines-new-target-in-law-to-slash-emissions-by-78-by-2035 (2021).

23. Ritchie, H., Roser, M. & Rosado, P. CO_2 and Greenhouse Gas Emissions. *Our World in Data* https://ourworldindata.org/co2-and-other-greenhouse-gas-emissions (2020).

24. Renewables – Global Energy Review 2021 . *International Energy Agency* https://www.iea.org/reports/global-energy-review-2021/renewables (2021).

25. United Kingdom - Countries & Regions - IEA. https://www.iea.org/countries/united-kingdom.

26. Bird, L. *et al.* Wind and solar energy curtailment: A review of international experience. *Renewable and Sustainable Energy Reviews* **65**, 577–586 (2016).

27. Impact of Curtailment on Wind Economics | Renewable Energy World. https://www.renewableenergyworld.com/baseload/impact-of-curtailment-on-wind-economics/.

28. Yang, Z. *et al.* Electrochemical Energy Storage for Green Grid. *Chem. Rev* **111**, 3577–3613 (2011).

29. Parkinson, G. How Tesla's big battery is bringing Australia's gas cartel to heel. *Guardian* https://www.theguardian.com/technology/2018/feb/06/how-teslas-big-battery-is-bringing-australias-gas-cartel-to-heel (2018).

30. Wahlquist, C. South Australia's Tesla battery on track to make back a third of cost in a year. *The Guardian* https://www.theguardian.com/technology/2018/sep/27/south-australias-tesla-battery-on-track-to-make-back-a-third-of-cost-in-a-year (2018).

31. Batteries charge up Australia's efforts to shift away from coal | Financial Times. https://www.ft.com/content/825e1816-69e5-453c-865b-248727166b71.

32. Greim, P., Solomon, A. A. & Breyer, C. Assessment of lithium criticality in the global energy transition and addressing policy gaps in transportation. *Nat Commun* **11**, 4570 (2020).

33. Olivetti, E. A., Ceder, G., Gaustad, G. G. & Fu, X. Lithium-Ion Battery Supply Chain Considerations: Analysis of Potential Bottlenecks in Critical Metals. *Joule* **1**, 229–243 (2017).

34. Faunce, T. A., Prest, J., Su, D., Hearne, S. J. & Iacopi, F. On-grid batteries for large-scale energy storage: Challenges and opportunities for policy and technology. *MRS Energy & Sustainability* **5**, 1–12 (2018).

35. Lithium, Cobalt and Nickel: The Gold Rush of the 21st Century. *Faraday Insights* (2020).

36. Chayambuka, K., Mulder, G., Danilov, D. L. & Notten, P. H. L. From Li-Ion Batteries toward Na-Ion Chemistries: Challenges and Opportunities. *Adv Energy Mater* **10**, (2020).

37. Reddy, M. V, Mauger, A., Julien, C. M., Paolella, A. & Zaghib, K. Brief History of Early Lithium-Battery Development. *Materials* **13**, 1884 (2020).

38. Tarascon, J. M. & Armand, M. Issues and challenges facing rechargeable lithium batteries. *Nature* **414**, 359–367 (2001).

39. Zhang, R. *et al.* State of the art of lithium-ion battery SOC estimation for electrical vehicles. *Energies (Basel)* **11**, 1820 (2018).

40. Duan, J. *et al. Building Safe Lithium-Ion Batteries for Electric Vehicles: A Review*. *Electrochemical Energy Reviews* vol. 3 (Springer Singapore, 2020).

41. Winter, M., Barnett, B. & Xu, K. Before Li Ion Batteries. *Chem Rev* **118**, 11433–11456 (2018).

42. Neumann, J. *et al.* Recycling of Lithium-Ion Batteries—Current State of the Art, Circular Economy, and Next Generation Recycling. *Adv Energy Mater* **12**, 2102917 (2022).

43. Goikolea, E. *et al.* Na-Ion Batteries—Approaching Old and New Challenges. *Adv Energy Mater* **10**, (2020).

44. Yabuuchi, N., Kubota, K., Dahbi, M. & Komaba, S. Research Development on Sodium-ion Batteries. *Chem. Rev.* **114**, 11636–11682 (2014).

45. Rudola, A., Wright, C. J. & Barker, J. Reviewing the Safe Shipping of Lithium-Ion and Sodium-Ion Cells: A Materials Chemistry Perspective. *Energy Material Advances* **2021**, 9798460 (2021).

46. Desai, P., Huang, J., Foix, D., Tarascon, J. M. & Mariyappan, S. Zero volt storage of Na-ion batteries: Performance dependence on cell chemistry! *J Power Sources* **551**, 232177 (2022).

47. Li, H., Bai, Y., Wu, F., Ni, Q. & Wu, C. Na3V2(PO4)3/C nanorods as advanced cathode material for sodium ion batteries. *Solid State Ion* **278**, 281–286 (2015).

48. Lyu, Y. *et al.* Recent advances in high energy-density cathode materials for sodium-ion batteries. *SM&T* **21**, e00098 (2019).

49. Hwang, J.-Y., Myung, S.-T. & Sun, Y.-K. Sodium-ion batteries: present and future. *Chem. Soc. Rev* **46**, 3529 (2017).

50. Fatima, H., Zhong, Y., Wu, H. & Shao, Z. Recent advances in functional oxides for high energy density sodium-ion batteries. *Materials Reports: Energy* **1**, 100022 (2021).

51. Palomares, V. *et al.* Na-ion batteries, recent advances and present challenges to become low cost energy storage systems. *Energy Environ Sci* **5**, 5884–5901 (2012).

52. Liu, Z. *et al.* Ultralow Volume Change of P2-Type Layered Oxide Cathode for Na-Ion Batteries with Controlled Phase Transition by Regulating Distribution of Na^+. *Angew. Chem. Int. Ed* **60**, 20960–20969 (2021).

53. Wang, P.-F., You, Y., Yin, Y.-X. & Guo, Y.-G. Layered Oxide Cathodes for Sodium-Ion Batteries: Phase Transition, Air Stability, and Performance. *Adv Energy Mater* **8**, 1701912 (2018).

54. Schmidt-Rohr, K. How Batteries Store and Release Energy: Explaining Basic Electrochemistry. *J Chem Educ* **95**, 1801–1810 (2018).

55. Nitta, N., Wu, F., Lee, J. T. & Yushin, G. Li-ion battery materials: Present and future. *Materials Today* **18**, 252–264 (2015).

56. Gao, J., Shi, S.-Q. & Li, H. Brief overview of electrochemical potential in lithium ion batteries*. *Chinese Physics B* **25**, 018210 (2015).

57. Zhang, H. *et al.* Organic Cathode Materials for Sodium-Ion Batteries: From Fundamental Research to Potential Commercial Application. *Adv Funct Mater* **32**, 2107718 (2022).

58. Kraytsberg, A., Ein-Eli, Y., Kraytsberg, A. & Ein-Eli, Y. Higher, stronger, better ... A review of 5 volt cathode materials for advanced lithium-ion batteries. *Adv Energy Mater* **2**, 922–939 (2012).

59. Yu, P. *et al.* Recent progress in plant-derived hard carbon anode materials for sodium-ion batteries: a review. *Rare Metals* **39**, 1019–1033 (2020).

60. You, Y. & Manthiram, A. Progress in High-Voltage Cathode Materials for Rechargeable Sodium-Ion Batteries. *Adv Energy Mater* **8**, 1701785 (2018).

61. Li, Y. *et al.* Ether-based electrolytes for sodium ion batteries. *Chem. Soc. Rev* **51**, 4484 (2022).

62. Xiao, Z. *et al.* Electrochemical Analysis for Enhancing Interface Layer of Spinel $LiNi_{0.5}Mn_{1.5}O_4$ Using p-Toluenesulfonyl Isocyanate as Electrolyte Additive. *Front Chem* **7**, 591 (2019).

63. Li, J. T. *et al.* Water Soluble Binder, an Electrochemical Performance Booster for Electrode Materials with High Energy Density. *Adv Energy Mater* **7**, 1701185 (2017).

64. Ponrouch, A. *et al.* Non-aqueous electrolytes for sodium-ion batteries. *J Mater Chem A Mater* **3**, 22–42 (2015).

65. Xie, F., Xu, Z., Guo, Z. & Titirici, M. M. Hard carbons for sodium-ion batteries and beyond. *Progress in Energy* **2**, (2020).

66. Asenbauer, J. *et al.* The success story of graphite as a lithium-ion anode material-fundamentals, remaining challenges, and recent developments including silicon (oxide) composites. *Sustain Energy Fuels* **4**, 5387–5416 (2020).

67. Goodenough, J. B. & Park, K. S. The Li-ion rechargeable battery: A perspective. *J Am Chem Soc* **135**, 1167–1176 (2013).

68. Ni, Q., Bai, Y., Wu, F. & Wu, C. Polyanion-Type Electrode Materials for Sodium-Ion Batteries. *Advanced Science* **4**, 1600275 (2017).

69. Xiang, X., Zhang, K. & Chen, J. Recent Advances and Prospects of Cathode Materials for Sodium-Ion Batteries. *Adv. Mater.* **27**, 5343–5364 (2015).

70. Hasa, I., Buchholz, D., Passerini, S. & Hassoun, J. A Comparative Study of Layered Transition Metal Oxide Cathodes for Application in Sodium-Ion Battery. *ACS Appl. Mater. Interfaces* **7**, 5206–5212 (2015).

71. Dai, Z., Mani, U., Tan, H. T. & Yan, Q. Advanced Cathode Materials for Sodium-Ion Batteries: What Determines Our Choices? *Small Methods* **1**, 1700098 (2017).

72. Guo, S.-P., Li, J.-C., Xu, Q.-T., Ma, Z. & Xue, H.-G. Recent achievements on polyanion-type compounds for sodium-ion batteries: Syntheses, crystal chemistry and electrochemical performance. *J Power Sources* **361**, 285–299 (2017).

73. Moradi, M. *et al.* Improving the Capacity of Sodium Ion Battery Using a Virus Templated Nanostructured Composite Cathode. *Nano Lett* **15**, 2917–2921 (2015).

74. Fang, Y. *et al.* High-Performance Olivine NaFePO4 Microsphere Cathode Synthesized by Aqueous Electrochemical Displacement Method for Sodium Ion Batteries. *ACS Appl Mater Interfaces* **7**, 17977–17984 (2015).

75. Liu, Q. *et al.* The Cathode Choice for Commercialization of Sodium-Ion Batteries: Layered Transition Metal Oxides versus Prussian Blue Analogs. *Adv Funct Mater* **30**, (2020).

76. Paolella, A. *et al.* A review on hexacyanoferrate-based materials for energy storage and smart windows: challenges and perspectives. *J Mater Chem A Mater* **5**, 18919–18932 (2017).

77. Peng, J. *et al.* Prussian Blue Analogues for Sodium-Ion Batteries: Past, Present, and Future. *Adv. Mater* **34**, 2108384 (2022).

78. Lee, H. W. *et al.* Manganese hexacyanomanganate open framework as a high-capacity positive electrode material for sodium-ion batteries. *Nat Commun* **5**, 5280 (2014).

79. Wang, S. *et al.* All Organic Sodium-Ion Batteries with Na4C8H2O6. *Angewandte Chemie International Edition* **53**, 5892–5896 (2014).

80. Arag, M. J. *et al.* On the use of guanidine hydrochloride soft template in the synthesis of $Na_{2/3}Ni_{1/3}Mn_{2/3}O_2$ cathodes for sodium-ion batteries. *J. Alloys Compd.* **789**, 1035–1045 (2019).

81. Bucher, N. *et al.* Layered Na_xMnO_{2+z} in Sodium Ion Batteries−Influence of Morphology on Cycle Performance. *ACS Appl. Mater. Interfaces* **6**, 8059–8065 (2014).

82. Delmas, C., Fouassier, C. & Hagenmuller, P. Structural classification and properties of the layered oxides. *Physica* **99B**, 81–85 (1980).

83. Zhao, C. *et al.* Revealing High Na-Content P2-Type Layered Oxides as Advanced Sodium-Ion Cathodes. *J Am Chem Soc* **142**, 5742–5750 (2020).

84. Tiwari, B. & Bhattacharya, I. Layered P2- type novel Na0.7Ni0.3Mn0.59Co0.1Cu0.01O2 cathode material for high-capacity & stable rechargeable sodium ion battery. *Electrochim Acta* **270**, 363–368 (2018).

85. Lee, D. H., Xu, J. & Meng, Y. S. An advanced cathode for Na-ion batteries with high rate and excellent structural stability. *Phys. Chem. Chem. Phys.* **15**, 3304–3312 (2013).

86. Slater, M. D., Kim, D., Lee, E. & Johnson, C. S. Sodium-Ion Batteries. *Adv. Funct. Mater.* **23**, 947–958 (2013).

87. Guo, S. *et al.* A Layered P2- and O3-type Composite as a High-Energy Cathode for Rechargeable Sodium-Ion Batteries. *Angew.Chem. Int. Ed.* **54**, 5894–5899 (2015).

88. Zhang, S. *et al.* P3/O3 Integrated Layered Oxide as High-Power and Long-Life Cathode toward Na-Ion Batteries. *Small* **17**, 2007236 (2021).

89. Han, M. H. *et al.* Synthesis and Electrochemistry Study of P2- and O3-phase $Na_{2/3}Fe_{1/2}Mn_{1/2}O_2$. *Electrochim Acta* **182**, 1029–1036 (2015).

90. Zhao, C. *et al.* Rational design of layered oxide materials for sodium-ion batteries. *Science (1979)* **370**, 708–712 (2020).

91. Bianchini, M. *et al.* The interplay between thermodynamics and kinetics in the solid-state synthesis of layered oxides. *Nat Mater* **19**, 1088–1095 (2020).

92. Guo, S. *et al.* Understanding sodium-ion diffusion in layered P2 and P3 oxides via experiments and first-principles calculations: a bridge between crystal structure and electrochemical performance. *NPG Asia Mater.* **8**, 266–274 (2016).

93. Wang, P. F. *et al.* Na^+/vacancy disordering promises high-rate Na-ion batteries. *Sci. Adv.* **4**, 1–9 (2018).

94. Zhang, L. *et al.* Preferential occupation of Na in P3-type layered cathode material for sodium ion batteries. *Nano Energy* **70**, 104535 (2020).

95. Wang, P.-F., You, Y., Yin, Y.-X. & Guo, Y.-G. An O3-type $NaNi_{0.5}Mn_{0.5}O_2$ cathode for sodium-ion batteries with improved rate performance and cycling stability. *J. Mater. Chem. A* **4**, 17660–17664 (2016).

96. Marelli, E., Marino, C., Bolli, C. & Villevieille, C. How to overcome Na deficiency in full cell using P2-phase sodium cathode – A proof of concept study of Na-rhodizonate used as sodium reservoir. *J Power Sources* **450**, 227617 (2020).

97. Keller, M., Buchholz, D. & Passerini, S. Layered Na-Ion Cathodes with Outstanding Performance Resulting from the Synergetic Effect of Mixed P- and O-Type Phases. *Adv. Energy Mater.* **6**, 1501555–1501566 (2016).

98. Sabi, N. *et al.* Layered P2-$Na_{2/3}Co_{1/2}Ti_{1/2}O_2$ as a high-performance cathode material for sodium-ion batteries. *J Power Sources* **342**, 998–1005 (2017).

99. Huang, Y. *et al.* Vitalization of P2-$Na_{2/3}Ni_{1/3}Mn_{2/3}O_2$ at high-voltage cyclability via combined structural modulation for sodium-ion batteries. *Energy Storage Mater* **29**, 182–189 (2020).

100. Manikandan, P., Ramasubramonian, D. & Shaijumon, M. M. Layered P2-type Na0.5Ni0.25Mn0.75O2 as a high performance cathode material for sodium-ion batteries. *Electrochim Acta* **206**, 199–206 (2016).

101. Mu, L. *et al.* Water-Processable P2-Na0.67Ni0.22Cu0.11Mn0.56Ti0.11O2 Cathode Material for Sodium Ion Batteries. *J Electrochem Soc* **166**, A251 (2019).

102. Liu, Q. *et al.* Recent Progress of Layered Transition Metal Oxide Cathodes for Sodium-Ion Batteries. *Small* **15**, 1805381 (2019).

103. Komaba, S. *et al.* Study on the Reversible Electrode Reaction of Na1–xNi0.5Mn0.5O2 for a Rechargeable Sodium-Ion Battery. *Inorg Chem* **51**, 6211–6220 (2012).

104. Ding, F. *et al.* A Novel Ni-rich O3-$Na[Ni_{0.60}Fe_{0.25}Mn_{0.15}]O_2$ Cathode for Na-ion Batteries. *Energy Storage Mater* **30**, 420–430 (2020).

105. Hwang, J. Y., Myung, S. T., Aurbach, D. & Sun, Y. K. Effect of nickel and iron on structural and electrochemical properties of O3 type layer cathode materials for sodium-ion batteries. *J Power Sources* **324**, 106–112 (2016).

106. Risthaus, T. *et al.* P3 Na0.9Ni0.5Mn0.5O2 Cathode Material for Sodium Ion Batteries. *Chem. Mater.* **31**, 5376–5383 (2019).

107. Chagas, L. G., Buchholz, D., Vaalma, C., Wu, L. & Passerini, S. P-type NaxNi0.22Co0.11Mn0.66O2 materials: Linking synthesis with structure and electrochemical performance. *J. Mater. Chem. A* **2**, 20263–20270 (2014).

108. Song, B. *et al.* A novel P3-type $Na_{2/3}Mg_{1/3}Mn_{2/3}O_2$ as high capacity sodium-ion cathode using reversible oxygen redox. *J. Mater. Chem. A* **7**, 1491–1498 (2019).

109. Wang, P. *et al.* Suppressing the P2-O2 Phase transition of Na0.67Mn0.67Ni0.33O2 magnesium substitution for improved sodium-ion batteries. *Angew. Chem. Int. Ed* **55**, 7445–7449 (2016).

110. Dang, R. *et al.* Na+-Conductive Na2Ti3O7-Modified P2-type Na2/3Ni1/3Mn2/3O2 via a Smart in Situ Coating Approach: Suppressing Na+/Vacancy Ordering and P2-O2 Phase Transition. *ACS Appl. Mater. Interfaces* **11**, 856–864 (2019).

111. Goyal, A. *et al.* Precision Manufacturing of NaNi1/3Mn1/3Co1/3O2 Cathodes: Study of Structure Evolution and Performance at Varied Calcination Temperatures. *J. Electron. Mater.* **48**, 5301–5309 (2019).

112. Kim, E. J. *et al.* Oxygen Redox Activity through a Reductive Coupling Mechanism in the P3-Type Nickel-Doped Sodium Manganese Oxide. *ACS Appl. Energy Mater.* **3**, 184–191 (2020).

113. Liu, J. *et al.* Elucidation of the high-voltage phase in the layered sodium ion battery cathode material P3–Na 0.5 Ni 0.25 Mn 0.75 O 2. *J Mater Chem A Mater* **8**, 21151–21162 (2020).

114. Kalapsazova, M. *et al.* P3-Type Layered Sodium-Deficient Nickel-Manganese Oxides: A Flexible Structural Matrix for Reversible Sodium and Lithium Intercalation. *Chempluschem* **80**, 1642–1656 (2015).

115. Ivanova, S. *et al.* Effect of Sodium Content on the Reversible Lithium Intercalation into Sodium-Deficient Cobalt-Nickel-Manganese Oxides NaxCo1/3Ni1/3Mn1/3O2($0.38 \leq x \leq 0.75$) with a P3 Type of Structure. *Journal of Physical Chemistry C* **120**, 3654–3668 (2016).

116. Zheng, L., Li, J. & Obrovac, M. N. Crystal Structures and Electrochemical Performance of Air-Stable $Na_{2/3}Ni_{1/3-x}Cu_xMn_{2/3}O_2$ in Sodium Cells. *Chem. Mater.* **29**, 1623–1631 (2017).

117. Zhang, Y., Zhang, R. & Huang, Y. Air-Stable NaxTMO2 Cathodes for Sodium Storage. *Front. Chem.* **7**, 335 (2019).

118. Clement, Raphaele. J., Bruce, Peter. G. & Grey, Clare. P. Review-Manganese-Based P2-Type Transition Metal Oxides as Sodium-Ion Battery Cathode Materials. *J. Electrochem. Soc.* **162**, A2589–A2604 (2015).

119. Tapia-Ruiz, N. *et al.* High voltage structural evolution and enhanced Na-ion diffusion in P2-Na2/3Ni1/3-xMgxMn2/3O2 ($0 < x < 0.2$) cathodes from diffraction, electrochemical and ab initio studies†. *Energy Environ. Sci* **11**, 1470 (2018).

120. Zhang, Y. *et al.* Revisiting the $Na_{2/3}Ni_{1/3}Mn_{2/3}O_2$ Cathode: Oxygen Redox Chemistry and Oxygen Release Suppression. *ACS Cent. Sci* **6**, 232–240 (2020).

121. Lu, Z. & Dahn, J. R. Intercalation of Water in P2, T2 and O2 Structure Az[CoxNi$_{1/3-x}$Mn$_{2/3}$]O$_2$. *Chem. Mater.* **13**, 1252–1257 (2001).

122. Jiang, J. *et al.* Improving Structural and Moisture Stability of P2-Layered Cathode Materials for Sodium-Ion Batteries. *ACS Appl. Energy Mater* **5**, 1252–1261 (2022).

123. Yoda, Y., Kubota, K., Isozumi, H., Horiba, T. & Komaba, S. Poly-γ-glutamate Binder To Enhance Electrode Performances of P2-Na 2/3 Ni 1/3 Mn 2/3 O 2 for Na-Ion Batteries. *ACS Appl. Mater. Interfaces* **10**, 10986–10997 (2018).

124. Wang, H. *et al.* Electrochemical Properties of P2-$Na_{2/3}[Ni_{1/3}Mn_{2/3}]O_2$ cathode material for sodium ion batteries when cycled in different voltage ranges. *Electrochim. Acta* **113**, 200–204 (2013).

125. Gutierrez, A. *et al.* On Disrupting the Na^+-Ion/Vacancy Ordering in P2-Type Sodium−Manganese−Nickel Oxide Cathodes for Na^+-Ion Batteries. *J. Phys. Chem. C* **122**, 23251–23260 (2018).

126. Liu, Y. *et al.* Hierarchical Engineering of Porous P2-$Na_{2/3}Ni_{1/3}Mn_{2/3}O_2$ Nanofibers Assembled by Nanoparticles Enables Superior Sodium-Ion Storage Cathodes. *Adv. Funct. Mater.* **30**, 1907837 (2020).

127. Sun, Y., Guo, S. & Zhou, H. Adverse effects of interlayer-gliding in layered transition-metal oxides on electrochemical sodium-ion storage. *Energy Environ. Sci* **12**, 825 (2019).

128. Risthaus, T. *et al.* A high-capacity P2 $Na_{2/3}Ni_{1/3}Mn_{2/3}O_2$ cathode material for sodium ion batteries with oxygen activity. *J Power Sources* **395**, 16–24 (2018).

129. Hong, J. H., Wang, M. Y., Du, Y. Y., Deng, L. & He, G. The role of Zn substitution in P2-type $Na_{0.67}Ni_{0.23}Zn_{0.1}Mn_{0.67}O_2$ cathode for inhibiting the phase transition at high potential and dissolution of manganese at low potential. *J. Mater. Sci.: Mater. Electron.* **30**, 4006–4013 (2019).

130. Li, C. *et al.* Cathode materials modified by surface coating for lithium ion batteries. *Electrochim Acta* **51**, 3872–3883 (2006).

131. Yang, Q. *et al.* Advanced P2-$Na_{2/3}Ni_{1/3}Mn_{7/12}Fe_{1/12}O_2$ Cathode Material with Suppressed P2−O2 Phase Transition toward High-Performance Sodium-Ion Battery. *ACS Appl. Mater. Interfaces* **10**, 34272−34282 (2018).

132. Yang, L. *et al.* Cu-doped layered P2-type $Na_{0.67}Ni_{0.33-x}Cu_xMn_{0.67}O_2$ cathode electrode material with enhanced electrochemical performance for sodium-ion batteries. *Chemical Engineering Journal* **404**, 126578 (2021).

133. Hu, G. *et al.* Highly stable Na0.67(Ni0.25Mn0.75)1−xCuxO2 cathode substituted by Cu for sodium-ion batteries. *Ionics (Kiel)* **27**, 657–666 (2021).

134. Kubota, K., Yoda, Y. & Komaba, S. Origin of Enhanced Capacity Retention of P2-Type Na2/3Ni1/3-xMn2/3CuxO2 for Na-Ion Batteries. *J Electrochem Soc* **164**, A2368–A2373 (2017).

135. Kang, S. M. *et al.* Na+/Vacancy Disordered P2-Na0.67Co1-xTixO2: High-Energy and High-Power Cathode Materials for Sodium Ion Batteries. *ACS Appl Mater Interfaces* **10**, 3562–3570 (2018).

136. Wen, Y. *et al.* Electrochemical and Structural Study of Layered P2-Type $Na_{2/3}Ni_{1/3}Mn_{2/3}O_2$ as Cathode Material for Sodium-Ion Battery. *Chem. Asian J.* **10**, 661–666 (2015).

137. Lu, Z., Donaberger, R. A. & Dahn, J. R. Superlattice ordering of Mn, Ni and Co in layered alkali transition metal oxides with P2, P3 and O3 structures. *Chem. Mater.* **12**, 3583–3590 (2000).

138. Wang, Y., Xiao, R., Hu, Y.-S., Avdeev, M. & Chen, L. P2-Na0.6[Cr0.6Ti0.4]O2 cation-disordered electrode for high-rate symmetric rechargeable sodium-ion batteries. *Nature Communications 2015 6:1* **6**, 1–9 (2015).

139. Tie, D. *et al.* Modulating the Interlayer Spacing and Na+/Vacancy Disordering of P2-Na0.67MnO2 for Fast Diffusion and High-Rate Sodium Storage. *ACS Appl Mater Interfaces* **11**, 6978–6985 (2019).

140. Tripathi, A., Xi, S., Reddy Gajjela, S. & Balaya, P. Introducing Na-sufficient P3-$Na_{0.9}Fe_{0.5}Mn_{0.5}O_2$ as a cathode material for Na-ion batteries †. *Chem. Commun* **56**, 10686 (2020).

141. Zhang, L. Electrochemical Performance and Structural Changes of $Na_{0.67}Mn_{0.67}Ni_{0.33}O_2$ as Cathode for Sodium Ion Batteries. (Technische Universität Berlin, 2019).

142. Zhang, L. *et al.* Stabilizing P3-Type Oxides as Cathodes for High-Rate and Long-Life Sodium Ion Batteries by Disordered Distribution of Transition Metals. *Small Methods* **4**, 2000422 (2020).

143. Zhang, L. *et al.* Preferential occupation of Na in P3-type layered cathode material for sodium ion batteries. *Nano Energy* **70**, 104535 (2020).

144. Li, R.-R. *et al.* Binders for sodium-ion batteries: progress, challenges and strategies. *Chem. Commun* **57**, 12406 (2021).

145. Chang, H. J. *et al.* Effects of water-based binders on electrochemical performance of manganese dioxide cathode in mild aqueous zinc batteries. *Carbon Energy* **3**, 473–481 (2021).

146. Keppeler, M., Tran, H. Y. & Braunwarth, W. The Role of Pilot Lines in Bridging the Gap Between Fundamental Research and Industrial Production for Lithium-Ion Battery Cells Relevant to Sustainable Electromobility: A Review. *Energy Technology* vol. 9 2100132 Preprint at https://doi.org/10.1002/ente.202100132 (2021).

147. He, J., Zhong, H., Wang, J. & Zhang, L. Investigation on xanthan gum as novel water soluble binder for LiFePO 4 cathode in lithium-ion batteries. *J Alloys Compd* **714**, 409–418 (2017).

148. Zhao, Y. M. *et al.* Advances of polymer binders for silicon-based anodes in high energy density lithium-ion batteries. *InfoMat* **3**, 460–501 (2021).

149. Wang, Y. B. *et al.* Strategies of binder design for high-performance lithium-ion batteries: a mini review. *Rare Metals* **41**, 745–761 (2022).

150. Lingappan, N., Kong, L. & Pecht, M. The significance of aqueous binders in lithium-ion batteries. *Renewable and Sustainable Energy Reviews* **147**, 111227 (2021).

151. Chen, Z., Christensen, L. & Dahn, J. R. Comparison of PVDF and PVDF-TFE-P as Binders for Electrode Materials Showing Large Volume Changes in Lithium-Ion Batteries. *J. Electrochem. Soc.* **150**, A1073 (2003).

152. He, W. *et al.* Challenges and Recent Advances in High Capacity Li-Rich Cathode Materials for High Energy Density Lithium-Ion Batteries. *Advanced Materials* **33**, (2021).

153. Divakaran, A. M. *et al.* Rational design on materials for developing next generation lithium-ion secondary battery. *Progress in Solid State Chemistry* **62**, 100298 (2021).

154. Jaiswal, A. *et al.* Nanoscale LiFePO 4 and LiTiO12 for High Rate Li-Ion Batteries. *J Electrochem Soc* **156**, A1041–A1046 (2009).

155. Sun, Y., Liu, N. & Cui, Y. Promises and challenges of nanomaterials for lithium-based rechargeable batteries. *Nat Energy* **1**, 16071 (2016).

156. West, A. Syntheis, Processing and Fabrication Methods. in *Solid State Chemistry and Its Applications* 187–195 (Wiley, 2014).

157. Zayat, M. & Levy, D. Blue CoAl2O4 particles prepared by the sol-gel and citrate-gel methods. *Chemistry of Materials* **12**, 2763–2769 (2000).

158. Wang, H., Gu, M., Jiang, J., Lai, C. & Ai, X. An O3-type NaNi0.5Mn0.3Ti0.2O2 compound as new cathode material for room-temperature sodium-ion batteries. *J Power Sources* **327**, 653–657 (2016).

159. Paulsen, J. M. & Dahn, J. R. Studies of the layered manganese bronzes, $Na_{2/3}[Mn_{1-x}M_x]O_2$ with M = Co, Ni, Li, and $Li_{2/3}[Mn_{1-x}M_x]O_2$ prepared by ion-exchange. *Solid State Ion* **126**, 3–24 (1999).

160. Mao, Q. *et al.* Mitigating the P2-O2 transition and Na+/vacancy ordering in $Na_{2/3}Ni_{1/3}Mn_{2/3}O_2$ by anion/cation dual-doping for fast and stable Na+ insertion/ extraction †. *J. Mater. Chem. A* **9**, 10803–10811 (2021).

161. Jamkhande, P. G., Ghule, N. W., Bamer, A. H. & Kalaskar, M. G. Metal nanoparticles synthesis: An overview on methods of preparation, advantages and disadvantages, and applications. *J Drug Deliv Sci Technol* **53**, 101174 (2019).

162. Ealia, S. A. M. & Saravanakumar, M. P. A review on the classification, characterisation, synthesis of nanoparticles and their application. *IOP Conf. Ser.: Mater. Sci. Eng.* **263**, 032019 (2017).

163. Zhang, X. *et al.* Improving the structural and cyclic stabilities of P2-type Na0.67MnO2 cathode material via Cu and Ti co-substitution for sodium ion batteries. *Chemical Communications* **56**, 6293–6296 (2020).

164. Chauque, S. *et al.* Lithium titanate as anode material for lithium ion batteries: Synthesis, post-treatment and its electrochemical response. *Journal of Electroanalytical Chemistry* **799**, 142–155 (2017).

165. Tarascon, J. M., Morcrette, M., Saint, J., Aymard, L. & Janot, R. On the benefits of ball milling within the field of rechargeable Li-based batteries. *Comptes Rendus Chimie* **8**, 17–26 (2005).

166. Pan, T. *et al.* Structural Degradation of Layered Cathode Materials in Lithium-Ion Batteries Induced by Ball Milling. *J Electrochem Soc* **166**, A1964–A1971 (2019).

167. Stein, M. *et al.* Probing the effect of high energy ball milling on the structure and properties of $LiNi_{1/3}Mn_{1/3}Co_{1/3}O_2$ cathodes for Li-ion batteries. *J. Electrochem. Energy Convers. Storage* **13**, 031001 1–10 (2016).

168. Wang, X. & Yushin, G. Chemical vapor deposition and atomic layer deposition for advanced lithium ion batteries and supercapacitors †. *Energy Environ. Sci* **8**, 1889 (2015).

169. Jung, D. S., Ko, Y. N., Kang, Y. C. & Park, S. bin. Recent progress in electrode materials produced by spray pyrolysis for next-generation lithium ion batteries. *Advanced Powder Technology* **25**, 18–31 (2014).

170. Liu, H., Wu, Y. P., Rahm, E., Holze, R. & Wu, H. Q. Cathode materials for lithium ion batteries prepared by sol-gel methods. *Journal of Solid State Electrochemistry* **8**, 450–466 (2004).

171. Wang, Y. *et al.* The novel P3-type layered Na0.65Mn0.75Ni0.25O2 oxides doped by non-metallic elements for high performance sodium-ion batteries. *Chem. Eng.* **360**, 139–147 (2019).

172. Kang, Y. S. *et al.* Shape control of hierarchical lithium cobalt oxide using biotemplates for connected nanoparticles. *J Power Sources* **436**, 226836 (2019).

173. Dong, B., Driscoll, L. L., Stockham, M. P., Kendrick, E. & Slater, P. R. Low temperature synthesis of garnet solid state electrolytes: Implications on aluminium incorporation in Li7La3Zr2O12. *Solid State Ion* **350**, (2020).

174. Boston, R., Carrington, A., Walsh, D. & Hall, S. R. Synthesis of spherical superconductors. *CrystEngComm* **15**, 3763–3766 (2013).

175. Zollfrank, C. *et al.* Biotemplating of inorganic functional materials from polysaccharides. *Bioinspired, Biomimetic and Nanobiomaterials* **1**, 1–28 (2012).

176. Schnepp, Z. Biopolymers as a Flexible Resource for Nanochemistry. *Angew. Chem. Int. Ed.* **52**, 1096–1108 (2013).

177. Li, C. *et al.* Cathode materials modified by surface coating for lithium ion batteries. *Electrochim Acta* **51**, 3872–3883 (2006).

178. Maddukuri, S., Valerie, P. & Upadhyayula, V. v. Synthesis and Electrochemical Study of New P3 Type Layered Na0.6Ni0.25Mn0.5Co0.25O2 for Sodium-Ion Batteries. *ChemistrySelect* **2**, 5660–5666 (2017).

179. Boston, R. *Chapter 1 Bioinspired Synthesis: History, Fundamentals and Outlook*. (The Royal Society of Chemistry, 2019). doi:10.1039/9781788015806-00001.

180. Tang, Z., Kotov, N. A., Magonov, S. & Ozturk, B. Nanostructured artificial nacre. *Nat Mater* **2**, 413–418 (2003).

181. Metzler, R. A. *et al.* Polarization-dependent imaging contrast in abalone shells. *Phys. Rev. B* **77**, 064110 (2008).

182. Chen, M. *et al.* A cross-like hierarchical porous lithium-rich layered oxide with (110)-oriented crystal planes as a high energy density cathode for lithium ion batteries. *J Mater Chem A Mater* **7**, 13120–13129 (2019).

183. Xu, M. *et al.* Tailoring Anisotropic Li-Ion Transport Tunnels on Orthogonally Arranged Li-Rich Layered Oxide Nanoplates Toward High-Performance Li-Ion Batteries. *Nano Lett* **17**, 1670–1677 (2017).

184. Tan, G. *et al.* Controllable crystalline preferred orientation in Li-Co-Ni-Mn oxide cathode thin films for all-solid-state lithium batteries. *Nanoscale* **6**, 10611–10622 (2014).

185. Zhang, D. *et al.* Morphological evolution and kinetic enhancement of $Li_2Fe_xMn_{1-x}SiO_4$/C cathodes for Li-ion battery. *Progress in Natural Science: Materials International* **28**, 535–541 (2018).

186. Song, J. *et al.* Controllable synthesis, morphology evolution and electrochemical properties of LiFePO4 cathode materials for Li-ion batteries. *Physical Chemistry Chemical Physics* **16**, 7728–7733 (2014).

187. Favors, Z. *et al.* Stable cycling of SiO_2 nanotubes as high-performance anodes for lithium-ion batteries. *Sci Rep* **4**, 4605 (2014).

188. Zhou, Y., Shen, C. & Li, H. Synthesis of high-ordered $LiCoO_2$ nanowire arrays by AAO template. *Solid State Ion* **146**, 81–86 (2002).

189. Xie, Y., Kocaefe, D., Chen, C. & Kocaefe, Y. Review of Research on Template Methods in Preparation of Nanomaterials. *J Nanomater* **2016**, 1–10 (2016).

190. Martakov, I. S. *et al.* Biotemplate synthesis of porous alumina fibers and filters with controlled structure and properties. *J Taiwan Inst Chem Eng* **95**, 281–289 (2019).

191. Xia, Y., Sun, B., Wei, Y., Tao, B. & Zhao, Y. Simple sol-gel method synthesis of 3-dimension Li4Ti5O12-TiO2nanostructures using butterfly wings as biotemplates for high rate performance lithium-ion batteries. *J Alloys Compd* **705**, 58–63 (2017).

192. Sotiropoulou, S., Sierra-Sastre, Y., Mark, S. S. & Batt, C. A. Biotemplated nanostructured materials. *Chemistry of Materials* **20**, 821–834 (2008).

193. Liu, G., Li, Y. & Wang, B. $LiNi_{0.5}Mn_{1.5}O_4$ with significantly improved rate capability synthesized by a facile template method using pine wood as a bio-template. *Mater Lett* **139**, 385–388 (2015).

194. Li, H. & Zhou, H. Enhancing the performances of Li-ion batteries by carbon-coating: present and future. *Chem. Commun* **48**, 1201–1217 (2012).

195. Wang, Y., Li, H., He, P., Hosono, E. & Zhou, H. Nano active materials for lithium-ion batteries. *Nanoscale* **2**, 1294–1305 (2010).

196. Wang, J. *et al.* Biomass derived fabrication of a novel sea cucumber-like LiMn2O4/C composite with a hierarchical porous structure as the cathode for lithium-ion batteries. *Electrochim Acta* **188**, 645–652 (2016).

197. Xia, Y. *et al.* Biotemplating of phosphate hierarchical rechargeable LiFePO4/C spirulina microstructures. *J Mater Chem* **21**, 6498 (2011).

198. Zhang, W.-J. Structure and performance of $LiFePO_4$ cathode materials: A review. *J Power Sources* **196**, 2962–2970 (2011).

199. Cao, Y., Feng, W. & Su, W. Bio-Synthesis of LiFePO4/C composites for lithium ion battery. *Int. J. Electrochem. Sci* **12**, 9084–9093 (2017).

200. Wang, D., Li, H., Shi, S., Huang, X. & Chen, L. Improving the rate performance of LiFePO4 by Fe-site doping. *Electrochim Acta* **50**, 2955–2958 (2005).

201. Su, D. W., Dou, S. X. & Wang, G. X. Hierarchical orthorhombic V 2 O 5 hollow nanospheres as high performance cathode materials for sodium-ion batteries †. *J. Mater. Chem. A* **2**, 11185 (2014).

202. Peng, T. *et al.* Hierarchical hollow microcuboid LiNi 0.5 Mn 1.5 O 4 as cathode material with excellent rate and cycling performance for lithium-ion batteries. *J. Solid State Electrochem.* **23**, 2927–2935 (2019).

203. Lou, X. W., Archer, L. A. & Yang, Z. Hollow micro-/nanostructures: Synthesis and applications. *Advanced Materials* **20**, 3987–4019 (2008).

204. Jamesh, M. I. Recent advances on flexible electrodes for Na-ion batteries and Li–S batteries. *Journal of Energy Chemistry* **32**, 15–44 (2019).

205. Deng, Y., Wan, L., Xie, Y., Qin, X. & Chen, G. Recent advances in Mn-based oxides as anode materials for lithium ion batteries. *RSC Adv* **4**, 23914–23935 (2014).

206. Zhu, W. *et al.* Synthesis of MnO/C composites derived from pollen template for advanced lithium-ion batteries. *Electrochim Acta* **152**, 286–293 (2015).

207. Xia, Y. *et al.* Green and Facile Fabrication of Hollow Porous MnO/C Microspheres from Microalgaes for Lithium-Ion Batteries. *ACS Nano* **7**, 7083–7092 (2013).

208. Wang, J. *et al.* Biotemplated MnO/C microtubes from spirogyra with improved electrochemical performance for lithium-ion batterys. *Electrochim Acta* **188**, 210–217 (2016).

209. Lee, S.-H. & Park, C.-H. Biosorption of Heavy Metal Ions by Brown Seaweeds from Southern Coast of Korea. *Biotechnology and Bioprocess Engineering* **17**, 853–861 (2012).

210. Boston, Rebecca. H. Control of Crystallisation in the Yttrium Barium Copper Oxide System. (University of Bristol, 2014).

211. Schnepp, Z. A. C., Wimbush, S. C., Mann, S. & Hall, S. R. Structural Evolution of Superconductor Nanowires in Biopolymer Gels. *Adv. Mater.Materials* **20**, 1782–1786 (2008).

212. Chiba, K., Shikano, M. & Sakaebe, H. Characterization of $Na_xLi_{0.67+y}Ni_{0.33}Mn_{0.67}O_2$ as a positive electrode material for lithium-ion batteries. *RSC Adv* **8**, 26335–26340 (2018).

213. Solpan, D. & Sahan, M. Concentration and separation of aqueous solutions of Cu2+, Ni2+, Fe3+ by dextran. *J. Appl. Polym. Sci.* **55**, 383–386 (1995).

214. Mo, M. *et al.* Gelatin-assisted synthesis of $LiNi_{0.5}Mn_{1.5}O_4$ cathode material for 5V lithium rechargeable batteries. *Appl Surf Sci* **276**, 635–640 (2013).

215. Zhang, L., He, W., Peng, D. L., Xie, Q. & Xie, R. J. A Layered Lithium-Rich Li(Li0.2Ni0.15Mn0.55Co0.1)O2 Cathode Material: Surface Phase Modification and Enhanced Electrochemical Properties for Lithium-Ion Batteries. *ChemElectroChem* **6**, 1542–1551 (2019).

216. Walsh, D., Wimbush, S. C. & Hall, S. R. Use of the polysaccharide dextran as a morphological directing agent in the synthesis of high-Tc superconducting YBa2Cu3O7-δ sponges with improved critical current densities. *Chem. Mater.* **19**, 647–649 (2007).

217. Dedman, J., Wimbush, S. C. & Hall, S. R. Biopolymer mediated sol-gel synthesis of $LuBa_2Cu_3O_{7-\delta}$. *Physica C* **470**, S237–S238 (2010).

218. Hung-Low, F., Peterson, G. R., Davis, M. & Hope-Weeks, L. J. Rapid preparation of high surface area iron oxide and alumina nanoclusters through a soft templating approach of sol-gel precursors. *New Journal of Chemistry* **37**, 245–249 (2013).

219. Shevchenko, L. I., Lugovaya, Z. A. & Tolmachev, V. N. Study of the complexing properties of the dextran carboxymethyl ether with transition metal ions in solutions. *Polym. Sci. (USSR)* **27**, 2242–2247 (1985).

220. Lugovaya, Z. A., Tolmachev, V. N. & Il'yenko, I. B. Study of the optical rotation of dextran solutions containing metal ions. *Polym. Sci. (USSR)* **23**, 484–489 (1981).

221. García-Molina, V., Esplugas, S., Wintgens, T. & Melin, T. Ultrafiltration of aqueous solutions containing dextran. *Desalination* **188**, 217–227 (2006).

222. Lawrance, G. A. *Introduction to Coordination Chemistry*. (Inorganic Chemistry, A Wiley Textbook Series, 2010).

223. Nikolić, G. S., Cakić, M., Mitić, Ž. & Ilić, Lj. Deconvoluted Fourier-transform LNT-IR study of coordination copper(II) compounds with dextran derivatives. *Russian Journal of Coordination Chemistry 2008 34:5* **34**, 322–328 (2008).

224. Vleugels, L. F. W., Ricois, S., Voets, I. K. & Tuinier, R. Determination of the 'apparent pKa' of selected food hydrocolloids using ortho-toluidine blue. *Food Hydrocoll* **81**, 273–283 (2018).

225. Yuba, E. *et al.* Development of pH-sensitive dextran derivatives with strong adjuvant function and their application to antigen delivery. *Membranes (Basel)* **7**, (2017).

226. Crini, G., Morin-Crini, N., Fatin-Rouge, N., Déon, S. & Fievet, P. Metal removal from aqueous media by polymer-assisted ultrafiltration with chitosan. *Arabian Journal of Chemistry* **10**, S3826–S3839 (2017).

227. Ain Zainuddin, N., Azwan Raja Mamat, T., Imam Maarof, H., Wahidah Puasa, S. & Rohana Mohd Yatim, S. Removal of Nickel, Zinc and Copper from Plating Process Industrial Raw Effluent Via Hydroxide Precipitation Versus Sulphide Precipitation. *IOP Conf Ser Mater Sci Eng* **551**, 012122 (2019).

228. de Repentigny, C., Courcelles, B. & Zagury, G. J. Spent MgO-carbon refractory bricks as a material for permeable reactive barriers to treat a nickel- and cobalt-contaminated groundwater. *Environmental Science and Pollution Research (2018)* **25**, 23205–23214 (2018).

2 Experimental and Characterisation Techniques

2.1 Synthesis Protocols

$Na_{2/3}Ni_{1/3}Mn_{2/3}O_2$ (NNM) and $Na_{2/3}Ni_{1/3}Mn_{2/3}O_2$ NNCM in chapters 3-5, were prepared using soluble acetate salts of sodium, nickel, manganese and copper, details shown in table 2.1. The chemicals were used without further purification. Batch calculations were based on the hydration states in table 2.1, however it is known that this can change over time when chemicals are stored in ambient conditions.

***Table 2.1**: Metal salts precursors and biotemplate used to synthesise NNM and NNCM in chapters 3-5.*

Name (Purity)	**Chemical formula**	**CAS number**	**Supplier**
Sodium acetate anhydrous (≥99%)	CH_3COONa	127-09-3	Sigma-Aldrich
Nickel acetate tetrahydrate (98%)	$Mn(CH_3COO)_2 . 4H_2O$	6018-89-9	Sigma-Aldrich
Manganese acetate tetrahydrate (≥99%)	$Ni(CH_3COO)_2 . 4H_2O$	6156-78-1	Sigma-Aldrich
Copper acetate monohydrate (98%)	$Cu(CH_3COO)_2 . H_2O$	6046-93-1	Fisher Scientific
Dextran from *Leuconostoc* spp. M_r = 70,000	$(C_6H_{10}O_5)_n$	9004-54-0	Sigma-Aldrich

2.1.1 Chapter 3: Effect of Dextran Biotemplate on the Synthesis of P3-$Na_{2/3}Ni_{1/3}Mn_{2/3}O_2$

2.1.1.1 Specimen Synthesis

Samples were prepared using the sodium, nickel and manganese precursors detailed in table 2.1. Stoichiometric amounts of metal salts required to produce 1 g of NNM product, table 2.2, were dissolved in 20 ml distilled water in an alumina crucible. Alumina crucibles were used due their chemical resistance and ability to withstand high temperatures.

***Table 2.2:** Masses of precursors for 1 g P3-NNM.*

Precursor	**Amount to synthesise 1g NNM /g**
Sodium acetate anhydrous	0.528
Nickel acetate tetrahydrate	0.801
Manganese acetate tetrahydrate	1.578

Different NNM specimens were prepared with different amounts of dextran: 0.5, 1, 2, 3 and 4 g. Dextran was added into the precursor solution and stirred until it all dissolved. In the results chapter 3, the specimens are referred to by the mass ratio of NNM to dextran; for 1 g NNM that used 0.5, 1, 2, 3 or 4 g of dextran during synthesis, the specimens were labelled as 1 : 0.5, 1 : 1, 1 : 2 and so on. The pH of the solution were around 7.5, when measured using a pH metre. The solution was then dried at 80 °C, until all water evaporated to form an amorphous glassy composite. Finally, the specimens were calcined in a muffle furnace and held at 650 °C for 2 h in air. The ramp rate to reach 650 °C was set to 10 °C/min, as well as the ramp down to room temperature, however practical cooling rate was slower. Dextran biotemplated P3-NNM exhibited the best electrochemical performance when synthesised using these conditions, apart from specimens calcined at 550 °C for 12 h,[1] hence such conditions were chosen here and the shorter dwell time is more industrially relevant. The specimens were then subjected to mechanical grinding using pestle and mortar. Specimen 1 : 4 was then used in chapter 5, for comparisons between XG and PVDF binder in P3-NNM electrodes.

2.1.1.2 Specimen preparation for High Temperature In- and Ex-Situ XRD

The method for preparation of the dried composite outlined in section 2.1.1.1, was also used in the specimen preparation for HT-XRD experiments. The dried precursor composite tends to expand once dextran begins to combust during biotemplating synthesis of P3-NNM, like the soufflé effect, therefore reliable XRD data cannot be collected due to sample height changes and non-flat surface. In the literature, Sephadex, similar polymer to dextran, undergoes significant mass loss around 300 °C, indication of combustion.[2] Specimens were calcined to 300 °C for 30 minutes to remove the majority of the biopolymer, where significant volume expansion was observed. The powder was then ground using agate pestle and mortar before being returned to the furnace, and calcined at 650 °C for 2 h. No obvious change in terms of volume was observed, therefore it was assumed that the initial calcination step at 300 °C was enough to remove most of the dextran. Hence, prior to *in-situ* HT-XRD measurements, specimens were calcined at 300 °C for 30 minutes, with a ramp up and down rate of 10 °C/min.

Ex-situ HT-XRD was conducted on specimens that were dwelled at 240, 250, 260, 270, 280, 290 and 300 °C for 30 minutes. A slower ramp rate of 5 °C/min was used to ensure the temperature in the furnace did not overshoot too far. A fresh specimen was made for each temperature. The powders were then ground using a pestle and mortar for a sufficient amount of time prior to XRD.

2.1.2 Chapter 4: Biotemplated Synthesis and Electrochemical performance of Cu substituted P3-$Na_{2/3}Ni_{1/3-x}Cu_xMn_{2/3}O_2$

2.1.2.1 Specimen preparation

A slightly different approach was used in P3-NNCM compared to P3-NNM in section 2.1.1.1, due to the relatively lower solubility limit copper acetate monohydrate.[3] Molarity ratios of Mn, Na and Ni + Cu precursors were 0.1, 0.1 and 0.05 M respectively, which were dissolved in 20 ml water, summarised in table 2.3. Lower concentrations ensures all precursor are able to dissolve. Different amounts of Ni were substituted for Cu in $Na_{2/3}Ni_{1/3-x}Cu_xMn_{2/3}O_2$ (x = 0, 1/12, 1/6, 1/4 and 1/3). In these specimens 1 g of dextran was dissolved in the precursor solution. This was equivalent to the mass ratio P3 to dextran of 1 : 3.2. The specimens were dried at 80 °C till all water evaporated and then calcined at 650 °C for 2 h in air, ramped up and down at 10 °C/min.

Table 2.3: *Molar ratios of precursors and batch calculations used in chapter 4.*

Material ($Na_{2/3}Ni_{1/3-x}Cu_xMn_{2/3}O_2$)	**Molarity of Mn**	**Mn in 20ml / g**	**Molarity of Na**	**Na in 20ml / g**	**Molarity of Ni**	**Ni in 20ml / g**	**Molarity of Cu**	**Cu in 20ml / g**
x = 0	0.1	0.490	0.1	0.164	0.050	0.249	-	-
x = 1/12	0.1	0.490	0.1	0.164	0.038	0.187	0.013	0.050
x = 1/6	0.1	0.490	0.1	0.164	0.025	0.124	0.025	0.100
x = 1/4	0.1	0.490	0.1	0.164	0.013	0.062	0.038	0.150
x = 1/3	0.1	0.490	0.1	0.164	-	-	0.050	0.200

2.2 Cathode Preparation

2.2.1 Electrode Slurry

2.2.1.1 With PVDF binder

Cathodes were prepared with the active material P3-NNM (specimens 1 : 1 and 1 : 4 from chapter 3 and 1 : 4 from chapter 5) and P3-NNCM (with Cu contents of x = 0, 1/12 and 1/6 from chapter 4). Prior to slurry preparation, the active material, conductive additive (Timical Super C65, MTI) and Polyvinylidene fluoride (PVDF) binder (MTI) were dried under vacuum at 120 °C.

In chapters 3-5, the slurry was prepared by mixing 80 wt.% of the active material, 10 wt.% of conductive additive and 10 wt.% binder using a pestle and mortar. The powder was then transferred to a container and with a sufficient amount of 1-methyl-2-pyrrolidone (NMP) (anhydrous 99.5%, Sigma-Aldrich). For 0.5 g total powder, 1.4 ml NMP was used. The slurry was mixed thoroughly with an planetary mixer (Thinky ARE-250 Mixer). The following mixing steps were used:

- Initial mixing step proceeded at 500 rpm for 2 minutes, followed by a degassing step at 2200 rpm for 30 seconds.
- The slurry was further mixed at 2000 rpm for 2 minutes, followed by a degassing step at 2200 rpm for 30 seconds. This step was repeated five times to ensure the PVDF was dissolved.

It was not obvious that the PVDF was dissolved at the end of the mixing procedure, due to the dark colour of the slurry. However it was assumed that this was sufficient because after casting, the electrode exhibited good adhesion to the current collector. However for future work, it would be better to dissolve the binder first before adding active material and conductive additive.

The slurries were then cast with a nominal thickness of 250 µm using a doctor blade onto a carbon coated aluminium foil (MTI) secured on a tape casting coater (MSK-AFA-I, MTI). The slurries were dried overnight in a fume hood. At the time of the experiment, a heating element on the tape caster was not available. In an ideal situation, the slurry would be dried at 80 °C to quicken the process and reduce the air exposure to the cathode sheet. Once all the NMP had evaporated, the electrode sheets were stored under vacuum at 80 °C.

The initial thickness of the electrode with the Al current collector foil ranged between 100 to 125 µm. The electrode sheets were calendared using a rolling mill (MTI, MSK-HRP-MR100DC) and thickness was gradually reduced to approximately 75 % of initial thickness. This was to ensure the cathode had proper contact with the Al current collector and any large voids were removed. Whatman weighing paper was used to protect the active side cathode side during calendaring which was sandwiched between 2 acrylic sheets for ease of handling during the process. Electrodes were prepared by punching 12 mm discs and were dried under vacuum at 80 °C before cell assembly.

2.2.1.2 With XG binder

In chapter 5, xanthan gum (XG, Sigma-Aldrich) was also used a binder in the preparation of P3-NNM cathode. However a slightly different approach was used compared to the PVDF containing slurry. The same mass ratio of active material, binder and carbon additive (total 0.5 g) were used and powders were all ground and mixed together using pestle and mortar. About 2 ml of distilled water was added to the powders and mixed with the same pestle and mortar to form a thick paste. As water evaporated, due to the thin spread of slurry across the mortar surface, additional water was added in small increments (*ca.* 1 ml) and mixed into the paste. The process was repeated for about 40 minutes to ensure the slurry was sufficiently mixed. The final consistency of the slurry was much thicker compared to PVDF containing mixture; it resembled very thick treacle, or gelatinous consistency. Although XG is significantly more viscous than PVDF,[4] it does exhibit shear-thinning behaviour,[5] so it would be castable on the current collector foil. The slurry was transferred to a Thinky pot for ease of handling, and tapped to remove any air bubbles before casting onto the carbon coated aluminium foil with a nominal thickness of 250 µm. Cathodes sheets were dried overnight in ambient conditions and then stored under vacuum at 80 °C. Prior to this method, other mixing regimes were tried, in terms of equipment and the addition of water, which is discussed in more detail in chapter 5.

2.2.2 Cell Manufacture

CR2016 or CR2032 304 stainless steel coin cells casing (Cambridge Energy Solutions or MTI) were used to obtain electrochemical data. The coin cells are 20 mm in diameter and either 1.6 or 3.2 mm thick. The components of the coin cell include stainless steel casing, spacer and a spring for CR2032. 16 mm glass fibre separators were punched from GF/F Whatman glass fibre sheet. All these components where dried under vacuum at 80 °C before transfer and storage into the glovebox.

The electrolyte used was 1.0 M NaPF6 in EC: DEC (1:1 v/v %) (Fluorochem). Salt concentrations of 1 M is typically chosen due to the high ionic conductivity, compared to higher salt concentrations.[6] No further analysis of water content was conducted due to lack of equipment.

The cells were assembled in an argon filled glovebox (< 0.5 ppm O_2 and H_2O, MBraun) and were assembled into half cells using Na metal (99.8 % purity, Alfa Aesar) as the counter electrode for an infinite supply of Na^+ so that intrinsic properties of the cathode can be investigated.[7] Na counter electrode was made from a sodium ingot, that was rolled to approximately 1 mm thickness using a pasta maker and punched into 12 mm discs.

The electrodes were constructed by starting with the coin cell casing with the gasket, followed by placing a spring for CR2032 cell, then a steel spacer, Na metal disc, followed by an electrolyte soaked separator, figure 2.1. The electrode was placed active side facing the separator, then the other coin cell casing was put on top. The coin cells were then finally sealed using a hydraulic crimper and rested for 4 hours before cycling.

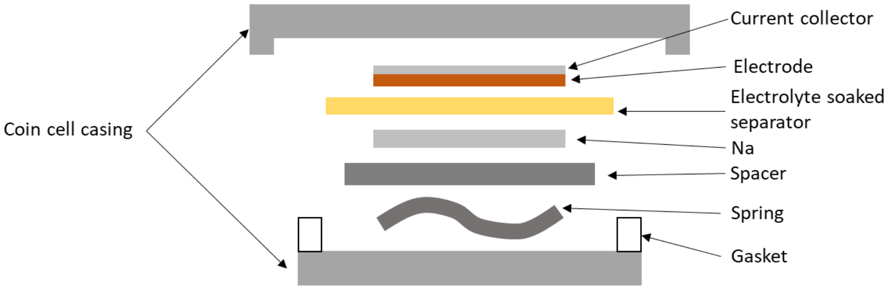

Figure 2.1: *schematic diagram of Na-ion coin cell.*

The electrochemical tests were obtained from a number of battery cyclers. Galvanostatic cycling was conducted on a Maccor Series 4000 Battery Cycler in a 25° C climate-controlled chamber and NEWARE BTS 8.0 in ambient conditions. Cyclic voltammetry was conducted on Maccor Series 4300 Battery Cycler in a temperature controlled room. Cells for *ex-situ* XRD used the NEWARE BTS 8.0 in ambient conditions, where certain charge voltages were held for at least 12 h before decrimping.

2.2.3 Cell Disassembly

Cycled cells were disassembled for SEM analysis and *ex-situ* XRD measurements at different charge voltages. In a Ar filled glovebox (MBraun) cells were decrimped and all the cell components were washed with dimethyl carbonate (DMC, Sigma-Aldrich). The DMC soaked electrodes were dried overnight under dynamic vacuum in the glovebox before further experiments.

2.3 Material Characterisation Techniques

2.3.1 Powder X-Ray Diffraction

2.3.1.1 Principles of Powder X-Ray Diffraction (PXRD)

PXRD is a non-destructive “fingerprinting” technique as most crystalline materials produce unique diffraction patterns that enable identification when comparing to materials on a database, such as the (International Centre for Diffraction Data) ICDD database. Structural analysis can also be conducted, where lattice parameters and atomic positions for example, can be determined.

When incident X-rays collide with atoms in the crystalline material, they are either scattered or absorbed. Coherent scattering causes diffraction patterns and this occurs when the energy of the scattered X-ray is the same as the incident X-rays. Incoherent scattering occurs when the scattered X-ray loses energy and this contributes to background in the diffraction pattern. Fluorescence is another factor that can also contribute to background in the diffraction patterns. It is where X-rays promote electrons to higher, unoccupied energy levels in an atom, which is followed by emission of radiation when the electron returns to ground state.

Atoms in a crystal form ordered arrays with a certain measurable distance "*d*" between planes. The planes of atoms cause diffraction and constructive interference occur when Bragg's law is satisfied, equation 2.1. Figure 2.2 shows the derivation of Bragg's law. Incident beam 1 hits an atom from the first plane and is coherently scattered at the same angle as the incident beam. Another beam that is not scattered passes through to the next plane of atoms and is also scattered with the same angle of incidence. Constructive interference occurs when diffracted beams 1' and 2' are in phase and this occurs if the extra distance travelled by beam 2 and 2' combined is a whole number wavelength. Then a peak in the diffraction pattern is visible at that angle, denoted as 2θ. During destructive interference the beams are out of phase no peak is visible that particular angle.

The Bragg equation describes the conditions for constructive interference:

$$2d\ sin\theta = n\lambda$$

Equation 2.1

Where *d* is the distance between adjacent planes, θ the angle of incidence, λ is the wavelength of the incident bean and *n* is a positive integer of the order of the diffracted beam.

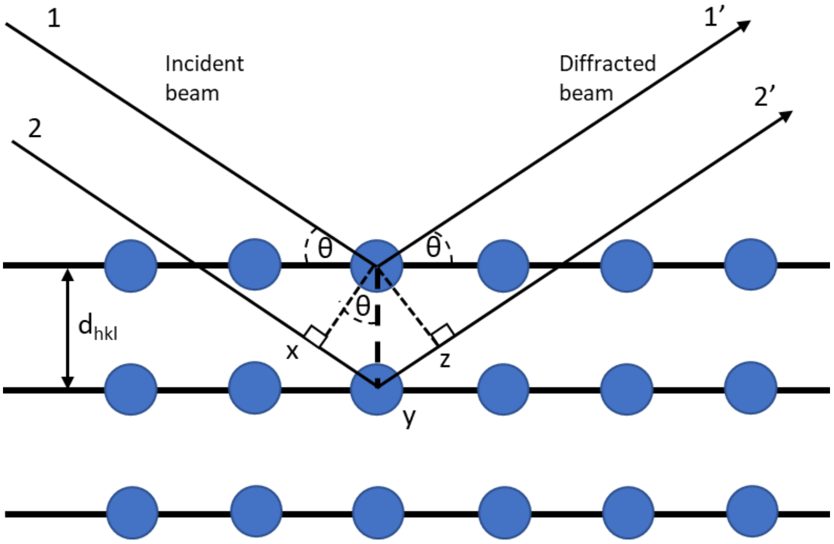

***Figure 2.2**: Derivation of Bragg's law.*

Typical lab-based diffractometers use Bragg-Brentano geometry, the incident and diffracted beam are focused on a fixed radius, same distance away from the specimen. The specimen is fixed in position and the source and detector are moved by -θ and θ respectively. At specific θ values, x-rays are detected, with large intensities when constructed interference occurs.

2.3.1.2 Principles of Pawley Refinement

Pawley fit was used to obtain accurate values for lattice parameters. The peak intensities are treated as arbitrary, therefore a better quality fit can be obtained. It works by refining a scale parameter for each peak, which does not allow for the refinement to give values of physical meaning for atomic positions, site and phase fractions. However, accurate values for lattice parameters can be obtained as the peak positions are able to be refined accurately.

2.3.1.3 Principles of The Rietveld Refinement Method

Rietveld refinements can obtain a variety of information from the crystalline material, such as lattice parameters, atomic positions, site occupation as well as phase fractions. It works by minimising the weighted sum of squared differences between observed and the model.

Weight fractions of a phase, W_p, is calculated by this equation:

$$W_P = \frac{(SZMV)_P}{\sum_i (SZMV)_i}$$

Equation 2.2

Where S is scale factor, Z is the number of formula units per unit cell, M is molecular wight of the formula unit, V is the unit cell volume, i is an index running over all phases.

R-factors indicate how well the model fits to the observed data. The weighted profile R-factor (R_{wp}) is defined by the equation:

$$R_{wp} = [\frac{\sum w_i (y_{io} - y_{ic})^2}{\sum w_i y_{io}^2}]^{1/2} \times 100$$

Equation 2.3

Where y_{io} is the intensity at point i 2θ for the observed pattern, y_{ic} is the intensity for the calculated pattern and w_i is the weighted factor which is $1/\text{ESD}^2$ (estimated standard deviation).

The best possible R_{wp} is defined by expected R factor (R_{exp}) with the equation:

$$R_{exp} = [\frac{N - P}{\sum w_i y_{io}^2}]^{1/2} \times 100$$

Equation 2.4

N is the number of data points and P is the number of parameters. In PXRD, there are significantly more data points than there are varied parameters, therefore is some instances in the literature P is omitted.

X^2 is another parameter that indicates the quality of the fit, it is also referred to "goodness of fit". In the HighScore programme, goodness for fit is defined by the equation:

$$\chi = \frac{R_{wp}}{R_{exp}}$$

Equation 2.5

The value of χ should either equal or be greater than 1. A significantly larger value could indicate several things; the refinement is incomplete, estimated standard deviation are underestimated or the model is wrong and does not fit the observed data well.[8]

There are no defined values for fit parameters that indicate the fit is satisfactory, because of the various factors can impact the fit such as background, peak shape and position and the quality of the data.[9] It is recommended to view the observed and calculated data to determine whether the fit is good enough, as well as determine whether the refined parameters physically make sense.[8]

The errors that Highscore displays is the estimated standard deviation, so the amount the parameters can change without changing the value of R_{wp}. These errors do not necessarily reflect on the quality of the refinement but how the specific parameter is coupled to the refined data. To obtain errors with physical meaning, multiple refinements from different batches need to be conducted.

The background is an important feature in a XRD pattern. Various factors can affect it such as scattering for the air and the specimen holder, amorphous phases and thermal motion of atoms. The "Shifted Chebyshev" function is a common model to describe the background:

$$I_b(2\theta) = \sum_{j=1}^{N} B_j T_{j-1}\,(2\theta)$$

Equation 2.6

It is a polynomial function where B_j are the coefficients to be refined, T_j are the shifted Chebyshev polynomial terms of order j.[10] So the function expands depending on the number of terms. A large number of terms may not accurately model the background.

Peak shape is another important feature in a XRD pattern and there are various functions to model it. The most common is Pseudo-Voigt and contains parameters that relate to both Gaussian and Lorentzian peak widths, which are normally not refinable. The Pseudo-Voigt function contains a full width half maximum (FWHM) parameter, *H*, which is calculated by the Caglioti function:

$$H = (Utan^2\theta + Vtan\theta + W)^{\frac{1}{2}}$$

Equation 2.7

The *U, V* and *W* are refinable parameters and are associated with peak width.

Atomic position and site fractions are a function of the structure factor, which affects peak intensity and can be refined. It quantifies the scattering from the type of atoms and their location in that particular plane. Form or scattering factor describes how atomic scattering for X-rays decreases with diffraction angle and is proportional to the number of electrons, so heavier atoms will have greater scattering than lighter elements. This explains why peaks gradually become smaller in intensity with increasing scattering angle in the diffraction pattern. Form factor can be affected by temperature. For example, at higher temperatures the size of the electron cloud increases and therefore increases the interference at higher angles and a more rapid decay in form factor be observed. Thermal parameters can be refined in Rietveld as this too has an impact on peak intensity.

Particles with morphologies such as nanorods and plates can exhibit preferred orientation and because of this, in the diffraction pattern some peaks may have greater intensities than what is shown in the simulated profile. This is due to some planes being over expressed. In some cases, this can be mitigated by sufficient sample preparation and using back-filled specimen holder. Although this may not always be the case and preferred orientation can still persist in the specimen. Rietveld refinement is able to model this with either March-Dollase or Spherical Harmonics. In March-Dollase, the user defines which *hkl* is over or under expressed. Spherical harmonics is better for materials that exhibit more complex orientations.

2.3.1.4 Specimen Preparation for XRD

Prior to XRD measurements, all specimens were ground using a pestle and mortar. At least 10 wt.% NIST 640e or 640f silicon standard was ground with the powder specimens. For most measurements, the specimens used a back filled holder to further prevent preferred orientation. For *in-situ* HT-XRD, powder specimens pre-calcined at 300 °C were filled in an alumina crucible, and the surface was flattened with a glass slide. The decrimped cycled electrodes for *ex-situ* XRD were prepared in a Ar filled glove box. The electrodes, with active material facing up were placed in the centre of a zero background plate and sealed with a kapton foil into an air sensitive specimen holder.

2.3.1.5 XRD measurements and refinements

XRD measurements were taken on PANalytical Aeris and X'pert powder diffractometer with Ni-filtered Cu Kα radiation (λ = 1.5406 Å) on a rotating sample stage. To gain good quality, high resolution scans for Rietveld refinement, the programme used in the X'pert powder diffractometer lasted for at least 45 minutes per specimen and were collected between 10 and 120 °2θ. Measurements taken on the Aeris were only 10 minutes and collected between 10 and 100 °2θ. Such short acquisition time was possible due to the high resolution and low noise capabilities of such diffractometer.

XRD measurements were taken on a PANalytical Empyrean for specimens (calcined between 240 °C and 300 °C, section 2.1.1.2) that were prepared for *ex-situ* HT-XRD using a Ag X-ray source. Acquisition time was 90 minutes. This was to ensure there was enough resolution to see peaks in the specimens that contained high amounts of amorphous phases that would contribute to a large background.

In-situ HT-XRD was performed on the same PANalyrical X'pert diffractometer with Anton Paar HTK 1200N heating stage. The following programme was used:

- Heating rate up to the desired temperature was 50 °C/min.
- XRD measurements were taken between 10-70 °2θ and took 15-20 minutes.
- Measurements were repeated as temperature increased in 100 °C increments.
- Once final temperature was reached, there were no further measurements upon cooling.

Phase matching was conducted on the International Center for Diffraction Data's (ICDD) PDF-4+ database, and SIeve+ software. Both Rietveld and Pawley refinements were conducted on PANalytical HighScore software.

Pawley refinement was conducted by using the Pawley fit fitting mode on Highscore software. The parameters that were refined included the background using the Shifted Chebyshev I method and the specimen displacement in relation to the Si standard. The lattice parameters, and in turn the profile variable Caglioti *W, V* and *U* and *peak shape 1* were also refined. This was repeated until there was minimal change in the R_{wp} before refining all the parameters together. Profile variables used the Caglioti function for peak width and Pseudo-Voigt to model the peak shape, which was the same for Rietveld refinement.

Rietveld refinement procceded by refining the background using the Shifted Chebyshev I function, then specimen displacement in relation to the Si standard. To obtain phase fractions, the scale factor for each phase was also refined as well as lattice parameters. Constraints were employed for atomic coordinates and thermal parameters for Ni and Mn as they occupy the same position. For each phase, the following parameters were refined in turn one at a time:

- Profile variables: Caglioti *W, V* and *U* and *peak shape 1*.
- Atomic *z* coordinate in the order of highest scattering to lowest scattering; Mn + Ni, Na, O1 then O2. However atomic position for Mn + Ni was fixed as it is in a special position (0,0,0) because it sits on a point-group symmetry element.
- Thermal parameters, B_{iso}, also in the same order.

These steps were repeated till there was very little change in the value of R_{wp}. Then all the parameters were refined at the same time. Spherical harmonics with 10 coefficients was then employed to model preferred orientation, as some peak heights in the observed data still appeared to be over expressed.

2.3.2 Scanning Electron Microscopy

Scanning electron microscopy enables visualisation of the microstructure of various materials. To obtain such topographical information, a beam of electrons is produced at the top of the microscope and proceeds down the column. Electromagnetic lenses focus and direct the beam to the sample. Secondary electron (SE) images provide the topographical information. This is where primary electrons from the incident beam undergo inelastic scattering with valence electrons from the specimen, causing ejection of the electron which emerges at the surface of the specimen. Topographical contrast is dependent on the angle of the specimen when the incident beam hits; steeper surfaces are able to produce more SEs compared to flatter surfaces. When it comes to biotemplating, this technique is very important to study particle morphologies and any microstructures aided by a template.

Backscattered electrons (BSE) can show phase contrast in the SEM image. They are produced by elastic scattering of the incident beam electrons with the atom nucleus deep within the specimen. This alters the direction of the incident electrons and the scattering probability is proportional to the atomic number. Hence distribution of elements can be seen as heavier elements scatter more strongly and therefore appear brighter in the image.

Specimens for SEM were prepared by affixing powders onto a carbon tab and excess was tapped off. The samples were then sputter coated with gold as the P3 layered oxide powders were sufficiently conductive. Prepared electrodes were also affixed onto a carbon tab and did not require gold coating. Phillips Inspect F50 SEM was used to examine the specimens, using 5 - 10 kV and a spot size of 3.5.

2.3.3 Thermal Gravimetric Analysis

Thermal gravimetric analysis (TGA) was used to record the mass changes of a material as it is heated up. This can identify at what temperature certain decomposition events occur. TGA was performed by technicians in the Materials Characterisation Lab in the Department of Materials Science and Engineering at the University of Sheffield. TGA was conducted on acetate precursors to determine water content using a Perkin Elmer SDT Q600 instrument. Small amount of powder (mg) was added to an alumina pan, which were heated from room temperature to 650 °C at a ramp rate of 10 °C/min under an air atmosphere. Normally loss of water occurs around 100 °C. The calculations for water content in the precursors are outlined in appendix A, section A.1.

2.3.4 Inductively Coupled Plasma-Optical Emission Spectroscopy

Inductively coupled plasma-optical emission spectroscopy (ICP-OES) was conducted on dextran biotemplated P3-NNM specimens to determine the stoichiometry. Experiments were conducted by the Faculty of Science Mass Spectrometry Centre at the University of Sheffield. The basic principle of ICP-OES relies on exposing material to plasma, where the atoms becomes excited as electrons move to higher energy levels. When electrons relax back to ground state, energy released in the form of photons. The wavelengths of the photons are different for each element, hence are able to be identified. Each element produces a unique visible emission spectrum due to the different levels of excitations and relaxations that can occur, like a fingerprint. The instrument measures the intensity of light at different wavelengths. The greater the intensity, the greater concentration of that atom is present in the specimen.

The concentrations of Na, Ni and Mn were given in mg/kg. To obtain stoichiometry, the following calculations were conducted:

- Divide concentration of the element by its by M_r to obtain mol/kg.
- Divide each value of mol/kg for the different elements with one of the calculated mol/kg values to obtain molar ratios between each element.

In the results chapter 3, the ratios are given in relation to Mn.

2.4 References

1. Zilinskaite, S., Rennie, A. J. R., Boston, R. & Reeves-McLaren, N. Biotemplating: A sustainable synthetic methodology for Na-ion battery materials. *J. Mater. Chem. A* **6**, 5346–5355 (2018).

2. Boston, R., Carrington, A., Walsh, D. & Hall, S. R. Synthesis of spherical superconductors. *CrystEngComm* **15**, 3763–3766 (2013).

3. Copper(II) acetate monohydrate, 99.9% (metals basis). https://www.fishersci.se/shop/products/copper-ii-acetate-monohydrate-99-9-metals-basis-1/11373637/en.

4. Zhang, Y.-Y. *et al.* Improvement of electrochemical properties of P2-type $Na_{2/3}Mn_{2/3}Ni_{1/3}O_2$ sodium ion battery cathode material by water-soluble binders. *Electrochim. Acta* **298**, 496–504 (2019).

5. Song, K. W., Kim, Y. S. & Chang, G. S. Rheology of concentrated xanthan gum solutions: Steady shear flow behavior. *Fibers and Polymers* **7**, 129–138 (2006).

6. Ravikumar, B., Mynam, M. & Rai, B. Effect of Salt Concentration on Properties of Lithium Ion Battery Electrolytes: A Molecular Dynamics Study. *Journal of Physical Chemistry C* **122**, 8173–8181 (2018).

7. Rowden, B. & Garcia-Araez, N. Estimating lithium-ion battery behavior from half-cell data. *Energy Reports* **7**, 97–103 (2021).

8. Toby, B. H. R factors in Rietveld analysis: How good is good enough? *Powder Diffr* **21**, 67–70 (2006).

9. David, W. I. F. Powder diffraction: Least-squares and beyond. *J. Res. Natl. Inst. Stand. Technol* **109**, 107–123 (2004).

10. Snellings, R., Machiels, L., Mertens, G. & Elsen, J. Rietveld refinement strategy for quantitative phase analysis of partially amorphous zeolitized tuffaceous rocks. *Geologica Belgica* **13**, 183–196 (2010).

3 Effect of Dextran Biotemplate on the Synthesis of P3-$Na_{2/3}Ni_{1/3}Mn_{2/3}O_2$

3.1 Aims & Objectives

The aim of this chapter was to investigate the crystallisation processes which govern the formation of biotemplated P3-NNM with the aid of dextran. By examining such processes, the impact of dextran and its suitability as a biotemplate for synthesis of P3-NNM was elucidated. The biotemplate can influence the temperature at which secondary phases crystallise and their growth, as well as the final product. This was observed by using *ex-* and *in-situ* high temperature (HT) XRD techniques.

The dextran concentration was also optimised, and the impact of low and high concentrations on phase progression was also investigated. This is because the number of binding sites in dextran, along with the potential preferred binding with certain cations can have a significant impact.

The electrochemical performance, in terms of observed discharge capacity, cycling stability and redox reactions was compared between P3-NNM synthesised with low and high concentration of dextran. This was to show the impact of secondary phases and deficiency of TM in P3-NNM.

3.2 Introduction

Although the P3-type materials can form at lower temperatures (below 800 °C) compared to the P2-type structures,[1,2] the dwell times can exceed 12 h during solid state synthesis for materials such as P3-$Na_{2/3}Mg_{1/3}Mn_{2/3}O_2$ and P3-$Na_{0.9}Ni_{0.5}Mn_{0.5}O_2$.[3,4] NiO impurity phases are commonly observed in Ni containing layered materials,[1,4–6] and longer dwell times and higher calcination temperatures are needed in such materials to reduce the amount of NiO secondary phase,[1,6,7] necessitating the energy-intense and lengthy synthesis protocols. This in turn means that it is often challenging to create phase-pure P3 materials for the Ni containing layered oxides,[4,8,9] especially with the high temperatures that needed to decompose NiO, which could encroach on conditions that favour crystallisation of the P2 phase. This could be one of the reasons why there is only a handful of studies on P3-NNM.

It has been demonstrated that phase pure P3-type materials containing Ni could be synthesised, often using modified solid state synthesis with a mixed transition metal precursor that had to be synthesised prior using co-precipitation methods.[2,10–12] Such precursors ensured better mixing of the different transitions at the atomic level. These methods, however, required multiple steps during synthesis, including the preparation of mixed transition metal precursor, followed by multiple calcination and grinding steps, resulting in a lengthy and complex process. Other synthesis methods are therefore sought-after which enable access to the low temperature polymorphs without a large energy and time cost.

Of the many low-temperature oxide synthesis methods available, recent work has demonstrated that low-temperature crystallisation of complex crystal structures can be regulated by introducing molecules which control mixing and agglomeration during heating.[13–15] One such method is biotemplating, which uses naturally-occurring molecules to bind with metal ions forming a homogenous distribution of well-dispersed metal cations mixed at the atomic level.[16] This enables crystallisation to occur at lower temperatures due to large number of nucleation sites as the crystallite sizes of the intermediate phases are kept small, which is discussed in more detail in chapter 1.

P3-NNM has been previously synthesised successfully using dextran biotemplating,[7] where it was demonstrated how the synthesis conditions could be used to enhance the electrochemical properties, linked to particle size. Although specific capacity improved with decreasing calcination temperature and/or time, the wt.% of NiO increased. Having large amounts of impurity phases is undesirable, particularly as Ni is the redox active species in NNM.[17] There has been research on NiO as an electrode material, however for conversion anodes in NIBs,[18,19] so in this case, Ni that is active at high cathode potentials in NNM is lost. This means that NiO takes up physical space inside the battery, reducing the overall specific capacity and energy density of the cathode. Schemes to reduce this NiO content in the cathodes are therefore required to further increase the specific capacity of such templated materials.

Intermediate phases, such as NiO, in biotemplated synthesis tend to form at low temperatures and persist at higher temperature to some extent,[7] and so obtaining a better understanding of the role of the template in the low-temperature reaction environment, and its effect on later phase formation is therefore key to improving the quality of the product. Herein, the crystallisation process of NNM and secondary phases in the presence of varying quantities of dextran was investigated, to better understand the role of template, especially during early stages of calcination, as well as determine the optimal dextran concentration. For 1 g P3-NNM product, dextran concentrations that were investigated were 0.5, 1, 2, 3 and 4 g which are denoted by the mass ratios 1 : 0.5, 1 : 1 and so on, as explained in chapter 2.

If there is a large amount of NiO present in the specimen, then P3-NNM is deficient in Ni and therefore vacancies in the TM layers are likely. Although Ni redox is the predominant capacity contributor in NNM, the lack of such species may not necessarily considerably reduce the capacity of the material significantly. In previous research, TM deficiency has shown to have a positive impact on electrochemical performance of various layered oxides. P2-$Na_{2/3}MnO_2$ suffers from rapid capacity fade due to the presence of Jahn-Teller active Mn^{3+} as well as the P2-O2 phase transition.[20–22] Mn^{3+} induces phase transitions, causing a stepwise voltage profile which negatively impacts the Na^+ diffusion kinetics. A common way to reduce the fraction of Mn^{3+} in this material is to substitute some Mn for Ni, such as $Na_{2/}Ni_{1/3}Mn_{2/3}O_2$, shifting the average valance of Mn closer to +4.[20,22] However, this material also experiences capacity fade due to the phase transition and irreversible oxygen redox.[23–25] Vacancies in $Na_{2/3}MnO_2$ improved the cycle stability due to the average valance of Mn being closer to +4, smoother voltage profile indicative of a more solid solution phase transition and maintained P2 structure at higher voltages.[26] When cycled between 1.5 and 4.3 V at 0.1 C, material without vacancies had an initial discharge capacity of 204 mAh g^{-1}, however after 100 cycles the capacity retention was 16 %. Under the same conditions, material with vacancies had an initial discharge capacity of 152 mAh g^{-1}, with a capacity retention of 56 % after 100 cycles. Vacancies in $Na_{0.67}Al_{0.1}Mn_{0.9}O_2$ improved the cycling stability due to the lack of P2-O2 phase transition when charged up to 4.5 V and smaller volume change of 1.4 %, compared to the regular material that exhibited a change of 4.35 %.[27] The material with no vacancies underwent a more complex phase transformation between 1.5 and 4.5 V, which contributed to cycling instability.

$Na_{0.8}Mg_{0.13}[Mn_{0.6}Co_{0.2}Mg_{0.07}\square_{0.13}]O_2$ ($\square$ = vacancies) exhibited excellent cycle stability at different c-rates when cycled between 1.6 and 4.4 V.[28] Most notably, at 4 C, the initial discharge capacity was *ca.* 90 mAh g^{-1}, with capacity retention of 89.9 % after 100 cycles.[28] The vacancies enabled oxygen redox and made the TMO_6 octahedron more flexible to distortions, which stabilised the structure, especially at low Na concentrations. Asymmetric and flexible TMO_6 octahedron was also found in P2-

$Na_{2/3}Mn_{7/9}Mg_{1/9}\square_{1/9}O_2$ and the P2 phase was still the dominant phase after change to 4.3 V.[29] In Mn based layered oxides, upon discharge to 1.5 V, Mn^{4+} is reduced to Mn^{3+} causing structural instability from the distortions.[30] These distortions are associated with the spin state of Mn^{3+}, where a high spin state causes formation of distorted MnO_6 octahedrons, whereas such distortions do no occur with the low spin state. Vacancies in $Na_{2/3}Zn_{1/9}Mn_{7/9}\square_{1/9}O_2$ have shown to increase the proportion of these low spin Mn^{3+} upon discharge to 1.5 V, as well as improving the reversibility on anionic redox of lattice oxygen.[30] Hence investigation of the electrochemical performance of the specimen with high levels of NiO and Ni deficiency was still worth undertaking, as potential vacancies could have a positive impact on the performance.

Herein, the impact of high NiO content/Ni deficient material synthesised with low dextran concentration was compared with the specimen with a low NiO phase fraction. If such material shows good potential, it is likely that biotemplating synthesis would be easier for materials with low Ni concentration.

3.3 Results & Discussion

3.3.1 Materials Characterisation

XRD patterns of biotemplated samples using different quantities of dextran are shown in figure 3.1. The observed Bragg reflections in data collected for all samples could be indexed using two phases, P3-NNM (space group $R3m$, PDF card no. 04-016-7123) and NiO (space group $Fm\bar{3}m$, PDF card no. 04-001-9373). The peaks from this secondary phase, NiO, decreased in intensity with increasing dextran concentration.

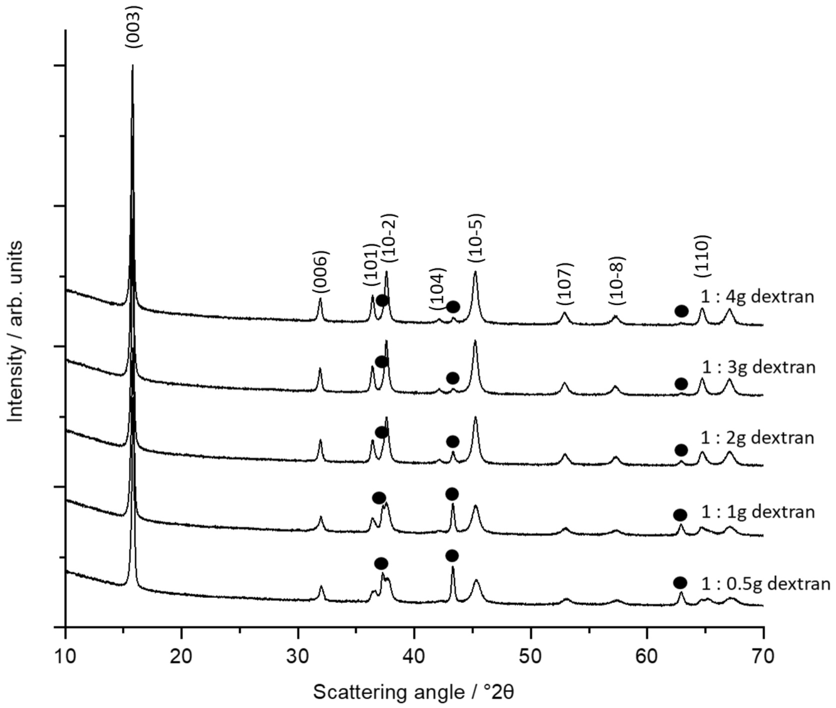

Figure 3.1: *XRD patterns of biotemplated P3-$Na_{2/3}Ni_{1/3}Mn_{2/3}O_2$ calcined at 650 °C for 2 h using different amount of dextran, per 1g of product. Circles indicate the NiO peaks.*

Average phase fractions and lattice parameters for the different amounts of dextran used during synthesis, table 3.1, were obtained from three separate batches. Phase fractions were obtained from Rietveld refinement, whereas lattice parameters were obtained by Pawley refinement with a NIST Si 640e standard to ensure reliability. As dextran concentration increased, less NiO formed and the lattice parameters increased, indication that more Ni is incorporated into the layered structure.

However, the increase in lattice parameters from specimen 1 : 0.5 to 1 : 4 was not linear with the decrease in NiO wt.%. Specimen 1 : 0.5 had NiO content of 21.9 wt.% and 1 : 1 had 18.9 wt.%, but exhibited the greatest difference in lattice parameters compared to between specimens 1 : 1 and 1 : 2, where the latter had NiO content of 7.9 wt.%. This could be due to increased repulsive forces between adjacent TMO_2 layers and within the TM layers in the *a*-b plane as more Ni is incorporated into the structure. The strength of the repulsive forces may not be linear with Ni content in the layered structure due to different shielding effects. Further investigation is required to understand this trend; to deconvolute the expected increase in lattice parameters due to incorporation of larger TM versus the repulsive forces. The difference in lattice parameters from specimen 1 : 2 to 1 : 4 is comparatively smaller due to the smaller change is NiO content.

Table 3.1: Phase fractions and lattice parameters of P3-$Na_{2/3}Ni_{1/3}Mn_{2/3}O_2$ synthesised with different amounts of dextran. Three batches were made for each sample to obtain an averages for the phase fractions and lattice parameters. Theoretically calculated ratios of cations to cation binding sites in dextran as calculations in appendix A.2.

Sample	**Phase fraction average of 3 batches / wt.%**		**Lattice parameters of NNM / Å**		**Ratio of cations to cation binding sites in dextran.**
Ratio of NNM to Dextran / g	**NNM**	**NiO**	**a**	**c**	
1 : 0.5	78.1 (± 1.0)	21.9	2.871 (± 0.001)	16.791 (± 0.004)	
1 : 1	81.1 (± 1.8)	18.9	2.878 (± 0.002)	16.817 (± 0.010)	1 : 0.75
1 : 2	92.1 (± 1.9)	7.9	2.879 (± 0.001)	16.840 (± 0.017)	
1 : 3	96.0 (± 1.4)	4.0	2.881 (± 0.001)	16.838 (± 0.010)	
1 : 4	97.3 (± 0.4)	2.7	2.882 (± 0.001)	16.842 (± 0.012)	1 : 3.11

The ratio of cations to binding sites were calculated, appendix A.2, and results are shown in table 3.1. For specimen 1 : 1 the ratio of precursor cations (C) to binding sites (BS) in dextran is 1 C : 0.75 BS, and for 1 : 4 it is 1 C: 3.11 BS. This clearly shows that using 0.5 or 1 g of dextran does not have as sufficient number of binding sites. In the literature, using deconvoluted Fourier-transform infrared spectroscopy, it was found that Cu^{2+} coordinates with four hydroxyl groups from dextran and two water molecules.[31] It is assumed that the cations here form similar octahedral complexes and therefore an ideal ratio of cations to dextran binding site would be 1 C : 4 BS.

These calculations assume that all hydroxyl groups in dextran are available to be binding sites, which is not realistic. Various factors can affect the availability of binding sites, such as stericity and pH of the solution.[32–34] The pH of the of the precursor solution with dextran was about 7 when using universal indicator paper. This is above the pKa of dextran which may be just above 5, judging by the absorbance levels of different metal cations,[34] and below the pH at which hydrolysis of the metal cations would be more favourable.[35,36] Therefore steric effects may have a bigger impact on binding site availability in such conditions.

Although specimen 1 : 4 appears to have insufficient number of binding sites, when greater amounts of dextran was used, for example in specimen 1 : 5, weight fraction of NiO was 3.4 wt.% and there was no significant different in the XRD, figure 3.2, compared to 1 : 4. Therefore, further analysis on specimen 1 : 5 was not conducted and the 1 : 4 is optimised. A variety of binding mechanisms could occur, negating the need for a cation to binding ratio beyond 1 C : 4 BS. For example, Na may have a slightly different binding mechanism compared to the transition metals, however there has been no evidence in the literature.

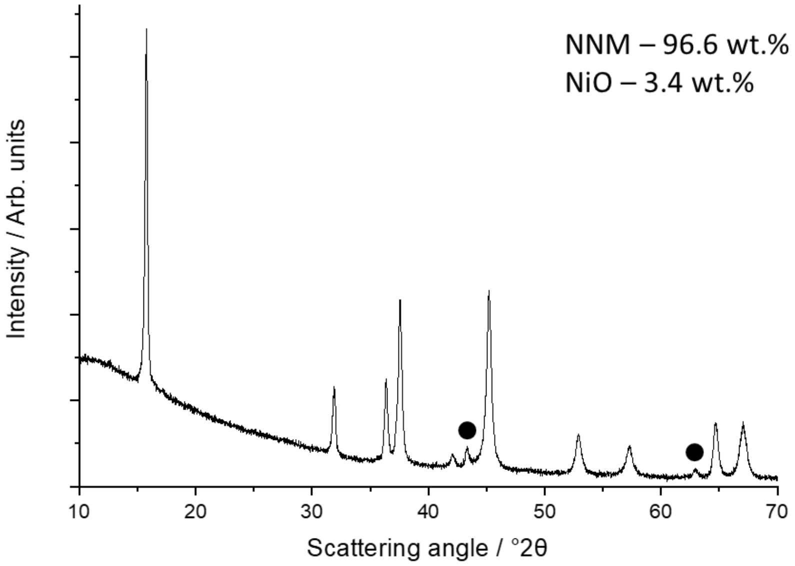

Figure 3.2: *XRD pattern of specimen 1 : 5 with weight fractions of NNM and NiO. NiO peaks are labelled with black circles and unlabelled peaks are P3-NNM.*

Weighing errors of the precursors and template can also cause different weight fractions between the batches. The water content in acetate salts can also vary throughout the year, if stored in ambient conditions. TGA was conducted on the precursor metal acetates at different times of the year, figure 3.3.

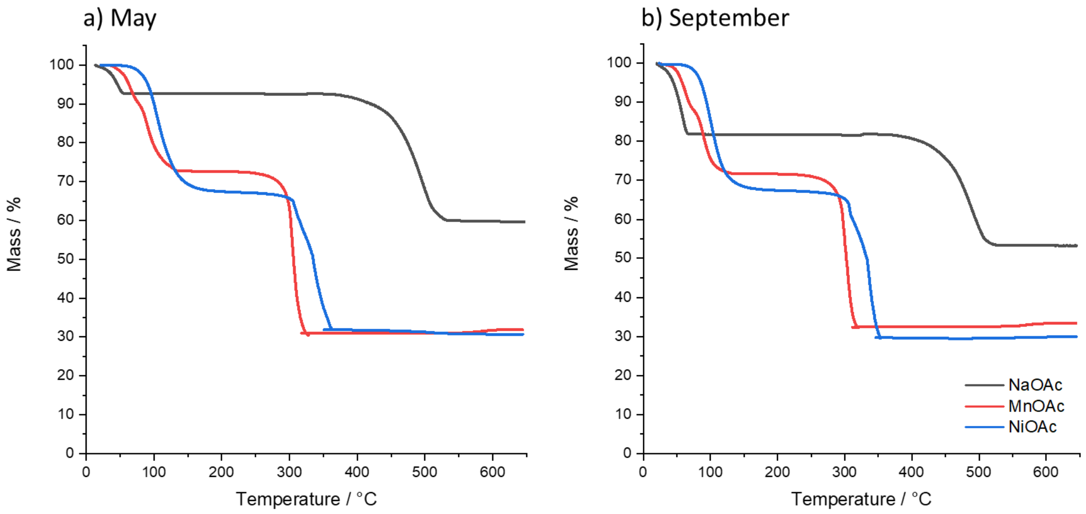

Figure 3.3: *TGA results for Na acetate, Ni acetate tetrahydrate and Mn acetate tetrahydrate conducted during a) May and b) September 2019.*

Table 3.2 shows the calculated number of water molecules in the formula unit for Na, Mn and Ni acetate (OAc), compared to the expected number. The values were obtained from TGA conducted during May and September 2019, the calculations are shown in appendix A.1. There is significant amount of variation in NaOAc and NiOAc, therefore likely to have a significant impact of the phase fractions between batches synthesised at different times of the year. This was not compensated for in the batch calculations.

Table 3.2: *Calculated number of water molecules in the formula unit of each precursor acetate from TGA conducted during May and September 2019.*

	NaOAc	**NiOAc**	**MnOAc**
Expected water	0.0	4.0	4.0
May 2019	0.4	4.8	4.0
September 2019	1.0	4.7	3.8

For specimens 1 : 0.5 and 1 : 3 that were synthesised in May 2019, inductively coupled plasma-optical emission spectroscopy (ICP-OES) was conducted to determine what impact varying quantities of water molecules in the precursor acetates had on the final stoichiometry of P3-NNM. Table 3.3 shows the measured concentrations of Na, Ni and Mn in P3-NNM calcined powder and their calculated stoichiometries/molar ratios. The calculations were done in respect to Mn, hence the stoichiometry is the same as the expected value. In relation to Mn, the ratios to Na and Ni are slightly lower than the expected values. The correct stoichiometry for Na is 0.667, and for specimens 1 : 0.5 and 1 : 3 it was 0.645 and 0.655 and for Ni the expected value is 0.333, with calculated values of 0.323 and 0.325 respectively. The lower calculated values compared to the expected values could be due to the slightly higher water content of the precursor acetates in table 3.2. However the differences were not significant enough to warrant change in batch calculations for future specimens. Instead precursors were stored in a dry atmosphere to prevent change in water content over time.

Another reason for why increasing the amount of dextran does not further decrease the NiO content is that 0.33 is the solid solution limit of Ni in such materials.[37,38] Operating close to the solid solution limit can make it difficult to make a completely phase pure material and combined with variations of water content in acetate precursors, low calcination temperatures and short dwell time, could be the reason as to why there is still a small amount of NiO (2.73 wt.%) present in specimen 1 : 4.

Table 3.3: *Measured concentrations of Na, Ni and Mn in P3-NNM from ICP-OES and the calculated molar ratios/stoichiometry.*

	Na		Ni		Mn	
	Concentration / mg/kg	**Calculated stoichiometry in P3-NNM**	**Concentration / mg/kg**	**Calculated stoichiometry in P3-NNM**	**Concentration / mg/kg**	**Calculated stoichiometry in P3-NNM**
Expected		0.667		0.333		0.667
1 : 0.5	130,000	0.645	166,000	0.323	321,000	0.667
1: 3	141,000	0.655	179,000	0.325	343,000	0.667

As a control, P3-NNM was synthesised in the same way in the absence of dextran, 1 : 0. The Rietveld refinement plots for specimens 1 : 0, 1 and 4 are shown in figure 3.4 and table 3.4 summaries the refined parameter values. The peak intensities of NiO are smaller compared to when smaller amounts of dextran were used, such as in 1 : 0.5 and 1 : 1. Without a template, NiO content was 9.8 wt.%, whereas in 1 : 1 and 1 : 0.5, the NiO content was 18.87 and 21.90 wt.% respectively. This indicates the importance of optimising the amount of template, otherwise in some cases the final product could have greater fraction of secondary phases compared to synthesis without a biotemplate. The greater concentration of NiO in some of the biotemplated specimens compared to 1 : 0, could be due to inhomogeneities caused by preferred binding of certain cations, allowing unbound precursors such as Ni to agglomerate, form intermediates with minimal growth restrictions. In addition, growth of phases from cations that are bound to dextran are likely to have delayed crystallisation kinetics.

Site occupancies, table 3.4, were difficult to refine as Na and O scatter X-rays lightly and Ni and Mn are similar, therefore it would be challenge to differentiate between the two, especially since they are in the same site. Hence the occupancies were not refined. Instead, the thermal parameters were refined to fit peak intensities. Although, there were still difficulties with refinement for the Ni and Mn sites due to similar scattering. Consequently, the values did not shift much from the initial 0.5, so reliable values for the sites have not been obtained. This could be why some peaks especially between 10 and 50 °2θ have larger difference plots, as occupancy and thermal parameters are contributing factors to peak intensity. The difference plots look very similar for all specimens, figure 3.4, indicating that relative comparisons between the specimens are reliable. The fit indicators (R_{wp} and χ) for all specimens in table 3.4 indicate a good fit, therefore values for phase fractions and lattice parameters also have a degree of reliability, especially with the small intensities in the difference plot. Cation site 2 consists of Na atoms and the B_{iso} for this site was between 2.30 and 3.13 Å^2 for the three specimens, which is likely to be reasonable. Although Na scatters X-rays weakly and can be masked by heavier elements such as Ni and Mn so it difficult to determine whether the B_{iso} value is reliable. This is the same for oxygen as the values for B_{iso}s are very low for oxygen site 1. Specimen 1 : 0 was not refined with a Si standard, so accurate values of lattice parameters were not obtained, however standard of fit is good with a R_{wp} of 3.64 and χ^2 of 1.67, therefore phase fractions are trustworthy. The other specimens were refined with a NIST Si standard, ensuring the lattice parameter values were reliable.

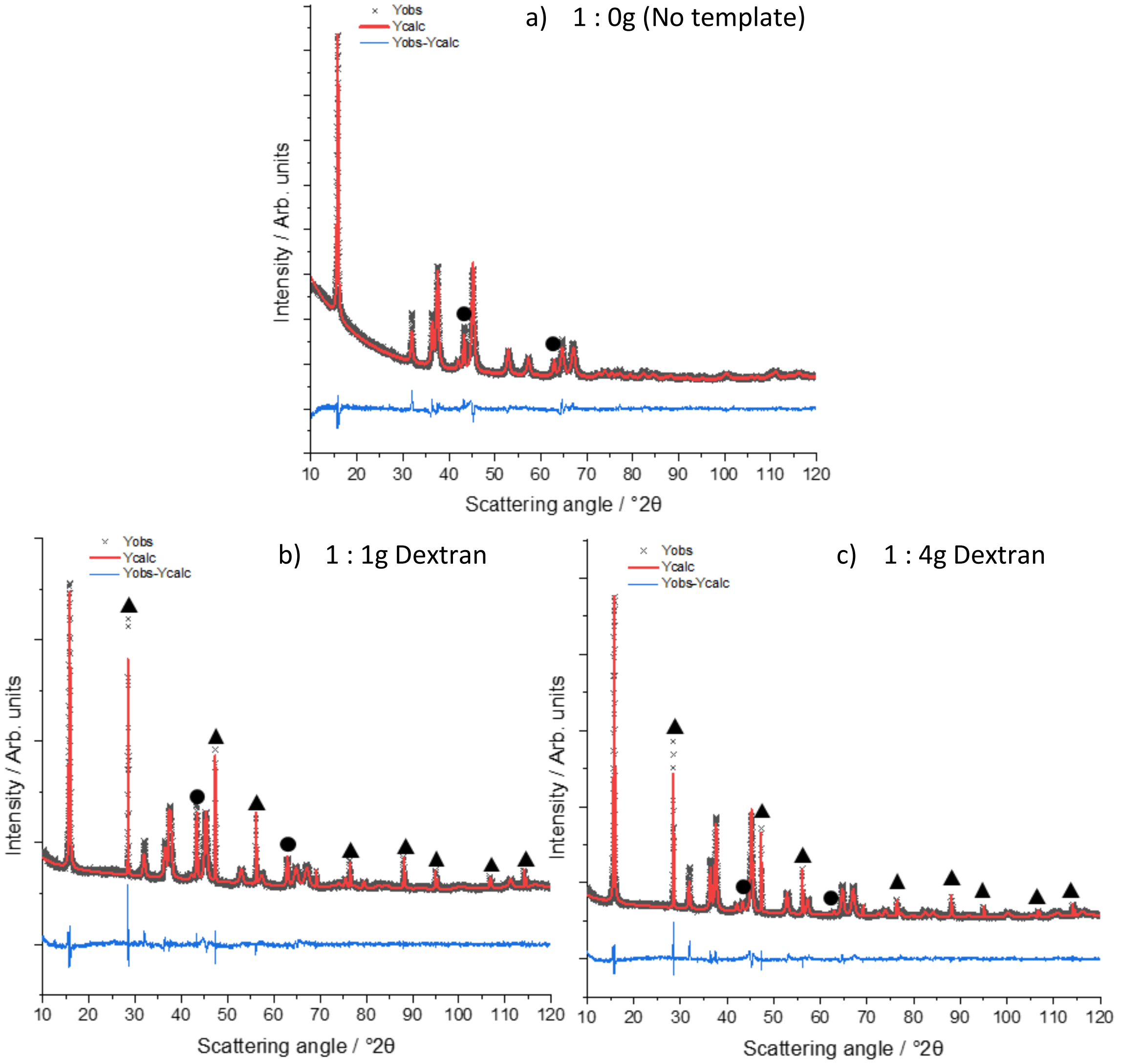

Figure 3.4: *Observed XRD patterns and refinement results of 1g P3-$Na_{2/3}Ni_{1/3}Mn_{2/3}O_2$ synthesised at 650 °C for 2h a) without template, b) 1g dextran with NIST Si 640f standard and c) 4g dextran with NIST Si 640f standard. Si standard peaks are labelled with black triangles, NiO with black circles and unlabelled peaks are P3-NNM.*

Table 3.4: *Structural refinement parameters for P3-*$Na_{2/3}Ni_{1/3}Mn_{2/3}O_2$ *specimens synthesised with different amounts of dextran with final calcination at 650 °C for 2 h. XRD data collected under ambient conditions. Initial values for* B_{iso} *were set to 0.5 Å.*

Parameter	**Value**		
Sample	No template	1 : 1g Dextran	1 : 4g Dextran
Structural formula	$Na_{2/3}Ni_{1/3}Mn_{2/3}O_2$	$Na_{2/3}Ni_{1/3}Mn_{2/3}O_2$	$Na_{2/3}Ni_{1/3}Mn_{2/3}O_2$
Space group	$R3m$	$R3m$	$R3m$
a/Å	Refined without Si standard	2.877	2.880
c/Å	Refined without Si standard	16.824	16.856
R_{wp}/%	3.64	2.73	2.95
R_{ep}/%	2.18	1.74	1.74
Goodness of fit / χ	1.67	1.56	1.69
NiO content wt.%	9.8	16.8	2.4
Cation site 1			
X(=y=z)	0	0	0
Site occupancy	0.667 Mn, 0.333 Ni	0.667 Mn, 0.333 Ni	0.667 Mn, 0.333 Ni
B_{iso}/Å^2	0.500	0.497	0.500
Cation site 2			
X(=y)	0	0	0
z	0.170	0.166	0.170
Site occupancy	0.667 Na	0.667 Na	0.667 Na
B_{iso}/Å^2	3.130	2.705	2.297
Oxygen site 1			
X(=y)	0	0	0
z	0.399	0.392	0.392
Site occupancy	1	1	1
B_{iso}/Å^2	0.018	0.050	0.050
Oxygen site 2			
X(=y)	0	0	0
z	0.609	0.608	0.606
Site occupancy	1	1	1
B_{iso}/Å^2	0	0.319	0.252

To better understand the role of dextran in terms of phase progression during the early parts of synthesis, low temperature *ex-situ* HT-XRD was performed on specimens 1 : 1 and 1 : 4 between 240 °C and 300 °C. The data in Figure 3.5 indicates clear differences in the crystallisation process of the two samples. For specimen 1 : 4, figure 3.5a, below 270 °C, the lack of Bragg peaks in the diffraction data indicates an amorphous sample, comprising of the metal cation and dextran complex and acetate groups. Previous research using Sephadex (a cross-linked form of dextran) indicated an onset decomposition temperature of around 250 °C when complexed with metal ions.[39] Similarly, in this work, intermediate phases began to form from 270 °C onwards which could be associated with the beginning of dextran decomposition. At 270 °C, Mn_3O_4 began to crystallise. At 280 °C, new peaks at 14.0, 14.9 °2θ appeared, which is likely to be a nickel-rich phase, similar structure to Ni_3C. As the temperature increased further, peaks for these phases increased in intensity and became sharper, indication of growth as there is more signal from the all the diffraction planes and increased crystallinity. At 300 °C, Mn_3O_4 and nickel rich phase peaks were replaced by sudden crystallisation of the P3-NNM end-product. The rapid crystallisation was likely due to the relatively smaller particle size of the intermediate phases, which was deduced from the broad diffraction peaks, that enabled a large number of nucleation sites for P3-NNM to form.

Figure 3.5b shows low temperature *ex-situ* HT-XRD for specimen 1 : 1, exhibiting a markedly different crystallisation pathway *vs.* 1 : 4. At 240 °C, the pattern showed many peaks which could not be indexed. Using the ICDD software, various phases were attempted to be phase matched with the XRD pattern, such as carbonates, acetates and hydroxides. However due to the large number of peaks and the potential peak overlap, very few peaks from these phases matched well with the peaks in the diffraction pattern. Hence, it was difficult to confidently identify the phases present. It is likely that some peaks may be due to the recrystallisation of precursor acetates of cations that were unable to chelate with dextran due to the lower number of chelation sites. At 260 °C these peaks reduced in intensity, due to decomposition of these phases. At 270 °C, similar cluster of peaks remained between 5 and 10 °2θ, however additional peaks appeared that were indexed to Mn_3O_4 and another nickel-rich phase, possibly Ni_3C. As the temperature increased to 280 °C, the cluster of peaks at low angles disappeared and the peaks for Mn_3O_4 and Ni_3C analogue increased in intensity. It is likely that other minor phases were present as there were some additional peaks that formed at this temperature, such as carbonates and oxides with various combinations of Mn, Ni and Na in their composition that could not be confidently identified. At 300 °C there was no crystallisation of P3-NNM, instead peak intensities for Mn_3O_4 and Ni_3C were increased.

The lack of crystallisation of P3-NNM in 1 : 1 at 300 °C is likely due to the greater number of unchelated cations, enabling unconstrained growth of these intermediates that are able to form larger particles, reducing the number of nucleation sites. In addition, the impact of preferential binding to certain cations may be enhanced at low dextran concentrations, leading to segregation of the different precursors and hence less homogenous distribution of said precursors. This would could cause reactions requiring more energy due to overcome the limitations associated with mass transport and diffusion at the reaction interface, similar to solid state synthesis. For future work, conducting HT-XRD below 300 °C for specimen 1 : 0 may highlight the impact of the potentially increased phase separation on the crystallisation process in specimen 1 : 1.

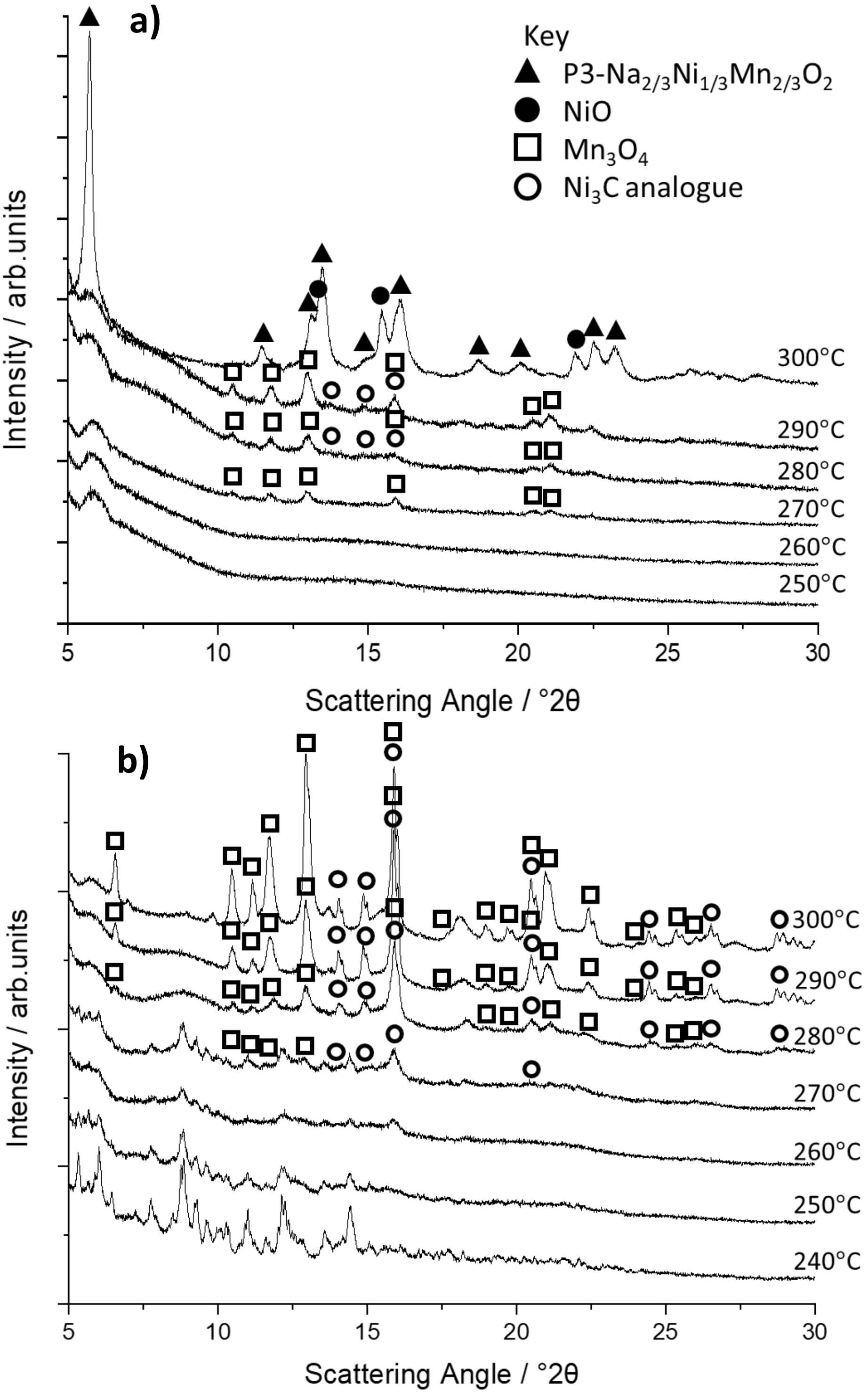

Figure 3.5: *Low temperature ex-situ XRD of sample prepared using mass ratios of $Na_{2/3}Ni_{1/3}Mn_{2/3}O_2$ to dextran a) 1: 4 and b) 1 : 1 dwelled at each temperature for 30 mins and cooled to RT before measurements. Unlabelled peaks are attributed to unknown phases. The key is relevant for both figures. X-ray source is Ag.*

In-situ HT-XRD was performed on biotemplated specimen 1 : 4, Figure 3.6, and showed that crystallisation of the P3-NNM phase was already well underway at 300 °C in line with the *ex-situ* data. As the temperature increased further, P3-NNM peaks became sharper and more intense, indicative of increased crystallinity and growth of single crystalline domain size. Peaks were observed to shift slightly to lower angles up to 500 °C, most likely due thermal expansion of the specimen. Above 500 °C all peaks shifted to higher angles, possibly due to reduction in lattice parameters or specimen displacement caused by shrinkage of the specimen which was observed the experiment. This was accompanied by an associated decrease in relative intensity of the NiO peaks up to 650 °C.

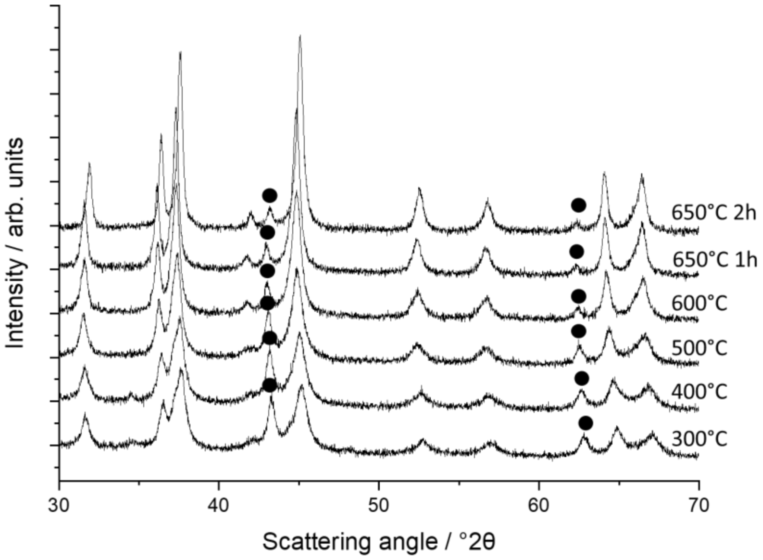

Figure 3.6*: In-situ HT-XRD of biotemplated sample using mass ratio of 1 : 4* $Na_{2/3}Ni_{1/3}Mn_{2/3}O_2$ *to dextran, pre-calcined at 300 °C for 0.5 h beforehand. NiO peaks labelled with black circles and unlabelled peaks are attributed to P3-NNM. The ramp rate to achieve each temperature was 50 °C/min and each scan took 15-20 minutes.*

Figure 3.7 shows the SEM images of specimens 1 : 0.5 and 1 : 4. The difference between the two specimens are not obvious in terms of particle morphology and size. Both specimens contain nanorods which is a rather unexpected result, as growth mechanism and how dextran may influence the formation of nanorods is still unknown. The particle size was analysed using ImageJ software, by measuring the diameter of at least 500 particles from different images for each specimen (not including nanorods). The average particle for specimen 1 : 0.5 was 207 nm (±118) and for 1 : 4 it was 140 nm (±63). The slightly smaller particle size and smaller standard deviation could be due the relatively large number of chelation sites, constraining growth of intermediate phase to a greater degree and creating more spatial separation between nucleation/crystallisation sites. This can lead to growth kinetics that are more homogenous throughout the specimen. The larger variation in particle size in specimen 1 : 0.5 can be attributed to preferred binding of certain cations with dextran and the lack of binding sites allowing for inhomogeneous growth of different phases within the specimen. However, such particle analysis is not accurate due to different depth of field within an image, as specimen surface is not flat and the particles appear to be anisotropic so width measurements may differ depending on particle orientation. Therefore alternative methods to analyse particle size is required.

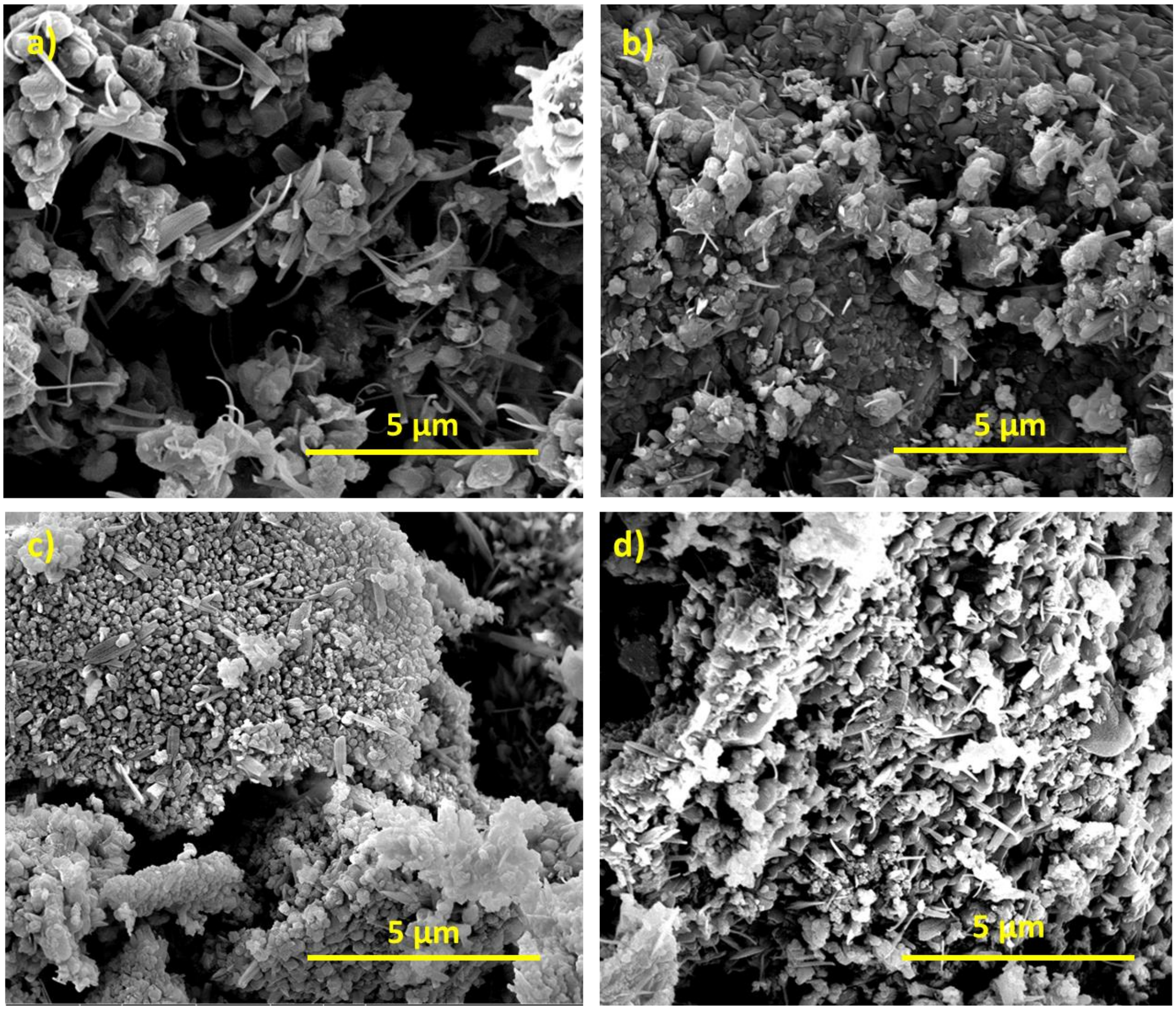

***Figure 3.7**: SEM images of specimens synthesised with mass ratios of P3-NNM to dextran of a&b) 1 : 0.5 c&d) 1 : 4. Both were calcined at 650 °C for 2h.*

In-situ HT-XRD was conducted during solid state synthesis to compare the phase progression with biotemplating, figure 3.8. In contrast to biotemplating, when using solid state synthesis P3-NNM crystallises between 500 °C and 600 °C, (filled triangles). Below this, peaks for starting reagents (sodium carbonate, manganese oxide and nickel oxide) were observed, however peak intensities decreased with increasing temperature. At 500 °C there were some peaks that can be attributed to the P3-NNM phase, however formation of this phase was more obvious at 600 °C. At 700 °C, crystallisation of the P2-NNM began (unfilled triangles), accompanied, above 800 °C, by a decrease in intensity of the P3-NNM peaks. In solid state synthesis, the relative intensity of the NiO peaks at 36.8 and 42.7 °2θ remained high up until 800 °C, at which point intensities began to decrease. The peak shape was also sharp, indicative of large crystallites, unlike in biotemplating, where the peaks were broader for NiO. This shows the effect that large particles and hence mass transport have on phase evolution: more energy is required to react NiO, and for it to participate in the crystallisation and growth of the NNM.

In-situ HT-XRD is not completely representative of what may occur in a usual muffle furnace, due to faster heating rates and smaller specimen size, however, it gives a good indication of the general crystallisation steps that occur in both methods, and enables the identification of any unstable or transient phases which would not be observed in the “snapshots” offered by *ex-situ* heating.

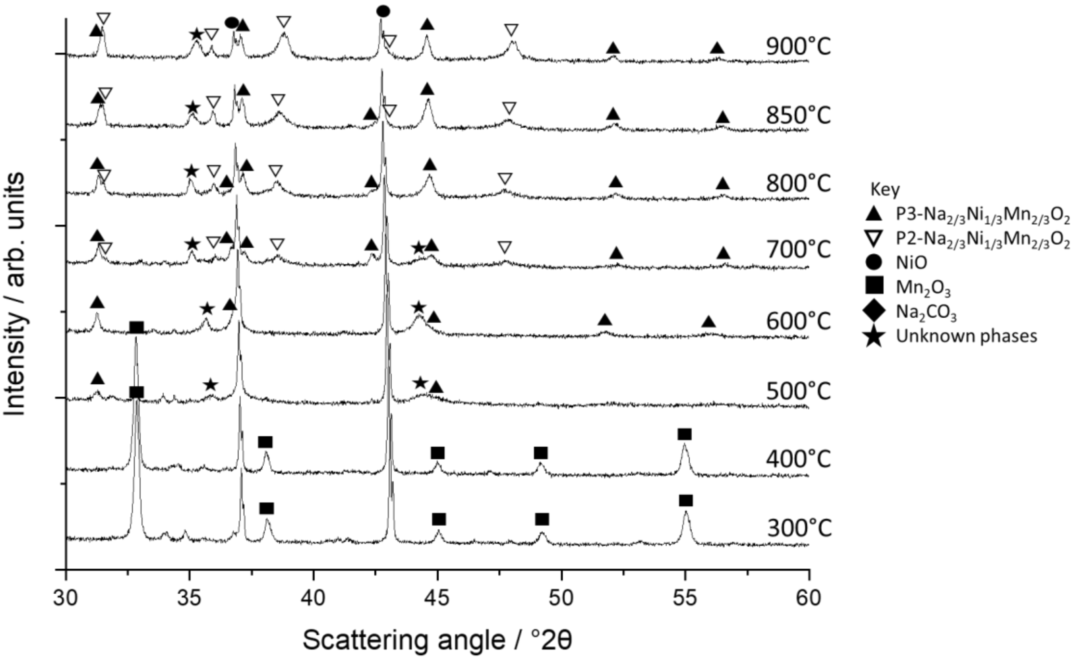

Figure 3.8*: In-situ HT-XRD of solid state sample starting with reagents at room temperature. At room temperature, the powder was a mixture of reagents: sodium carbonate, nickel oxide and manganese oxide. The key is relevant for both figures. Significant peaks for unknown phases labelled, however there are additional small unknown peaks that have not been labelled.*

It is highly likely that chelation strength between hydroxyl groups in dextran and different cations species vary, hence the rate at which these phases crystallise at low temperatures may be directly affected by the chosen biotemplate. While there are no direct studies of this for biotemplating of oxides, other similar studies on water filtration may shed some light on template-cation affinity,[34,40–42] that is different metal cations in a mixed solution compete for binding sites. Those with better complex stability tended to bind more readily, allowing for unbound cations to pass through the filter.[43] Such affects may have a negative impact in biotemplating synthesis.

Both the *ex-situ* and *in-situ* HT-XRD indicate that regardless of the amount of dextran used, Ni intermediates form early during synthesis, and persist throughout. At the final calcination temperature (650 °C), however, it is clear that the quantity of dextran used during synthesis has a significant effect on the NiO content. This could be due to weaker binding between nickel ions and dextran compared to sodium and manganese ions, although there have been no studies on the competing binding effects for this mixture of cations. It is likely there is some level of preferred binding, as dextran has found to have preferential binding for some cations over others.[34,44] Determining the different cation affinities with different biotemplates can have profound implications for selecting suitable polymers for different compositions, and could give insights into predicting the success of biotemplate/product combinations.

If there is preferred binding at the expense of Ni, this could be why nickel-rich phases may form more readily as dextran decomposes, enabling crystallisation and growth in the early stages of synthesis. This appears to be exacerbated when a low concentration of dextran is present, as there may be a larger number of unbound Ni that would have different growth kinetics to the bound Na and Mn, causing significant phase separation. When there is sufficient amount of dextran used during synthesis, although NiO appears to form readily, the broad peak shape represent smaller crystallites, indicating a degree of constrained growth due to the biotemplate. In addition, the biotemplate ensures good spatial distribution of the metal cations, impeding on agglomeration. These combined effects allows formation of a large number of nucleation sites for P3-NNM.

3.3.2 Electrochemistry

3.3.2.1 Cyclic voltammetry of P3-NNM

Cyclic voltammetry (CV) was conducted to identify at which voltages redox reactions occur and how they vary between specimens 1 : 1 and 1 : 4 due to their different stoichiometries. Figure 3.9a and 3.9b show CV curves of the 2nd, 5th and 10th cycle between 2.0 and 4.5 V, conducted at a scan rate of 0.1 mV s^{-1} for specimens 1 : 4 and 1 : 1 respectively. Both showed similar redox peaks, where there were four obvious redox pairs at anodic/cathodic voltages around 4.3/4.0 V, 3.7/3.4 V, 3.3/3.1 V and 3.2/3.0 V. P2-NNM has been widely studied,[5,45–48] unlike P3-NNM discussed here, however both polymorphs seem to have similar redox behaviour.[1,49,50] In the literature, in P2-NNM, the redox peaks between 3.7 and 3.0 V are attributable to $Ni^{2+}/Ni^{3+}/Ni^{4+}$ reactions, the main contributor to capacity as Mn^{4+} is electrochemically inactive above 2.0 V.[48] The redox pair at 4.3/4.0 V has increasing evidence that it is due to oxygen redox, at least in the case for P2-NNM which occurs at 4.2 V upon charge.[23] Further increasing the voltage leads to oxygen gas evolution, accompanied by surface densification of the P2-NNM particles, causing rapid decrease in capacity when charging to 4.5 V. Irreversible anionic redox of lattice oxygen could be the reason as to why there is a rapid decrease in peak height on the redox pair at 4.3/4.0 V in Figure 3.9. Oxygen redox has not been investigated in P3-NNM in the published literature to date, however there has been evidence in other P3 structures in a similar voltage regions.[9,11,12,51]

Studies found that in P2-NNM, Mn^{4+} reduction upon discharge occurs below 2.0 V.[17,52] However, some studies have shown Mn redox between 2.0 and 2.5 V in the CV data where the peaks are quite small, whereas others do not seem to have any activity in this region.[1,24,53–55] Different factors can affect Mn redox in this voltage region. For instance, if the average oxidation state is between +3 and +4, then redox activity of Mn^{3+} from the pristine material is activated in this voltage region. This can arise if the Mn and Ni ratio is not quite 2/3 : 1/3.[56] Other factors that can affect the average oxidation state of Mn include the synthesis conditions, such as slow cooling or different concentrations of biotemplate.[24,55]

Specimen 1 : 4 in Figure 3.9a, exhibited weak peaks in the voltage region between 2.0 and 2.5 V, however after a few cycles they were less visible. Whereas the peaks in this region were more prominent for 1 : 1, figure 3.9b. TM deficiency is likely to cause a change in Mn valence compared to 1 : 4. If there is any Mn^{3+}, this would oxidise to Mn^{4+} upon charge, which has occurred in P2-NNM.[1,24,55]

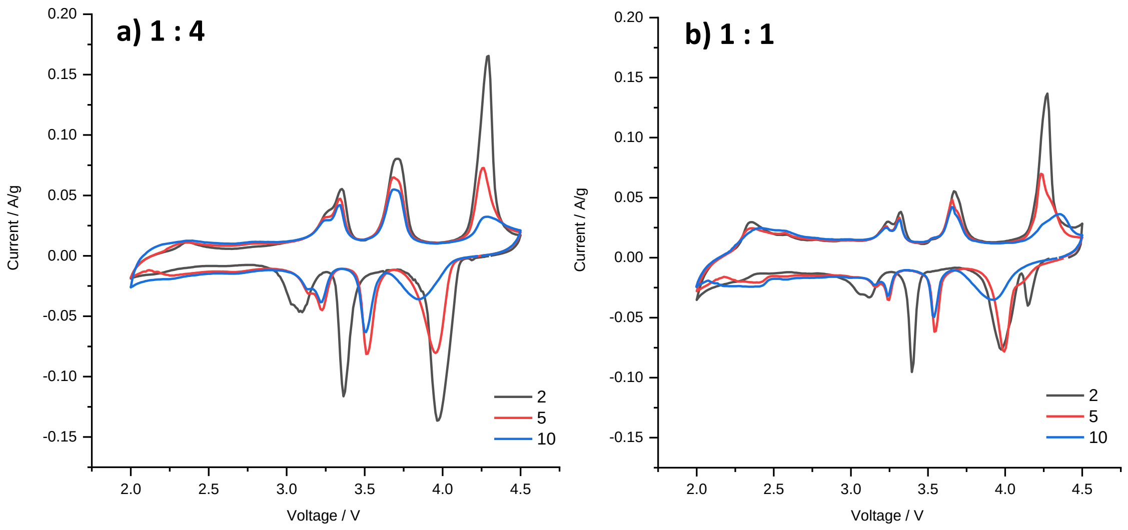

Figure 3.9: *CV curves when cycled between 2.0 and 4.5 V at a scan rate of 0.1 mV s^{-1} of specimen synthesised with a) 4 g and b) 1 g dextran per 1 g P3-NNM.*

Previous research on P2-NNM may give some insight into the redox behaviour of the less studied P3-NNM, however one study has found that the two structures have a slightly different charge compensation mechanism,[49] calling into question the validity of this. In this particular study, the P2 phase, when charging from 2.0 and 4.5 V, there was no Mn redox, whilst there is such activity in P3-NNM after 4.0 V. During discharge to 2.0 V, Ni is reduced in both materials. Upon further discharge to 1.5 V, Ni is P3-NNM is further reduced, whereas Mn in P2-NNM is reduced.[49] However, this study did not conduct CV analysis for both phases to determine at what voltages such redox activities occur, therefore direct comparisons with the data shown in figure 3.9 is not possible. But what is clear is that Ni redox is the main capacity contributor between 2.0 and 4.0 for P3-NNM in both 1 : 1 and 1: 4.

3.3.2.2 Redox comparisons between specimens 1 : 1 and 1 :4

Figure 3.10a-c show the CV curves for both samples for the 2nd, 10th and 20th cycle respectively. During the 2nd cycle, figure 3.10a, there were slight differences between the two specimens. Although the redox peaks occurred at similar voltages, peak heights and areas under the curve differed. Specimen 1 : 4 had greater peak heights and areas between 3.0 and 4.5 V. This would be expected, as the redox pairs between 3.0 and 3.7 V are likely attributed to Ni redox and Ni content in 1 : 1 is significantly lower as shown in figure 3.1 and table 3.1. In 1 : 1, there was greater redox activity below 2.5 V possibly from Mn^{3+} in the pristine material. After 10 cycles, figure 3.10b, all peak intensities and areas decreased in both samples, especially the redox pair 4.3/4.0 V, potentially due to irreversible oxygen reduction.[51] The cathodic peak at 4.0 V at the 2nd cycle, shift to lower voltage whereas there is no significant change in the anodic peak. This increase in potential difference is an indication of increased polarisation. This could result from the P3-O3 phase transition as the potential in which this occurs is close to this redox pair.[49] Transitioning to an O-type phase during cycling results in slower Na^+ diffusion kinetics.[57] The decrease in peak heights are not drastic for the pairs associated with Ni redox at 3.7/3.4 V, 3.3/3.1 V and 3.2/3.0 V, when comparing between the 2nd and 10th cycle. Also the cathodic peaks shifted to higher voltages, closer to the voltage values of the anodic peaks, indication of reduction in resistance. This could be due to improved cathode-electrolyte interface.

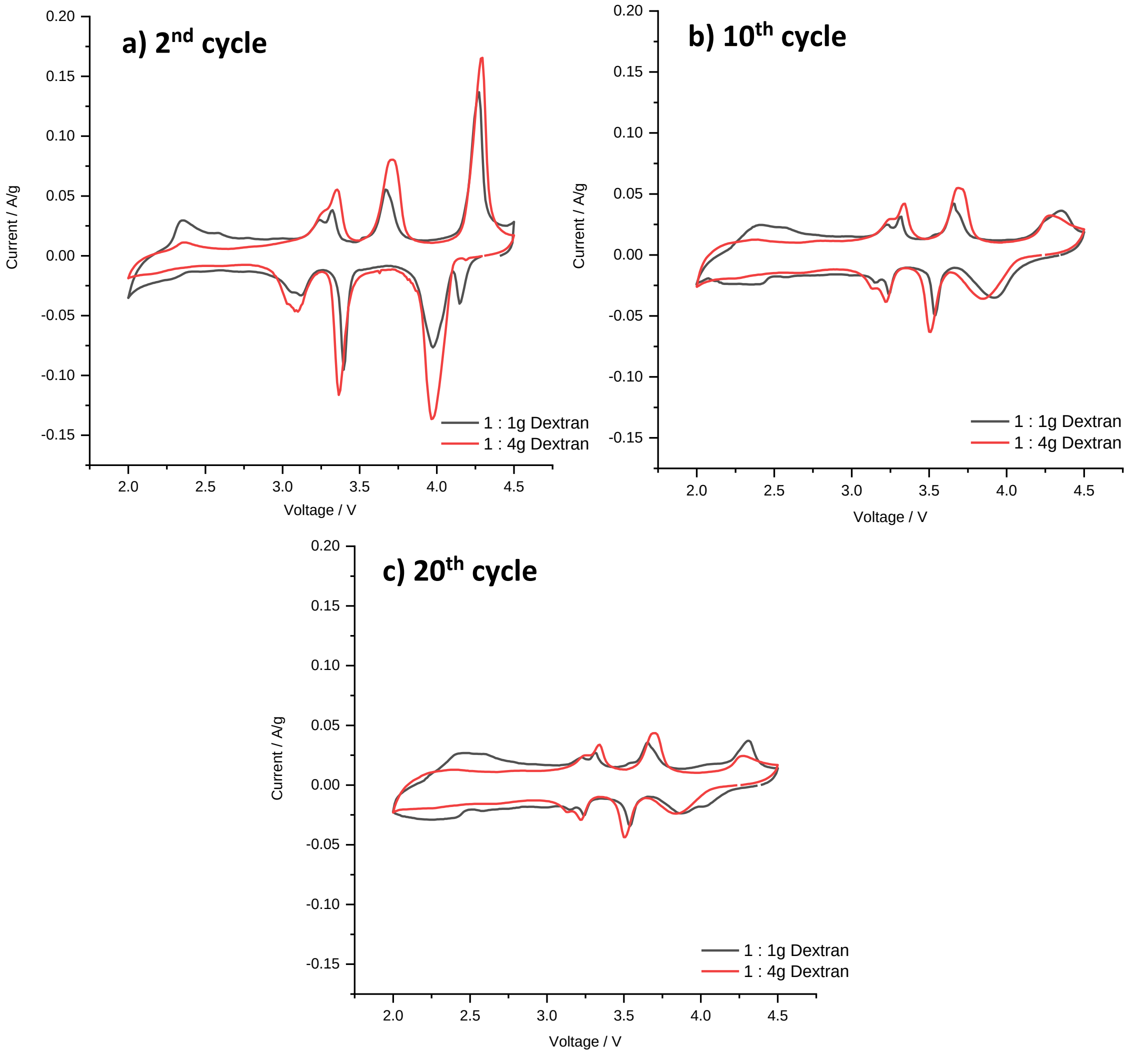

Figure 3.10: *CV comparisons of specimens 1 : 1 and 1 : 4 between 2.0 and 4.5 V at a scan rate of 0.1 mV s^{-1} at the a) 2nd, b) 10th and c) 20th cycle.*

The main difference between the two specimens between 3.0 and 3.7 V is the rate of peak height reduction for the 3.7/3.4 V redox pair. 1 : 4 exhibited a cathodic and anodic peak height decrease of *ca.* 30 % and 25 % respectively from 2nd to 5th cycle and continued to decrease upon subsequent cycles. Whereas in 1 : 1 the cathodic and anodic peak heights decrease by 33 % and 13% from 2nd to 5th cycle, with little change by the 10th cycle. Similar trend is seen in the redox pairs located at 3.3/3.1 V and 3.2/3.0 V, which can be seen more clearly in figure 3.9.

3.3.2.3 Anionic redox

Oxygen redox has been found in similar materials, such as P3-$Na_{0.65}Mn_{0.75}Ni_{0.25}O_2$, at 4.1/4.2 V, where the CV peaks decrease in height quickly after a few cycles,[12] similarly to what is reported here for the redox pair 4.3/4.0 V, figure 3.11. In P3-$Na_{0.67}Ni_{0.2}Mn_{0.8}O_2$, oxygen redox was found to occur between 4.1 and 4.4 V.[51] In P2-NNM this starts to occur at 4.2 V with the O^{2-}/O_2^{n-} redox couple.[23] Further increasing the voltage to 4.3 V, oxygen gas evolution occurs from the oxidation reaction O_2^{n-}/O_2. This causes formation of an inactive dense layer on the active particles, leading to poor Na^+ kinetics. Although there is no CV data in that study, a redox pair in this voltages region would be expected and the peak intensity would decrease rapidly upon subsequent cycles, as shown in both P3-NNM specimens, figure 3.11.

Figure 3.11 shows a magnified region of the CV data from figure 3.9, between 3.6 and 4.5 V. In figure 3.11b, there was an extra cathodic peak at 4.17 V for specimen 1 : 1 which was not present in figure 3.11a, for 1 : 4. After the 5th cycle, this peak shifted to lower voltages and gradually decreased in intensity and became a shoulder to the broad 4.0 V peak. After the 10th cycle, the peak around 4.0 V, shifted to a lower voltage and further broadened due to the cathodic peaks at 4.17 and 4.0 V from the second cycle eventually overlapping. The anodic peak at 4.3 V for specimen 1 : 1, did not appear to have any obvious splitting on the second cycle, unlike on the cathodic sweep. Although on the 5th cycle, along with decreased peak height, there was a shoulder on the 4.3 V peak. After 10 cycles, there was asymmetric broadening due to increased peak overlap.

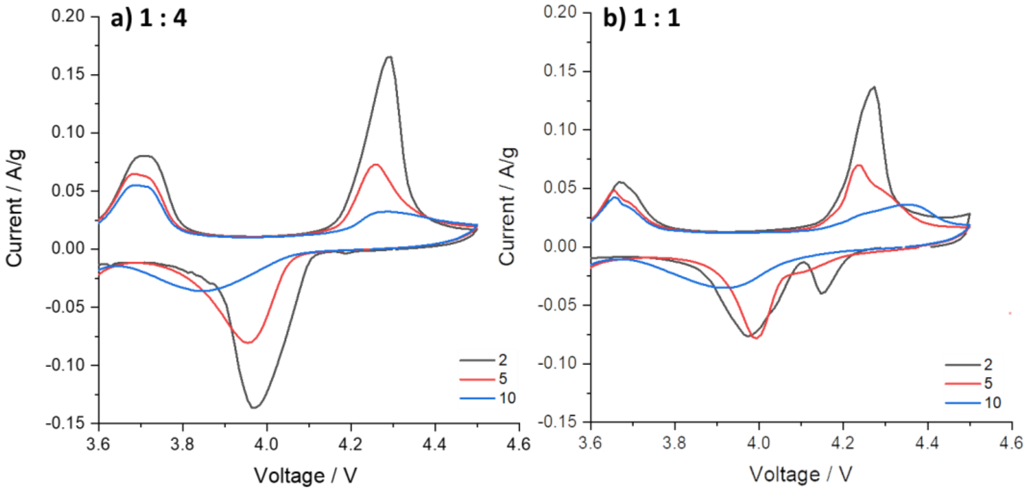

***Figure 3.11**: CV data from figure 3.9 in the voltage range 3.6 – 4.5 V for specimens a) 1 : 4 and b) 1 : 1.*

The 1 : 1 specimen appeared to undergo two redox events when charged above 4.0 V. After 20 cycles in figure 3.10c, the two different redox events appeared to be a bit more apparent, with the redox pairs at 4.3/4.0 V and 4.1/3.9 V. In the 1 : 4 specimen, there was only one singular redox pair in the same voltage region.

There have been some studies that found vacancies can alter anionic redox. Mg^{2+} and vacancies triggered oxygen redox and in P2-$Na_{0.63}\square_{0.036}Mg_{0.143}Mn_{0.820}O_2$ there were two separate oxygen redox events.[58] It was postulated that this was due to different environments around the oxygen caused by the Mg ions and vacancies which give rise to non-bonding O2p states at different energy levels. The CV data for this material in the literature showed that in the presence of vacancies, there were two anodic peaks above 4.0 V, which are only paired with one cathodic peak at around 2.8 V, showing large hysteresis for this set of redox reactions. The anodic peak at the lower voltage of 4.1 V was attributed to oxygen redox from Na-O-$\square$, whereas the peak at 4.3 V was due to Na-O-Mg. This is because the energy state of the non-bonding oxygen near a vacancy is higher,[59] leading to a lower voltage in the CV curves as it is more easily available to participate in electrochemical reactions. A similar effect is seen in $Na_{2/3}Zn_{1/9}Mn_{7/9}\square_{1/9}O_2$, when comparing with the vacancy free analogue.[30] The vacancy free material had a sharp anodic peak at 4.2 V and a broad cathodic one at 2.9 V. Material with vacancies had a broad anodic asymmetric peak starting at 3.75 V and ended just under 4.5 V, indication of different redox reaction occurring in the is voltage region.

In specimen 1 : 1, the lack of Ni in the structure would lead to vacancies in the TM layers. The two redox pairs above 4.0 V could therefore be due to the different oxygen environments, such as Na-O-Ni and Na-O-□, causing the potentials for anionic redox to differ between the different environments. Whereas in specimen 1 : 4, there is one type of oxygen environment, hence there is only one redox pair above 4.0 V. However, future work requires an in depth characterisation of the charge compensation mechanism using techniques such as x-ray absorption near edge structure (XANES) and x-ray photoelectron spectroscopy (XPS).

3.3.2.4 Capacity calculations

The discharge specific capacities were calculated from the CV curves between 2.0 and 4.5 V at a scan rates of 0.1 and 0.5 mV s^{-1}, figure 3.12a and 3.12b respectively. This was calculated by using the equation based from the literature:[60,61]

$$mAh\ g^{-1} = \frac{1}{(3.6\ \times m\ \times v)}\int IdV$$

Equation 3.1

Where $\int IdV$ is the area under the CV curve (I x V), m is the active mass, v is the scan rate in V s^{-1} and 3.6 is the conversation from A.s to mAh. In this instance, to calculate discharge specific capacity the area was calculated from the cathodic sweep with negative current, as voltage decreased. From the equation, area is proportional to capacity. For specimen 1 : 1, the active mass did not include the mass of NiO, because it is assumed that is electrochemically inactive, so the phase fraction obtained in table 3.1 was used.

At a scan rate of 0.1 mV s^{-1}, specimen 1 : 4 exhibited a higher discharge capacity of 152 mAh g^{-1} on the 2nd cycle and after 19 cycles it was 92 mAh g^{-1}, corresponding to a capacity retention of 60 %. Whereas 1 : 1 had a capacity retention of 92 % from 2nd to 19th cycle, with values 124 mAh g^{-1} and 115 mAh g^{-1} respectively. At a faster scan rate of 0.5 mV s^{-1}, 1 : 4 had an initial capacity of 133 mAh g^{-1} and after 50 cycles it was 62 mAh g^{-1}, a capacity retention of 46%, figure 3.12b. Whereas 1 : 1 exhibited an initial capacity of 112 mAh g^{-1} with retention of 65 %. This correlates with the change in the peak height and area of the CV curves in figure 3.9, where specimen 1 : 1 shows a smaller rate of change upon subsequent cycles.

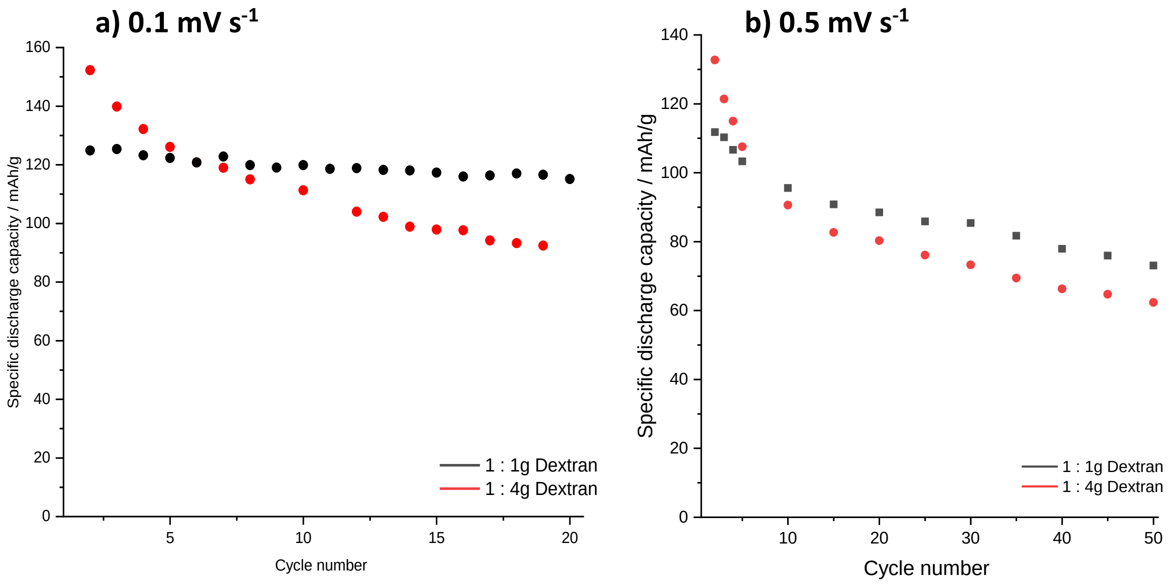

Figure 3.12: *Calculated discharge capacities for both specimens from the CV curves at 2.0 and 4.5 V at a scan rate of a) 0.1 mV s^{-1} and 0.5 mV s^{-1}.*

Confirming previous work in the literature, vacancies contribute to the flexible TMO_6 octahedron that accommodate distortions and inhibit high voltage phase transitions. Such effects could be present in the 1 : 1 specimen, hence the better cycling stability compared to 1 : 4 with sufficient TM.

3.3.3 Overall discussion

Polymers that can be used in biotemplating synthesis of functional oxides can exhibit preferred binding to certain metal cations in mixed solutions. Studies on water treatment using polymer assisted ultrafiltration (PAUF) have shown to what extent this can occurs.[34,62,63] These finding can help to elucidate suitability of biotemplate depending on the type of precursor ions. Although, there are no studies on the interactions between dextran and Na^+, Mn^{2+} and Ni^{2+} in a mixed solution, the literature on PAUF identify various factors that should be considered that would affect binding affinity such as pH and template concentration,[62] and hence impact the biotemplating process.

Concentration of dextran during the synthesis of P3-NNM had a significant impact on the crystallisation process and hence the phase fractions in the final product. With an insufficient amount of dextran, NiO was able to crystallise in the early stages of synthesis with minimal constraints on growth, potentially due the lack of binding with biotemplate caused by preferential binding. This could have also led to increased phase separation as the precursor cations that were bound to dextran may have had different growth kinetics. These factors were most likely enhanced compared to the specimen synthesised without a template. Hence the importance of optimising biotemplate concentration. Although the specimen 1 : 4 showed early onset crystallisation of NiO at 300 °C, growth was constrained as indicated by broad diffraction peaks. This allowed the formation of large number of nucleation sites for P3-NNM. Very small amounts of NiO remined in the final product (*ca.* 2.73 wt.%), showing the success of the synthesis process.

Specimen 1 : 1 had a large phase fraction of NiO (18.87 wt.%), therefore P3-NNM was likely to be lacking in Ni in the structure, which might have given rise to vacancies in the TM layers. Large amounts of secondary phases is disadvantages, as they would not contribute to capacity and take up space in the cell. When cycling between 2.0 and 4.0 V, Ni redox is the main contributor to capacity and therefore capacities in such materials were expected to be lower compared to specimens such as 1 : 4. The capacities were calculated from the CV data for specimens 1 : 1 and 1 : 4, where the active mass without NiO was used in the calculations for 1 : 1. Specimen 1 : 4 had higher initial capacities, however exhibited poor cycling stability compared to 1 : 1 which then had higher capacities after a few cycles.

Vacancies in the TM layers have shown to have a positive impact on cycle stability. This is because layered oxides with vacancies have shown to supress high voltage phase transitions, such as the P2-O2 transition,[26,27] which is often associated with large volume changes. Vacancies enhance the flexibility of the TMO_6 octahedrons, which improve structural stability during cycling.[29] In some of these materials, vacancies have shown to activate anionic redox of lattice oxygen and improve the reversibility.[29] However, this has not been the case in some studies, where $Na_{0.67}Al_{0.1}Mn_{0.9}O_2$ with 7.8 and 1.6 % vacancies, both experienced poor cycling stability when cycled to 4.5 V due to irreversible anionic redox compared to when only cycled between 2.0 and 4.0 V.[27] However, the material with a higher concentration of vacancies exhibited better diffusion kinetics at a larger cycling range due to maintaining the P2 structure between 1.5 and 4.5 V, whereas material with lower concentration of vacancies exhibited more complex phase transitions.

In the data presented here, the redox pair around 4.3/4.0 V for both 1 : 1 and 1 : 4, exhibited rapid decline after only a few cycles, indication that vacancies did not improve the reversibility of anionic redox of lattice oxygen. However, the other redox pairs below 4.0 V, associated with Ni redox appeared to have better reversibility upon subsequent cycles in specimen 1 : 1. This is likely due to improved structural stability, potentially leading to improved reversibility. However, further investigated is needed to determine the structural evolution during cycling for the two specimens.

As 0.33 is the solid solution limit of Ni in NNM, it is not surprising that some NiO was present in 1 : 4. Regardless dextran biotemplating synthesis has shown to be an easy an effective way to synthesise P3-NNM with minimal NiO. Obtaining phase pure materials may be easier with a lower concentration of Ni. Although Ni redox is the main capacity contributor in P3-NNM, extra capacity can be obtained from oxygen redox, especially if its reversibility could be improved through a combination of substituting in other metals into the TM layers as well as introduction of vacancies to manipulate the potentials at which it occurs.

3.4 Conclusion

Dextran impacts the formation and growth of intermediate phase and therefore P3-$Na_{2/3}Ni_{1/3}Mn_{2/3}O_2$. Most importantly, the concentration of template can have a significant impact. Higher concentration of dextran, like in specimen 1 : 4, had a significantly smaller weight fraction of NiO (2.73 wt.%) compared to specimens 1 : 0.5 and 1 : 1. This is due to the sufficient number of binding sites in the biotemplate that ensures majority of precursor cations are bound and unable to agglomerate, constricting growth of the intermediate phases. This allows for numerous nucleation sites for P3-NNM, enabling for it to crystalise at significantly lower temperatures compared to specimen prepared by solid state and biotemplated 1 : 1. In specimen 1 : 1, at temperatures below 300 °C, peak intensities for Ni rich compounds are relatively high and sharp, indication of large crystallites. The impact of this included delayed crystallisation of P3-NNM and secondly at the final calcination temperature, the weight fraction of NiO was *ca.* 19 wt.%. This could be due preferred binding of dextran with Na and

Mn, that may have led to a large concentration on unbound Ni that was able to agglomerate. As the particles of Ni rich phases grew, they were able to persist to higher temperatures. Specimen 1 : 1 had a higher NiO content compared to 1 : 0. A smaller concentration of dextran could exacerbate agglomeration and phase separation, especially with the potential preferential binding of certain cations. Hence it is important to optimise the concentration of biotemplate.

Nickel deficiency in P3-NNM, such as in specimen 1 : 1, exhibited better cycling stability compared to 1 : 4. The literature found that vacancies enabled more flexible TMO_6 that can accommodate distortions and inhibited high voltages phase transitions, which may have occurred in specimen 1 : 1 as the CV data exhibited better reversibility upon subsequent cycles. However further investigation is needed to determine the charge compensation mechanism and the structural evolution during cycle for both specimens 1 : 4 and 1 : 1. Study of the impact of vacancies in such materials provide plenty of scope for future research, where biotemplating can be a sustainable synthesis choice for these materials.

3.5 Future Work

The work presented here, showed that P3-NNM synthesised without dextran had a smaller phase fraction of NiO compared to 1 : 1. To be understand why this happened, a temperature study needs to be conducted for specimen synthesised without a template as a control. It is hypothesised that an insufficient amount of dextran, like in specimen 1 : 1, may create discrete areas with different growth kinetics and with the combined effects of potential preferential binding, eventually lead to increased amount of NiO at the final calcination temperature.

Although it is clear that the optimised amount of dextran can control the formation and growth of intermediate phases at the early stages of synthesis, NiO is still prominent. This is likely due to weak interactions between Ni ions and template, therefore Ni rich compounds are able to form at the early stages of synthesis, potentially while the template is still present. Pair Distribution Function (PDF) can be conducted to determine what bonds are forming as the template is burning off, while there is still a large proportion of amorphous phase present. This would give an indication as to which ions are more or less constrained by the template. Comparison could be made with different biopolymers, such as chitosan or carrageenan, to determine the suitability for a specific material. Similar studies that are used in PAUF could also be used to investigate the interactions between the biopolymers and the different cations in the solution. This would show to what extend preferential binding occurs. In the case of P3-NNM, a better biopolymer may be identified that can better control crystallisation of NiO and aid the formation of a phase pure material.

Alternatively, dextran may already be the optimal template, and that synthesising a phase pure material close to the Ni solid solution is difficult. Therefore investigation into alternative stoichiometries with lower Ni contents would be of interest. The drive to produce materials with Ni content of 0.33 is that Ni is the redox active component between 2.5 and 4.0 V, and reducing the Ni concentration would reduce the capacity from this voltage region. However if reversibility of anionic redox of lattice oxygen, which generally occurs above 4.0 V, can be improved, then this would overcome the reduced capacity contribution from lower Ni concentration. This could be achieved through introduction of TM vacancies and substituting in for other metals into the TM layers.

Further investigation in warranted in TM deficient P3-NNM, as preliminary results reported here show a positive impact on the electrochemical performance. Therefore P3-NNM needs to be synthesised purposely with vacancies so that NiO would not be in the specimen. *In-situ* XANES can determine the charge compensation mechanism for both vacancy and vacancy-free specimens (e.g. 1 : 1 and 1 : 4 respectively). XPS can be used to determine what voltage oxygen redox occurs and *in-situ* differential electrochemical mass spectrometry (DEMS) to measure if there is oxygen gas release which would indicate the extent of irreversible anionic redox. To investigate the structural stability of these materials, *in-operando* XRD would show what phase transitions occur, at what voltage and how this would differ in the material with TM vacancies. To go along with this, Na^+ diffusion kinetic studies such as galvanostatic intermittent titration technique (GITT) would highlight the impact of such phase transitions, or lack thereof.

3.6 References

1. Lee, S. Y., Kim, J. H. & Kang, Y. C. Electrochemical properties of P2-type $Na_{2/3}Ni_{1/3}Mn_{2/3}O_2$ plates synthesized by spray pyrolysis process for sodium-ion batteries. *Electrochim. Acta* **225**, 86–92 (2017).
2. Chagas, L. G., Buchholz, D., Vaalma, C., Wu, L. & Passerini, S. P-type NaxNi0.22Co0.11Mn0.66O2 materials: Linking synthesis with structure and electrochemical performance. *J. Mater. Chem. A* **2**, 20263–20270 (2014).
3. Song, B. *et al.* A novel P3-type $Na_{2/3}Mg_{1/3}Mn_{2/3}O_2$ as high capacity sodium-ion cathode using reversible oxygen redox. *J. Mater. Chem. A* **7**, 1491–1498 (2019).
4. Risthaus, T. *et al.* P3 Na0.9Ni0.5Mn0.5O2 Cathode Material for Sodium Ion Batteries. *Chem. Mater.* **31**, 5376–5383 (2019).
5. Dang, R. *et al.* Na+-Conductive Na2Ti3O7-Modified P2-type Na2/3Ni1/3Mn2/3O2 via a Smart in Situ Coating Approach: Suppressing Na+/Vacancy Ordering and P2-O2 Phase Transition. *ACS Appl. Mater. Interfaces* **11**, 856–864 (2019).
6. Goyal, A. *et al.* Precision Manufacturing of NaNi1/3Mn1/3Co1/3O2 Cathodes: Study of Structure Evolution and Performance at Varied Calcination Temperatures. *J. Electron. Mater.* **48**, 5301–5309 (2019).
7. Zilinskaite, S., Rennie, A. J. R., Boston, R. & Reeves-McLaren, N. Biotemplating: A sustainable synthetic methodology for Na-ion battery materials. *J. Mater. Chem. A* **6**, 5346–5355 (2018).
8. Kalapsazova, M. *et al.* P3-Type Layered Sodium-Deficient Nickel-Manganese Oxides: A Flexible Structural Matrix for Reversible Sodium and Lithium Intercalation. *Chempluschem* **80**, 1642–1656 (2015).
9. Liu, J. *et al.* Elucidation of the high-voltage phase in the layered sodium ion battery cathode material P3–Na 0.5 Ni 0.25 Mn 0.75 O 2. *J Mater Chem A Mater* **8**, 21151–21162 (2020).
10. Zhang, L. *et al.* Preferential occupation of Na in P3-type layered cathode material for sodium ion batteries. *Nano Energy* **70**, 104535 (2020).
11. Wang, Y. *et al.* The novel P3-type layered Na0.65Mn0.75Ni0.25O2 oxides doped by non-metallic elements for high performance sodium-ion batteries. *Chem. Eng.* **360**, 139–147 (2019).

12. Wang, Y. *et al.* Improved cycle and air stability of P3-$Na_{0.65}Mn_{0.75}Ni_{0.25}O_2$ electrode for sodium-ion batteries coated with metal phosphates. *Chem. Eng. J.* **372**, 1066–1076 (2019).

13. Mottram, L., Martin, D. Z. C., Reeves-McLaren, N. & Boston, R. Low-temperature crystallization of La0.15Sr0.775TiO3 using ionic liquids. *J. Am. Ceram. Soc* **101**, 4468–4471 (2018).

14. Motta, M., Deimling, C. v., Saeki, M. J. & Lisboa-Filho, P. N. Chelating agent effects in the synthesis of mesoscopic-size superconducting particles. *J. Sol-Gel Sci. Technol.* **46**, 201–207 (2008).

15. Zayat, M. & Levy, D. Blue $CoAl_2O_4$ particles prepared by the sol-gel and citrate-gel methods. *Chem. Mater.* **12**, 2763–2769 (2000).

16. Danks, Ashleigh. E., Hall, S. R. & Schnepp, Z. The evolution of 'sol-gel' chemistry as a technique for materials synthesis. *Mater. Horiz.* **3**, 91–112 (2016).

17. Wen, Y. *et al.* Electrochemical and Structural Study of Layered P2-Type $Na_{2/3}Ni_{1/3}Mn_{2/3}O_2$ as Cathode Material for Sodium-Ion Battery. *Chem. Asian J.* **10**, 661–666 (2015).

18. Sun, W. *et al.* Ultrathin nickel oxide nanosheets for enhanced sodium and lithium storage. *J Power Sources* **274**, 755–761 (2015).

19. Mosa, J., García-García, F. J., González-Elipe, A. R. & Aparicio, M. New insights on the conversion reaction mechanism in metal oxide electrodes for sodium-ion batteries. *Nanomaterials* **11**, 1–11 (2021).

20. Han, M. H., Gonzalo, E., Singh, G. & Rojo, T. A comprehensive review of sodium layered oxides: powerful cathodes for Na-ion batteries. *Energy Environ Sci* **8**, 81–102 (2015).

21. Zhang, X. *et al.* Improving the structural and cyclic stabilities of P2-type Na0.67MnO2 cathode material via Cu and Ti co-substitution for sodium ion batteries. *Chemical Communications* **56**, 6293–6296 (2020).

22. Hemalatha, K., Jayakumar, M., Bera, P. & Prakash, A. S. Improved electrochemical performance of Na0.67MnO2 through Ni and Mg substitution. *J Mater Chem A Mater* **3**, 20908–20912 (2015).

23. Zhang, Y. *et al.* Revisiting the $Na_{2/3}Ni_{1/3}Mn_{2/3}O_2$ Cathode: Oxygen Redox Chemistry and Oxygen Release Suppression. *ACS Cent. Sci* **6**, 232–240 (2020).

24. Liu, Q. *et al.* P2-type $Na_{2/3}Ni_{1/3}Mn_{2/3}O_2$ as a cathode material with high-rate and long-life for sodium ion storage. *J. Mater. Chem. A* **7**, 9215–9221 (2019).

25. Wang, H. *et al.* Electrochemical Properties of P2-$Na_{2/3}[Ni_{1/3}Mn_{2/3}]O_2$ cathode material for sodium ion batteries when cycled in different voltage ranges. *Electrochim. Acta* **113**, 200–204 (2013).

26. Islam, M. *et al.* Unraveling vacancy-induced oxygen redox reaction and structural stability in Na-based layered oxides. *Chemical Engineering Journal* **431**, 1385–8947 (2022).

27. Xiao, Z. *et al.* Insights of the Electrochemical Reversibility of P2-Type Sodium Manganese Oxide Cathodes via Modulation of Transition Metal Vacancies. *ACS Appl. Mater. Interfaces* **13**, 38305–38314 (2021).

28. Li, X. L. *et al.* Stabilizing Transition Metal Vacancy Induced Oxygen Redox by Co2+/Co3+ Redox and Sodium-Site Doping for Layered Cathode Materials. *Angewandte Chemie International Edition* **60**, 22026–22034 (2021).

29. Yang, L. *et al.* Superiority of native vacancies in activating anionic redox in P2-type Na2/ 3[Mn7/9Mg1/9□1/9]O2 . *Nano Energy* **78**, 105172 (2020).

30. Yang, L. *et al.* Effect of vacancy-tailored Mn 3 + spinning on enhancing structural stability. *Energy Storage Mater* **44**, 231–238 (2022).

31. Nikolić, G. S., Cakić, M., Mitić, Ž. & Ilić, Lj. Deconvoluted Fourier-transform LNT-IR study of coordination copper(II) compounds with dextran derivatives. *Russian Journal of Coordination Chemistry 2008 34:5* **34**, 322–328 (2008).

32. Hancock, R. D. & Martell, A. E. Ligand Design for Selective Complexation of Metal Ions in Aqueous Solution. *Chem Rev* **89**, 1875–1914 (1989).

33. Lawrance, G. A. *Introduction to Coordination Chemistry*. (Inorganic Chemistry, A Wiley Textbook Series, 2010).

34. Solpan, D. & Sahan, M. Concentration and separation of aqueous solutions of Cu2+, Ni2+, Fe3+ by dextran. *J. Appl. Polym. Sci.* **55**, 383–386 (1995).

35. de Repentigny, C., Courcelles, B. & Zagury, G. J. Spent MgO-carbon refractory bricks as a material for permeable reactive barriers to treat a nickel- and cobalt-contaminated groundwater. *Environmental Science and Pollution Research (2018)* **25**, 23205–23214 (2018).

36. Ain Zainuddin, N., Azwan Raja Mamat, T., Imam Maarof, H., Wahidah Puasa, S. & Rohana Mohd Yatim, S. Removal of Nickel, Zinc and Copper from Plating Process Industrial Raw Effluent Via Hydroxide Precipitation Versus Sulphide Precipitation. *IOP Conf Ser Mater Sci Eng* **551**, 012122 (2019).

37. Paulsen, J. M. & Dahn, J. R. Studies of the layered manganese bronzes, $Na_{2/3}[Mn_{1-x}M_x]O_2$ with M = Co, Ni, Li, and $Li_{2/3}[Mn_{1-x}M_x]O_2$ prepared by ion-exchange. *Solid State Ion* **126**, 3–24 (1999).

38. Liu, Y. *et al.* Hierarchical Engineering of Porous P2-$Na_{2/3}Ni_{1/3}Mn_{2/3}O_2$ Nanofibers Assembled by Nanoparticles Enables Superior Sodium-Ion Storage Cathodes. *Adv. Funct. Mater.* **30**, 1907837 (2020).

39. Boston, R., Carrington, A., Walsh, D. & Hall, S. R. Synthesis of spherical superconductors. *CrystEngComm* **15**, 3763–3766 (2013).

40. Shevchenko, L. I., Lugovaya, Z. A. & Tolmachev, V. N. Study of the complexing properties of the dextran carboxymethyl ether with transition metal ions in solutions. *Polym. Sci. (USSR)* **27**, 2242–2247 (1985).

41. Lugovaya, Z. A., Tolmachev, V. N. & Il'yenko, I. B. Study of the optical rotation of dextran solutions containing metal ions. *Polym. Sci. (USSR)* **23**, 484–489 (1981).

42. García-Molina, V., Esplugas, S., Wintgens, T. & Melin, T. Ultrafiltration of aqueous solutions containing dextran. *Desalination* **188**, 217–227 (2006).

43. Verbych, S., Bryk, M., Alpatova, A. & Chornokur, G. Ground water treatment by enhanced ultrafiltration. *Desalination* **179**, 237–244 (2005).

44. Azmeera, V., Rastogi, P. K., Adhikary, P., Ganesan, V. & Krishnamoorthi, S. Synthesis, characterization and cyclic voltammetric study of copper(II) and nickel(II) polymer chelates. *Carbohydr. Polym.* **110**, 388–395 (2014).

45. Lu, Z. & Dahn, J. R. In Situ X-Ray Diffraction Study of P2-$Na_{2/3}[Ni_{1/3}Mn_{2/3}]O_2$. *J Electrochem Soc* **148**, A1225–A1229 (2001).

46. Zhao, W., Kirie, H., Tanaka, A., Unno, M. & Yamamoto, S. Synthesis of metal ion substituted P2-$Na_{2/3}Ni_{1/3}Mn_{2/3}O_2$ cathode material with enhanced performance for Na ion batteries. *Mater Lett* **135**, 131–134 (2014).

47. Zhang, Y., Ye, K., Cheng, K., Wang, G. & Cao, D. Three-dimensional lamination-like P2-Na2/3Ni1/3Mn2/3O2 assembled with two-dimensional ultrathin nanosheets as the cathode material of an aqueous capacitor battery. **148**, 195–202 (2014).

48. Zhang, J., Wang, W., Wang, W., Wang, S. & Li, B. Comprehensive Review of P2-Type $Na_{2/3}Ni_{1/3}Mn_{2/3}O_2$, a Potential Cathode for Practical Application of Na-Ion Batteries. *ACS Appl. Mater. Interfaces* **11**, 22051–22066 (2019).

49. Zhang, L. Electrochemical Performance and Structural Changes of $Na_{0.67}Mn_{0.67}Ni_{0.33}O_2$ as Cathode for Sodium Ion Batteries. (Technische Universität Berlin, 2019).

50. Zhang, L. *et al.* Stabilizing P3-Type Oxides as Cathodes for High-Rate and Long-Life Sodium Ion Batteries by Disordered Distribution of Transition Metals. *Small Methods* **4**, 2000422 (2020).

51. Kim, E. J. *et al.* Oxygen Redox Activity through a Reductive Coupling Mechanism in the P3-Type Nickel-Doped Sodium Manganese Oxide. *ACS Appl. Energy Mater.* **3**, 184–191 (2020).

52. Zhang, Y.-Y. *et al.* Improvement of electrochemical properties of P2-type $Na_{2/3}Mn_{2/3}Ni_{1/3}O_2$ sodium ion battery cathode material by water-soluble binders. *Electrochim. Acta* **298**, 496–504 (2019).

53. Luo, R. *et al.* Habit plane-driven P2-type manganese-based layered oxide as long cycling cathode for Na-ion batteries. *J Power Sources* **383**, 80–86 (2018).

54. Zheng, X. *et al.* New insights into understanding the exceptional electrochemical performance of P2-type manganese-based layered oxide cathode for sodium ion batteries. *Energy Storage Mater.* **15**, 257–265 (2018).

55. Arag, M. J. *et al.* On the use of guanidine hydrochloride soft template in the synthesis of $Na_{2/3}Ni_{1/3}Mn_{2/3}O_2$ cathodes for sodium-ion batteries. *J. Alloys Compd.* **789**, 1035–1045 (2019).

56. Gutierrez, A. *et al.* On Disrupting the Na^+-Ion/Vacancy Ordering in P2-Type Sodium−Manganese−Nickel Oxide Cathodes for Na^+-Ion Batteries. *J. Phys. Chem. C* **122**, 23251–23260 (2018).

57. Lee, D. H., Xu, J. & Meng, Y. S. An advanced cathode for Na-ion batteries with high rate and excellent structural stability. *Phys. Chem. Chem. Phys.* **15**, 3304–3312 (2013).

58. Bai, X., Iadecola, A., Tarascon, J. M. & Rozier, P. Decoupling the effect of vacancies and electropositive cations on the anionic redox processes in Na based P2-type layered oxides. *Energy Storage Mater* **31**, 146–155 (2020).

59. Yahia, M. ben, Vergnet, J., Saubanère, M. & Doublet, M.-L. Unified picture of anionic redox in Li/Na-ion batteries. *Nat Mater* **18**, 496–502 (2019).

60. Pandit, B., Dubal, D. P. & Sankapal, B. R. Large scale flexible solid state symmetric supercapacitor through inexpensive solution processed V2O5 complex surface architecture. *Electrochim Acta* **242**, 382–389 (2017).

61. Floraki, C., Androulidaki, M., Spanakis, E. & Vernardou, D. Effect of Electrolyte Concentration on the Electrochemical Performance of Spray Deposited LiFePO4. *Nanomaterials* **13**, 1–12 (2023).

62. Crini, G., Morin-Crini, N., Fatin-Rouge, N., Déon, S. & Fievet, P. Metal removal from aqueous media by polymer-assisted ultrafiltration with chitosan. *Arabian Journal of Chemistry* **10**, S3826–S3839 (2017).

63. Desbrières, J. & Guibal, E. Chitosan for wastewater treatment. *Polym Int* **67**, 7–14 (2018).

4 Biotemplated Synthesis and Electrochemical performance of Cu substituted P3-$Na_{2/3}Ni_{1/3-x}Cu_xMn_{2/3}O_2$

4.1 Aims & Objectives

P3-$Na_{2/3}Ni_{1/3}Mn_{2/3}O_2$ (NNM) undergoes the P3-O3 phase transition,[1,2] most likely after charging beyond 4.2 V. Such phase transitions are normally associated with large volume change causing structural instability, as well as slow Na^+ diffusion kinetics.[3,4] Common methods to prevent such phase transitions involve substituting in other metals to stabilise the pristine structure to higher voltages as done so in P2-NNM.[5–8] Cu^{2+} substitution has shown to be effective at supressing the P2-O2 phase transition in P2-NNM, thus improving cycle stability and rate capability.[9–12] To date, there have only been a handful studies on supressing the P3-O3 phase transition in P3-NNM by metal cation substitution and none that use Cu^{2+} to substitute for Ni^{2+}.

Biotemplating is an ideal synthesis method for complex systems that involve multiple and/or fractional species,[13] such as in P3-$Na_{2/3}Ni_{1/3-x}Cu_xMn_{2/3}O_2$. The aim of this work was to produce P3 cathode with various Cu concentrations of x = 0, 1/12, 1/6, 1/4 and 1/3 using dextran-biotemplating. Electrochemical tests on the stoichiometries that produced almost phase pure materials were conducted to determine the impact of Cu substitution had on phase transitions and cycle stability. In addition, cyclic voltammetry (CV) was conducted to determine the change in redox behaviour in the different samples.

4.2 Introduction

Recent studies have shown that P3-NNM undergoes P3-O3 phase transition upon charge to around 4.2 V,[1,2] similar to P2-NNM.[3,14] Although P2-NNM has obtained greater attention, similar avenues to improving electrochemical performance can be use on P3-NNM as a starting point. P2-NNM begins to undergo a P2-O2 phase transition causes large volume changes, leading to structural instability.[15] Also upon change to the O2 phase, NNM experiences slower Na^+ diffusion kinetics,[3] thus limiting rate capability. Many studies have focused on supressing this phase transition by substituting some Ni for other metals, such as Mg^{2+}, Cu^{2+}, Ti^{4+} and Fe^{3+}.[5,6,8,16,17] These cations are able to stabilise the P2 structure by ensuring higher concentration of Na remain in the structure at high voltages, that act as pillars between TMO_2 layers.[4,18] This is because they are either electrochemically inactive or extent of redox does not go as far as Ni^{2+}/Ni^{4+}, therefore less electrons are transferred. Although cycling stability is improved with the use of electrochemically inactive species, some capacity is lost in exchange.

However, in some cases, small concentrations are enough to supress the high voltage phase transitions, such as P2-$Na_{0.67}Ni_{0.33-x}Mg_xMn_{0.67}O_2$ with Mg content of x = 0.05.[5] Between 2.5 and 4.35 V at 0.1 C, the initial discharge capacity of P2-$Na_{0.67}Ni_{0.28}Mg_{0.05}Mn_{0.67}O_2$ (P2-NNMM) is around 120 mAh g^{-1} and after 50 cycles it is *ca.* 100 mAh g^{-1}. Whereas P2-$Na_{0.67}Ni_{0.33}Mn_{0.67}O_2$ (P2-NNM), initial discharge capacity is around 150 mAh g^{-1} and after 50 cycles it outputs around 70 mAh g^{-1}. Greater cycling stability is achieved with Mg content of x = 0.10, with capacity remaining around 100 mAh g^{-1} for at least 100 cycles. Another study cycled P2-$Na_{0.67}Ni_{0.23}Mg_{0.10}Mn_{0.67}O_2$ at an extended range of 2.0 – 4.5

V, where P2-NNM and P2-NNMM exhibit initial discharge capacities of 160 and 150 mAh g^{-1} and after 50 cycles it is around 75 and 125 mAh g^{-1} respectively.[19]

The benefit of substituting with electrochemical active cations is that in theory higher capacities can be obtained compared with materials containing redox inactive species. Examples include Cu^{2+}/Cu^{3+} and Fe^{3+}/Fe^{4+}.[20] When cycled between 2.6 and 4.3 V at 0.5 C, the initial discharge capacity of P2-$Na_{2/3}Fe_{2/9}Ni_{2/9}Mn_{5/9}O_2$ was 135 mAh g^{-1} and after 100 cycles it was 102 mAh g^{-1}.[16] Whereas in the same study, P2-NNM exhibited initial discharge 140 mAh g^{-1} and 58 mAh g^{-1} was retained after 100 cycles. P2-$Na_{0.67}Ni_{0.18}Cu_{0.15}Mn_{0.67}O_2$ was cycled between 2.0 and 4.3 V at 0.1 C and exhibited an initial discharge capacity of 120 mAh g^{-1} and after 200 cycles 100 mAh g^{-1} was observed, whereas P2-NNM exhibited 145 mAh g^{-1} and after 200 cycles only 24 % of the capacity was retained.[21]

Cation substitution in P3-NNM could be an effective method to supress the P3-O3 phase transition and improve cycle life. In this chapter, Cu^{2+} has been chosen to substituted for some Ni^{2+} in P3-NNM, due to its success in supressing the P2-O2 phase transition in P2-$Na_{0.67}Ni_{0.33-x}Cu_xMn_{0.67}O_2$, as well as being electrochemically active.[9,11,22,23] If degradation mechanisms and redox activities between P2- and P3-NNM are similar, it is hypothesised that Cu^{2+} in P3-NNM will improve the cycle stability. In this chapter, P3-$Na_{2/3}Ni_{1/3-x}Cu_xMn_{2/3}O_2$ with different Cu contents were synthesised using dextran-biotemplating method and electrochemical performance compared with P3-NNM.

4.3 Results & Discussion

4.3.1 Materials Characterisation

Specimens with Cu contents of x = 0, 1/12, 1/6, 1/4 and 1/3 in P3-$Na_{2/3}Ni_{1/3-x}Cu_xMn_{2/3}O_2$ were synthesised using dextran-biotemplating method, calcined at 650 °C for 2 h in air. The XRD patterns for the specimens are shown in figure 4.1. The main Bragg reflections for x = 0 were indexed to P3-NNM and NiO as the secondary phase, as found in Chapter 3. For x = 1/12, ($Na_{2/3}Ni_{1/4}Cu_{1/12}Mn_{2/3}O_2$), the main phase was indexed to the same P3-NNM phase. There were also additional small peaks, indexed to NiO and CuO. In x = 1/6 ($Na_{2/3}Ni_{1/6}Cu_{1/6}Mn_{2/3}O_2$), the peak intensities for CuO phase were greater and NiO was negligible compared to specimen x = 1/12. In specimens x = 1/4 ($Na_{2/3}Ni_{1/12}Cu_{1/4}Mn_{2/3}O_2$) and 1/3 ($Na_{2/3}Cu_{1/3}Mn_{2/3}O_2$), the CuO Bragg reflections continued to increase in intensity. There were peaks that could be indexed to P3-NNM in these two specimens. However the peaks for the P3-NNM phase were wider for specimen x = 1/4 and in x = 1/3 because of the apparent peak splitting in some of the reflections. The additional peaks in x = 1/3 and x = 1/4 were located at lower angles next to all P3-NNM peaks. However, there was no peak splitting in the peaks associated with the 00*l* plane. The peak at 45 °2θ for specimen x = 1/6 also appears to have a shoulder at slightly lower angle, similarly to the high Cu content specimens. There could be two layered structures with similar values for the *c*-axis present in these specimens. But it is clear that the solid solution limit of Cu is slightly below 1/6 under current synthesis conditions. Identification in terms of approximate stoichiometry of these layered structures may be possible using high resolution Transmission Electron Microscopy (TEM) and Energy Dispersive X-Ray Spectroscopy (EDS), however this goes beyond the scope of this thesis.

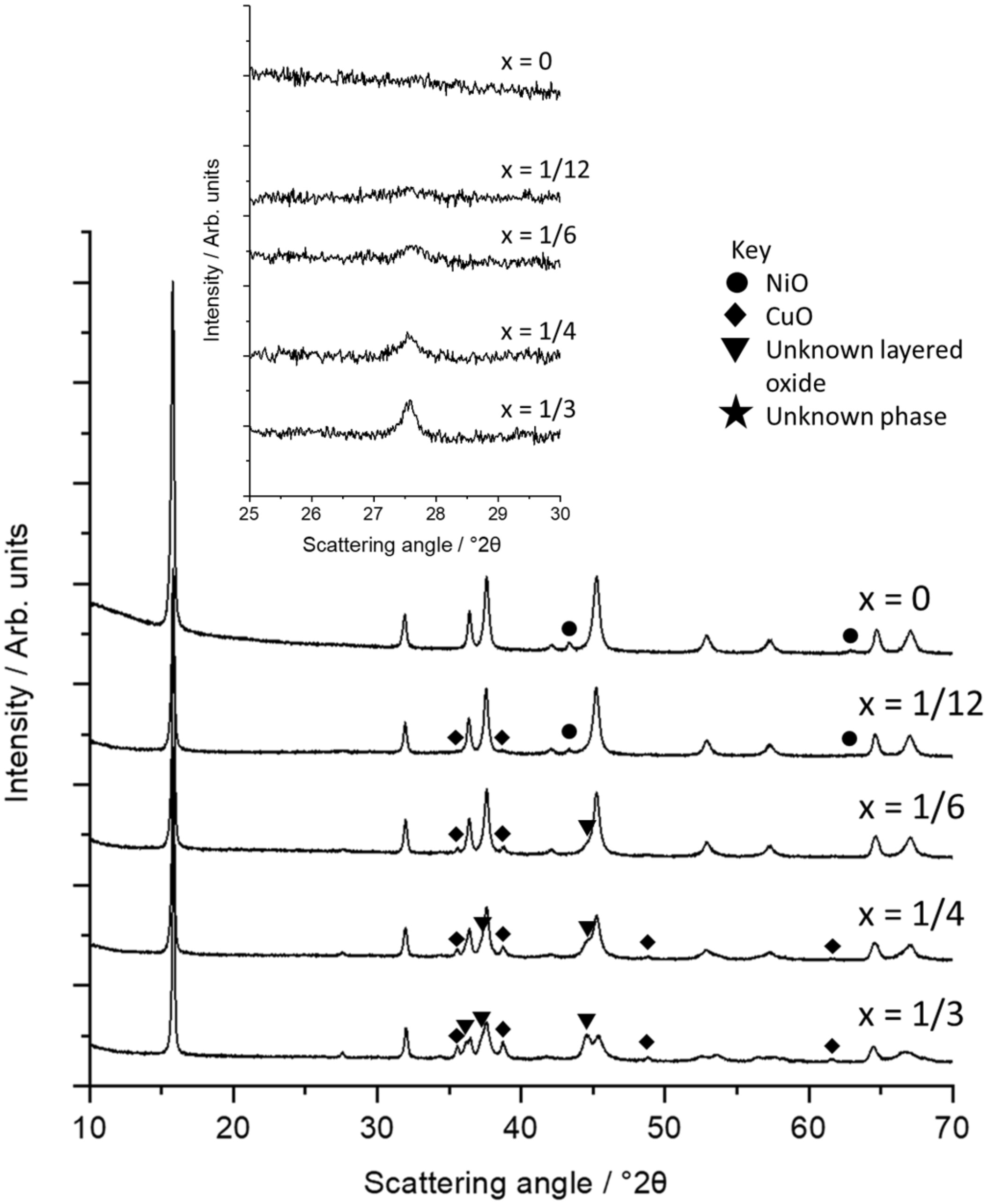

Figure 4.1: *XRD patterns of dextran biotemplated a* $Na_{2/3}Ni_{1/3-x}Cu_xMn_{2/3}O_2$ *calcined at 650 °C dwelled at 2h, with an inset showing a magnified region between 25 and 30 °2θ. Unlabelled peaks are attributed to P3 phase.*

Rietveld refinement was conducted on the specimens against a NIST silicon 640f standard to obtain lattice parameters, figure 4.2. There are no error bars in the figure because Rietveld refinement was conducted on one batch, unlike in chapter 3 where the lattice parameters of P3-NNM were from an average of 3 batches. The estimated standard deviation from Highscore software, is very small (on the 4th decimal place), which means that small changes will cause the R_{wp} to change. To obtain uncertainties, refinements need to be conducted on multiple batches for future work.

As Cu content increases, both the *a*- and *c*-axis show small increases, as expected as Cu^{2+} has a slightly larger ionic radius of 0.73 Å compared to Ni^{2+} with 0.69 Å.[24] However for specimen x = 1/4, the *c*-axis drops to 16.825 Å, similar values as P3-NNM (x = 0, 16.824 Å). The broadening and splitting of Bragg reflections may be due to phase separation, forming different layered structures with similar values in *c*-axis. Thus remaining layered structures are likely to have a lower concentration of Cu, hence lower value for the *c*-axis compared to x = 1/6.

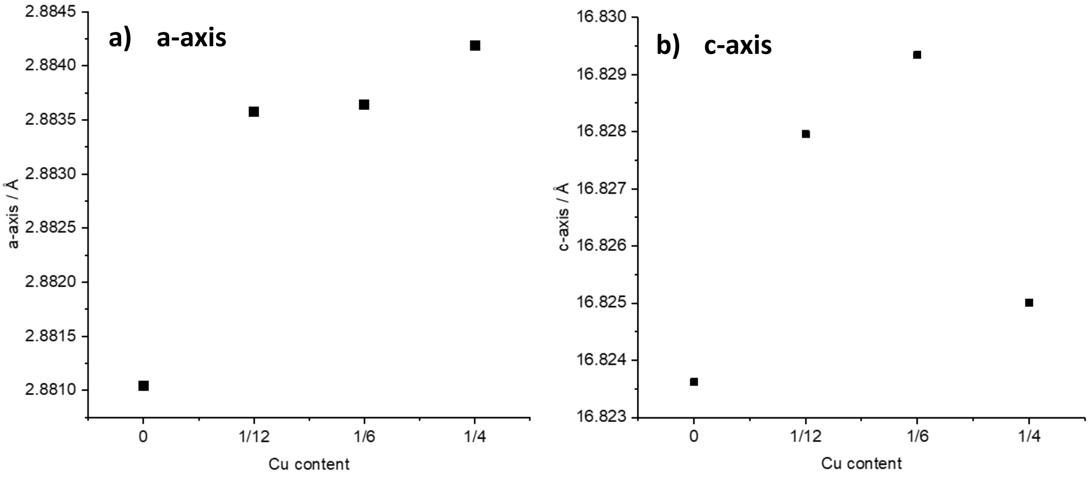

Figure 4.2: *a) a-axis and b) c-axis for* $Na_{2/3}Ni_{1/3-x}Cu_xMn_{2/3}O_2$ *obtained by Rietveld refinement and compared against a NIST silicon 640f standard.*

Rietveld refinement plots for specimens x = 0, 1/12 and 1/6 with NIST 640f silicon standard reference material are shown in figure 4.3. The difference plot shown in blue, indicated a decent fit for all specimens, however they were similar which may be due to systematic error in the fit. The fit for peak intensities are not ideal, at least below 50 °2θ.

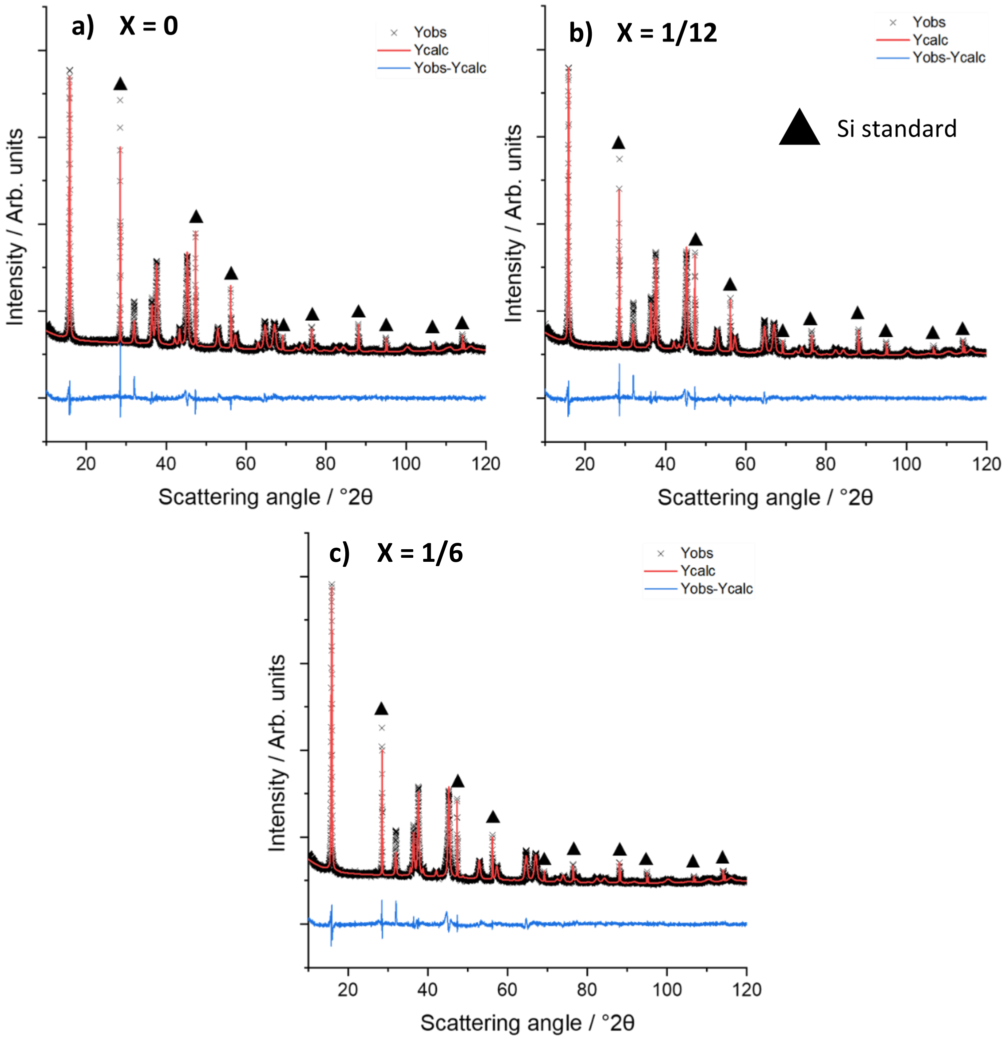

Figure 4.3: *Observed and calculated XRD patterns from Rietveld refinement of a) P3-$Na_{2/3}Ni_{1/3}Mn_{2/3}O_2$, x = 0, b) P3-$Na_{2/3}Ni_{1/4}Cu_{1/12}Mn_{2/3}O_2$, x = 1/12 and c) P3-$Na_{2/3}Ni_{1/6}Cu_{1/6}Mn_{2/3}O_2$, x = 1/6 synthesised at 650 °C with NIST Si 640f standard. Si standard labelled with black triangles. The remaining peaks are the same as those labelled in figure 4.1*

Table 4.1 summaries the values for the refined parameters. The values for the B_{iso} for cation site 1 (Mn, Ni and Cu) did not shift far from the initial 0.5 value, which could mean the values are not reliable. Similarly, in chapter 3, there were difficulties refining the occupancies, as all three cations have similar atomic numbers and therefore would have similar scattering factors. Hence they were fixed during refinement, including the remaining atomic sites. This may be why some peak intensities appeared to have a relatively large difference between observed and calculated data because peak intensities are affected by such parameters. The B_{iso}s for cation site 2 for all specimens appeared to be quite high, however reasonable for a light element. Whereas the B_{iso} both oxygen sites are quite low, which may indicate a problem with the fit. The z atomic positions were refined apart from cationic site 1, containing Mn, Ni and Cu, as they were located in a special position. The z atomic positions for cationic site 2 and oxygen site 1 did not change significantly between the different specimens. The oxygen site 2 for x = 1/12 and 1/6 appeared to shift, however they are equivalent coordinates.

It is clear that values for occupancies and thermal parameters are not reliable. There may also be a small error for the phase fractions, as peak height is impacted by occupancy, type of atom and thermal parameter. Although, the difference plot shows a systematic error in the fits, so errors are likely to be similar for all the specimens, which means that relative comparisons between the specimens can be made. However, the difference plot is significantly small compared to the intensities of the diffraction pattern, which could mean the error on phase fractions is not significant. The lattice parameters have a high degree of certainty due to the addition of Si standard. Regardless, the values for R_{wp} and χ were below 3.4 and 1.9 which indicated a good fit for all specimens. Errors from Highscore are not included in the refinable parameters in table 4.1, because it is the estimated standard deviation and are very small.

Specimen x = 0 contained 4.8 wt.% of NiO, similar value as to what was reported in chapter 3. Once scaled up to the quantities of precursors used in chapter 3, for 1 g P3-NNM, the amount of dextran used was essentially 3.2 g hence the mass ratio was 1 : 3.2. The amount of NiO produced in this specimen is in line with figure 3.4 in chapter 3 when 3.2 g of dextran used. Specimen x = 1/12 contained 1.39 wt.% NiO and 0.46 wt.% CuO and x = 1/6 contained 0.11 wt.% NiO and 1.69 wt.% Cu.

***Table 4.1**: Structural refinement parameters for P3-$Na_{2/3}Ni_{1/3-x}Cu_xMn_{2/3}O_2$ x = 0, 1/12 & 16 calcained at 650 °C for 2 h. XRD data collected under ambient conditions. Initial values for B_{iso} were set to 0.5 Å.*

Parameter	**Value**		
Sample	x = 0	x = 1/12	x = 1/6
Structural formula	$Na_{2/3}Ni_{1/3}Mn_{2/3}O_2$	$Na_{2/3}Ni_{1/4}Cu_{1/12}Mn_{2/3}O_2$	$Na_{2/3}Ni_{1/6}Cu_{1/6}Mn_{2/3}O_2$
Space group	$R3m$	$R3m$	$R3m$
a/Å	2.881	2.883	2.884
c/Å	16.823	16.827	16.829
R_{wp}/%	2.94	3.08	3.31
R_{ep}/%	1.78	1.85	1.88
Goodness of fit /χ	1.65	1.67	1.76
NiO / wt.%	4.8	1.39	0.11
CuO / wt.%	-	0.46	1.69
Cation site 1			
X(=y=z)	0	0	0
Site occupancy	0.667 Mn, 0.333 Ni	0.667 Mn, 0.250 Ni, 0.083 Cu	0.667 Mn, 0.167 Ni, 0.166 Cu
B_{iso}/Å^2	0.5	0.500	0.505
Cation site 2			
X(=y)	0	0	0
z	0.1667	0.169	0.168
Site occupancy	0.667 Na	0.667 Na	0.667 Na
B_{iso}/Å^2	2.061	2.699	2.731
Oxygen site 1			
X(=y)	0	0	0
z	0.399	0.393	0.392
Site occupancy	1	1	1
B_{iso}/Å^2	0.258	0.355	0.377
Oxygen site 2			
X(=y)	0	0	0
z	0.607	-0.394	-0.394
Site occupancy	1	1	1
B_{iso}/Å^2	0	0.247	0.164

In-situ HT-XRD was conducted on some of the Cu containing P3 materials to gain a better understanding of phase progression that eventually lead to the XRD patterns in figure 4.1. Prior to *in-situ* HT-XRD the amorphous cation-dextran complex was calcined at 300 °C to remove the biotemplate to prevent expansion of the specimen during measurements. Figure 4.4 shows the XRD patterns of the specimens x = 1/6 and 1/3 calcined at 300 °C. Specimen x = 1/6 contained Bragg reflections that are similar P3-NNM, as seen in x = 0 in Chapter 3. Other significant phases present in this specimen at this temperature were CuO and NiO. Specimen x = 1/3 exhibited a small peak around 15.6 °2θ, which is normally associated with (00L) plane, perpendicular to the *c*-axis in layered oxides. It is normally the strongest because it corresponds to the interlayer spacing. This peak, however was significantly smaller in intensity compared to x = 1/6. Regardless, there was no obvious indication that the P3-type structure had formed in x = 1/3. Other phases in x = 1/3 included Mn_3O_4, CuO and Cu at 300 °C.

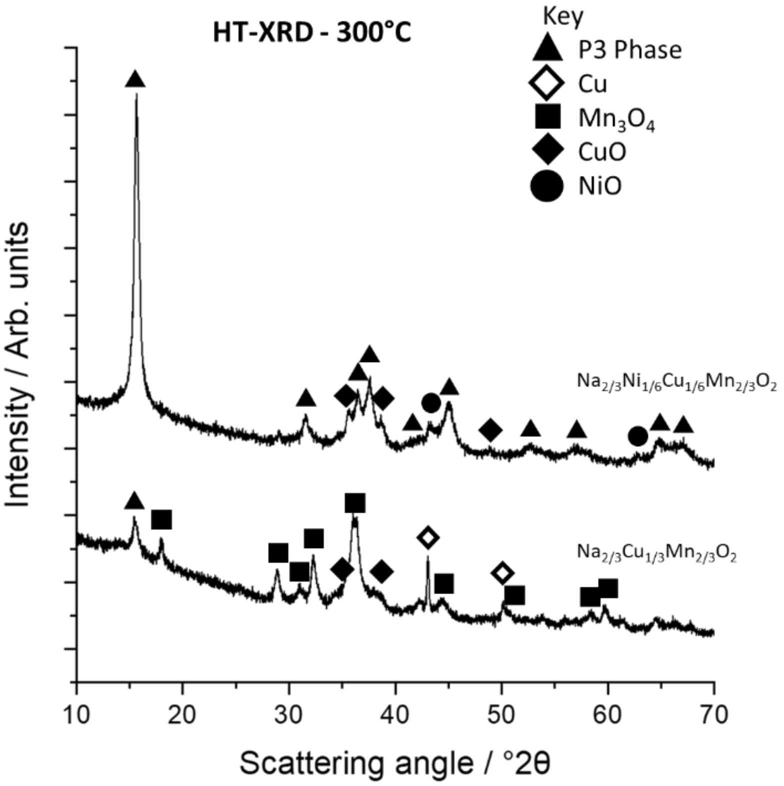

Figure 4.4: *HT-XRD pattens of P3-*$Na_{2/3}Ni_{1/3-x}Cu_xMn_{2/3}O_2$ *with x = 1/6 and 1/3 heated to 300 °C. Specimens were pre-calcined to 300 °C for 30 minutes to remove most of the biotemplate before the experiment.*

In-situ HT-XRD of x = 1/3, figure 4.5a, at 300 °C, as mentioned earlier, exhibited Bragg reflections mostly from Mn_3O_4, CuO and Cu. At 400 °C, peaks that were indexed to Mn_3O_4 were negligible and Cu disappeared as the Cu oxidised to CuO. Peaks indexed to P3 structure were more apparent at 400 °C and the peak intensities for this phase increased with temperature, indication of increased crystallinity and particle growth. At 800 °C, crystallisation of the P2 phase began and at the same time peak intensities for the P3 phase decreased in intensity, indication of a temperature driven P3-P2 phase transition. The peaks that are not labelled in figure 4.5 are common to both P2 and P3 phases, for example the 00l peaks; the strong overlap suggests very similar interlayer spacing. At 850 °C, there were no longer Bragg reflections from the P3 phase and the P2 structure was the prominent phase along with small amounts of CuO. As the temperature is held at 850 °C for two hours the XRD patterns did not show any significant difference with increased dwell time.

At 300 °C, *in-situ* HT-XRD for specimen x = 1/6 showed that crystallisation of the P3-type structure was already well underway, Figure 4.5b. As the temperature increased, peak intensities for the P3 phase continued to grow whereas peak intensities for NiO and CuO appeared to decrease due to decomposition. As discussed in chapter 3, with a sufficient amount of biotemplate, intermediate phases are kept small as growth is constrained by dextran. This aids the nucleation and rapid growth of the P3 structure. The P3 phase persisted to 850 °C, whereas in x = 1/3, by this temperature the P3 phase was no longer present. At this temperature crystallisation of the P2-type structure also began, 50 °C higher compared to x = 1/3. After 1 h at 850 °C, the P3 phase was no longer present, with only P2-type structure as the dominant phase and small amounts of CuO remained.

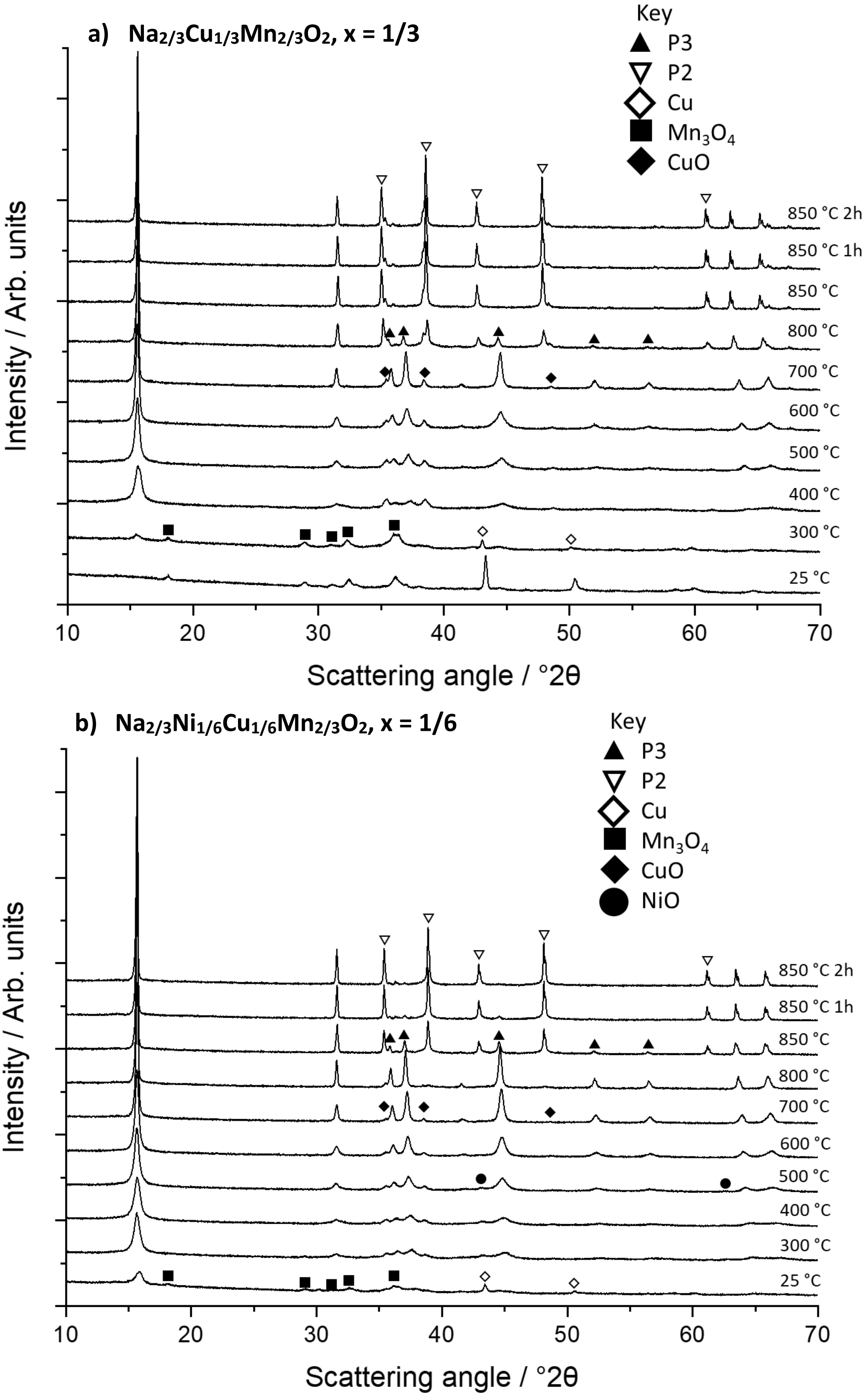

Figure 4.5: *HT-XRD pattens of P3-$Na_{2/3}Ni_{1/3-x}Cu_xMn_{2/3}O_2$ with a) x = 1/3 and b) x = 1/6. Specimens were pre-calcined to 300 °C to remove most of the biotemplate before the experiment. Unlabelled peaks are common to both P2 and P3 phases.*

Figure 4.6 shows the in-situ HT-XRD data to highlight the difference in phase progression between specimens x = 1/3 and 1/6. The P3-type structure persisted to a higher temperature in x = 1/6, potentially due to greater crystallinity and particle size as it was able to crystallise much earlier than in x = 1/3. It is worth noting that in-situ HT-XRD patterns did not exhibit the same peak splitting as seen in figure 4.1 for x = 1/3. The conditions during HT-XRD were not the same as regular synthesis in the muffle furnace; specimens for in-situ HT-XRD were calcined to 300 °C prior to the experiment, specimen size was significantly smaller for XRD experiments, so reactions were likely to occur faster and easily and the heating rate was significantly faster. The resolution may also be compromised as scans have to be conducted quickly so that the specimen does not dwell at the temperatures for too long. With a low resolution, peak splitting may be difficult to see. The peaks for the P3-type structure appeared to be fairly broad below 600 °C for both specimens which could either be due to crystallite size or peak overlap, hence peak splitting is not visible in figure 4.6. In-situ HT-XRD may not be an accurate representation of what occurs in the furnace but gives a good insight into the phase progression.

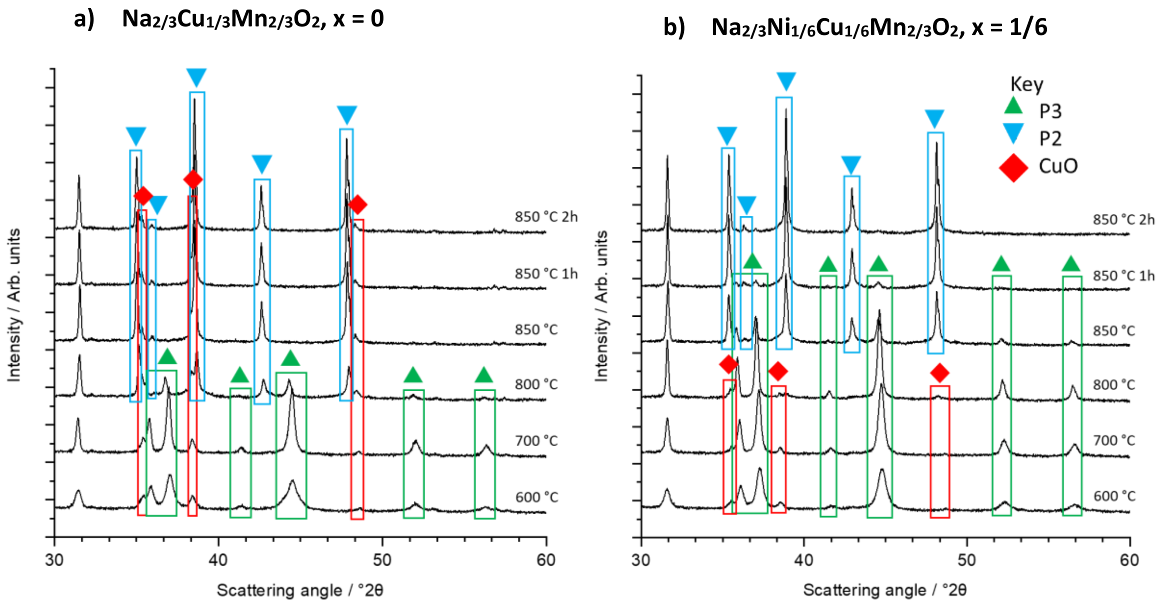

a) $Na_{2/3}Cu_{1/3}Mn_{2/3}O_2$, x = 0

b) $Na_{2/3}Ni_{1/6}Cu_{1/6}Mn_{2/3}O_2$, x = 1/6

Figure 4.6: *HT-XRD pattens of P3-$Na_{2/3}Ni_{1/3-x}Cu_xMn_{2/3}O_2$ with a) x = 1/3 and b) x = 1/6. Specimens were pre-calcined to 300 °C to remove most of the biotemplate before the experiment. Unlabelled peaks are common to both P2 and P3 phases.*

From figure 4.6, it is clear that the amount of Cu affected the rate at which the P3 structure crystallised and the P3-P2 phase transition. This is likely associated with the solid solution limit of Cu in the P3 phase. However further work is needed to determine this.

4.3.2 Electrochemistry

4.3.2.1 Cyclic voltammetry of P3-NNCM with different Cu concentrations

Cyclic voltammetry was conducted on specimens x = 1/6 and 1/12 between 2.0 and 4.5 V at a scan rate of 0.1 mV s^{-1}, figure 4.7. Both exhibited peaks below 2.5 V that can be attributed to Mn^{3+}/Mn^{4+} redox couple.[25–27] For the 2nd cycle, similar to P3-NNM (x = 0), the redox pair at anodic/cathodic voltages of 4.3/4.0 V is likely due to oxygen redox,[1,16,28,29] and Ni redox caused the peaks at anodic/cathodic voltages around 3.3/3.1, 3.4/3.2 and 3.7/3.4 V.[25,30] Specimens x = 1/6 and 1/12 exhibit an additional redox pair located at 4.0/3.6 V due to Cu^{2+}/Cu^{3+} redox.[9,31,32] On the 2nd cycle, specimen x = 1/6 had an additional cathodic peak located at 3.8 V, figure 4.7a and 4.7c, with no obvious corresponding anodic peak. However the anodic peak at 4.3 V was rather broad compared to specimen = 0, so there could be two overlapping peaks. This additional redox pair could be due anionic redox at different potential due to the different oxygen environment adjacent to Cu. Two set of oxygen redox peaks have been found in other materials that have two different lattice oxygen environments.[33,34] This additional redox pair was not as obvious in x = 1/12, figure 4.7b, although there was a small broad cathodic peak at 3.8 V in the 2nd cycle.

The CV curves changed for all specimens after the 5th and 10th cycle. Figure 4.7a shows the CV curves for the 2nd, 5th and 10th cycle for specimen x = 1/6. The cathodic peak at 4.0 V, shifted to 3.8 V from the 2nd to the 5th cycle, increasing the potential difference from the anodic peak, associated with increased polarisation and resistance. This may be due irreversible anionic oxidation, where oxygen evolution can cause formation of a dense layer on the particle surface that lead to increased sluggish Na^+ diffusion kinetics, as found in P2-NNM.[16] Alternatively, if this redox couple overlaps voltages at which the P3-O3 phase transition occurs, the greater polarisation could be due to slower Na^+ diffusion kinetics in the O3 phase.[3] The cathodic peaks for Ni reduction shifted to higher voltage from the 2nd to the 5th cycle, reducing the potential difference between oxidation and reduction. Similar trend most likely occurred with the Cu cathodic peak at 3.6 V in the 2nd cycle, but the lack of peak in the 5th cycle is due to the overlap with the large peak at 3.8 V from anionic reduction that shifted to the lower voltage.

Figure 4.7b shows the CV curves for x = 1/12 for the 2nd, 5th and 10th cycles. The peak intensities for Ni redox are significantly higher than Cu redox compared to x = 1/6. The cathodic peak for Cu reduction around 3.7 V appeared broader compared to 1/6 for the 2nd cycle. There was another small cathodic peak at 3.8 V potentially from oxygen reduction due to Cu environment, as seen in x = 1/6. After the 5th cycle, these peaks were no longer visible, due to similar trends in peak shift as in x = 1/6. Therefore the broad peak at 3.9 V encompasses the Cu and the two oxygen reduction reactions.

Although both x = 1/6 and 1/12 exhibited significant difference in the CV curves between the 2nd and 5th cycle, after the 5th cycle this appeared to stabilise as there was very little changes compared to the 10th cycle. Figure 7.4c compares the 2nd cycle for specimens x = 0, 1/12 and 1/6. The redox pair at 4.3/4.0 V in x = 0 was significantly higher in intensity compared to x = 1/12 and 1/6. Since area under the CV curves is proportional to capacity, equation 3.1, it appeared that Cu substitution reduced the capacity contribution from this redox pair. The redox peaks associated with Ni redox decreased in intensity with increasing Cu content and shifted to slightly higher voltages. Shift in Ni redox potentials upon Cu substitution had also been found in other studies.[9] Figure 7.4d shows the CV curves for the three specimens after the 10th cycle. All peaks for all specimens decreased in intensity compared to the 2nd cycle due to irreversible reactions. However the anodic/cathodic peaks for anionic redox in specimens x = 1/6 and 1/12 had higher intensities compared to x = 0, contrary to the 2nd cycle.

It is apparent that Cu affected anionic redox, associated with high voltage redox peaks. In the literature, anionic oxidation to O_2, causes gas evolution making it irreversible and hence reduction in cycle life was observed in P2-NNM.[16] Fe substitution in P2-NNM prevented irreversible oxygen redox through a reductive coupling mechanism.[16] When charged to 4.15 V, Fe^{3+} is oxidised and anionic oxidation O^{2-} to O_2^{n-} occurs and after 4.3 V it is reduced back to Fe^{3+}, maintaining O_2^{n-}. This is enabled by a high covalent Fe-(O-O) bonding state that allows charge transfer from O to Fe. Cu substitution has found to prevent over oxidation of the anionic species in P2-$Na_{0.73}Li_{0.21}Mn_{0.74}Cu_{0.05}O_2$, when cycling beyond 4.2 V which was attributed to the strong covalency between Cu and oxygen, where electrons were more localised around Cu^{3+} due to the d^8 configuration, stabilising the oxygen framework.[10]

If the extent to which oxygen redox is weakened, then the capacity contribution would be reduced. This could be why the peak intensities and areas for the 4.3/4.0 V redox pair were smaller for specimens x = 1/12 and 1/6 compared to x = 0, as seen in the 2nd cycle. In addition, there was very little change between the 5th and the 10th cycle for these sets of peaks for the Cu containing specimens, indication this redox reaction has somewhat stabilised, potentially due to reversible O^{2-}/O_2^{n-} redox reaction. Whereas in P3-NNM, it is likely the full extent of anion oxidation occurred, with the irreversible $O^{2-}/O_2^{n-}/O_2$ redox reaction, hence the redox pair at 4.3/4.0 V degraded rapidly after 10 cycles, figure 7.4d.

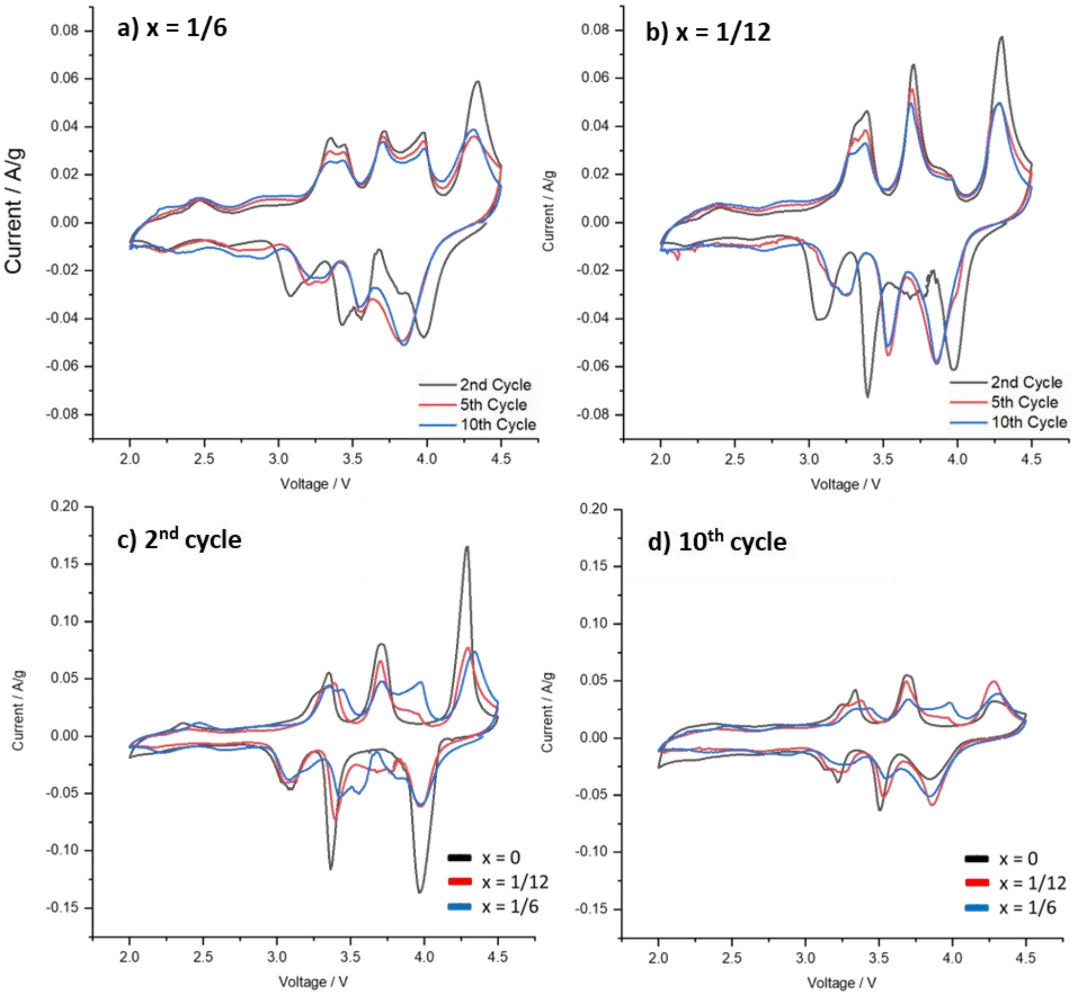

***Figure 4.7**: Cyclic voltammogram of specimen with a Cu content of a) x = 1/6 and b) x= 1/12 showing the 2nd, 5th and 10th cycle. Specimens prepared with different Cu content of x = 0, 1/6 and 1/12 are compared during the c) 2nd cycle and d) 10th cycle. Data was collected between 2.0 and 4.5 V at a scan rate of 0.1 mV s^{-1}.*

When cycled at an extended voltage range of 1.5 - 4.5 V, both specimens x = 1/6 and x = 1/12, figure 4.8a and 4.8b respectively, exhibit an additional redox couple at anodic/cathodic peaks *ca.* 2.3/1.7 V, which can be attributed to Mn^{3+}/Mn^{4+}.[8,35] The rest of the CV curves above 2.0 V was the same as in figure 4.7. The 2.3/1.7 V redox pair exhibited the greatest potential difference, which may be due to the Jahn-Teller active Mn^{3+}, distorting the structure which can have an impact on the Na^+ diffusion kinetics,[36] possibly leading to increased polarisation. However, after the 5th cycle, the cathodic peak shifted from 1.7 to 1.9 V, decreasing the potential difference.

Cu may also have an impact on Mn redox, as specimen x = 1/6 appeared to have better stability in the lower voltage region. The anodic peak at 2.3 V did not change much in x = 1/6 from the 2nd to the 10th cycle, as well as its corresponding cathodic peak after the 5th cycle. Specimen x = 1/12 appeared to have slightly greater change in peak shape from the 2nd and 10th cycle. In the literature it has been found that Cu can impede on the formation of Mn^{3+} during cycling, which would reduce Jahn-Teller distortion and Mn^{2+} dissolution to electrolyte.[10] This may be why the peak area for this redox couple appeared slightly smaller for = 1/6 compared to x = 1/12, figure 4.8c. Figure 4.8d compares the 10th cycle for both specimens, where x = 1/6 had greater capacity contribution from Mn oxidation, as it had a greater peak area.

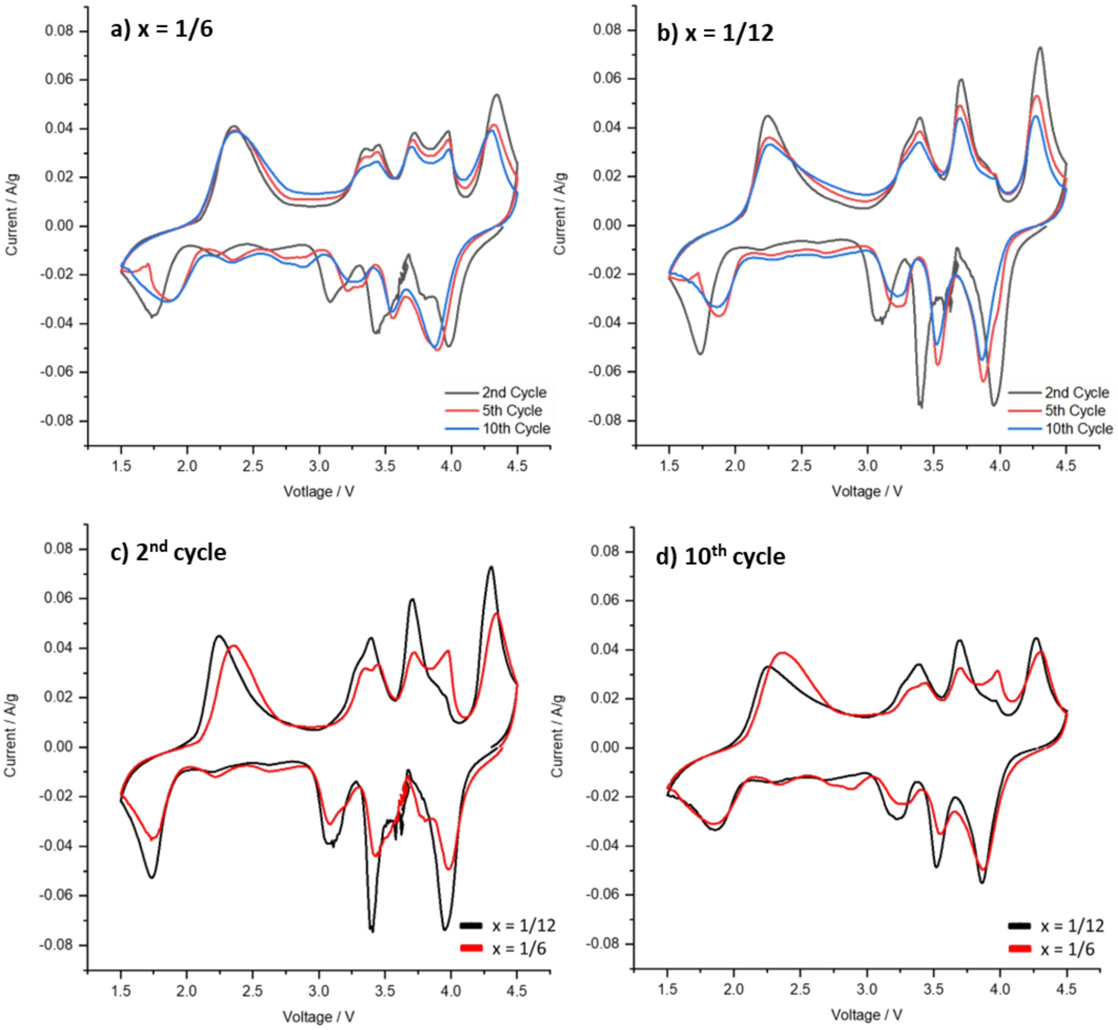

Figure 4.8: *Cyclic voltammogram of specimen with a Cu content of a) x = 1/6 and b) x= 1/12 showing the 2nd, 5th and 10th cycle. Specimens prepared with different Cu content of x = 1/6 and 1/12 are compared during the c) 2nd cycle and d) 10th cycle. Data was collected between 1.5 and 4.5 V at a scan rate of 0.1 mV s^{-1}.*

4.3.2.2 Galvanostatic cycling

Figures 4.9 and 4.10 show the electrochemical performance of specimens x = 0, 1/12 and 1/6 where there are a minimum of two cells for each cycling regime to show reproducibility. The variations are likely due to differences in the cathodes such as thickness or cell assembly and ambient conditions in which most of the measurements were conducted in, rather than intrinsic properties of the active material.

Specimens x = 0, 1/12 and 1/6 were cycled at 0.1 C between 2.0 and 4.5 V, figure 4.9a, and 2.0 – 4.2 V, figure 4.9b. At 2.0 - 4.5 V, increasing Cu concentration improved the cycling stability, but at the expense of initial discharge capacity. As there are multiple cells for each cycling regime, the median cell will be referred to in the text.

Specimens x = 0, 1/12 and 1/6 when cycled between 2.0 and 4.5 V exhibited initial discharge capacities of 135, 130 and 125 mAh g^{-1} and after 50 cycles discharge capacities were 71, 81 and 97 mAh g^{-1} respectively, figure 4.9a. After 50 cycles, x = 1/6 had the best capacity retention of 77.6 %. The lower initial capacity as Cu concentration increased is due fewer electrons transferred in Cu^{2+}/Cu^{3+} redox compared to Ni^{2+}/Ni^{4+},[11] as it is difficult to further oxidise Cu^{3+}, therefore more Na remained in the structure. With greater Na content in the layered structure at higher voltages, the P3 structure was most likely stabilised at higher voltages, as found in P2-type materials.[11]

Figure 4.9b shows the cycling performance at 2.0 – 4.2 V at 0.1 C for specimens x = 0, 1/12 and 1/6 with initial discharge capacities are 112, 80 and 78 mAh g^{-1}, and after 50 cycles the capacities were 72, 75 and 73 mAh g^{-1} respectively. P3-NNM (x = 0) had a capacity retention of 64% after 50 cycles, however most of the capacity degradation was observed in the first ten cycles. Specimens x = 1/6 and 1/12 had similar retention rates of 94 %.

Figure 9.4c shows the cycling data at an extended voltage range of 1.5-4.5 V at 0.1 C. Initial discharge capacities for x = 0, 1/12 and 1/6 were 210, 177 and 154 mAh g^{-1} and after 50 cycles it is 86, 86 and 90 mAh g^{-1} with retention rates of 41, 49 and 58 % respectively. Specimen x = 1/6 had better cycling stability in this voltage range, especially for the first 10 cycles as capacity did not drop significantly. After this, there was a gradual decline. Degradation in x = 1/6 may not be as severe due to lack of the P3-O3 phase transition after charging to 4.2 V, reversible oxygen redox and less Mn^{3+} forming at lower voltages.[10]

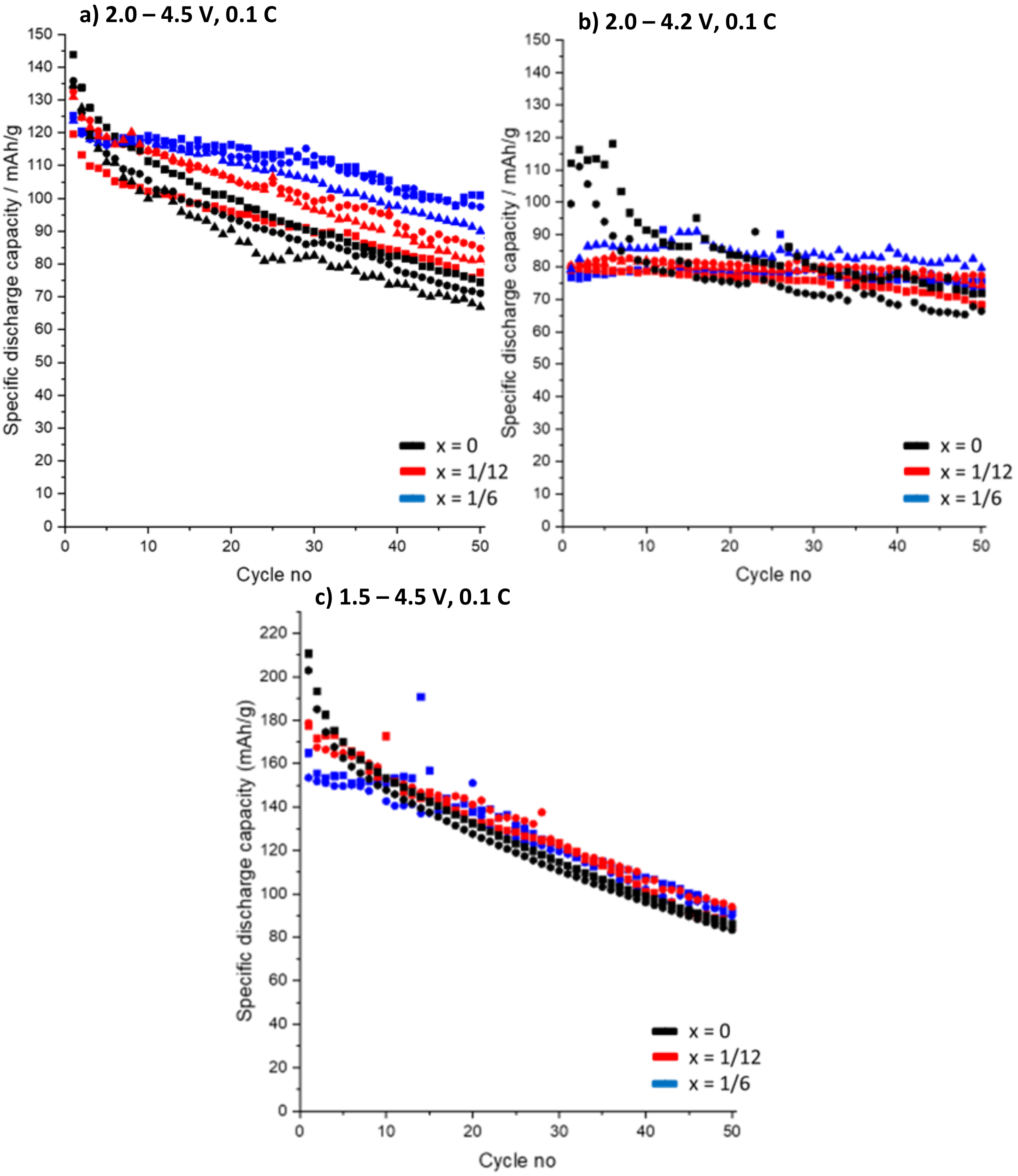

Figure 4.9: *Specific discharge capacities versus cycle number for specimens with Cu content of x = 0 (black), 1/12 (red) and 1/6 (blue), cycled at 0.1 C in the voltage ranges of a) 2.0 – 4.5 V, b) 2.0 – 4.2 V and c) 1.5 – 4.5 V. Each cycle regime had a minimum of two repeats; cell 1, 2 and 3 of each specimen for each voltage range are denoted with square, circle and triangle data points.*

The specimens were also cycled at a faster rate of 1 C at 2.0 - 4.5 V, figure 4.10a. x = 0 (P3-NNM) exhibited an initial discharge capacity of 130 mAh g^{-1}, dropped quickly after 20 cycles and capacity continued to fall at a relatively fast rate. After 200 cycles, the discharge capacity was only 23 mAh g^{-1}. Specimens x = 1/12 and 1/6 exhibited initial discharge capacities of 121 and 95 mAh g^{-1} respectively. X = 1/6 had fairly good cycle stability for the first 20 cycles, dropped only to 88 mAh g^{-1}, before the rapid decline in capacity. Similar trend was seen in x = 1/12. Cu improved the cycle stability at fast cycling rates, but only for a small number of cycles. Hence, these materials may not be suitable for applications that require fast charging for many successive cycles.

Figure 4.10b shows the results of galvanostatic cycling between 2.0 and 4.2 V at 1 C. All specimens appeared to have slightly better cycling stability compared to when cycled to 4.5 V, figure 4.10a. The median performing cells for specimens x = 0, 1/12 and 1/6 had initial discharge capacities of 68, 72 and 67 mAh g^{-1} and after 200 cycles it is 39, 50 and 37 mAh g^{-1} respectively. x = 1/12 had the best performance under this cycling regime. This could be due to lack of phase transition, slight increase in the *c*-axis that may improve Na^+ mobility and greater concentration of $Ni^{2+}/Ni^{3+}/Ni^{4+}$.

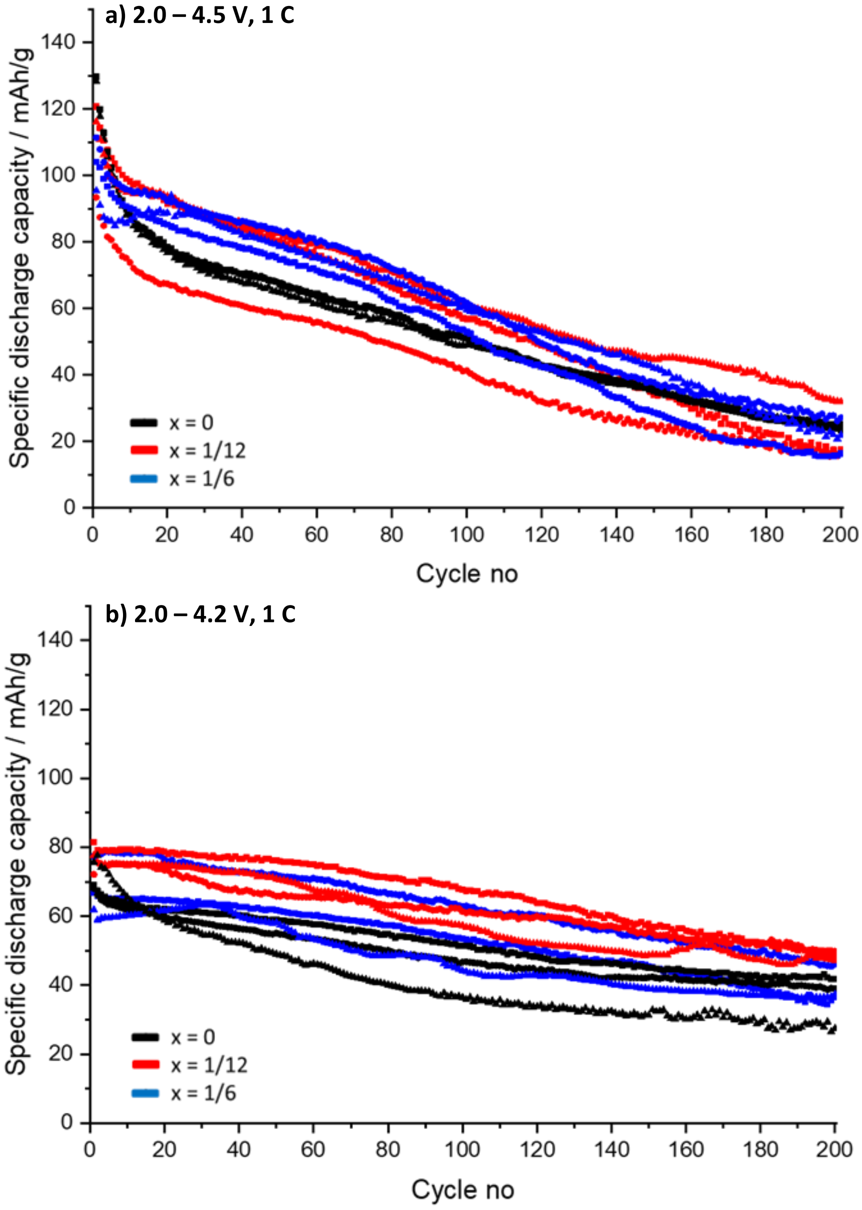

Figure 4.10: *Specific discharge capacities versus cycle number for specimens prepared with x = 0 (black), 1/12 (red) and 1/6 (blue) Cu, cycled at 1 C in the voltage ranges of a) 2.0 – 4.5 V and b) 2.0 – 4.2 V. Each cycle regime had a minimum of two repeats; cell 1, 2 and 3 of each specimen for each voltage range are denoted with square, circle and triangle data points.*

Figure 4.11a shows the voltage profiles for x = 1/6, which gradually smoothened on later cycles. Figure 4.11b shows the voltage profiles x = 1/12, with more prominent plateaus compared to x = 1/6. Figure 4.11c compares the voltage profiles between x = 0, 1/12 and 1/6 for the 1st cycle where both have plateaus at 3.3, 3.6 and 4.2 V on charge and on discharge at 3.1, 3.5 and 4.1 V. The plateaus below 4.0 V can be associated with Na^+/vacancy ordering,[9] and above 4.0 V is likely due to P3-O3 phase transition.[37] In P3-NNM, Na prefers to occupy the positions around Ni atoms, often leaving the positions around Mn unoccupied.[38] Studies have found, regardless of polymorph (P2 and P3), the transition metals in $Na_{2/3}Ni_{1/3}Mn_{2/3}O_2$ exhibited highly ordered sequence in the TM layers which affects the ordering of Na atoms in the structure,[38–40] causing multiple plateaus in P3-NNM. Figure 4.11d compares the voltages curves for x = 0, 1/12 and 1/6 after 20 cycles. Specimen x = 0 still had very prominent plateaus after the 20th cycle, however compared to the 1st cycle, they were not as severe. Although the plateaus are not as prominent for x = 1/12 and 1/6 compared to x = 0, they also experienced some plateau degradation after 20 cycles.

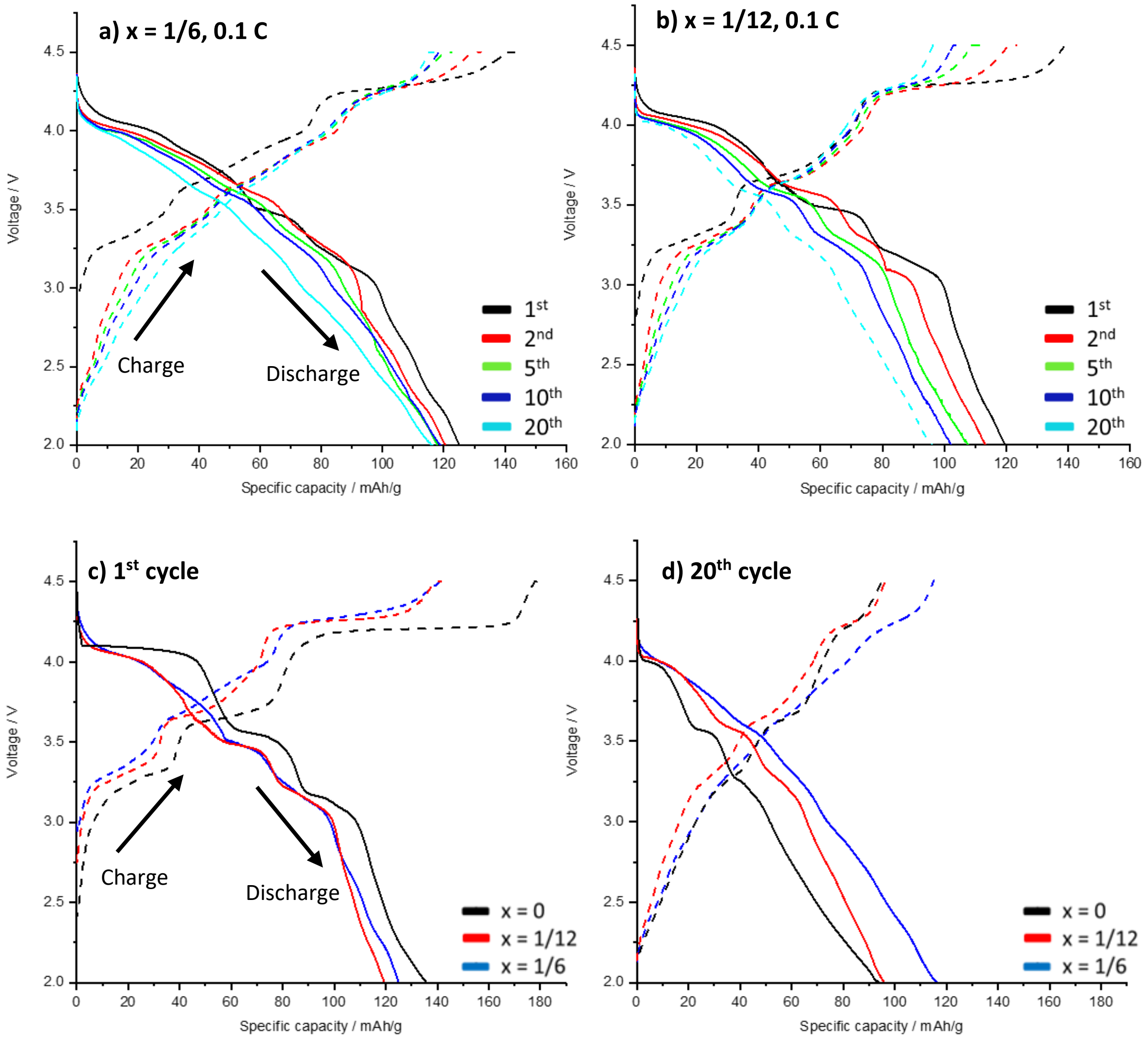

Figure 4.11: *Voltage profiles for 1st, 2nd, 5th, 10th and 20th cycles of specimens containing a) x = 1/6 and b) x = 1/12, cycled between 2.0 and 4.5 V at 0.1 C. Voltage profiles of specimens x = 0, 1/12 and 1/6 during the c) 1st and d) 20th cycle.*

The voltage curves were smoother with increasing Cu concentration, however plateaus were still visible. A smoother voltage curves generally indicates a solid solution transitions upon Na (de-)intercalation where Na^+/vacancy ordering and structural changes are supressed.[39–41] Such structural changes can have a negative impact on electrochemical properties, inducing slow kinetics limiting the rate capability of the material.[42]

Substituting in other metals like Mg, Fe, Al and Zn into materials such as P2-NNM normally smooths out the voltage profiles which improves cycle stability and rate capability.[5,6,8] There are a number of studies on Cu substitution in P2-NNM and it has been suggested that it does not supress ordering in the TM layers.[23] Ordering of Ni and Mn occurs in P2-NNM,[43,44] which is difficult to determine with regular XRD as they scatter X-rays similarly.[3] Hence some studies on these materials do not show superstructure peaks in the XRD data,[45,46] although they are visible with synchrotron XRD or neutron diffraction.[43] Synchrotron radiation is ideal for studying superstructure due to weak diffuse scattering and high resolution, thus allowing for greater detail in the material to be seen such as small superstructure peaks, that would otherwise be lost to the background.[47,48] However, with development of lab XRD, it has become possible to see superstructure peaks caused by in-plane Na^+/vacancy ordering,[23,25,37] which can be affected by TM ordering.[39]

In the literature, superstructure peaks around 27.2 and 28.3 °2θ were visible in the XRD data in P2-$Na_{2/3}Ni_{1/3-x}Cu_xMn_{2/3}O_2$, attributed to Na^+/vacancy ordering.[23] As Cu content increased, the small superstructure peaks increased in intensity, due to greater Na^+/vacancy ordering. The voltage curves also appeared smoother, as the plateaus that are normally attributed Na^+/vacancy were not as obvious. It was speculated that with the increased *c*-axis due to Cu, there was less repulsion between the TMO_2 layers that allowed greater occupancy of the Na_f site, which is normally less energetically favourable than the Na_e site.[23] Occupation of the Na_f site has found to form a large zigzag ordering pattern in the Na layers, which causes the superstructure peaks at low angles in the XRD pattern.[3]

Many studies aim to prevent Na^+/vacancy ordering as it can affect kinetics,[40,49] however diffusion coefficients on average are larger in Cu-containing cathodes compared to P2-NNM,[23] despite the presence of Na^+/vacancy ordering. This is potentially due to increase value in *c*-axis as well as the supressed P2-O2 phase transition that may negate the effects of ordering. This may be in the case in the materials investigated in this chapter.

Although with increasing Cu content the voltage curves were smoother, figure 4.11, there was a small peak at 27.6 °2θ in the XRD pattern that increased in intensity with increasing Cu substitution, figure 4.1a inset. This could be due to Na^+/vacancy ordering, however further investigation is required to identify superstructures in the P3 structure. Just like P2, the P3-NNM polymorph tends to exhibit TM ordering,[38,43] which affects Na ordering, as Na prefers to occupy sites around Ni.[38] As Cu content increased, the *c*-axis also increased, figure 4.2, which could allow for greater superstructure formation, causing the small peak at 27.6 °2θ to increase in intensity. However in-plane Na ordering patterns in P3-NNM have not been investigated in the literature, as done so with P2-NNM. Therefore further investigation to fully characterise the potential superstructure peak is needed.

4.3.2.3 Ex-situ XRD of P3-NNM and P3-NNCM

Ex-situ XRD was conducted on P3-$Na_{2/3}Ni_{1/3}Mn_{2/3}O_2$ (x = 0) and P3-$Na_{2/3}Ni_{1/6}Cu_{1/6}Mn_{2/3}O_2$ (x = 1/6) at charge voltages of 3.65, 4.2 and 4.5 V where plateaus are located in the voltage curves, figure 4.11. *Ex-situ* XRD of P3-NNM (x = 0), figure 4.12, showed the formation of a O3-type structure at 3.65 V. Both O3- and P3-type structures are quite similar, however the main identifying features are the ratios of peaks (101)/(10-2) and (104)/(10-5). For P3-type stacking, the ratios are below 1 and for O3-type stacking they are above 1, as identified in P3-$Na_{0.9}Ni_{0.5}Mn_{0.5}O_2$.[2] At 3.65 V, there was no obvious changes in the ratio of (101)/(10-2) and there was no significant reduction in peak intensity in the (10-5) peak. However, the main identifying feature for the O3 structure in figure 4.12 was the (104) peak. Also, P3 (003) peak had an additional shoulder at higher angle, that can be attributed to O3 (003) peak. Therefore at 3.65 V, both P3 and O3 phases coexisted. As the voltage increased to 4.2 V, the (00*l*) peaks shifted significantly to lower angles, from 15.8 to 12.5 °2θ, indication of a significant increase in the *c*-axis, contrary to what usually occurs during the P3-O3 phase transition, where there is a slight shift of the (003) to higher angles.[2,50,51] The shift of the (003) peak to significantly lower angles, such as 12.5 °2θ, is characteristic of a hydrated layered structure, where water molecules intercalate into the Na layers.[52] The water could have contaminated the electrode through *ex-situ* XRD sample preparation or water from electrolyte.

Some *ex-situ* experiments have found hydrated phases in the charged state of materials that have found to be stable in the pristine state.[17,37] In-operando XRD of other P3-type layered oxides show that as Na is deintercalated, the *c*-axis increases slightly due to the repulsion from adjacent TMO_2 layers, before the P3-O3 phase transition.[50] This increase in the *c*-axis can make the material more susceptible to water intercalation.[37] Presence of the hydrated layered oxide phase at high charged states is fairly common *in ex-situ* XRD experiments.[9,16,26,37,53,54] This is not ideal as it may not give a realistic insight into what is happening in the cell, especially if exposed to moisture during sample preparation for *ex-situ* XRD. Hence *in-operando* XRD would be a better method to investigate phase progression during cycling as there is less exposure to moisture from outside the cell. In the literature it appears there are no hydrated peaks in the discharged cells and there does not seem any impact on the other peaks with respect to water exposure, only those related to the *c*-axis.[26,37,54] Therefore it was still possible to decipher what is happening in terms of P3-O3 phase transition by observing the (101), (10-2), (104) and (10-5) peaks. At 4.2 V, although there was no significant difference in the (101) and (10-2) peaks, the O3 (104) became more prominent and the P3 (10-5) peak disappeared, characteristic of O3-type structure.[55,56] At 4.5 V, there was no significant difference in the XRD pattern compared to when charged to 4.2 V. Therefore, by 4.2 V, the material appeared to be predominantly the O3-phase.

There is an additional peak at around 26 °2θ in the pristine cathode and potentially in others to some small extent, which is likely due to super C65 conductive additive.[57]

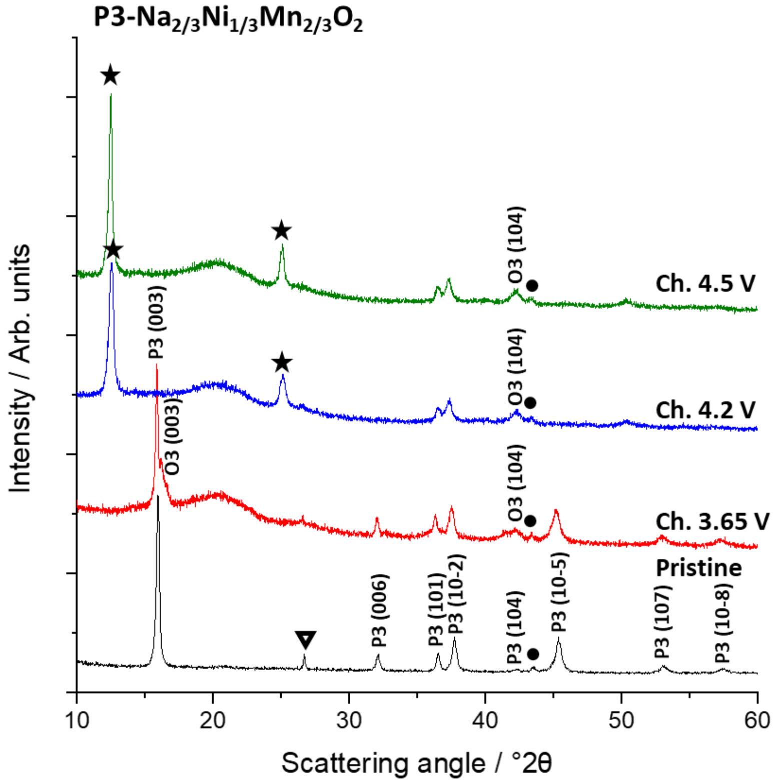

Figure 4.12: *Ex-situ XRD of P3-$Na_{2/3}Ni_{1/3}Mn_{2/3}O_2$ (x = 0) in pristine state (black), charged to 3.65 V (red), 4.2 V (blue) and 4.5 V (green). Black star is hydrated layered oxide, black circle is NiO and inverted triangle is super C65.*

Figure 4.13 shows the *ex-situ* data for P3-NNM $Na_{2/3}Ni_{1/6}Cu_{1/6}Mn_{2/3}O_2$ (x = 1/6). After charging to 3.56 V and at 4.2 V, there was no obvious change in the XRD pattern, indication that the P3 phase is preserved. There was also no sign of the hydration phase. This could be due to handling of the specimen or as more Na remains in the structure at higher voltages, there may be less expansion in the *c*-axis due to lack of repulsion from the adjacent TMO_2 from the greater shielding from in the Na layers. As there is only *ex-situ* XRD data for x = 1/6 up to 4.2 V upon charge, it is still yet to be determined whether the P3 phase is maintained up to 4.5 V. Regardless, Cu substitution is an effective way to supress or at least delay the P3-O3 phase transition in P3-NNM, which has not been previously reported for this material.

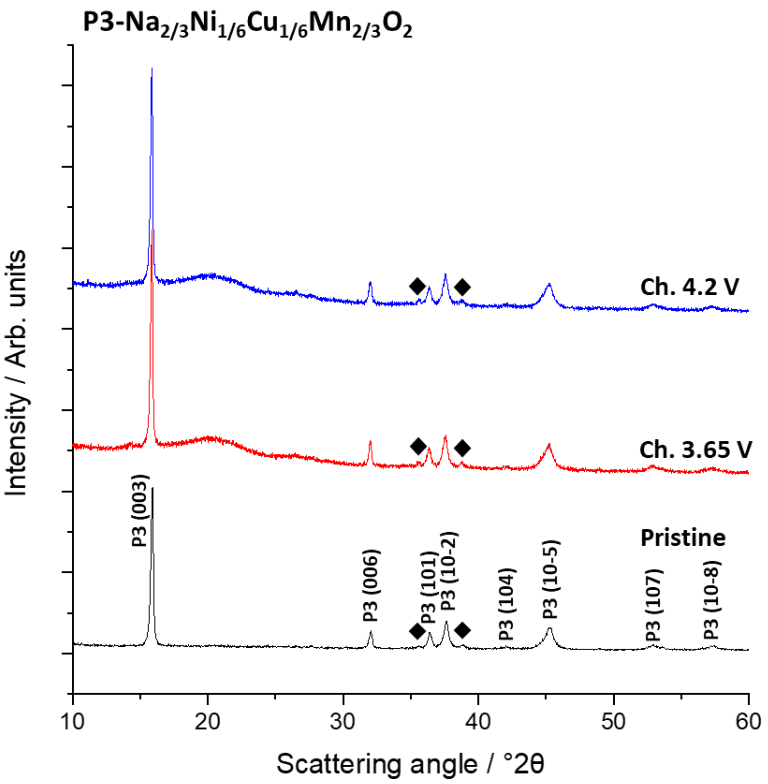

Figure 4.13: *Ex-situ XRD of P3-*$Na_{2/3}Ni_{1/6}Cu_{1/6}Mn_{2/3}O_2$ *(x = 0) in pristine state (black), charged to 3.65 V (red) and 4.2 V (blue). Black diamond is CuO.*

4.3.3 Water stability

P3-NNM is stable under ambient conditions, which is further investigated in chapter 5, most likely to the TM ordering.[38] Water stability of these materials can be destroyed by substituting in other metals such as Fe and Co as TM ordering is inhibited and the interlayer interactions are weakened.[58,59] Such sensitivity to ambient conditions is not ideal, as handling can be difficult and expensive. Although, the literature has found that Cu substitution in P2-NNM does not negatively impact the moisture stability, even after exposure to air or immersion in water for about a month.[11,23] Specimens x = 1/12 and 1/6 did not exhibit formation of the hydrated phase after immersion in water for 24 h, figure 4.14a & 4.15b. There was no significant difference in the XRD patterns between the pristine powder, after immersion in water and then followed by further drying the vacuum oven at 120 °C. This clearly shows that Cu substitution does not impact the water sensitivity of the P3-type structure. If the small peak at 27.6 °2θ is attributed to a superstructure, then Cu substitution in the P3 structure does not destroy TM ordering.

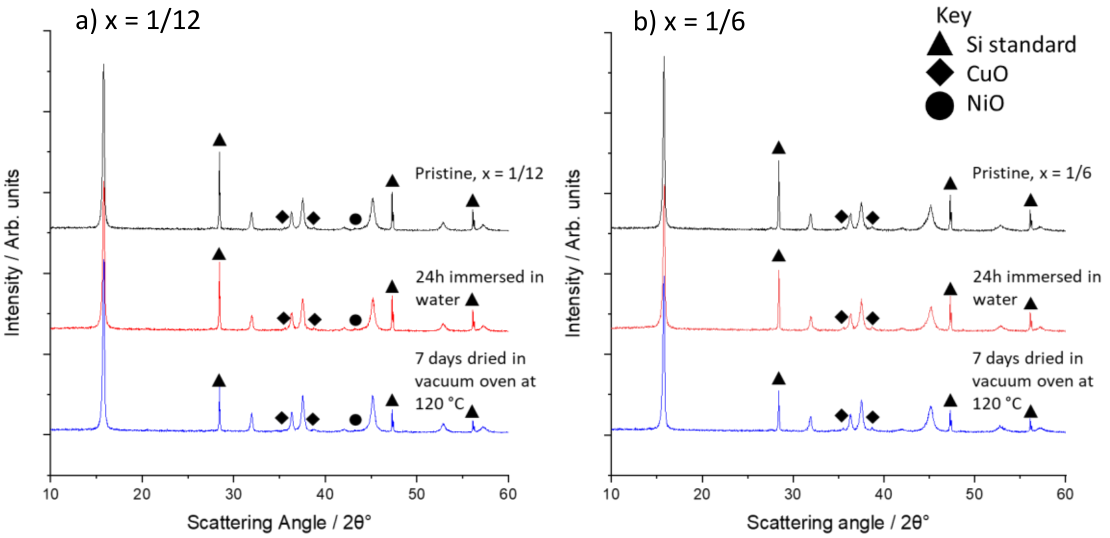

Figure 4.14: *XRD patterns of specimens a) x = 1/12 and b) x = 1/6 in pristine state, after 24 h immersed in water then dried at 80 °C till excess water is removed, then finally dried under vacuum at 120 °C for 7 days. Unlabelled peaks are from the P3 phase.*

To ensure that even a minute amount of solvent was not in the structure and to validate the data in figure 4.14, Pawley refinement with a NIST Si 640f standard was conducted to determine if there was any variation in the lattice parameters. The fit parameters indicated a decent fit, table 4.2. Both x = 1/12 and 1/6 exhibited minimal difference in the *a*-axis. The *c*-axis showed slightly more variation between the conditions for both specimens, however not enough to conclude solvent has intercalated into material. In x = 1/12, the *c*-axis for the pristine material was 16.823 Å, after immersion in water it was 16.817 Å and after drying under vacuum it was 16.825 Å. In x = 1/6, the *c*-axis for the pristine material was 16.826 Å, after immersion in water it was 16.817 Å and after drying under vacuum it was 16.838 Å. The small changes could be due to some Na leeching from the structure after submersion in water,[20,52] hence the slightly smaller *c*-axis, however this seems reversible after drying and the *c*-axis recovers for both materials. Further investigation is required to determine if leeching does actually occur.

Table 4.2: *Pawley refinement results of specimens is x = 1/12 and 1/6 in pristine state, after water immersion and then dried under vacuum.*

	x = 1/12			**x = 1/6**		
	$Na_{2/3}Ni_{1/4}Cu_{1/12}Mn_{2/3}O_2$			**$Na_{2/3}Ni_{1/6}Cu_{1/6}Mn_{2/3}O_2$**		
Condition	Pristine	24h immersed in water	7 days vacuum dried at 120 °C	Pristine	24h immersed in water	7 days vacuum dried at 120 °C
R_{wp}%	11.3	10.9	11.6	12.0	11.7	11.6
R_{ep}%	9.2	9.0	9.2	8.7	8.6	8.8
Chi^2	1.2	1.2	1.3	1.4	1.4	1.3
a-axis/Å	2.886	2.886	2.885	2.888	2.887	2.886
c-axis/Å	16.823	16.817	16.825	16.826	16.817	16.838

4.4 Conclusion

Although P3-$Na_{2/3}Ni_{1/3}Mn_{2/3}O_2$ has already been synthesised using biotemplating,[60] the ability to synthesise more complex systems with ease, highlights the versatility of the method. Specimens containing Cu contents of x = 1/12 and 1/6 in P3-$Na_{2/3}Ni_{1/3-x}Cu_xMn_{2/3}O_2$ produced only a small amount of secondary phases (< 3 wt.%), less than what is seen in chapter 3. When Cu content was x = 1/4 and 1/3, there was additional phases present, potentially formation of another layered structure with similar values for the *c*-axis. There is also small signs of this in specimen 1/6. This is likely due to a solid solution limit of Cu in the P3 structure under the tested synthesis conditions.

Electrochemical performance of specimens x = 0, 1/12 and 1/6 were compared at different cycling regimes. Overall, x = 1/6 had the best cycling stability, especially at extended voltage range of 2.0 – 4.5 V at 0.1 C. However at 1 C, there does not seem to be a significant difference between x = 1/12 and 1/6, however both outperformed x = 0. This could be that Cu prevented over oxidation of lattice oxygen, as well as suppressed P3-O3 phase transition. *Ex-situ* XRD had shown that P3-NNM beings to transition to the O3 phase at 3.65 V and completely transformed at 4.2 V. Whereas with x = 1/6, the structure did not change at 4.2 V and remained P3. However there is no structural data beyond 4.2 V, so it is still unknown to what extent the P3-O3 phase transition is impeded when cells are cycled to 4.5 V. Regardless, the phase transition is hindered to higher voltage in x = 1/6 compared to x = 0.

Na^+/vacancy ordering is likely to be present in all specimens, which has been the case in the literature for P2-NNM and Cu substituted materials.[23,43] However this did not affect performance of the Cu containing specimens. It is likely that the kinetics were improved due to the lack of P3-O3 phase transition and slightly larger *c*-axis, which can ease Na^+ mobility.

Substitution of other metals in materials such as P2-NNM often negatively impact the stability in ambient conditions as water molecules are able to intercalate into the Na layers, due to the weakened interactions of the adjacent TM layers as TM ordering suppressed. P3-NNM has found to be stable relatively stable, even after a prolonged time immersed in water, as investigated in chapter 5. Addition of Cu did not impact the water stability of the structure, as TM ordering could be present in the structure.

Cu substitution in P3-NNM greatly improved electrochemical performance. The preliminary evidence suggested that the P3-O3 phase transition was suppressed upon charge and that over oxidation of the anionic species was prevented to some extent. However further work is required to characterise the phase transitions and kinetics of P3-NNM to fully understand how Cu substitution impacts the electrochemical performance.

4.5 Further Work

Although almost phase pure P3 structures with Cu contents of x = 1/12 and 1/6 was synthesised using dextran-templating method at 650 °C for 2 h, the solid solution is likely to be slightly below x = 1/6 in P3-$Na_{2/3}Ni_{1/3-x}Cu_xMn_{2/3}O_2$. Further work is needed to determine this, so that the full solid solution limit can be electrochemically tested, to identify the best stoichiometry for the P3 structure as this may differ to P2.

More in-depth characterisation of phase progression between 2.0 and 4.5 V is required for both P3-NNM and P3-NNCM with Cu content of x = 1/6. This is to identify at which point the P3-O3 phase transitions begins and what voltage it fully transitions to the O3 phase. *In-operando* XRD would be the best method as water intercalation during sample preparation is less likely. This would highlight the impact Cu on the phase transition, thus explain how this affect cycling stability. Galvanostatic intermittent titration technique (GITT) would determine the diffusion coefficient at different voltages and how the coefficients vary at different transitions such as different Na^+/vacancy ordering configurations and at the P3-O3 phase transition.

Alongside this, synchrotron XRD or neutron diffraction would be able to identify the presence of superstructures. If this is conducted at different charge states, this can be linked back to diffusion coefficients calculated from GITT. It is hypothesised that although the addition of Cu retains the superstructures, this does not impact the kinetics of Na^+ in the material, therefore such degradation mechanism can be ruled out. Whereas in P3-NNM, it is likely that this is one of the causes for capacity degradation.

Another aspect that needs further investigation is oxygen redox that may occur in P3-NNM. XPS can be used to determine charge progression of lattice oxygen,[16,31] and *in-situ* differential electrochemical mass spectrometry (DEMS) can be used to measure gas evolution during charge and would determine at what voltage irreversible anionic oxidation begins.[16] If this is one of the degradation mechanisms in P3-NNM, such methods would help to determine to what extent Cu substitution would prevent irreversible oxygen loss at high charge voltages.

Performance of a cell is greatly impacted by the electrolyte. The electrolyte used in this study, 1 M $NaPF_6$ in EC:DEC (1:1 v/v%) begins to oxidise from 3.7 V if there is any moisture present.[61] Therefore the extent of the capacity degradation shown in this chapter may not be entirely due to the cathode material. Investigation into the water content is needed to ensure whether the electrolyte requires removal of water. Additives such as fluoroethylene carbonate (FEC) are used to stabilise the SEI and have shown to improve performance of cells and has been used in a variety of studies.[11,21,45,62] Using similar electrolyte to those used in the literature could make it easier to make comparisons between the different cathode materials.

4.6 References

1. Zhang, L. Electrochemical Performance and Structural Changes of $Na_{0.67}Mn_{0.67}Ni_{0.33}O_2$ as Cathode for Sodium Ion Batteries. (Technische Universität Berlin, 2019).
2. Risthaus, T. *et al.* P3 Na0.9Ni0.5Mn0.5O2 Cathode Material for Sodium Ion Batteries. *Chem. Mater.* **31**, 5376–5383 (2019).
3. Lee, D. H., Xu, J. & Meng, Y. S. An advanced cathode for Na-ion batteries with high rate and excellent structural stability. *Phys. Chem. Chem. Phys.* **15**, 3304–3312 (2013).
4. Liu, Z. *et al.* Ultralow Volume Change of P2-Type Layered Oxide Cathode for Na-Ion Batteries with Controlled Phase Transition by Regulating Distribution of Na^+. *Angew. Chem. Int. Ed* **60**, 20960–20969 (2021).

5. Wang, P. *et al.* Suppressing the P2-O2 Phase transition of Na0.67Mn0.67Ni0.33O2 magnesium substitution for improved sodium-ion batteries. *Angew. Chem. Int. Ed* **55**, 7445–7449 (2016).

6. Zhao, W., Kirie, H., Tanaka, A., Unno, M. & Yamamoto, S. Synthesis of metal ion substituted P2-$Na_{2/3}Ni_{1/3}Mn_{2/3}O_2$ cathode material with enhanced performance for Na ion batteries. *Mater Lett* **135**, 131–134 (2014).

7. Luo, R. *et al.* Insight into effects of divalent cation substitution stabilizing P2-Type layered cathode materials for sodium-ion batteries. *Electrochim Acta* **368**, 137614 (2021).

8. Hong, J. H., Wang, M. Y., Du, Y. Y., Deng, L. & He, G. The role of Zn substitution in P2-type $Na_{0.67}Ni_{0.23}Zn_{0.1}Mn_{0.67}O_2$ cathode for inhibiting the phase transition at high potential and dissolution of manganese at low potential. *J. Mater. Sci.: Mater. Electron.* **30**, 4006–4013 (2019).

9. Hu, G. *et al.* Highly stable Na0.67(Ni0.25Mn0.75)1−xCuxO2 cathode substituted by Cu for sodium-ion batteries. *Ionics (Kiel)* **27**, 657–666 (2021).

10. Hu, B. *et al.* Tailoring Anionic Redox Activity in a P2-Type Sodium Layered Oxide Cathode via Cu Substitution. *ACS Appl Mater Interfaces* **14**, (2022).

11. Wang, L. *et al.* Copper-substituted $Na_{0.67}Ni_{0.3-x}Cu_xMn_{0.7}O_2$ cathode materials for sodium-ion batteries with suppressed P2-O2 phase transition. *J Mater Chem A Mater* **5**, 8752–8761 (2017).

12. Wen, Y. *et al.* Copper Substitution in P2-Type Sodium Layered Oxide To Mitigate Phase Transition and Enhance Cyclability of Sodium-Ion Batteries. *ACS Appl. Mater. Interfaces* **14**, (2022).

13. Danks, Ashleigh. E., Hall, S. R. & Schnepp, Z. The evolution of 'sol-gel' chemistry as a technique for materials synthesis. *Mater. Horiz.* **3**, 91–112 (2016).

14. Lu, Z. & Dahn, J. R. In Situ X-Ray Diffraction Study of P2-$Na_{2/3}[Ni_{1/3}Mn_{2/3}]O_2$. *J Electrochem Soc* **148**, A1225–A1229 (2001).

15. Wang, K., Yan, P. & Sui, M. Phase transition induced cracking plaguing layered cathode for sodium-ion battery. *Nano Energy* **54**, 148–155 (2018).

16. Zhang, Y. *et al.* Revisiting the $Na_{2/3}Ni_{1/3}Mn_{2/3}O_2$ Cathode: Oxygen Redox Chemistry and Oxygen Release Suppression. *ACS Cent. Sci* **6**, 232–240 (2020).

17. Dang, R. *et al.* Na+-Conductive Na2Ti3O7-Modified P2-type Na2/3Ni1/3Mn2/3O2 via a Smart in Situ Coating Approach: Suppressing Na+/Vacancy Ordering and P2-O2 Phase Transition. *ACS Appl. Mater. Interfaces* **11**, 856–864 (2019).

18. Kubota, K., Yoda, Y. & Komaba, S. Origin of Enhanced Capacity Retention of P2-Type Na2/3Ni1/3-xMn2/3CuxO2 for Na-Ion Batteries. *J Electrochem Soc* **164**, A2368–A2373 (2017).

19. Tapia-Ruiz, N. *et al.* High voltage structural evolution and enhanced Na-ion diffusion in P2-Na2/3Ni1/3-xMgxMn2/3O2 ($0 < x < 0.2$) cathodes from diffraction, electrochemical and ab initio studies†. *Energy Environ. Sci* **11**, 1470 (2018).

20. Zhang, J., Wang, W., Wang, W., Wang, S. & Li, B. Comprehensive Review of P2-Type $Na_{2/3}Ni_{1/3}Mn_{2/3}O_2$, a Potential Cathode for Practical Application of Na-Ion Batteries. *ACS Appl. Mater. Interfaces* **11**, 22051–22066 (2019).

21. Yang, L. *et al.* Cu-doped layered P2-type $Na_{0.67}Ni_{0.33-x}Cu_xMn_{0.67}O_2$ cathode electrode material with enhanced electrochemical performance for sodium-ion batteries. *Chemical Engineering Journal* **404**, 126578 (2021).

22. Ma, P. *et al.* Binary metal co-substituted P2-type Na0.67Mn0.7Cu0.15Ni0.15O2 microspheres as robust cathode for high-power sodium ion battery. *Appl Surf Sci* **529**, 147105 (2020).

23. Zheng, L., Li, J. & Obrovac, M. N. Crystal Structures and Electrochemical Performance of Air-Stable $Na_{2/3}Ni_{1/3-x}Cu_xMn_{2/3}O_2$ in Sodium Cells. *Chem. Mater.* **29**, 1623–1631 (2017).

24. Shannon, R. D. Revised effective ionic radii and systematic studies of interatomic distances in halides and chalcogenides. *Acta Cryst.* **A32**, 751–767 (1976).

25. Lee, S. Y., Kim, J. H. & Kang, Y. C. Electrochemical properties of P2-type $Na_{2/3}Ni_{1/3}Mn_{2/3}O_2$ plates synthesized by spray pyrolysis process for sodium-ion batteries. *Electrochim. Acta* **225**, 86–92 (2017).

26. Arag, M. J. *et al.* On the use of guanidine hydrochloride soft template in the synthesis of $Na_{2/3}Ni_{1/3}Mn_{2/3}O_2$ cathodes for sodium-ion batteries. *J. Alloys Compd.* **789**, 1035–1045 (2019).

27. Liu, Q. *et al.* P2-type $Na_{2/3}Ni_{1/3}Mn_{2/3}O_2$ as a cathode material with high-rate and long-life for sodium ion storage. *J. Mater. Chem. A* **7**, 9215–9221 (2019).

28. Kim, E. J. *et al.* Oxygen Redox Activity through a Reductive Coupling Mechanism in the P3-Type Nickel-Doped Sodium Manganese Oxide. *ACS Appl. Energy Mater.* **3**, 184–191 (2020).

29. Liu, J. *et al.* Elucidation of the high-voltage phase in the layered sodium ion battery cathode material P3–Na 0.5 Ni 0.25 Mn 0.75 O 2. *J Mater Chem A Mater* **8**, 21151–21162 (2020).

30. Wang, Y. *et al.* Improved cycle and air stability of P3-$Na_{0.65}Mn_{0.75}Ni_{0.25}O_2$ electrode for sodium-ion batteries coated with metal phosphates. *Chem. Eng. J.* **372**, 1066–1076 (2019).

31. Zheng, W. *et al.* Oxygen redox activity with small voltage hysteresis in Na0.67Cu0.28Mn0.72O2 for sodium-ion batteries. *Energy Storage Mater* **28**, 300–306 (2020).

32. Shu-Yin, X. *et al.* Novel copper redox-based cathode materials for room-temperature sodium-ion batteries. *Chinese Physics B* **23**, 118202 (2014).

33. Bai, X., Iadecola, A., Tarascon, J. M. & Rozier, P. Decoupling the effect of vacancies and electropositive cations on the anionic redox processes in Na based P2-type layered oxides. *Energy Storage Mater* **31**, 146–155 (2020).

34. Yang, L. *et al.* Effect of vacancy-tailored Mn 3 + spinning on enhancing structural stability. *Energy Storage Mater* **44**, 231–238 (2022).

35. Hasa, I., Buchholz, D., Passerini, S. & Hassoun, J. A Comparative Study of Layered Transition Metal Oxide Cathodes for Application in Sodium-Ion Battery. *ACS Appl. Mater. Interfaces* **7**, 5206–5212 (2015).

36. Xiao, Z. *et al.* Insights of the Electrochemical Reversibility of P2-Type Sodium Manganese Oxide Cathodes via Modulation of Transition Metal Vacancies. *ACS Appl. Mater. Interfaces* **13**, 38305–38314 (2021).

37. Zhou, Y. N. *et al.* Air-Stable and High-Voltage Layered P3-Type Cathode for Sodium-Ion Full Battery. *ACS Appl. Mater. Interfaces* **11**, 24184–24191 (2019).

38. Zhang, L. *et al.* Preferential occupation of Na in P3-type layered cathode material for sodium ion batteries. *Nano Energy* **70**, 104535 (2020).

39. Gutierrez, A. *et al.* On Disrupting the Na^+-Ion/Vacancy Ordering in P2-Type Sodium−Manganese−Nickel Oxide Cathodes for Na^+-Ion Batteries. *J. Phys. Chem. C* **122**, 23251–23260 (2018).

40. Mao, Q. *et al.* Mitigating the P2-O2 transition and Na+/vacancy ordering in $Na_{2/3}Ni_{1/3}Mn_{2/3}O_2$ by anion/cation dual-doping for fast and stable Na+ insertion/ extraction †. *J. Mater. Chem. A* **9**, 10803–10811 (2021).

41. Kang, S. M. *et al.* Na+/Vacancy Disordered P2-Na0.67Co1-xTixO2: High-Energy and High-Power Cathode Materials for Sodium Ion Batteries. *ACS Appl Mater Interfaces* **10**, 3562–3570 (2018).

42. Medarde, M. *et al.* 1D to 2D Na+ ion diffusion inherently linked to structural transitions in Na0.7CoO2. *Phys Rev Lett* **110**, 266401 (2013).

43. Lu, Z., Donaberger, R. A. & Dahn, J. R. Superlattice ordering of Mn, Ni and Co in layered alkali transition metal oxides with P2, P3 and O3 structures. *Chem. Mater.* **12**, 3583–3590 (2000).

44. Cabana, J. *et al.* Study of the Transition Metal Ordering in Layered Na x Ni x/2 Mn 1−x/2 O 2 (2/3 ≤ x ≤ 1) and Consequences of Na/Li Exchange. *Inorg. Chem.* **52**, 8540–8550 (2013).

45. Wang, H. *et al.* Electrochemical Properties of P2-$Na_{2/3}[Ni_{1/3}Mn_{2/3}]O_2$ cathode material for sodium ion batteries when cycled in different voltage ranges. *Electrochim. Acta* **113**, 200–204 (2013).

46. Liu, G., Wen, L., Li, Y. & Kou, Y. Synthesis and electrochemical properties of P2-$Na_{2/3}Ni_{1/3}Mn_{2/3}O_2$. *Ionics (Kiel)* **21**, 1011–1016 (2015).

47. Cheng, H. *et al.* Synchrotron radiation X-ray powder diffraction techniques applied in hydrogen storage materials - A review. *Progress in Natural Science: Materials International* **27**, 66–73 (2017).

48. Clegg, W. The development and exploitation of synchrotron single-crystal diffraction for chemistry and materials. *Philosophical Transactions of the Royal Society A* **377**, 20180239 (2019).

49. Wang, P. F. *et al.* Na^+/vacancy disordering promises high-rate Na-ion batteries. *Sci. Adv.* **4**, 1–9 (2018).

50. Tripathi, A., Xi, S., Reddy Gajjela, S. & Balaya, P. Introducing Na-sufficient P3-$Na_{0.9}Fe_{0.5}Mn_{0.5}O_2$ as a cathode material for Na-ion batteries †. *Chem. Commun* **56**, 10686 (2020).

51. Sun, L. *et al.* Insight into Ca-Substitution Effects on O3-Type NaNi1/3Fe1/3Mn1/3O2Cathode Materials for Sodium-Ion Batteries Application. *Small* **14**, 1–7 (2018).

52. Zuo, W. *et al.* The stability of P2-layered sodium transition metal oxides in ambient atmospheres. *Nat Commun* **11**, 3544 (2020).

53. Kalapsazova, M. *et al.* P3-Type Layered Sodium-Deficient Nickel-Manganese Oxides: A Flexible Structural Matrix for Reversible Sodium and Lithium Intercalation. *Chempluschem* **80**, 1642–1656 (2015).

54. Yang, Q. *et al.* Advanced P2-$Na_{2/3}Ni_{1/3}Mn_{7/12}Fe_{1/12}O_2$ Cathode Material with Suppressed P2−O2 Phase Transition toward High-Performance Sodium-Ion Battery. *ACS Appl. Mater. Interfaces* **10**, 34272−34282 (2018).

55. Ding, F. *et al.* A Novel Ni-rich O3-$Na[Ni_{0.60}Fe_{0.25}Mn_{0.15}]O_2$ Cathode for Na-ion Batteries. *Energy Storage Mater* **30**, 420–430 (2020).

56. Maddukuri, S., Valerie, P. & Upadhyayula, V. v. Synthesis and Electrochemical Study of New P3 Type Layered Na0.6Ni0.25Mn0.5Co0.25O2 for Sodium-Ion Batteries. *ChemistrySelect* **2**, 5660–5666 (2017).

57. Rezqita, A., Hamid, R., Schwarz, S., Kronberger, H. & Trifonova, A. Conductive Additive for Si/Mesoporous C Anode in Li-Ion Batteries: Conductive Graphite Vs Carbon Black C65. *ECS Trans* **66**, 17–27 (2015).

58. Zhang, Y. *et al.* Water-Stable Cathode for High Rate Na-Ion Batteries. *ACS Appl. Mater. Interfaces* **12**, 15220–15227 (2020).

59. Lu, Z. & Dahn, J. R. Intercalation of Water in P2, T2 and O2 Structure $Az[CoxNi_{1/3-x}Mn_{2/3}]O_2$. *Chem. Mater.* **13**, 1252–1257 (2001).

60. Zilinskaite, S., Rennie, A. J. R., Boston, R. & Reeves-McLaren, N. Biotemplating: A sustainable synthetic methodology for Na-ion battery materials. *J. Mater. Chem. A* **6**, 5346–5355 (2018).

61. Ould, D. M. C. *et al.* New Route to Battery Grade NaPF6 for Na-Ion Batteries: Expanding the Accessible Concentration. *Angew. Chem. Int. Ed.* **60**, 24882–24887 (2021).

62. Ponrouch, A. *et al.* Non-aqueous electrolytes for sodium-ion batteries. *J Mater Chem A Mater* **3**, 22–42 (2015).

5 Xanthan gum as a water-based binder for P3-$Na_{2/3}Ni_{1/3}Mn_{2/3}O_2$

Silvija Zilinskaite, Nik Reeves-McLaren and Rebecca Boston

Front. Energy Res., vol. 10, pp. 909486, 2022

https://doi.org/10.3389/fenrg.2022.909486

Majority of the figures and text in this chapter are taken directly from work that I have published with my supervisors in *Frontiers in Energy Research* [1]. All work conducted is my own.

5.1 Aims & Objectives

Many Na-ion layered oxides suffer with poor stability in ambient conditions, where water molecules are able to intercalate into the Na layers. Therefore, during slurry preparation only binders that are dissolved with non-aqueous solvents can be used, such as Polyvinylidene fluoride (PVDF) binder and expensive and toxic N-methyl pyrrolidone (NMP) solvent. However, there are a small number of layered oxides that are stable after immersion in water, making them good candidates for water soluble binders and one of these materials is P2-NNM.[2] it is likely that P3-NNM is also stable after water exposure as it has the same stoichiometry and similar structure.

The aim of this chapter was to determine the water stability of P3-NNM. Once stability of P3-NNM was established, water soluble binder was employed during slurry preparation. Xanthan gum binder was chosen to be investigated in this chapter due to its successes with different materials such as P2-NNM and $LiFePO_4$.[2–4] Electrochemical performance at different cycling regimes was compared between P3-NNM electrodes that have either been prepared with XG or PVDF.

5.2 Introduction

Current work on Na-ion batteries often focuses on understanding and enhancing the properties of cathode and anode materials. Whilst these are critical steps on the route to commercialization, development of novel battery technologies also provides the opportunity to investigate and implement more sustainable chemicals and electrode fabrication processes across the broader remit of cell assembly. Binders, for example, play a key role in the stability and architecture of electrode materials.

PVDF, figure 5.1a, is a commonly used binder in both Li- and Na-ion batteries due to its electrochemical and thermal stability, and good adhesion between current collector and electrode.[5,6] During cell fabrication, NMP is used to dissolve PVDF. NMP is costly and toxic, and PVDF can be difficult to recycle,[7,8] making this combination a poor choice for low-cost sustainable batteries from preparation to recycling. PVDF has shown to accommodate volume changes of up to 15 % during electrochemical cycling,[6,9] however there have been no studies as to whether it can for volume changes of 20 % that occur due to the P2-O2 phase transition in some Na-ion layered oxides.[10,11] Exceeding the limits of the binder can cause areas of the electrode to be electrochemically isolated due to disconnection from the matrix,[6,9] impacting performance. This has been demonstrated with Si anodes where volume changes of up to 300 % cause mechanical failure.[6,12,13] P3-type Na materials are promising candidates for Na-ion cathodes, [14–16] however they exhibit even larger volume changes and distortions compared to P2-type materials,[17,18] Binder choice, taking into account the different requirements of these emergent cathode materials, is therefore key to ensuring electrode stability, and presents an opportunity to use more environmentally friendly, and easy to handle materials.

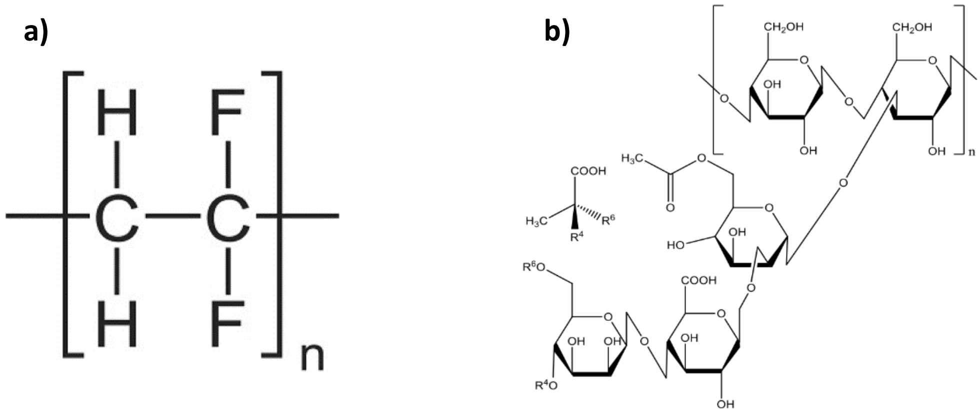

Figure 5.1: *Molecular structure of a) polyvinylidene fluoride (PVDF)* [19] *and b) xanthan gum (XG)* [20].

PVDF binds to the electrode components by weak Van Der Waals forces and generally has weak adhesion to the active material, and along with poor flexibility and mechanical strength (e.g. Young's modulus), such binder would struggles to maintain structural integrity of the electrode.[21–23] As such, biopolymer binders are attracting increasing attention as alternative due to the large number of functional groups (e.g. hydroxyls and carboxyl), which can lead to good adhesion between active material, conductive additives and current collector.[2,8] The adhesion mechanism is by hydrogen bonding due to the negative dipole moment on the oxygens in the functional groups, which are stronger than Van Der Waals forces.[24] In addition, the hydrogen bonding is able to "self-heal", hence the ability to accommodate significant volume changes during cycling.[12,25]

Biopolymers such as guar gum, xanthan gum and sodium alginate have been used as binders in P2-$Na_{2/3}Ni_{1/3}Mn_{2/3}O_2$ (P2-NNM) and electrodes prepared with such binders exhibited better cycling stability and faster rate capability compared to electrodes prepared with PVDF.[2] This is likely due to better dispersion of conductive additive and active material and maintenance of the conductive network as a result of the high viscosity of the slurries, leading to slow rates of segregation of the different components.[3,26] Many biopolymers are water soluble, and so are significantly easier to handle than PVDF during slurry preparation.

Xanthan gum (XG), figure 5.1b, is a naturally derived polysaccharide, produced by the bacteria *Xanthomonas campestris,* and is used in the food, cosmetic and pharmaceutical industries.[27] It contains (1,4)-β-D-glucose units with trisaccharide side chains, containing numerous -OH and -COOH groups. Previous work that had used XG as a binder to fabricate P2-NNM cells exhibited an initial discharge capacity of 86.7 mAh g^{-1} (between 1.5 and 4.3 V at 1 C), only falling to 75.4 mAh g^{-1} after 300 cycles [2]. Whilst initially showing a similar discharge capacity, cells fabricated using a PVDF binder dropped to 6.8 mAh g^{-1} after 300 cycles, demonstrating the significant advantages afforded by the XG binder. Improvement in cycle stability was attributed to better Na^+ diffusion due to better integrated conductive network afforded by XG, as more active material are in contact with it. In addition, manganese dissolution was inhibited.[2] XG was also used to fabricate $LiFePO_4$ (LFP) cathodes, where there was an improvement in the rate capability: with XG binder, discharge capacity was *ca.* 80 mAh

g^{-1} vs *ca.* 50 mAh g^{-1} using PVDF, both at 5 C.[3] Similar results were observed with a locust bean gum binder in $LiFePO_4$ and $Li_4Ti_5O_{12}$ [28]. Hence, biopolymers therefore represent attractive alternatives to the existing organic binders.

There are challenges in applying these to sodium ion batteries, however, as many Na-ion electrode materials easily take up water due to the larger alkali interlayer spacing,[29,30] resulting in the formation of birnessite-type phase. This phase is detrimental because it can affect morphology where cracks and gliding can be induced in the crystallites, particularly the *00l* plane where the Na layers are located.[31] There can also be side reactions between water and electrolyte, as well as blocking diffusion pathways of Na^+ diffusion and leeching of Na from active material to form electrochemically inactive phases.[32,33]

In previous research, both P2- and P3-NNM, showed negligible structural change after storage under ambient conditions or after immersion in water,[2,29,30] making them good candidates for use with water-based binders. In this chapter the stability of P3-NNM under ambient conditions and after immersion in water was investigated, and the practical requirements for controlling/removing hydrated phases were found. The cycling stability and rate capability of P3-NNM electrodes prepared using XG and PVDF were then compared. It was found that the choice of binder had a negligible impact on the measured capacity or cycling stability, indicating that water exposure during electrode preparation with XG did not negatively impact electrochemical performance.

5.3 Results & Discussion

5.3.1 Stability of P3-NNM in Water and Ambient Conditions

Firstly, to determine whether P3-NNM is suitable for water soluble binders, the structure must be able to withstand water intercalation for at least one day. During cathode preparation, the slurries are dried in air overnight before storage under vacuum at 80 °C.

Specimen 1 : 4 (mass ratio of P3-NNM : dextran) that was studied in chapter 3 was used in these studies. It was calcined at 650 °C for 2 h, because these were the conditions that exhibited the best electrochemical performance for dextran-templated P3-NNM.[34] Comparison of X-ray diffraction data for freshly prepared (Figure 5.2a) and stored (3-months in desiccator, Figure 5.2b) specimens showed no obvious structural changes nor the development of additional Bragg reflections, indicating that there was no detectable formation of hydrated phases following long term storage of specimens under relatively dry conditions. In each instance, the observed Bragg reflections were indexed to P3-NNM (PDF card 04-016-7123) with small quantity of NiO, Figure 5.2, typical in synthetic studies of materials with this or similar compositions,[35–37] and also in chapter 3.

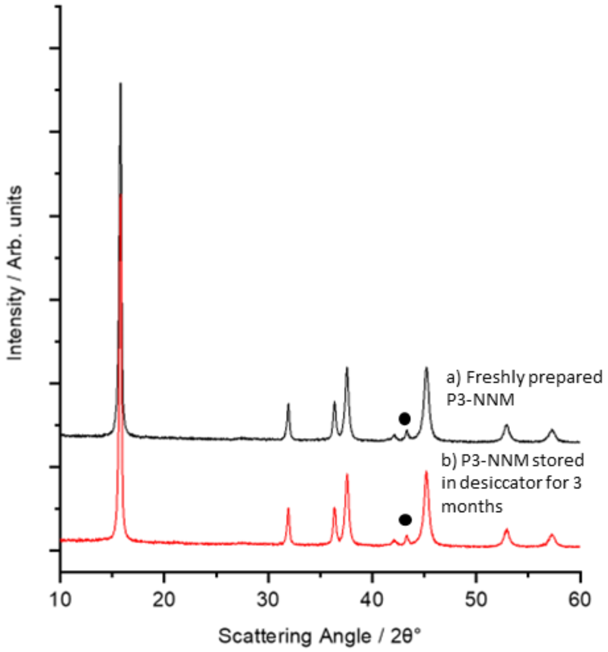

***Figure 5.2:** XRD data for P3-NNM a) freshly prepared (black) and b) after storage in a desiccator for 3 months (red). NiO is indicated using a filled circle and unlabelled peaks are attributed to the P3 phase.*

Longer-term ambient storage, outside a desiccator where humidity is greater was also investigated: Figure 5.3a shows the XRD pattern of P3-NNM stored in ambient conditions for 4 months and here additional Bragg reflections of low intensity were observed, indexed to the formation of a hydrated phase.[31] This is indicative of water molecules inserting into the structure, increasing the *c*-axis layer spacing forming a birnessite-type phase,[31] similar to previous work.[30,38] The ratio of hydrated phase to main phase in figure 5.3a was lower than those reported previously, indicating that P3-NNM may be have better ambient stability than other reported compositions, (*e.g.* $Na_{2/3}Fe_{1/9}Ni_{1/6}Mn_{2/3}O_2$, $Na_{2/3}Co_{1/9}Ni_{1/6}Mn_{2/3}O_2$, and $Na_{2/3}MnO_2$).[30–32] Figure 5.3b shows the XRD pattern of specimen from figure 5.3a that was stored under vacuum at 120 °C, followed by immersion in water and subsequent drying at 80 °C in air, Figure 5.3c. Here the small hydration peaks did emerge, in contrast to previous work which showed P3-NNM to be stable when immersed in water.[29] Hence it is important to dry the material at higher temperatures and under vacuum to ensure it is fully dehydrated. Pawley refinement was conducted on a specimen that was immersed in water, then dried at 80 °C, figure 5.4. Lattice parameters for P3-NNM and its hydrated analogue are shown in table 5.1. There was minimal difference in the *a*-axis, with values of 2.88 and 2.89 Å respectively. The hydrated P3-NNM had a *c*-axis of 20.93 Å; which was significantly larger than the pristine layered oxide with a value of 16.85 Å. The significant shift of the 00*l* plane to lower angles is due to the insertion of water molecules in the Na layer, as found with many other similar materials.[30,31,38]

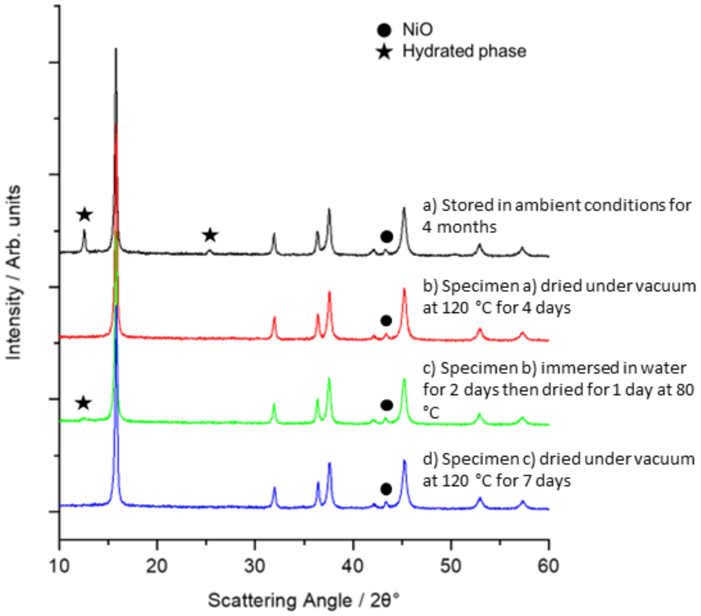

Figure 5.3: *XRD data for P3-NNM after a) storage in a cupboard for 4 months (black), b) then dried in vacuum oven for 4 days at 120 °C (red), c) then immersed in water for 2 days and dried for 1 day at 80 °C (green), d) then finally dried in vacuum oven for 7 days at 120 °C (blue). Additional Bragg reflections from secondary phases are indicated using a filled circle (NiO) or star (hydrated phase) symbol. Unlabelled peaks are attributed to the P3 phase.*

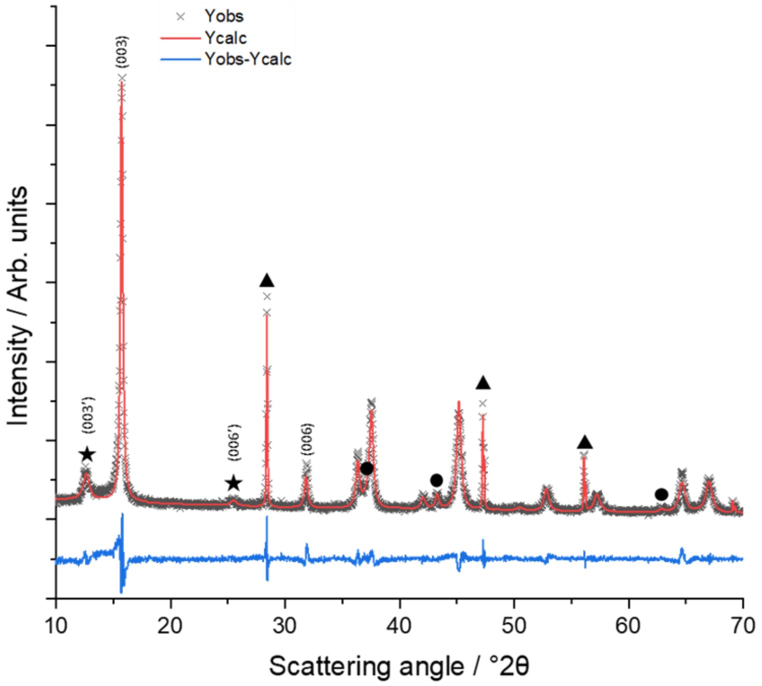

Figure 5.4*: Pawley refinement of P3-NNM soaked in water for one day, then dried at 80 °C for two days. Peaks labelled with dashes belong to the hydrated phase. NIST Si 640f standard was mixed with specimen before XRD was conducted. Si standard is labelled with black triangles, NiO with black circles and hydrated P3 phase with black stars.*

Table 5.1: *Lattice parameters obtained by Pawley refinement for P3-NNM and its hydrated analogue.*

Parameter	**Value**
R_{wp} / %	12.02
R_{ep} / %	9.76
Goodness of fit / χ^2	1.23
P3-NNM	
a/Å	2.88
c/Å	16.85
Hydrated phase	
a/Å	2.89
c/Å	20.93

There are various factors that can affect the stability of these layered structures. In P2-NNM, it has been shown that superlattice ordering prevents water intercalation due to the strong coupling between adjacent TMO_2 layers, as well as surface adsorption energy of water that is dependent on TM.[30,38] The superlattice structure occurs when there is ordering of Ni and Mn in the TM layers, especially with the 1:2 Ni to Mn ratio,[39] hence giving a possible reason for the stability of P3-NNM in aqueous conditions.[29] Some materials that demonstrate water stability in ambient condition do not necessarily have superlattice ordering. Alternatively, materials that have shown water stability have Mn valence close to +4 or those with relatively higher redox potentials or high degree of crystallinity.[31] There has been a study on reducing superlattice ordering of P3-NNM which was achieved by the synthesis method used, however water stability was not investigated.[40] In this case, it was postulated that biotemplated P3-NNM may have some disordered TM arrangement, or is less crystalline due to the short calcination time, hence small amounts of the hydrated phase formed after a while in ambient conditions. With longer calcination time, crystallinity and TM ordering may increase, which may lead to better stability in ambient and water conditions. This is something that will need to be investigated further.

It was possible to convert the hydrated phase back into the original P3-NNM phase, as demonstrated in similar materials.[38] After drying in a vacuum oven at 120 °C, the reflection(s) indexed to the hydrated phase were completely removed, figure 5.3d, and it appeared that the pristine cathode material was recovered. This firstly indicated that the hydration of P3-NNM appeared to be fully reversible, and secondly gave insight into the conditions required to use water-based binders with P3-NNM, *i.e.* once the binder is incorporated, electrode tapes must be dried under a vacuum at ≥ 120 °C to fully dehydrate.

SEM was conducted to examine the impact of water on crystallite morphology. Figures 5.5a shows SEM image of as prepared P3-NNM powder specimens and figure 5.5b following immersion in water and subsequent drying at 80 °C till excess water had evaporated before vacuum drying at 120 °C. There was no obvious sign of intragrain cracks or layer glide which has been found in other materials after exposure to water.[31] Higher magnification images in figure 5.5c & 5.5d, also showed no observable difference pre and post water immersion. If water intercalation did any lasting damage, to the extent electrochemical performance would be affected, it would likely be evident even after drying under vacuum at 120 °C.

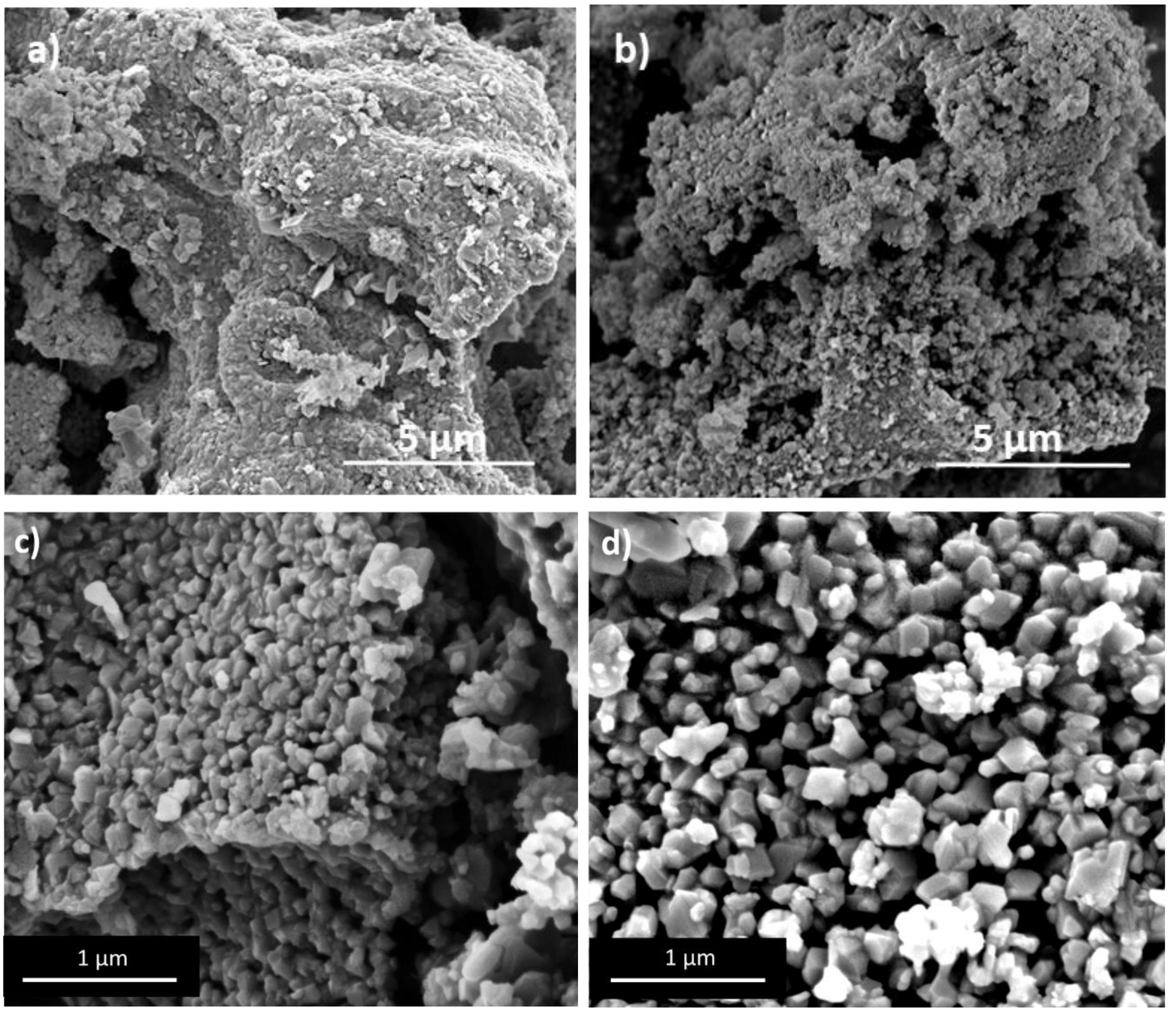

Figure 5.5: *SEM images of P3-NMM a&c) freshly prepared b&d) powder immersed in water then dried at 80 °C to remove excess water before drying at 120 °C under vacuum.*

5.3.1 Electrode Preparation Using Xanthan Gum

As the rheology and the viscosity of XG is significantly different compared to PVDF,[2,27] different methods for cathode preparations for the two slurries were used. For good comparisons between the two binders, the same weight fractions of active material, binder and conductive additive were used (80:10:10). Initially the same slurry preparation regime was used with XG as with PVDF, outlined in methods chapter 2 (methods). In the first few attempts of slurry preparation with XG, more water was added than NMP compared to the slurry containing PVDF binder, due to the viscosity of XG. This was then mixed using the same regime with the Thinky planetary mixer. When the slurry was cast onto the Al foil, a very thin coating was produced, figure 5.6a & 5.6b, potentially due to the combined effects of too much water and the shear thinning behaviour XG can exhibit.[27] Gradually less water was used in subsequent attempts. This produced thicker coatings where there was some powder agglomerates and cracks upon drying, figure 5.6c & 5.6d. In addition, despite the defoaming step during orbital mixing, it is likely that bubbles were in the slurry, because once the coating dried, there were pores which made the Al foil visible. This could be due XG forming a gel quickly after contact with water, making it difficult to disperse the powder constituents and therefore can produces a viscous, foamy slurry with clumps.[41]

Figure 5.6: *XG slurry coatings on Al foil prepared with a) 5ml, b) 3 ml, x) 2ml and d) 2.5 ml water for 0.5 g of powder, mixed in an orbital mixer.*

Final attempts used hand grinding with pestle and mortar. Prior to the addition of water, mixing of the dry powers can help with slowing down the gelation of XG, thus enabling better dispersion with water.[4] This step was also done in the initial attempts. With the hand grinding method, water was added to the mixed powder in small increments as some water evaporated due to the large surface area of the mortar, as detailed in methods chapter 2. This was repeated until there were no visible clumps, the slurry appeared homogenous and castable in terms of viscosity. The consistency of the final was slurry was much thicker than the one prepared with PVDF. However, after casting onto the Al foil and drying, the electrode sheet appeared to be of similar quality to the one prepared with PVDF. The amounts used in this study, initially hand grinding was sufficient. For greater quantities of powder (> 1 g), ball milling may be more appropriate to mix the slurry, as a few studies in the literature have done so with XG binder,[2,4,12] or high hear shear mixing methods using lab dissolver. These techniques may also be mor effective at overcoming the rapid gelling that can form coagulated regions and agglomerated powders.

As shown in a previous work, the biotemplating synthetic process produces agglomerated particles of P3-NNM with individual average particle size in the range of 100-200 nm,[34] which can be observed in Figures 5.5a and 5.5b. Such morphologies have been found in other dextran-templated materials.[42] Particle agglomeration had been shown to lead to increased charge-transfer resistances due to the abundance of particle-particle interfaces,[43–45] and so this may have a detrimental impact on electrochemical performance. Figures 5.7a and 5.7b show secondary and backscattered electron (BSE) images of cathode prepared using PVDF binder. Figure 5.7a clearly shows evidence of particle agglomeration, and regions of lighter contrast in the BSE image in Figure 5.7b can be attributed to the P3-NNM phase with darker regions to the carbon and binder. The same agglomeration is seen when the sample is prepared using XG in Figures 5.7c and 5.7d, indicating that the two binders formed electrodes with similar electrode microstructure. This showed that agglomeration is due to synthesis method rather than electrode fabrication, despite that viscosities of PVDF and XG are largely different.[2] There were cracks in both cathodes on the macroscale that were likely due to over calendaring and/or during sample preparation for SEM. Since there were fairly large agglomerates, when the electrodes are being calendared, crack propagation is likely to occur due to lack of binder to keep the particles together.

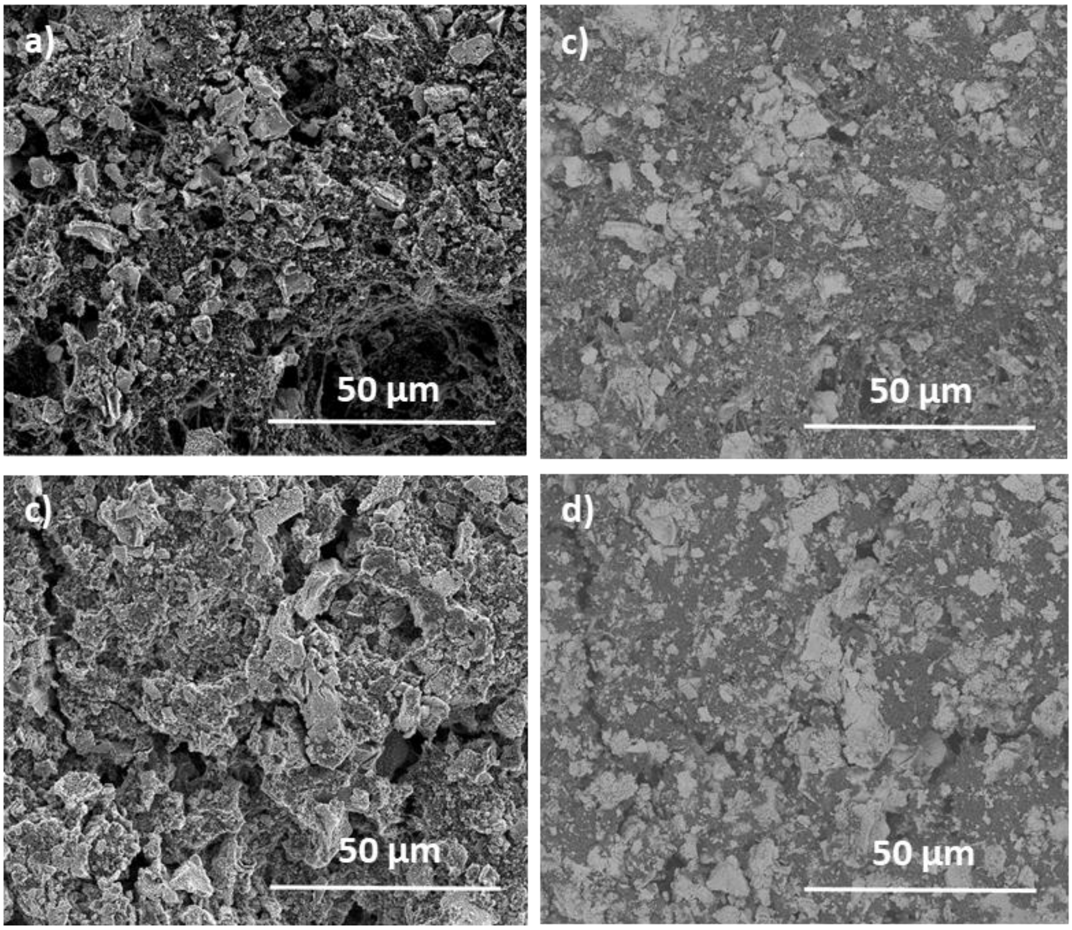

Figure 5.7*: a) secondary electron image of a P3-NNM cathode prepared using PVDF and b) corresponding BSE image, c) secondary electron image of a P3-NNM cathode prepared using XG and d) corresponding BSE image.*

In order to address the agglomeration of biotemplated P3-NNM particles, prior to slurry preparation, the active powder was immersed in water and placed into an ultrasonic bath for 40 minutes. The powder was thoroughly dried before slurry preparation. Figure 5.8 shows the SEM images of electrode prepared with the sonicated active material. Figure 5.8a and 5.8b show the low magnification SE and its BSE image and figure 5.8c and 5.8d are higher magnification. There was no obvious difference compared to the images shown in figures 5.7, as agglomeration was still very prominent in the electrode. It is clear that sonication of the active powder was not enough to break up the agglomerates. Alternatively, the agglomerates could have reformed during the slurry making process. Different mixing regimes will need to be investigated further. Ball milling the powders as well as mixing the slurry is likely to address the particle agglomeration and ensure better coating of carbon around the active material.[43,46,47] It was also found to be the most effective way to produce a homogenous slurry.

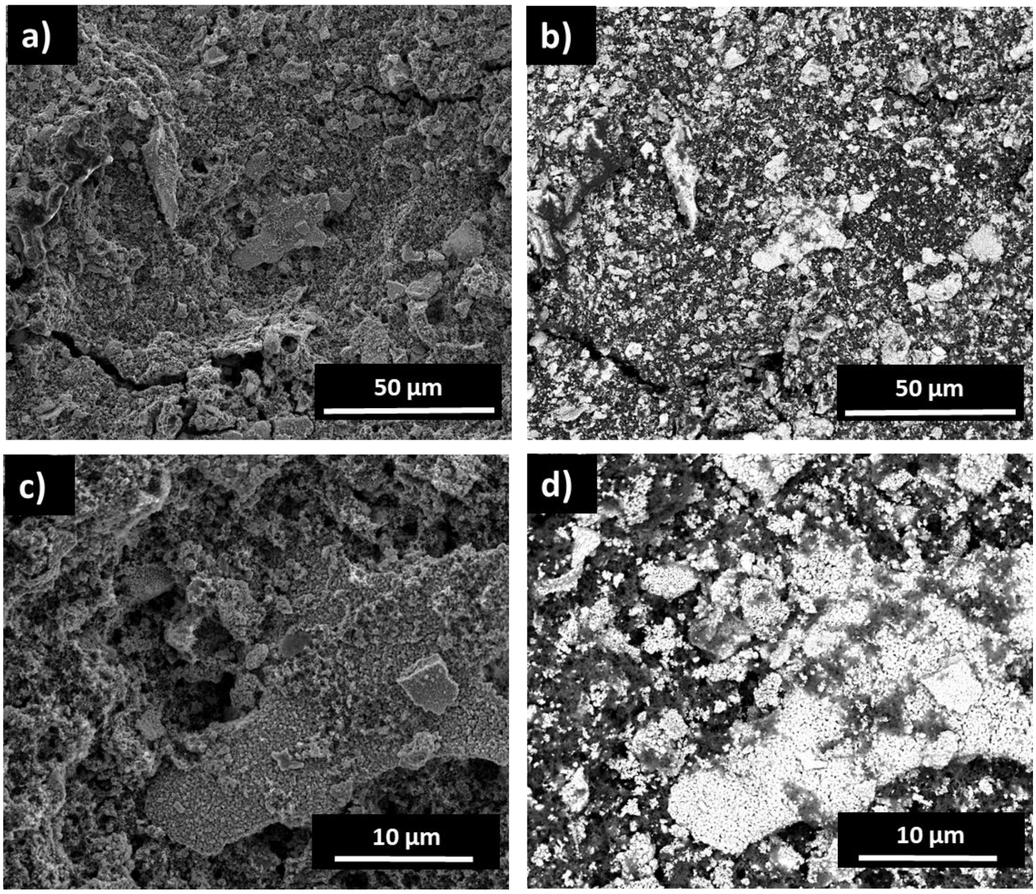

Figure 5.8*: SEM images of P3-NMM cathode prepared with XG binder, where active material was sonicated for at least 40 minutes prior slurry preparation. a) and c) are SE images and b) and d) are BSE images. a) and b) are low magnification images whereas c) and d) are higher magnification images.*

In summary, P3-NNM showed good stability after immersion in water. Although small amount of the hydrated phase did form, this was easily reversed after drying under vacuum at 120 °C for a few days. XG containing slurry cannot use the same preparation regime as NMP and PVDF, due to significantly different viscosities. Hand grinding and adding gradual amounts of water helped to remove any large powder agglomerates, break up coagulates and reduce the change of introducing air bubbles into the XG containing slurry. However, this was not sufficient enough to break up the intrinsic agglomerates in the dextran biotemplated P3-NNM powder. Therefore, different mixing regimes are required to break up these aggregates and aid better dispersion of carbon additive.

All electrochemical data in this chapter was from electrodes prepared the usual way as discussed in the methods, chapter 2, where the XG slurries were prepared with hand grinding without the sonication step and PVDF containing slurries were prepared with an planetary mixer.

5.3.2 Electrochemistry

Cells containing working electrodes fabricated using either PVDF or XG as binder were cycled galvanostatically at 0.1 C over the potential range of 2.0 to 4.2 V or over extended ranges to lower (1.5 V) and/or higher (4.5 V) potential limits in order to accentuate the effects from any degradation mechanisms, with the resulting discharge capacities plotted in Figure 5.9. Irrespective of voltage range, there was no significant difference in cycling stability between cells that use XG or PVDF binder. At 2.0

- 4.2 V, initial discharge capacities of *ca.* 115 mAh g^{-1} were observed. In both cases when cycled between 1.5 and 4.5 V, P3-NNM exhibited initial discharge capacities in excess of 200 mAh g^{-1}, higher than the theoretical capacity for P3-NNM of 173 mAh g^{-1}, irrespective of binder. This higher measured capacity could be due to a variety of additional contributions such as oxygen redox which is normally seen above 4 V [48–50] and Mn redox below 2 V, [51,52] both of which have been seen in similar materials but not thoroughly studied in P3-NNM. The higher capacity could also be due to electrolyte degradation, where presence of water can cause oxidation of 1M $NaPF_6$ in EC:DEC (1:1 v/v) to start at 3.7 V and reduction below 2 V for the first few cycles.[53] It is also likely that water may prevent the formation of stable electrolyte interphase on the electrodes, causing capacity fade.[53] Normally the stability window of such electrolytes is around 0.5 V to just above 4.5 V.[54–56] Analysis of water content in the electrolyte was not conducted, so it is not certain whether this is affecting the performance of the cells in figures 5.9 and 5.10. However, if there was trace amount of water, this would likely be from the electrolyte, as the specimens did not have hydrated phases present after vacuum drying, figure 5.3, and the electrodes that were prepared with PVDF/NMP also experienced the same rate of capacity degradation. Therefore investigation of water content in electrolyte is necessary for future studies to help determine degradation mechanisms. The voltage stability window of XG was demonstrated to be from 0 V to 4.3 V,[2,57] hence at this stage, binder degradation at 4.5 V cannot be completely ruled out. PVDF is stable up to 4.7 V vs Na^+/Na,[58] so binder degradation is unlikely for these cells. Since rate of capacity decline is similar for both cells prepared with XG and PVDF, it is likely that XG is stable in the tested potentials.

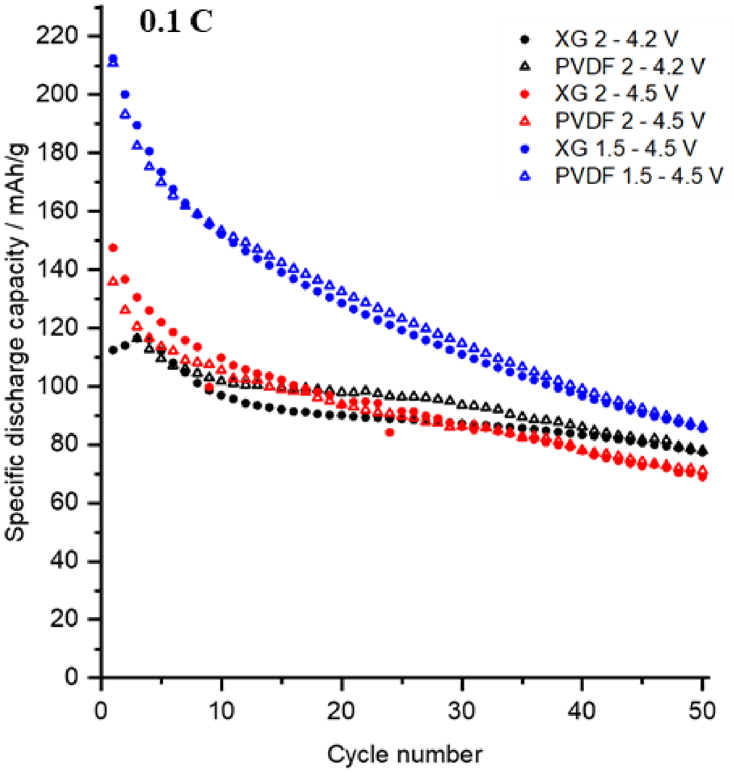

Figure 5.9: *Cycling performance on P3-NNM with either XG or PVDF binder cycled at different voltages at 0.1 C. Data obtained in a temperature controlled chamber at 25 °C using Maccor Series 4000 Battery Cycler.*

Figure 5.10 shows the discharge capacities of cells prepared with either XG or PVDF at different voltages ranges, at a faster cycling rate of 1 C. The cells in this figure were not cycled in a temperature controlled chamber, hence periodic peaks and troughs can be seen due to change in ambient temperature throughout the day. Regardless, there was no significant differences between electrodes with different binders. When cycling between 2 – 4.5 V, both specimens exhibited initial discharge capacities of *ca.* 125 mAh g^{-1}. XG containing cell was only cycled up to 110 cycles and had a capacity of only 31 mAh g^{-1}, whereas PVDF cell exhibited 47 mAh g^{-1} at the same cycle number. However, the XG cell showed a lot of noise compared to the PVDF cell due to more severe changes in ambient conditions when the cell was cycled, which may be a contributing factor to the lower observed discharge capacity. Cycling at 1.5 – 4.1 V, both specimens displayed initial discharge capacities of *ca* 118 mAh g^{-1} and after 200 cycles, only 23 mAh g^{-1} was observed. Cells cycled between 2.0 and 4.2 V exhibited slightly better capacity retention. XG cell had a slightly higher initial discharge capacity of 84 mAh g^{-1}, whereas the PVDF cell exhibited 69 mAh g^{-1}. After 200 cycles, both cells only displayed a capacity of *ca*. 40 mAh g^{-1}. With a faster cycling rate of 1 C, changes in ambient temperature throughout the day had a significant impact on the data compared to a slower charge rate, therefore, due to greater number of data points throughout the day.

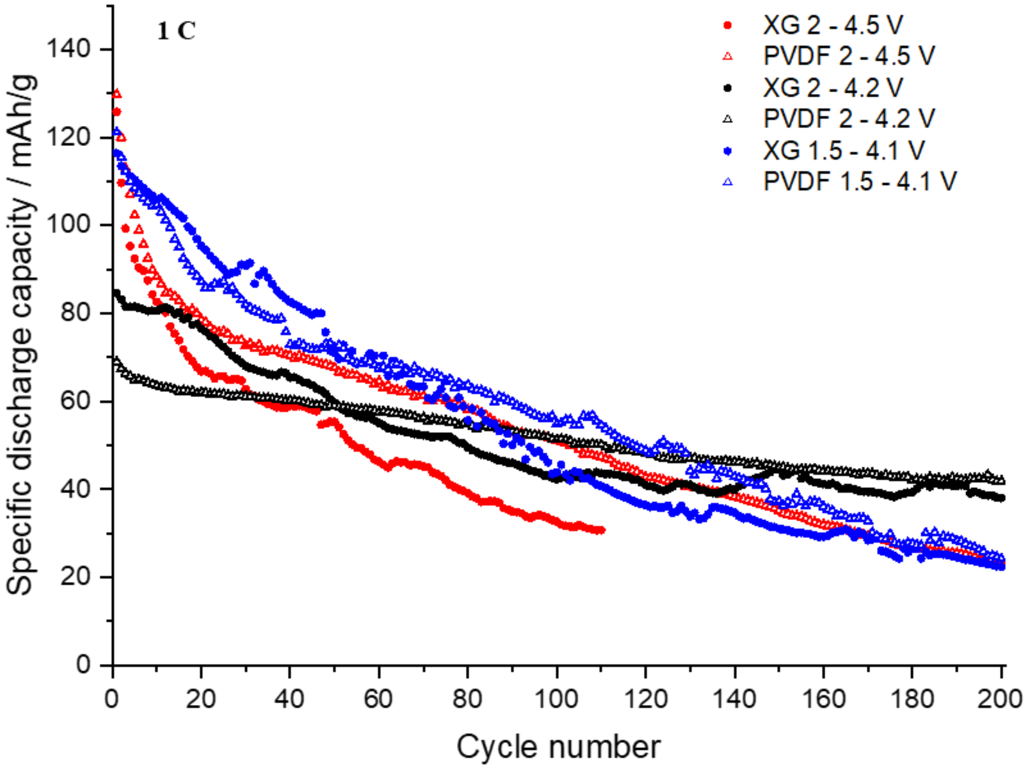

***Figure 5.10:** Cycling performance on P3-NNM with either XG or PVDF binder a) cycled at different voltages at 1 C. Data was collected in ambient conditions using and NEWARE BTS 8.0.*

Figure 5.11a shows the voltage profiles of P3-NNM with XG and Figure 5.11b with PVDF. Both profiles showed the same plateaus on discharge at *ca.* 1.9, 3.3, 3.6 and 4.1 V. The most prominent plateaus were around 1.9 and 4.1 V, however they quickly faded upon subsequent cycles. A plateau at 4.1 V upon charge can be attributed to the P3-O3 phase transition,[14,16] and at 1.9 V upon discharge the plateau is due to a P3-P3' transition, with an increase in number of Na atoms in the Na layers.[18] The P3-O3 phase transition is associated with a large change in unit cell volume, however effects of this phase transition are not as well understood as the P2-O2 transition in P2-NNM.[17] In P2-NNM, the phase transition at high voltages has been associated with intergranular cracking,[59] as well as sluggish Na$^+$-ion migration kinetics as the diffusion coefficient decreases in the O2-type phase.[52] It may be that similar phenomena occur during the P3-O3 phase transition.[18] The other plateaus at 3.3 and 3.6 V can be attributed to different Na$^+$/vacancy ordering, as noted for the P2-NNM polymorph in the literature.[60,61] For both cathodes prepared with XG and PVDF show similar rate of plateau degradation.

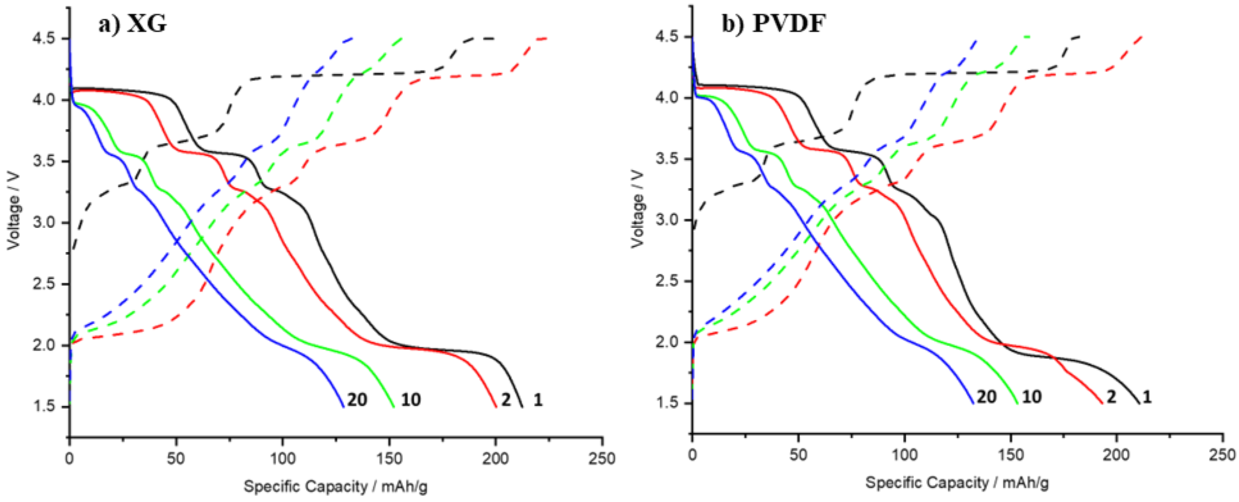

Figure 5.11: *Voltage profiles of the first, second, tenth and twentieth galvanostatic charge and discharge (dashed lines) for biotemplated P3-NNM cycled at 0.1 C between 1.5 and 4.5 V, where the working electrode was made using a) XG and b) PVDF binders.*

Cyclic voltammograms were collected for cells using electrodes made with XG (Figure 5.12a, c) and PVDF (figure 5.12b, d) binders. The findings were broadly similar regardless of binder choice, with five main redox pairs at anodic/cathodic voltages of around 4.3/4.0 V, 3.7/3.4 V, 3.3/3.1 V, 3.2/3.0 V and 2.2/1.8 V. Samples prepared with XG had an additional cathodic peak at 3.8 V when cycled between 2.0 and 4.5 V in Figure 5.12a, which was not observed in the samples containing PVDF, Figure 5.12c. This could be due to water, causing side reactions with the electrolyte which needs to be confirmed. In Figure 5.12d, NNM-PVDF showed an additional small cathodic peak at 3.6 V when cycled between 1.5 and 4.1 V, which decreased in intensity upon subsequent cycles, though the cause of this peak is also unknown. It is apparent here that the CV peaks at 4.3/4.0 V diminish with repeated cycling to 4.5 V, and such could be contributing to fast capacity fade in Figure 5.9. Further investigation is needed to determine the degradation mechanism at higher voltages for P3-NNM, to deconvolute potential oxygen redox and the P3-O3 phase transition. This is because oxygen redox and such phase transitions occur at similar potentials, in at least for the P2 form of this composition, and for other P3 structures with similar stoichiometries.[16,18,48,49]

The three pairs of peaks at intermediate potentials all showed similar behavior irrespective of binder and have all been associated in reported studies with Ni^{2+}/Ni^{3+}/Ni^{4+}.[35,50] The redox activity occurring at the lower potentials, *ca.* 2.0 V, can be attributed to the Mn$^{3+/4+}$ redox couple, as reported in P2-NNM.[2,62,63] With an extended lower voltage cutoff (1.5 V), greater initial discharge capacities were observed, along with faster capacity fading, Figure 5.9. This could be due to the formation of Jahn-Teller active Mn^{3+}, which may lead to local structural distortions and it is also prone to disproportionate to form Mn^{2+} and Mn^{4+} when in contact with electrolyte, where the former is liable to dissolution into the electrolyte.[51,62] With significant volume change, fresh surface can be exposed, where further dissolution of Mn can occur, leading to poor cycle stability.[51,59] This is an ongoing discussion, however, with some contradictory results in previously published studies. For example, some studies on P3-NNM have shown no Mn redox activity at low potentials, while Mn$^{3+/4+}$ redox has been reported in work on other very similar compositions, such as P3-Na$_{0.67}$Ni$_{0.2}$Mn$_{0.8}$O$_2$.[18,48]. XG binder had found to impede Mn^{2+} dissolution, potentially due to the strong interactions between the binder and active material.[2] A slight difference in the CV data was observed when cells were cycled below 2.0 V, figure 5.12c & 5.12d. XG exhibited minimal different in the redox couple that may be due to $Mn^{3+/4+}$, whereas there was a reduction in peak area from the 2nd to the 5th cycle for electrode containing PVDF binder. This could be an indication of suppressed Mn dissolution in XG containing electrode, which needs further investigation.

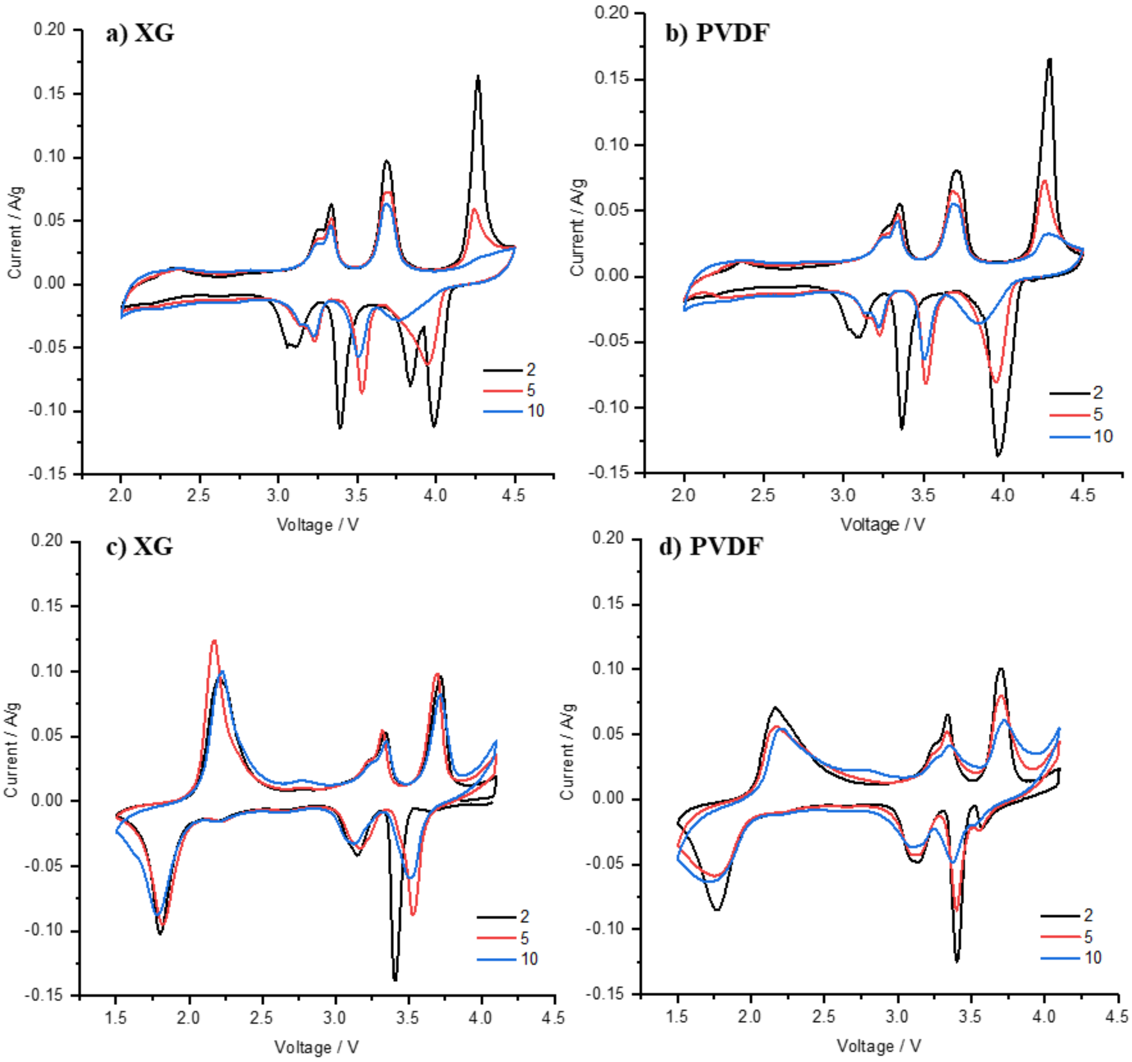

Figure 5.12: *Cyclic voltammograms recorded at 0.1 mV s^{-1} for cells containing P3-NNM with a&c) XG and b&d) PVDF. Cells were cycled between (a, c) 2.0 and 4.5 V or (c, d) 1.5 and 4.1 V.*

Figure 5.13 compares the rate capability of cathodes with different binders cycled between 2.0 and 4.5 V. Cells using each type of binder showed comparable performance at different C-rates, though the discharge capacities were slightly higher for the XG containing electrodes at all charge rates, and especially so at 2 C. This could be due to XG facilitating a more comprehensive conductive network, thus reducing charge transfer resistance.[2] The full potential of XG may not be realized as the SEM images, figure 5.7, showed fairly large agglomerates. This can lead to increased charge transfer resistance as there may be a large proportion of particles that are not in contact with conductive material and the binder, affecting the Na^+ kinetics.[64] Because of this, aggregation has been shown to negatively impact rate capability.[43,64]

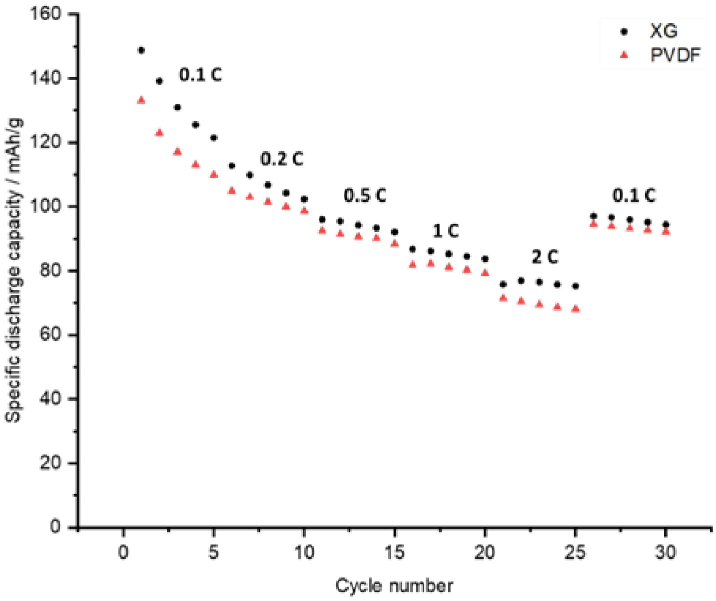

Figure 5.13: *Rate capability of P3-NNM when using xanthan gum (black circles) or PVDF (red triangles) as binder. Cells cycled galvanostatically between 2.0 and 4.5 V. Data obtained in a temperature controlled chamber at 25 °C using Maccor Series 4000 Battery Cycler.*

It is clear that exposure to water did not have a negative impact on key metrics of electrochemical performance for P3-NNM powder. The use of either PVDF or XG as binders lead to comparable cycling performance and stability and similar rate capability, regardless of voltage range of cycling. P3-NNM is therefore a good candidate for water-based binders, such as xanthan gum, which offers significant possible benefits in handling and safety through the elimination of toxic solvents such as NMP, without compromising electrochemical performance.

5.4 Conclusion

P3-$Na_{2/3}Ni_{1/3}Mn_{2/3}O_2$ (P3-NNM) has shown to be relatively stable under standard ambient conditions and on immersion on water, and that while the limited formation of hydrated phases did occur these were easily reversible on mild heating under vacuum. This suggests that P3-NNM is a suitable candidate material for the development of water-based binders. P3-NNM electrodes using xanthan gum binder showed similar microstructures and comparable performance. Most literature exhibited improved performance with XG , due to the ability of the binder to accommodate large volume change, reduce polarization, improve Li^+/Na^+ diffusion due to better dispersion of electrode components leading to a more comprehensive conductive network.[2–4] In this chapter, cycling at 0.1 C between 2.0 and 4.2 V, both electrodes prepared with XG and PVDF exhibited initial discharge capacities of *ca.* 115 mAh g^{-1} and after 50 cycles exhibit a capacity of 77 mAh g^{-1}. When the voltage range was extended to 1.5 – 4.5 V, both exhibited initial discharge capacities of *ca.* 210 mAh g^{-1}, higher than the theoretical capacity of 173 mAh g^{-1}, which could be due to oxygen and Mn redox and electrolyte oxidation. At this extended voltage range, both specimens exhibited poor capacity retention (41 %) after 50 cycles. The use of XG was expected to show an improvement in the P3-NNM electrochemical performance, however this did not come to fruition. This could have been due to agglomerated P3-NNM particles which was present in both electrodes containing XG and PVDF, therefore fewer particles were in contact with binder and conductive additive. Hence the additional benefits were not obvious. Regardless, XG represents a realistic and easily implementable water-based binder for P3-NNM, offering a timely pathway towards improved sustainability of battery fabrication without loss of performance.

5.5 Further Work

Overall, exposure to moisture and the use of xanthan gum binder did not negatively impact the performance of P3-NNM compared to PVDF. However, in the literature there have been studies that have shown the use of such binders conclusively improved the performance of the electrode, both in terms of capacity retention and rate capability. However, such significant improvement was not seen in this chapter, due to the agglomerated particles as shown in the SEM images in figure 5.7, regardless of binder used. This prevented a homogenous mixture of active material, conductive additive and binder, therefore fewer active particles were actually in contact with other electrode constituents. Hence, the benefits from XG such as accommodating volume change, impeding Mn dissolution, enhancing conductive network, were not realised in P3-NNM. Either the agglomerates in the active powder need to be broken up prior electrode preparation or use of an alternative mixing regime for the slurry. Studies that have used xanthan gum as a binder used ball milling to mix the slurry.[2,12] Future work would require XG containing slurries to be mixed using ball milling to break up agglomerates and ensure a homogenous mixture. Once this has been achieved for both electrodes containing XG and PVDF, electrochemical tests will need to be redone in order to obtain better comparison and determine whether the added benefits from XG can be achieved with P3-NNM.

Additional experiments to conduct would be Galvanostatic Intermittent Titration Technique (GITT) and electrochemical impedance spectra (EIS) to determine the Na^+ kinetics in the different electrodes which would elucidate the dispersion of the conductive additive. In P2-NNM, it has been reported that XG inhibits the dissolution of Mn to the electrolyte.[2] After optimisation of electrode preparation and the specimen containing XG binder performs significantly better, investigated into Mn dissolution is warranted. In the literature x-ray photoelectron spectroscopy (XPS) was used to determine to what extent this happens in the electrodes with different binders.[2] In addition, post cycling analysis using SEM and XRD can be used to determine differences in degradation mechanisms between the two electrodes. There are a variety of different soluble binders that has been studied in the literature. It is worth testing a variety of them, just in case there may be one that would be better suited for P3-NNM.

5.6 References

1. Zilinskaite, S., Reeves-McLaren, N. & Boston, R. Xanthan gum as a water-based binder for P3-Na2/3Ni1/3Mn2/3O2. *Front Energy Res* **10**, 909486 (2022).
2. Zhang, Y.-Y. *et al.* Improvement of electrochemical properties of P2-type $Na_{2/3}Mn_{2/3}Ni_{1/3}O_2$ sodium ion battery cathode material by water-soluble binders. *Electrochim. Acta* **298**, 496–504 (2019).

3. He, J., Zhong, H., Wang, J. & Zhang, L. Investigation on xanthan gum as novel water soluble binder for LiFePO 4 cathode in lithium-ion batteries. *J Alloys Compd* **714**, 409–418 (2017).

4. Leonard, A. F. & Job, N. Safe and green Li-ion batteries based on LiFePO 4 and Li 4 Ti 5 O 12 sprayed as aqueous slurries with xanthan gum as common binder. *Mater Today Energy* **12**, 168–178 (2019).

5. Li, R.-R. *et al.* Binders for sodium-ion batteries: progress, challenges and strategies. *Chem. Commun* **57**, 12406 (2021).

6. Lingappan, N., Kong, L. & Pecht, M. The significance of aqueous binders in lithium-ion batteries. *Renewable and Sustainable Energy Reviews* **147**, 111227 (2021).

7. Patra, J. *et al.* A Water-Soluble NaCMC/NaPAA Binder for Exceptional Improvement of Sodium-Ion Batteries with an SnO_2-Ordered Mesoporous Carbon Anode. *ChemSusChem* **11**, 3923–3931 (2018).

8. Versaci, D. *et al.* New eco-friendly low-cost binders for Li-ion anodes. *Journal of Solid State Electrochemistry* **21**, 3429–3435 (2017).

9. Chen, Z., Christensen, L. & Dahn, J. R. Comparison of PVDF and PVDF-TFE-P as Binders for Electrode Materials Showing Large Volume Changes in Lithium-Ion Batteries. *J. Electrochem. Soc.* **150**, A1073 (2003).

10. Yabuuchi, N., Kubota, K., Dahbi, M. & Komaba, S. Research Development on Sodium-ion Batteries. *Chem. Rev.* **114**, 11636–11682 (2014).

11. Liu, Z. *et al.* Ultralow Volume Change of P2-Type Layered Oxide Cathode for Na-Ion Batteries with Controlled Phase Transition by Regulating Distribution of Na^+. *Angew. Chem. Int. Ed* **60**, 20960–20969 (2021).

12. Li, S. *et al.* A compared investigation of different biogum polymer binders for silicon anode of lithium-ion batteries. *Ionics (Kiel)* **27**, 1829–1836 (2021).

13. Zhao, Y. M. *et al.* Advances of polymer binders for silicon-based anodes in high energy density lithium-ion batteries. *InfoMat* **3**, 460–501 (2021).

14. Shi, Y. *et al.* Unlocking the potential of P3 structure for practical Sodium-ion batteries by fabricating zero strain framework for Na+ intercalation. *Energy Storage Mater* **37**, 354–362 (2021).

15. Song, B. *et al.* A novel P3-type $Na_{2/3}Mg_{1/3}Mn_{2/3}O_2$ as high capacity sodium-ion cathode using reversible oxygen redox. *J. Mater. Chem. A* **7**, 1491–1498 (2019).

16. Liu, J. *et al.* Elucidation of the high-voltage phase in the layered sodium ion battery cathode material P3–Na 0.5 Ni 0.25 Mn 0.75 O 2. *J Mater Chem A Mater* **8**, 21151–21162 (2020).

17. Guo, S. *et al.* Understanding sodium-ion diffusion in layered P2 and P3 oxides via experiments and first-principles calculations: a bridge between crystal structure and electrochemical performance. *NPG Asia Mater.* **8**, 266–274 (2016).

18. Zhang, L. Electrochemical Performance and Structural Changes of $Na_{0.67}Mn_{0.67}Ni_{0.33}O_2$ as Cathode for Sodium Ion Batteries. (Technische Universität Berlin, 2019).

19. Saxena, P. & Shukla, P. A comprehensive review on fundamental properties and applications of poly(vinylidene fluoride) (PVDF). *Adv Compos Hybrid Mater* **4**, 8–26 (2021).

20. Wang, Z., Dang, G., Zhang, Q. & Xie, J. Xanthan Gum as a potential binder for graphite anode in lithium-ion batteries. *Int J Electrochem Sci* **12**, 7457–7468 (2017).

21. Cholewinski, A., Si, P., Uceda, M., Pope, M. & Zhao, B. Polymer binders: Characterization and development toward aqueous electrode fabrication for sustainability. *Polymers (Basel)* **13**, 631 (2021).

22. Zhao, Y. *et al.* Rational design of functional binder systems for high-energy lithium-based rechargeable batteries. *Energy Storage Mater* **35**, 353–377 (2021).

23. Yim, T. *et al.* Effect of binder properties on electrochemical performance for silicon-graphite anode: Method and application of binder screening. *Electrochim Acta* **136**, 112–120 (2014).

24. Wang, Y. B. *et al.* Strategies of binder design for high-performance lithium-ion batteries: a mini review. *Rare Metals* **41**, 745–761 (2022).

25. Li, J. T. *et al.* Water Soluble Binder, an Electrochemical Performance Booster for Electrode Materials with High Energy Density. *Adv Energy Mater* **7**, 1701185 (2017).

26. Keppeler, M., Tran, H. Y. & Braunwarth, W. The Role of Pilot Lines in Bridging the Gap Between Fundamental Research and Industrial Production for Lithium-Ion Battery Cells Relevant to Sustainable Electromobility: A Review. *Energy Technology* vol. 9 2100132 Preprint at https://doi.org/10.1002/ente.202100132 (2021).

27. Song, K. W., Kim, Y. S. & Chang, G. S. Rheology of concentrated xanthan gum solutions: Steady shear flow behavior. *Fibers and Polymers* **7**, 129–138 (2006).

28. Jakóbczyk, P., Bartmański, M. & Rudnicka, E. Locust bean gum as green and water-soluble binder for $LiFePO_4$ and $Li_4Ti_5O_{12}$ electrodes. *J. Appl. Electrochem.* **51**, 359–371 (2021).

29. Zhou, Y. N. *et al.* Air-Stable and High-Voltage Layered P3-Type Cathode for Sodium-Ion Full Battery. *ACS Appl. Mater. Interfaces* **11**, 24184–24191 (2019).

30. Zhang, Y. *et al.* Water-Stable Cathode for High Rate Na-Ion Batteries. *ACS Appl. Mater. Interfaces* **12**, 15220–15227 (2020).

31. Zuo, W. *et al.* The stability of P2-layered sodium transition metal oxides in ambient atmospheres. *Nat Commun* **11**, 3544 (2020).

32. Zhang, Y., Zhang, R. & Huang, Y. Air-Stable NaxTMO2 Cathodes for Sodium Storage. *Front. Chem.* **7**, 335 (2019).

33. Han, M. H. *et al.* Moisture exposed layered oxide electrodes as Na-ion battery cathodes. *J. Mater. Chem. A* **4**, 18963–18975 (2016).

34. Zilinskaite, S., Rennie, A. J. R., Boston, R. & Reeves-McLaren, N. Biotemplating: A sustainable synthetic methodology for Na-ion battery materials. *J. Mater. Chem. A* **6**, 5346–5355 (2018).

35. Lee, S. Y., Kim, J. H. & Kang, Y. C. Electrochemical properties of P2-type $Na_{2/3}Ni_{1/3}Mn_{2/3}O_2$ plates synthesized by spray pyrolysis process for sodium-ion batteries. *Electrochim. Acta* **225**, 86–92 (2017).

36. Wang, P. *et al.* Suppressing the P2-O2 Phase transition of Na0.67Mn0.67Ni0.33O2 magnesium substitution for improved sodium-ion batteries. *Angew. Chem. Int. Ed* **55**, 7445–7449 (2016).

37. Zhang, J., Wang, W., Wang, W., Wang, S. & Li, B. Comprehensive Review of P2-Type $Na_{2/3}Ni_{1/3}Mn_{2/3}O_2$, a Potential Cathode for Practical Application of Na-Ion Batteries. *ACS Appl. Mater. Interfaces* **11**, 22051–22066 (2019).

38. Lu, Z. & Dahn, J. R. Intercalation of Water in P2, T2 and O2 Structure Az[CoxNi$_{1/3-x}$Mn$_{2/3}$]O$_2$. *Chem. Mater.* **13**, 1252–1257 (2001).

39. Lu, Z., Donaberger, R. A. & Dahn, J. R. Superlattice ordering of Mn, Ni and Co in layered alkali transition metal oxides with P2, P3 and O3 structures. *Chem. Mater.* **12**, 3583–3590 (2000).

40. Zhang, L. *et al.* Stabilizing P3-Type Oxides as Cathodes for High-Rate and Long-Life Sodium Ion Batteries by Disordered Distribution of Transition Metals. *Small Methods* **4**, 2000422 (2020).

41. Courtel, F. M., Niketic, S., Duguay, D., Abu-Lebdeh, Y. & Davidson, I. J. Water-soluble binders for MCMB carbon anodes for lithium-ion batteries. *J Power Sources* **196**, 2128–2134 (2011).

42. Walsh, D., Arcelli, L., Ikoma, T., Tanaka, J. & Mann, S. Dextran templating for the synthesis of metallic and metal oxide sponges. *Nat. Mater.* **2**, 386–390 (2003).

43. Stein, M. *et al.* Probing the effect of high energy ball milling on the structure and properties of $LiNi_{1/3}Mn_{1/3}Co_{1/3}O_2$ cathodes for Li-ion batteries. *J. Electrochem. Energy Convers. Storage* **13**, 031001 1–10 (2016).

44. Hu, Y., Doeff, M. M., Kostecki, R. & Fiñones, R. Electrochemical Performance of Sol-Gel Synthesized $LiFePO_4$ in Lithium Batteries. *J. Electrochem. Soc.* **151**, A1279–A1285 (2004).

45. Liu, Y. *et al.* Hierarchical Engineering of Porous P2-$Na_{2/3}Ni_{1/3}Mn_{2/3}O_2$ Nanofibers Assembled by Nanoparticles Enables Superior Sodium-Ion Storage Cathodes. *Adv. Funct. Mater.* **30**, 1907837 (2020).

46. Tarascon, J. M., Morcrette, M., Saint, J., Aymard, L. & Janot, R. On the benefits of ball milling within the field of rechargeable Li-based batteries. *Comptes Rendus Chimie* **8**, 17–26 (2005).

47. Li, H. & Zhou, H. Enhancing the performances of Li-ion batteries by carbon-coating: present and future. *Chem. Commun* **48**, 1201–1217 (2012).

48. Kim, E. J. *et al.* Oxygen Redox Activity through a Reductive Coupling Mechanism in the P3-Type Nickel-Doped Sodium Manganese Oxide. *ACS Appl. Energy Mater.* **3**, 184–191 (2020).

49. Zhang, Y. *et al.* Revisiting the $Na_{2/3}Ni_{1/3}Mn_{2/3}O_2$ Cathode: Oxygen Redox Chemistry and Oxygen Release Suppression. *ACS Cent. Sci* **6**, 232–240 (2020).

50. Wang, Y. *et al.* Improved cycle and air stability of P3-$Na_{0.65}Mn_{0.75}Ni_{0.25}O_2$ electrode for sodium-ion batteries coated with metal phosphates. *Chem. Eng. J.* **372**, 1066–1076 (2019).

51. Hong, J. H., Wang, M. Y., Du, Y. Y., Deng, L. & He, G. The role of Zn substitution in P2-type $Na_{0.67}Ni_{0.23}Zn_{0.1}Mn_{0.67}O_2$ cathode for inhibiting the phase transition at high potential and dissolution of manganese at low potential. *J. Mater. Sci.: Mater. Electron.* **30**, 4006–4013 (2019).

52. Liu, Q. *et al.* P2-type $Na_{2/3}Ni_{1/3}Mn_{2/3}O_2$ as a cathode material with high-rate and long-life for sodium ion storage. *J. Mater. Chem. A* **7**, 9215–9221 (2019).

53. Ould, D. M. C. *et al.* New Route to Battery Grade NaPF6 for Na-Ion Batteries: Expanding the Accessible Concentration. *Angew. Chem. Int. Ed.* **60**, 24882–24887 (2021).

54. Bhide, A., Hofmann, J., Katharina Dürr, A., Janek, J. & Adelhelm, P. Electrochemical stability of non-aqueous electrolytes for sodium-ion batteries and their compatibility with Na0.7CoO2. *Physical Chemistry Chemical Physics* **16**, 1987–1998 (2014).

55. Ponrouch, A. *et al.* Non-aqueous electrolytes for sodium-ion batteries. *J Mater Chem A Mater* **3**, 22–42 (2015).

56. Li, Y. *et al.* Ether-based electrolytes for sodium ion batteries. *Chem. Soc. Rev* **51**, 4484 (2022).

57. Cuesta, N., Ramos, A., Cameán, I., Antuña, C. & García, A. B. Hydrocolloids as binders for graphite anodes of lithium-ion batteries. *Electrochim Acta* **155**, 140–147 (2015).

58. Solvay. Solef® PVDF Improves Battery Performance. https://www.solvay.com/en/brands/solef-pvdf/li-ion-batteries.

59. Wang, K., Yan, P. & Sui, M. Phase transition induced cracking plaguing layered cathode for sodium-ion battery. *Nano Energy* **54**, 148–155 (2018).

60. Wang, P. F. *et al.* Na^+/vacancy disordering promises high-rate Na-ion batteries. *Sci. Adv.* **4**, 1–9 (2018).

61. Lee, D. H., Xu, J. & Meng, Y. S. An advanced cathode for Na-ion batteries with high rate and excellent structural stability. *Phys. Chem. Chem. Phys.* **15**, 3304–3312 (2013).

62. Wen, Y. *et al.* Electrochemical and Structural Study of Layered P2-Type $Na_{2/3}Ni_{1/3}Mn_{2/3}O_2$ as Cathode Material for Sodium-Ion Battery. *Chem. Asian J.* **10**, 661–666 (2015).

63. Gutierrez, A. *et al.* On Disrupting the Na^+-Ion/Vacancy Ordering in P2-Type Sodium−Manganese−Nickel Oxide Cathodes for Na^+-Ion Batteries. *J. Phys. Chem. C* **122**, 23251–23260 (2018).

64. Zhang, X. *et al.* Understanding aggregation hindered Li-ion transport in transition metal oxide at mesoscale. *Energy Storage Mater* **19**, 439–445 (2019).

6 Conclusions

There are different factors to consider when improving sustainability of electrochemical energy storage, from the development of electrode materials to actual synthesis methods and cell preparation. The development of Na-ion technologies gives us the opportunity to build in sustainability from the ground up, in a way that has been more challenging with Li-ion. For example, polymers derived from nature are cheap, abundant and are environmentally friendly and can be used in numerous applications associated with Na-ion fabrication. Biotemplating uses these polymers during the synthesis process of functional materials to control the crystallisation and growth of intermediate phases so that reactions can occur quickly and at lower temperatures,[1] making such processes less energy intensive. This method also enables the formation of smaller particles, thus improving performance of battery materials due to shorted Na^+ diffusion lengths.[2]

Here, one of the aims was to investigate the crystallisation process of dextran biotemplated P3-$Na_{2/3}Ni_{1/3}Mn_{2/3}O_2$ (P3-NNM) Na-ion cathode material and to understand how the reaction intensity conditions were able to be significantly lowered, compared to methods such as traditional solid state synthesis. It was found that P3-NNM began to crystallise around 300 °C when the optimised amount of dextran was used, whereas during solid state it was around 500 °C. This was because during dextran biotemplating, there was minimal growth of intermediate phase while the biotemplate was still present, hence enabling the formation of numerous nucleation sites. Whereas in solid state synthesis, reactions relied on mass transport and concentration of nucleation sites were small due to the lack of atomic mixing from large precursors particles.

The other aim in this chapter was to optimise the amount of dextran used during synthesis and to compare the impact on phase progression with different biotemplate concentrations. The optimised quantity of dextran for 1 g of P3-NNM was 4 g (1 : 4) in terms of lower quantities of secondary phases after calcination at 650 °C for 2 h, which increased with lower concentration of dextran. However, specimen 1 : 1 formed more NiO compared to specimen synthesised without a template (1 : 0). This may be due to preferred binding of dextran with some cations over Ni which may have allowed unconstrained growth of NiO and constrained growth of other phases, leading to enhanced phase separation compared to specimen that did not use a template. In specimen 1 : 4, such effects were likely mitigated due to the sufficient amount of binding sites, which allowed early crystallisation of the P3 phase compared to 1 : 1.

Electrochemical performance was compared between the specimens synthesised with low and high concentrations of dextran (1 : 1 and 1 : 4 respectively). Specimen 1 : 1 had lower initial capacities but better cycling stability compared to 1 : 4, possibly due to vacancies in the TM layers in specimen 1 : 1, as most Ni was present in the form of NiO. In the literature it was found that vacancies inhibited high voltage phase transition such as the P2-O2 in P2-type materials and due to the more flexible TMO_6, distortions during cycling were better accommodated.[3–5] This may be the case in P3-NNM, however further investigation is needed. These preliminary findings give opportunity to investigate alternative methods to improve electrochemical performance of such materials.

Materials that undergo high voltage phase transitions such as P2-O2 in $Na_{2/3}Ni_{1/3}Mn_{2/3}O_2$ exhibit poor cycling stability caused by structural instability.[6] A common way to prevent such phase transitions is to substitute some Ni for other transition metals that are either electrochemically inactive or transfer less electron during the redox reactions compared to Ni^{2+}/Ni^{4+}.[7] This ensures more Na remains in the Na layers, hence stabilising the structure to higher voltages. Here, Ni^{2+} was substituted for Cu^{2+} in P3-

$Na_{1/3}Ni_{1/3-x}Cu_xMn_{2/3}O_2$, which has not been attempted in the literature for this polymorph. These materials were also synthesised using dextran biotemplating, due to the intrinsic ability of this method to aid the formation of complex ternary and quaternary systems.[1] P3-type phases were successfully synthesised, with minimal secondary phases up to a Cu content of x = 1/6. Specimen x = 1/6 exhibited significantly improved cycling stability when cycled at 2.0 – 4.5 V at 0.1 C compared to x = 0 (P3-NNM). Initial results showed that this was likely attributed to inhibited P3-O3 phase transition and possibly better reversibility of anionic redox of lattice oxygen. Cu containing specimens also exhibited better performance at 1 C when either cycled from 2.0 V to 4.2 V or 4.5 V.

Normally, substituting in other metals into NNM causes destruction of TM ordering, leading to smoother voltage profiles and hence improved rate capability.[8] In the literature it was found that Cu substitution improved performance of P2-NNM, while maintaining ordering.[9] This may be the case for the P3 polymorph, as voltage profiles were smoother with increased Cu content but XRD patterns showed presence of a small peak at low angles which could be from superstructure Na^+/vacancy ordering. Therefore improved performance may be due to an increase *c*-axis, negating the impacts of Na^+/vacancy and TM ordering in the structure. The Cu containing materials also showed good stability after immersion in water, making them good candidates for water soluble binders.

P3-NNM was found to be relatively stable in ambient conditions as well as after immersion in water. In some instances, relatively small quantities of the hydrated phase formed which was easily removed after vacuum drying at 120 °C. This allowed for P3-NNM slurries to be prepared with a water soluble binder, xanthan gum (XG). Electrochemical performance was compared to electrodes prepared with PVDF and NMP. There was no significant difference between the two different cathodes, indicating that exposure during slurry preparation did not cause lasting damage to the material.

In the literature, the use of XG in other electrode materials exhibited improved performance compared to those that were prepared with PVDF due the high viscosity which preserved the conductive network and the "self-healing" hydrogen bonds that enable the binder to accommodate volume change.[10–12] Such improvement were not observed here, due to the agglomerated P3-NNM particles that are a product of the synthesis process, minimising contact with the binder and conductive additive Improvement in performance can be achieved through better mixing regimes.

The use of biopolymers are an easy way to improve sustainability across the remit of electrochemical energy storage. Once amount of dextran was optimised for biotemplating synthesis of P3-NNM, crystallisation was able to occur at lower temperatures, hence less energy was required during the process. Layered oxides with increased complexity such as P3-$Na_{2/3}Ni_{1/3-x}Cu_xMn_{2/3}O_2$ were also synthesised with ease using the same method. Such materials also showed suitability for water-soluble binders, removing the need for toxic, expensive and difficult to recycle PVDF binder and NMP solvent. Preliminary results showed that there was no negative impact on electrochemical performance after water exposure during slurry preparation with XG. This enables the use of cheap and environmentally friendly binder. Other materials that are also stable after contact with water can also benefit from such binders.

The demand for electrochemical energy storage will continue to rapidly increase, especially with the rise of electric vehicles and stationary grid storage for renewable energy. Therefore the ability to quickly synthesise material in a sustainable way is just as important as developing materials from sustainable sources. Such simple synthesis techniques like biotemplating, can be used for a variety of electrode materials, especially where energy use during the process could be greatly reduced.

6.1 References

1. Danks, Ashleigh. E., Hall, S. R. & Schnepp, Z. The evolution of ‘sol-gel’ chemistry as a technique for materials synthesis. *Mater. Horiz.* **3**, 91–112 (2016).
2. Zilinskaite, S., Rennie, A. J. R., Boston, R. & Reeves-McLaren, N. Biotemplating: A sustainable synthetic methodology for Na-ion battery materials. *J. Mater. Chem. A* **6**, 5346–5355 (2018).
3. Yang, L. *et al.* Superiority of native vacancies in activating anionic redox in P2-type Na2/ 3[Mn7/9Mg1/9□1/9]O2 . *Nano Energy* **78**, 105172 (2020).
4. Bai, X., Iadecola, A., Tarascon, J. M. & Rozier, P. Decoupling the effect of vacancies and electropositive cations on the anionic redox processes in Na based P2-type layered oxides. *Energy Storage Mater* **31**, 146–155 (2020).
5. Yang, L. *et al.* Effect of vacancy-tailored Mn 3 + spinning on enhancing structural stability. *Energy Storage Mater* **44**, 231–238 (2022).
6. Wang, K., Yan, P. & Sui, M. Phase transition induced cracking plaguing layered cathode for sodium-ion battery. *Nano Energy* **54**, 148–155 (2018).
7. Zhang, J., Wang, W., Wang, W., Wang, S. & Li, B. Comprehensive Review of P2-Type $Na_{2/3}Ni_{1/3}Mn_{2/3}O_2$, a Potential Cathode for Practical Application of Na-Ion Batteries. *ACS Appl. Mater. Interfaces* **11**, 22051–22066 (2019).
8. Zhang, Y. *et al.* Water-Stable Cathode for High Rate Na-Ion Batteries. *ACS Appl. Mater. Interfaces* **12**, 15220–15227 (2020).
9. Zheng, L., Li, J. & Obrovac, M. N. Crystal Structures and Electrochemical Performance of Air-Stable $Na_{2/3}Ni_{1/3-x}Cu_xMn_{2/3}O_2$ in Sodium Cells. *Chem. Mater.* **29**, 1623–1631 (2017).
10. He, J., Zhong, H., Wang, J. & Zhang, L. Investigation on xanthan gum as novel water soluble binder for LiFePO 4 cathode in lithium-ion batteries. *J Alloys Compd* **714**, 409–418 (2017).
11. Zhang, Y.-Y. *et al.* Improvement of electrochemical properties of P2-type $Na_{2/3}Mn_{2/3}Ni_{1/3}O_2$ sodium ion battery cathode material by water-soluble binders. *Electrochim. Acta* **298**, 496–504 (2019).
12. Li, S. *et al.* A compared investigation of different biogum polymer binders for silicon anode of lithium-ion batteries. *Ionics (Kiel)* **27**, 1829–1836 (2021).

A. Appendix for chapter 3

A.1 Calculations for water content in acetate precursors

The amount of water for each acetate precursor was calculated from TGA results in figure 3.3 using the method outlined below, using NaOAc from May as an example:

1. Mass of dehydrated acetate salt was obtained between 150 and 250 °C, assuming the mass loss was due to water.

Starting mass of NaOAc is 7.19 mg, with a mass loss of 8 % at 150 °C. Therefore dry acetate mass is $6.6148 \mathrm{x} 10^{-3}$ *g and mass of water is the mass loss which is* $5.7520 \mathrm{x} 10^{-4}$ *g.*

2. Moles of dried acetate was obtained by dividing mass of dried acetate by Mr of dehydrated acetate.

$6.6148 \mathrm{x} 10^{-3}$ *g / 82.0342 =* $8.0635 \mathrm{x} 10^{-5}$ *mols*

3. This was then multiplied by Avogadro's constant to obtain number of dried acetate molecules.

$8.0635 \mathrm{x} 10^{-5}$ *mols x* $6.0221 \mathrm{x} 10^{23}$ *=* $4.8560 \mathrm{x} 10^{19}$ *molecules of sodium acetate*

4. To calculated the number of water molecules from the initial mass in TGA data, the mass loss from dehydration was divided by Mr of water to obtain moles.

$5.7520 \mathrm{x} 10^{-4}$ *g / 18 =* $3.1956 \mathrm{x} 10^{-5}$ *mols*

5. Moles of water was then multiplied by Avogadro's constant to obtain number of water molecules.

$3.1956 \mathrm{x} 10^{-5}$ *mols x* $6.0221 \mathrm{x} 10^{23}$ *=* $1.9244 \mathrm{x} 10^{19}$ *molecules of water*

6. The amount of water in the acetate salt was obtained by comparing the ratio of acetate salt molecules to water molecules.

Sodium acetate: $4.8560 \mathrm{x} 10^{19} / 4.8560 \mathrm{x} 10^{19} = 1$

Water: $1.9244 \mathrm{x} 10^{19} / 4.8560 \mathrm{x} 10^{19} = 0.40$

Hence the formula of acetate is $NaC_2H_3O_2 \cdot 0.4H_2O$

A.2 Calculations for number of cations in precursor solution to synthesise 1 g $Na_{2/3}Ni_{1/3}Mn_{2/3}O_2$ (NNM)

Mol of NNM

1 g / 103.514 M_r = $9.661x10^{-3}$ mol

Number of Na cations

Molar ratio of Na in NNM is 2/3

Mols of Na is 2/3 x $9.661x10^{-3}$ = $6.441x10^{-3}$

Number of Na cations $6.441x10^{-3}$ x $6.022x10^{23}$ = $3.879x10^{21}$

Number of Mn cations

Molar ratio of Mn in NNM is 2/3

Mols of Mn is 2/3 x $9.661x10^{-3}$ = $6.441x10^{-3}$

Number of Mn cations $6.441x10^{-3}$ x $6.022x10^{23}$ = $3.879x10^{21}$

Number of Ni cations

Molar ratio of Ni in NNM is 1/3

Mols of Ni is 1/3 x $9.661x10^{-3}$ = $3.220x10^{-3}$

Number of Mn cations $3.220x10^{-3}$x $6.022x10^{23}$ = $1.939x10^{21}$

Total number of cations

$3.879x10^{21}$ + $3.879x10^{21}$ + $1.939x10^{21}$ = **$9.697x10^{21}$**

<u>**Calculations for number of binding sites in dextran**</u>

M_r of linear formula $(C_6H_{10}O_5)_n$ is 162.139

Binding sites in 1 g dextran

Mol is 1 / 162.139 = $6.168x10^{-3}$

Number of hydroxyl groups that would act as a binding site in each glycosidic ring is 2

Molar ratio of binding sites 2 x $6.168x10^{-3}$ = 0.012

Total of number of binding sites in 1 g dextran 0.012 x $6.022x10^{23}$ = $7.226x10^{21}$

Binding sites in 4 g dextran

Mol is 4 / 162.139 = 0.025

Molar ratio of binding sites 2 x 0.025 = 0.050

Total of number of binding sites in 4 g dextran 0.050 x $6.022x10^{23}$ = $3.011x10^{22}$

Specimen	**Cations : binding sites**
1 : 1	1 : 0.75
1 : 4	1 : 3.11